Development of a silicon photomultiplier based scintillator detector for cosmic air showers

Von der Fakultät für Mathematik, Informatik und Naturwissenschaften der RWTH Aachen University zur Erlangung des akademischen Grades eines Doktors der Naturwissenschaften genehmigte Dissertation

vorgelegt von

Julian Kemp, M.Sc. RWTH

aus Datteln

Berichter: Universitätsprofessor Dr. rer. nat. Thomas Hebbeker
Professor als Juniorprofessor Dr. rer. nat. Thomas Bretz

Tag der mündlichen Prüfung: 07.12.2020

Diese Dissertation ist auf den Internetseiten der Universitätsbibliothek online verfügbar.

Abstract

The study of cosmic rays was always driven by the development and application of new technologies to enhance the precision of experiments. In recent years, the huge advancements in the photon detection using Silicon Photomultipliers (SiPMs) led to outstanding performance of these devices and promise an important step forward in detector technology. In this thesis, their characteristics are studied with special focus on simulating their response and understanding the behavior when being exposed to bright or long lasting light pulses.

An SiPM based optical module has been developed to prove their maturity for applications in cosmic ray induced air shower detectors. A perfect candidate for studying its performance is the Scintillator Surface Detector (SSD) developed for an upgrade of the Pierre Auger Observatory, AugerPrime. The SSD was designed to improve the sensitivity of the current detector on the mass composition of the primary cosmic rays and to possibly reveal their origin. The SiPM based optical module was installed in prototype SSDs at the Pierre Auger Observatory. It has proven excellent performance and allows to study Ultra High Energy Cosmic Rays (UHECRs) with good precision.

Zusammenfassung

Das Studium kosmischer Strahlung wurde stets durch die Entwicklung und Anwendung neuer Technologien vorangetrieben, um die Präzision der Experimente zu verbessern. In den letzten Jahren wurden große Fortschritte in der Detektion von Photonen mit Silizium Photomultipliern (SiPMs) gemacht, die heute für eine ausgezeichnete Leistung sorgen und einen wichtigen Meilenstein in der Detektortechnologie darstellen. Im Rahmen dieser Arbeit wurden ihre Charakteristiken untersucht mit besonderem Fokus auf die Simulation ihrer Signale und dem Verständnis ihres Verhaltens bei Beleuchtung mit hellen oder lang andauernden Lichtpulsen.

Ein auf SiPMs basierendes optisches Modul wurde entwickelt, um ihre Leistung bei der Anwendung in Detektoren zum Nachweis der durch kosmische Strahlung induzierten Luftschauer zu untersuchen. Ein perfekter Kandidat, um ihre Eigenschaften zu verstehen, ist der Scintillator Surface Detector (SSD), der im Rahmen der Nachrüstung AugerPrime für das Pierre Auger Observatorium entwickelt wurde. Der SSD wurde entworfen, um die Sensitivität des Observatoriums auf die Massenkomposition der primären kosmischen Strahlung zu erhöhen und möglicherweise ihre Quellen zu finden. Das auf SiPMs basierende optische Modul wurde in Prototypen des SSD am Pierre Auger Observatorium installiert. Es hat exzellente Leistung gezeigt und erlaubt das Studium von ultra hochenergetischer kosmischer Strahlung mit hoher Präzision.

Contents

Chapter 1

Introduction

Cosmic rays were discovered in 1912 when Victor Hess, through balloon flights, realized that the natural radioactivity measured on Earth's ground does not solely originate from the soil. Instead, he detected the bombardment of the Earth's atmosphere with energetic particles from space and got honored with the Nobel prize together with Carl Anderson in 1936. The investigation of the nature of cosmic rays commenced and an important milestone was reached in 1938 by Pierre Auger's discovery of particle cascades initiated by the primary cosmic rays in the atmosphere. It motivated the implementation of a new class of experiments dedicated to the precise study of these so called air showers and the characteristics of the primary particle. Due to the low flux of cosmic rays of one particle per century and km^2 at the highest energies close to 10^{20} eV, the measurement of air showers is the only possibility for their study. So far, these detectors are only ground based experiments but plans exist to detect air showers also from satellites.

Despite the more than 100 year old knowledge of the existence of cosmic rays, several key questions on their nature remain unanswered. While the all particle energy spectrum is known to good precision, the composition of the types of cosmic ray particles is not. This question is tightly connected to their origin. Cosmic rays, being charged particles, are deflected in galactic and extragalactic magnetic fields producing an isotropic distribution of arrival directions. Only at the highest energies particles with low charge such as protons might point back to their source locations. The details and current status of the studies of cosmic rays will be discussed in chapter 2.

Most recent cosmic ray air shower detectors aim at solving these riddles by exploiting improved detector technologies, allowing for unprecedented precision in the measurements of air showers. The different types of measurement techniques will be introduced in chapter 3. The largest experiment of this kind, the Pierre Auger Observatory, is currently undergoing a major upgrade of its detector, AugerPrime, to, among other goals, achieve improved sensitivity on the mass of the primary particle. It will be discussed in detail in chapter 4. A main contribution is the installation of additional scintillator detectors, enhancing the performance of the currently installed water-Cherenkov detectors. Their design is presented in chapter 5 followed by a description of their production and the test procedure that was developed by the author of this thesis.

The main work presented in this thesis is closely connected to the scintillator detectors. An optical module on the base of Silicon Photomultipliers (SiPMs) has been developed and proposed as a readout system. It will be introduced in chapter 7. It was installed and tested at the Pierre Auger Observatory proving the maturity of this concept. Results of these measurements are discussed in chapter 8.

At the same time, SiPMs which are semiconductor based light detectors have been studied in great detail. Despite their usage for several years, their behavior is not fully understood especially when being exposed to bright light pulses. The focus of the experiments performed in the scope of this thesis is the determination of the dynamic range. Algorithms have been developed to make use of signals even in a highly non-linear regime of the SiPM response. These studies are described in chapter 6.

Until now, no large scale application of SiPMs in astroparticle physics was established but several experiments, especially Cherenkov telescopes, have already proven the performance of SiPMs. The measurements performed in the scope of this thesis add valuable information for future prospects of using SiPMs.

Chapter 2

Cosmic rays

Cosmic rays are charged energetic particles propagating through space. When reaching Earth, they interact with the atmosphere and initiate particle cascades allowing for their detection. The study of cosmic rays began with their discovery by Victor Hess in 1912 when an increase in the radiation level was detected during balloon flights at high altitudes [1]. Prior to these balloon flights, it was believed that the natural radiation originates from the soil.

In the early days of the study of cosmic rays on balloon flights or on high mountains, primary cosmic rays were thought to be directly going through the detector. Only in the late 1930s, air showers were identified as being a cascade of secondary particles initiated by cosmic rays high in the atmosphere [2]. Cosmic rays are therefore only detected indirectly and a reconstruction of the air shower is necessary to estimate properties of the incident primary cosmic ray. Good overviews about the historic development of cosmic ray research can be found for example in [3, 4].

Nowadays, experiments studying cosmic rays can be separated in two main classes depending on the energy range to be studied. Detectors hosted by a satellite in space or balloon in the stratosphere allow for a direct measurement of the cosmic ray particle [5, 6]. These detectors are rather small sized and therefore a high flux is needed to achieve sufficient statistics. Alternatively, ground based detectors observe the air shower that develops in the atmosphere [7, 8, 9]. Being on the Earth's surface, they can cover large areas but the energy of the primary cosmic rays must be sufficient to initiate a large air shower.

The work of the author of this thesis contributes to the Pierre Auger Observatory which will be introduced in chapter 4. It is a ground based array studying cosmic rays with energies $E \gtrsim 10^{18}\,\mathrm{eV}$. These cosmic rays are usually referred to as Ultra High Energy Cosmic Rays (UHECRs) and this chapter will focus on the research in their field.

The information on cosmic rays and air showers given in this chapter is based on [10, 11, 12]. The interested reader is referred to these publications for further details.

2.1 The energy spectrum of cosmic rays

The energy spectrum of cosmic rays has been measured by a multitude of experiments over several orders of magnitude in energy and flux. These measurements are summarized

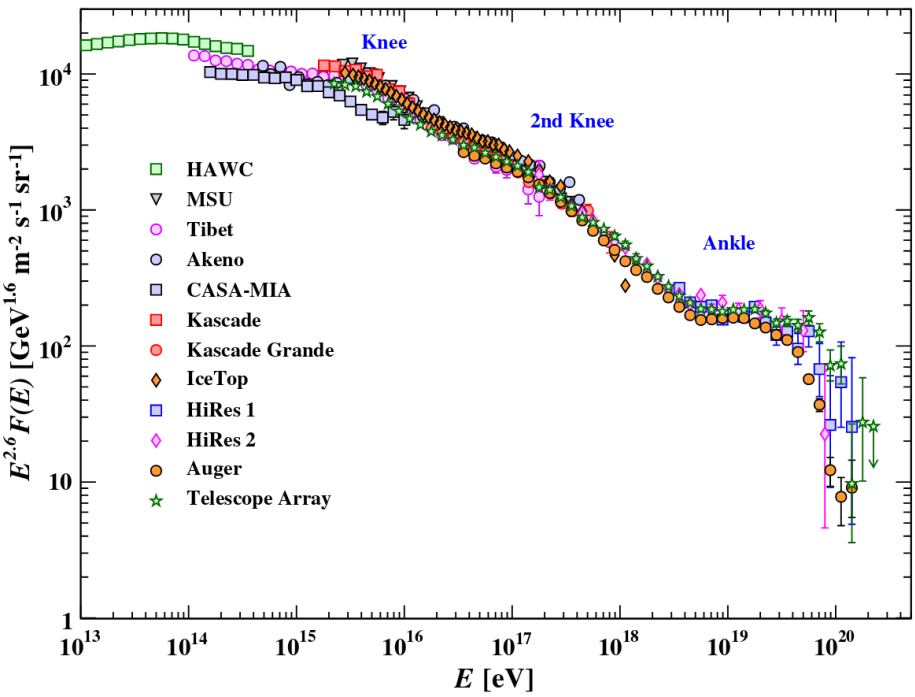

Figure 2.1: The energy spectrum of cosmic rays as measured by ground based experiments detecting cosmic ray air showers. The differential flux is multiplied by $E^{2.6}$ to improve visibility of features in the spectrum. The errorbars show the statistical uncertainty. The systematic uncertainty, especially on the energy scales of the different experiments, are not shown. Taken from [13].

in figure 2.1 for energies above 10^{13} eV. The spectrum can be well described by a broken power law:

$$F(E) = \frac{\mathrm{d}^4 N}{\mathrm{d}E\mathrm{d}\Omega\mathrm{d}t\mathrm{d}A} \propto \left(\frac{E}{\mathrm{eV}}\right)^{-\gamma} \tag{2.1}$$

with the spectral index γ. Different regions of the spectrum can be described by different spectral indices. At an energy of $\approx 4 \times 10^{15}$ eV, it changes from $\gamma \approx 2.7$ to $\gamma \approx 3.1$ [14, 15]. This steepening of the spectrum is called the *knee*. A *second knee* can be seen at an energy of about 10^{17} eV where the spectral index changes to $\gamma \approx 3.3$ [16]. At the *ankle* at $E = 4 \times 10^{18}$ eV, the spectrum flattens to $\gamma \approx 2.7$ [16]. The last feature is the *cut-off* at an energy of $E_{1/2} = 2.3 \times 10^{19}$ eV where the spectrum drops dramatically [17]. The energy $E_{1/2}$ corresponds to the energy where the flux drops below 50 % compared to the expectation without a cut-off.

The origin of these features is unclear but several models have been proposed to explain the energy spectrum of cosmic rays. It is typically assumed that the knee marks the beginning of the transition from a galactic to an extragalactic origin of the cosmic rays [14]. For energies of $E \gtrsim 10^{18}$ eV and a Galactic Magnetic Field (GMF) of $B \sim$ µG [18], the Larmor radius[1] of a proton would be $r_l \sim$ kpc. This is already at the order of the thickness

[1]The Larmor radius is the radius of the trajectory a charged particle describes when moving through a magnetic field. From electrodynamics it can be determined as $r_l = p_\perp c / (|q|B)$, with q the charge of the particle, B the magnetic field strength and $p_\perp$ the momentum of the particle perpendicular to the magnetic field.

of the galactic disc and these high energy particles are not confined in the Galaxy. When discussing these models, the main topics of interest are the acceleration of cosmic rays to all the energies present in the spectrum and their propagation through galactic and extragalactic space. These studies are affected by the lack of knowledge of the origin of UHECRs due to the deflection in magnetic fields.

2.2 Acceleration of cosmic rays

Given that the energy spectrum of cosmic rays follows a power law, typical acceleration mechanisms considered are of non-thermal nature. The mechanisms are separated in two major classes: *top-down* and *bottom-up* models. In top-down models, the cosmic ray particle is not accelerated but is produced directly either in the decay or annihilation of a super heavy particle or in the collapse of topological defects [19, 20, 21]. As this class of production mechanisms of cosmic rays is disfavored by current measurements of the flux of ultra-high energy photons [22], they will not be discussed in further detail. The interested reader is referred to the aforementioned publications.

In contrast, in bottom-up models the cosmic ray particle is accelerated from an initially low energy to a higher energy. The most prominent models considered nowadays base on a theory proposed by Fermi, and hence, is called *Fermi acceleration* [23]. For *second order Fermi acceleration*, interactions with magnetized clouds are considered. Later, the more efficient but similar *first order Fermi acceleration* mechanism was developed by using shock fronts that form when dense matter moves faster than the speed of sound in the interstellar medium [11, 24]. A good review of the mechanism of both types of Fermi acceleration can be found for example in [12, 25], where the following description is based on.

2.2.1 Second order Fermi acceleration

In homogeneous magnetic fields, charged particles are bent on a circular orbit with a radius known as Larmor radius. They do not gain energy but only the component of their momentum perpendicular to the magnetic field changes.

This picture changes when the magnetic field is assumed to be non-homogeneous. It can be shown that the ratio of the kinetic energy perpendicular to the magnetic field $E_\perp$ and the magnetic field B is constant:

$$\frac{E_\perp}{B} = \text{const.} \qquad . \tag{2.2}$$

This means that in an increasing magnetic field also $E_\perp$ has to increase and vice versa. Due to energy conservation, the energy parallel to the magnetic field $E_\parallel$ must then also change to compensate the change in $E_\perp$. Again, in an increasing magnetic field this leads to a decrease in $E_\parallel$. At some point, $E_\parallel = 0$ and $E_\perp$ cannot increase anymore. In fact, the direction of the particle is reversed such that it experiences a decreasing magnetic field leading to a decrease in $E_\perp$ and an increase in $E_\parallel$. The particle is thus reflected off the inhomogeneous magnetic field and magnetic fields can pose a barrier that cannot be traversed by charged particles with too low energy. A charged particle between two areas of increasing magnetic field can therefore be trapped and reflected back and forth between the two.

Inhomogeneous magnetic fields can, for example, develop in gas clouds. For a non-moving gas cloud, an incident charged particle would thus be reflected but no energy is gained.

For a moving cloud this picture changes. In the following, a one dimensional analysis is performed assuming that the particle and the cloud move along the same axis. A particle with energy E_1 in the frame of an observer has an energy E_1' in the rest frame of the cloud:

$$E_1' = \gamma E_1 (1 \pm \beta) \tag{2.3}$$

with the relativistic velocity $\beta = v/c$, v the velocity of the cloud and $\gamma = \left(1 - \beta^2\right)^{-1/2}$ the Lorentz factor. The positive sign in the bracket corresponds to a head-on collision while for the negative sign both cloud and particle are moving in the same direction. In the rest frame of the cloud, the energy of the particle after the collision, E_2', is the same as before the collision. Transforming the energy E_2' back to the frame of the observer yields:

$$E_2 = \gamma E_2' (1 \pm \beta) \tag{2.4}$$

with the positive and negative sign as in equation (2.3). Inserting equation (2.3) into (2.4) with $E_2' = E_1'$ connects the energies before and after the collision in the observer frame:

$$E_2 = \gamma^2 E_1 (1 \pm \beta)^2 \qquad . \tag{2.5}$$

The relative gain or loss in energy is then given by

$$\frac{\Delta E_\pm}{E_1} = \frac{E_2 - E_1}{E_1} = \gamma^2 (1 \pm \beta)^2 - 1 = \pm \frac{2\beta}{1 \mp \beta} \qquad . \tag{2.6}$$

The particle can be scattered off multiple clouds back and forth leading to consecutive changes in the energy. The probability P of hitting a cloud depends on its direction of motion:

$$P_\pm \propto 1 \pm \beta \qquad . \tag{2.7}$$

The average gain in energy per collision is then given by:

$$\frac{\Delta E}{E} = P_+ \frac{\Delta E_+}{E} + P_- \frac{\Delta E_-}{E} = 4 \frac{\beta^2}{1 - \beta^2} \overset{\beta \ll 1}{\approx} 4\beta^2 \tag{2.8}$$

which is proportional to the square of the velocity of the cloud. As a consequence, this mechanism is known as *second order* Fermi acceleration[2]. Because of the typically non-relativistic movements of magnetic clouds ($\beta \ll 1$) this mechanism is quite inefficient. In addition, the distance d between different clouds is huge, i.e. $d \sim 0.1\,\mathrm{pc}$ leading to only a few collisions per year [12]. This mechanism is thus not able to explain the energy spectrum of cosmic rays.

2.2.2 First order Fermi acceleration

The main constraint for efficient acceleration in second order Fermi acceleration is the energy loss in collisions when the direction of motion of the particle and the cloud are parallel. The efficiency could be significantly increased if only head-on collisions occur. In a rather naive approach, the probabilities given in equation (2.7), would become $P_+ = 1$ and

[2] The factor of 4 on the right side of equation (2.8) should actually be a factor of 4/3. The additional factor of 1/3 would result from a correct three dimensional calculation taking into account all the possible incident and scattering angles.

$P_- = 0$. This yields an energy gain of:

$$\frac{\Delta E}{E} = \frac{\Delta E_+}{E} = \frac{2\beta}{1-\beta} \overset{\beta \ll 1}{\approx} 2\beta \quad . \tag{2.9}$$

The energy gain is now proportional to β and therefore called *first order* Fermi acceleration[3]. Because of the small velocity of magnetic clouds ($\beta = \mathcal{O}\left(10^{-2}\right)$), the efficiency of the first order Fermi acceleration can significantly exceed that of second order Fermi acceleration.

A situation where only head-on collisions are realized is known as Diffusive Shock Acceleration (DSA). These occur for example from supernova remnants that eject a huge amount of matter with supersonic speed into the interstellar medium. This interaction forms a shock front where an abrupt change in the density, pressure and temperature occurs. A particle moving to the downstream side of the shock front will get reflected in the shock and gain energy according to equation (2.9). Now, the matter upstream the shock front is moving opposite to the direction of the particle. Again, a head-on collision occurs and the particle is bounced back and forth between the two sides of the shock front.

Besides the fact that only head-on collisions occur in this scenario, also the distances to be traveled between two consecutive reflections is significantly lower compared to second order Fermi acceleration. This leads to a faster acceleration of the particle.

After n collisions, the particle has an energy of

$$E_n = E_0 \left(1 + \Delta E\right)^n \tag{2.10}$$

with E_0 the initial energy of the particle. Between each collision, the particle has a probability P to escape the shock region. The probability to undergo at least n collisions is then given by:

$$P_n = (1-P)^n = (1-P)^{\ln\left(E_n/E_0\right)/\ln\left(1+\Delta E\right)} \tag{2.11}$$

where in the last step equation (2.10) was used to replace n. The probability P_n is equal to the number of particles N escaping after n collisions with respect to the total number of particles N_0. Using this fact and simplifying equation (2.11) leads to a power law for the number of particles escaping from the shock region with an energy larger E_n:

$$P_n = \frac{N}{N_0} = \left(\frac{E_n}{E_0}\right)^{-\alpha} \tag{2.12}$$

with $\alpha = -\ln\left(1-P\right)/\ln\left(1+\Delta E\right)$. The derivative of N with respect to E then yields the differential energy spectrum:

$$\frac{\mathrm{d}N}{\mathrm{d}E} \propto \left(\frac{E}{E_0}\right)^{-\gamma} \tag{2.13}$$

where $\gamma = \alpha + 1$ is the spectral index.

It can be shown that for first order Fermi acceleration in shocks $\gamma \approx 2$. The described process is thus able to phenomenologically describe the measured energy spectrum. In order to also get the correct spectral index, effects of the propagation from the source to Earth through the interstellar or extragalactic medium have to be taken into account.

[3]The factor of 2 in equation (2.9) is oversimplified. A full derivation would yield a factor of 4/3 instead.

2.2.3 Propagation of cosmic rays

Propagation of cosmic rays is a complex and not yet fully understood process. In general, various contributions need to be taken into account. These include diffusion due to gradients in the particle density, convection, energy losses and gains by, for example, ionization or further acceleration, and decay and spallation processes. Magnetic fields pervading Galactic and Extragalactic space deflect the charged cosmic rays and need to be considered. Dedicated simulation frameworks exist in order to provide an understanding of at least parts of these processes [26, 27].

Already from significantly simplified models, so called *leaky-box models*, conclusions can be drawn. These assume a uniformly distributed source population inside a finite volume (box). The cosmic rays can freely propagate but with some probability they can leave the box through its walls. The probability of escaping the box can be energy dependent leading also to different characteristic escape times τ_{esc}. Even though the dependence of the escape time is not known a priori, measurements of the flux ratio of secondary boron and carbon, allow to deduce [28]:

$$\tau_{\text{esc}} \propto E^{-\delta} \tag{2.14}$$

with $\delta \approx 0.6$.

This energy dependence needs to be taken into account when describing the cosmic ray energy spectrum as measured at Earth. The energy spectrum at the source (eq. (2.13)) needs to be corrected for the energy dependence of the escape time leading to

$$\frac{\mathrm{d}N}{\mathrm{d}E} \propto \left(\frac{E}{E_0}\right)^{-\gamma-\delta} \quad . \tag{2.15}$$

The spectral index is thus $\gamma + \delta \approx 2.6$ which agrees well with the measurement up to the knee.

2.2.4 The knee of the spectrum

At the knee, the spectral index changes. Two major scenarios can be distinguished that are able to explain this transition [10].

The first scenario denotes effects of propagation of the cosmic rays in the interstellar medium, limiting the maximum energy these particles can have when reaching Earth. The leaky-box model, as described above, is a significant simplification of the true processes. Differences can thus be expected. Cosmic rays being charged particles are deflected in magnetic fields. If the Larmor radius, r_l, is in the order of the coherence length of the turbulences in the GMF, the cosmic rays are not confined in the Galaxy anymore but can escape [29]. Thus, the flux of high energy cosmic rays would be suppressed and the spectrum steepens at the energy where r_l gets too large. The energy where suppression sets in would be rigidity[4] dependent leading to a change in the composition of cosmic ray species [29]. The main problem in determining the feasibility of these models is the lack of knowledge of the GMF. Different models exist [18, 30] but they also lead to different assumptions of the coherence length and thus different predictions.

In the second scenario, the knee originates from the maximum energy that can be reached by galactic cosmic ray sources [10]. The chance of escaping the acceleration region increases

[4]Rigidity, R, is given as $R = p/|q|$, with p the momentum of the particle and q its charge. Particles of same rigidity have the same Larmor radius in a magnetic field.

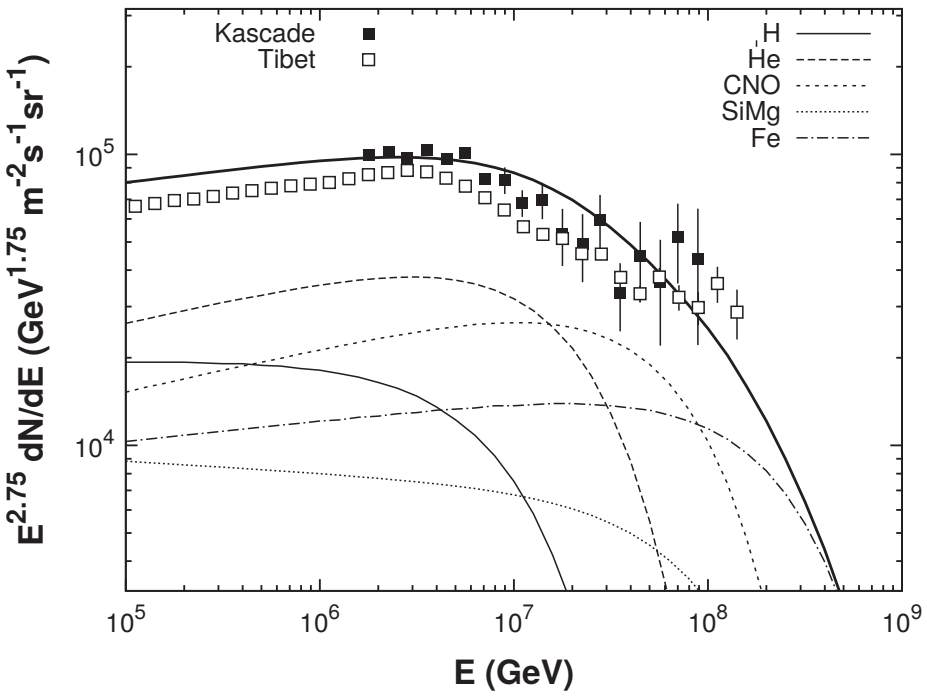

Figure 2.2: A rigidity dependent model of the knee. The model is normalized to the KASCADE data [31] with the thick, black, solid line being the all particle spectrum. The Tibet data is taken from [32]. Figure taken from [11].

with the Larmor radius because the particle cannot be confined anymore. For particles with different charge number Z, the escape probability is the same for same rigidity R. The maximum achievable rigidity $R_{\max}$ yields the maximum energy $E_{\max}$ for different particle species:

$$R_{\max} \propto \frac{E_{\max}}{Ze} \Rightarrow E_{\max} \propto ZeR_{\max} \qquad . \tag{2.16}$$

Particles with a higher charge number Z can therefore reach higher energies.

In figure 2.2, a rigidity dependent model for the change of spectral index around the knee is shown. It can well describe the knee shape and is thus a good explanation. The knee marks the natural beginning of the transition of galactic sources which cannot achieve higher energies and extragalactic sources start to set in. The ankle region will be dominated by extragalactic cosmic rays.

2.3 Ultra High Energy Cosmic Rays

The acceleration of particles up to the highest energies $\sim 10^{20}$ eV needs either strong magnetic fields to ensure a long confinement of the particle in the acceleration region or huge spatial expanses to also allow for acceleration of particles with large Larmor radii. A criterion to estimate the maximum energy achievable by different source classes was introduced in 1984 by Hillas [33]:

$$E_{\max} = \beta ZeBR \qquad . \tag{2.17}$$

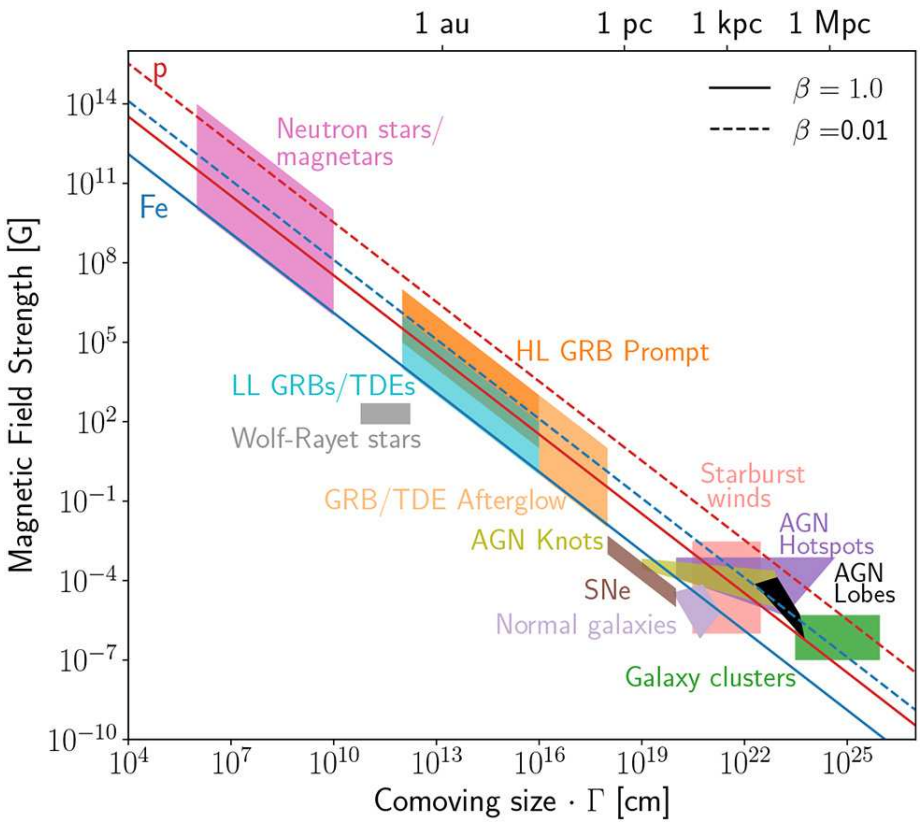

Figure 2.3: Hillas plot showing different possible source candidates for UHECRs. The diagonal lines indicate the values of B and R needed to accelerate protons (red) or iron (blue) to an energy of 10^{20} eV for two different velocities of the shock. Figure taken from [10].

Here, β is the velocity of the shock and R is the size of the acceleration region. Relating the magnetic field strength and the radius of various phenomena in the universe yields the Hillas plot as shown in figure 2.3. As can be seen, acceleration to 10^{20} eV becomes difficult. Especially in the case of protons a high β is needed for the shock. It should also be noted that the data shown in the plot only take into account a confinement of the accelerated particle. Other effects such as the time scale for acceleration [10] might reduce the maximum achievable energy.

2.3.1 The cut-off of the spectrum

The cut-off seems to mark the highest energy cosmic-rays that can reach the Earth. The reason for the suppression is still unclear but two major scenarios similar to the explanations for the knee are discussed.

First, the accelerators might have reached the maximum possible energy. As can be seen in the Hillas plot 2.3, the cut-off energy of $\lesssim 10^{20}$ eV is about at the theoretical limit for the known cosmic phenomena. In this case, the cosmic rays at the highest energies would be dominated by heavy particles as these can reach higher energies in the accelerators due to their smaller Larmor radius.

The second scenario considers propagation effects and is called *GZK-effect*. Cosmic ray protons can undergo interactions with photons of the Cosmic Microwave Background (CMB) producing a Δ^+-resonance [34, 35]:

$$\begin{aligned} &p + \gamma_{\mathrm{CMB}} \to \Delta^+ \to p + \pi^0 \\ &\qquad\qquad\qquad\qquad \hookrightarrow \gamma + \gamma \\ &p + \gamma_{\mathrm{CMB}} \to \Delta^+ \to n + \pi^+ \\ &\qquad\qquad\qquad\qquad \hookrightarrow \mu^+ + \nu_\mu \to e^+ + \nu_e + \bar{\nu}_\mu \\ &\qquad\qquad\qquad \hookrightarrow p + e^- + \bar{\nu}_e \end{aligned} \tag{2.18}$$

The energy threshold for cosmic ray protons at which this effect happens is $E_{\mathrm{GZK}} \gtrsim 6 \times 10^{19}\,\mathrm{eV}$, leading to a suppression of higher energies when the protons propagate a long distance above $\sim 100\,\mathrm{Mpc}$. Only protons from closer sources can therefore reach Earth with even higher energies. The process will be accompanied by a flux of high energetic photons and neutrinos. Current limits on the photon flux already set constraints on this model but cannot yet rule it out or claim detection of photons from the GZK-effect [22].

A similar effect occurs for heavy nuclei by photo-disintegration. When a high energetic nucleus interacts with a photon it can get split resulting in two nuclei with lower mass number. Heavy nuclei will thus disintegrate before reaching Earth and the composition of cosmic rays is shifted to lower mass numbers.

The main difference in the two scenarios for the cut-off is the different composition at the highest energies. In the propagation scenario, a light composition is predicted while for the scenario of the maximum energy of the sources, a heavy composition is expected [36].

An additional constraint on the two scenarios can be determined from a measurement of the isotropy of the arrival directions. In the case of the GZK-effect, the propagation distance at the highest energy is limited and the arrival directions should thus correlate with the matter distribution in the nearby universe.

Current measurements cannot sufficiently discriminate between the two scenarios. The Pierre Auger Observatory has reported the measurement of a dipolar anisotropy in the arrival directions [37] and also measures an increase in the average mass of cosmic rays with increasing energy [38]. Details of these measurements will be discussed in dedicated sections 2.4.3 and 2.5.

2.4 Cosmic ray induced air showers

The flux of cosmic rays near the cut-off is extremely low with about 1 particle per km^2 and century above $E \gtrsim 70\,\mathrm{EeV}$. Huge detection areas of at least $\mathcal{O}\,(100)\ \mathrm{km}^2$ are thus needed to achieve sufficient statistics for precise flux measurements. Such detectors cannot be realized in space for direct measurements. Instead, detectors installed at the surface of the Earth measure the secondary particles created when a primary cosmic ray interacts with the molecules in the atmosphere. These measurements nowadays are the only possibility to study UHECRs above $\sim E > 100\,\mathrm{TeV}$ [13].

These particle cascades are referred to as cosmic ray induced *air showers*. They can host a tremendous amount of particles and spread over large areas. For a primary particle with an energy of $10^{19}\,\mathrm{eV}$, at sea level the shower contains more than 10^{10} particles and covers an area of several km^2 [12].

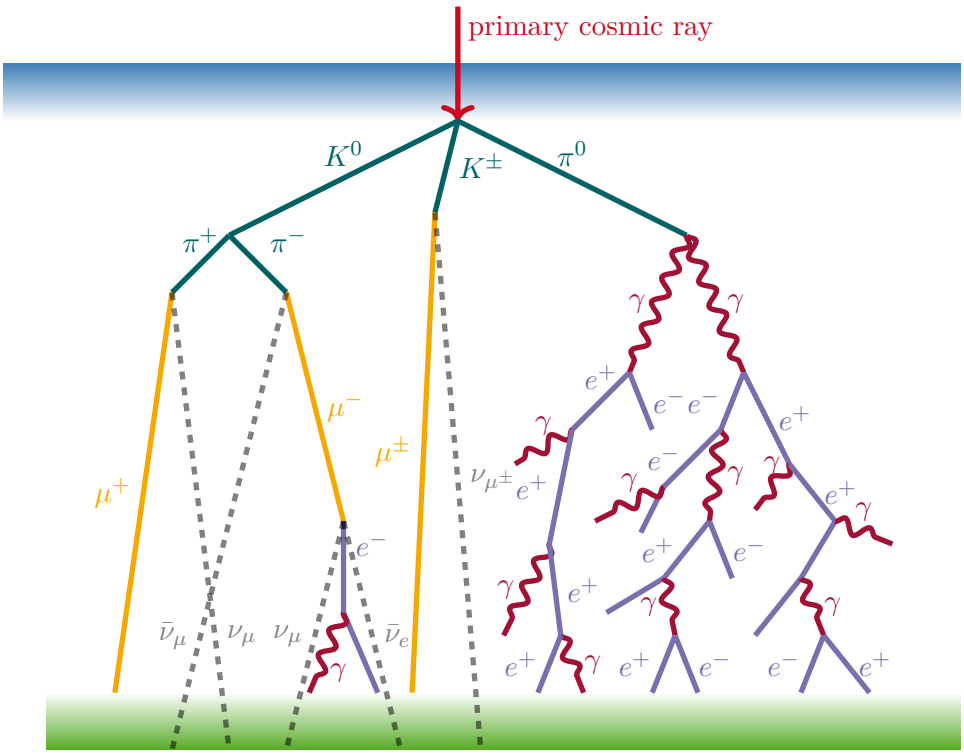

Figure 2.4: Idealized sketch of the longitudinal development of an air shower. Muons, electrons and photons are produced from decays or interactions of hadrons resulting in a cascade that can contain several million of particles. The different types of particles are not spatially separated as is indicated in the sketch.

Good reviews and introductions about the development of air showers in the atmosphere can be found in [12, 39, 11] where the following sections are based on.

The contributions of different particles to the air shower are typically separated in three classes which are sketched in figure 2.4:

1. The *electromagnetic component* is made up by electrons, positrons and photons. At sea level, they have energies of a few MeV and contribute by far most to both the number of particles and the total energy of the air shower [12].

2. The *muonic component* contains the second largest amount of energy in the cascade at sea level [12]. They can travel large distances and can therefore reach ground even if produced high in the atmosphere. Due to the early production in the air shower, they have high energies compared to the electromagnetic particles of typically $\mathcal{O}\,(\mathrm{GeV})$ at sea level. If a muon decays into an electron and two neutrinos before reaching ground, it can also feed the electromagnetic component.

3. The *hadronic component* mainly contains pions, kaons and few heavier hadrons. These are mostly created in early stages of the development of the air shower and feed the electromagnetic and muonic component of the air shower by decaying or interacting in the atmosphere. Their contribution to the number of particles and the energy is thus low at sea level.

In addition, neutrinos are produced in the decays of hadrons and muons. Due to their low interaction probability, they do not contribute to the further development of the air shower and are typically not measured. Some fraction of the energy is carried away by muons and neutrinos and not deposited in the atmosphere which has to be taken into account in measurements of air showers [40].

The development of the cascade is influenced by the amount of matter traversed. For a vertical incident primary particle, the *atmospheric depth* X is the integrated atmospheric density along its path:

$$X(h) = \int_h^\infty \rho(h')\,\mathrm{d}h' = \int_h^\infty \rho_0 e^{-h'/h_0}\mathrm{d}h' = X_0 e^{-h'/h_0} \tag{2.19}$$

with $X_0 = 1030\,\mathrm{g/cm^2}$ and $h_0 = 8.4\,\mathrm{km}$ the scale height of the atmosphere [41]. These values are approximations assuming an isothermal atmosphere. Simulations of air showers using Monte Carlo generators use more complex models in order to achieve more realistic results.

The atmosphere thus acts like a calorimeter. Its length can be described in terms of the hadronic interaction length λ_I or electromagnetic radiation length λ_em[5]:

$$\begin{aligned} X_0 &\approx \begin{cases} 11\lambda_\mathrm{I} \\ 28X_\mathrm{em} \end{cases} \\ \lambda_\mathrm{I} &= 90\,\mathrm{g/cm^2}\ [12] \\ \lambda_\mathrm{em} &= 36.66\,\mathrm{g/cm^2}\ [42] \qquad . \end{aligned} \tag{2.20}$$

For primary particles with an incident zenith angle $\theta > 0$ the atmospheric depth has to be corrected for the higher geometrical path length through the atmosphere. Assuming a flat atmosphere[6], the *slant atmospheric depth* can be determined:

$$X(h,\theta) \approx \frac{X(h)}{\cos\theta} \qquad . \tag{2.21}$$

The amount of traversed matter thus significantly increases by up to a factor of 3 at 70°.

In the following sections, the *Heitler model* of electromagnetic cascades [43] will be introduced as well as an extension to hadronic cascades [44]. These theories allow to estimate the characteristics of air showers.

For modern experiments, Monte Carlo simulations taking into account the interactions of individual particles are performed. The main difficulty for these simulations is the lack of knowledge of the hadronic cross sections at the highest energies. The center-of-mass energy of a proton with $E = 10^{19}\,\mathrm{eV}$ interacting in the atmosphere is $\sqrt{s} \approx 500\,\mathrm{TeV}$. This is far beyond current accelerator measurements and models describing the interaction cross sections have therefore to be extrapolated to these highest energies. Various models exist making different predictions.

[5] The hadronic interaction length is the traveled depth in a medium in which only a fraction of $1/e$ of the initial hadrons has not interacted. The electromagnetic radiation length corresponds to the distance after that an electron has radiated all but a fraction of $1/e$ of its initial energy.

[6] This approximation is valid up to an incident angle of about 70°.

2.4.1 The Heitler model of electromagnetic showers

In the Heitler model, the interactions of electrons or positrons[7] with photons are significantly simplified.

The energy loss rate of electrons by Bremsstrahlung is given by [39]

$$\frac{\mathrm{d}E}{\mathrm{d}X} = -\frac{E}{\lambda_{\mathrm{em}}} \tag{2.22}$$

with the electromagnetic radiation length λ_{em} as introduced in the previous section. This results in an exponential decrease of the energy of the electron:

$$E = E_0 e^{-X/\lambda_{\mathrm{em}}} \tag{2.23}$$

with E_0 the initial energy of the electron. After a distance $X_{\mathrm{step}} = \ln 2 \cdot \lambda_{\mathrm{em}}$ its energy is thus halved. To simplify the derivations, it is assumed that the energy loss occurs at once and the electron radiates a photon with energy $E_\gamma = E_0/2$ after a distance X_{step}.

Photons undergo pair production with the characteristic depth of $\lambda_{\mathrm{pair}} \approx 9/7 \cdot \lambda_{\mathrm{em}}$, after that only a fraction of $1/e$ survived [13]. In the Heitler model, the factor $9/7$ is approximated as 1. The produced electron and positron have an energy of $E_{e^\pm} = E_\gamma/2$ each, with E_γ the initial energy of the photon. The pair production of all photons is assumed to take place after the same distance:

$$X_{\mathrm{step}} = \ln 2 \cdot \lambda_{\mathrm{em}} = \ln 2 \cdot \lambda_{\mathrm{pair}} \quad . \tag{2.24}$$

All electrons and photons in the cascade thus interact after traversing the same amount of matter. This principle is sketched in figure 2.5a.

The number of particles doubles each time a distance of X_{step} has been propagated. The total number of particles N_i after i generations is $N_i = 2^i$ leading to the energy E_i of an individual particle in the i-th generation:

$$E_i = \frac{E_0}{2^i} \quad . \tag{2.25}$$

The cascade stops when the energy E_i of the individual particles in the i-th generation drops below the critical energy E_{c}. In this energy regime, energy loss of electrons by ionization becomes more likely than Bremsstrahlung. The maximum number of particles in the cascade N_{max} can be calculated as:

$$E_{\mathrm{c}} = \frac{E_0}{N_{\mathrm{max}}} \Rightarrow N_{\mathrm{max}} = \frac{E_0}{E_{\mathrm{c}}} \quad . \tag{2.26}$$

The number of generations i_{max} necessary to produce N_{max} particles can directly be concluded:

$$i_{\mathrm{max}} = \frac{\ln N_{\mathrm{max}}}{\ln 2} = \frac{1}{\ln 2} \ln\left(\frac{E_0}{E_{\mathrm{c}}}\right) \quad . \tag{2.27}$$

The critical energy for electrons in air is $E_{\mathrm{c}} = 86\,\mathrm{MeV}$ [12]. For an initial energy of $E_0 = 100\,\mathrm{TeV}$ the shower contains about 10^6 particles at its maximum.

[7] For the rest of this section, the term *electrons* will refer to electrons and positrons if not explicitly stated otherwise.

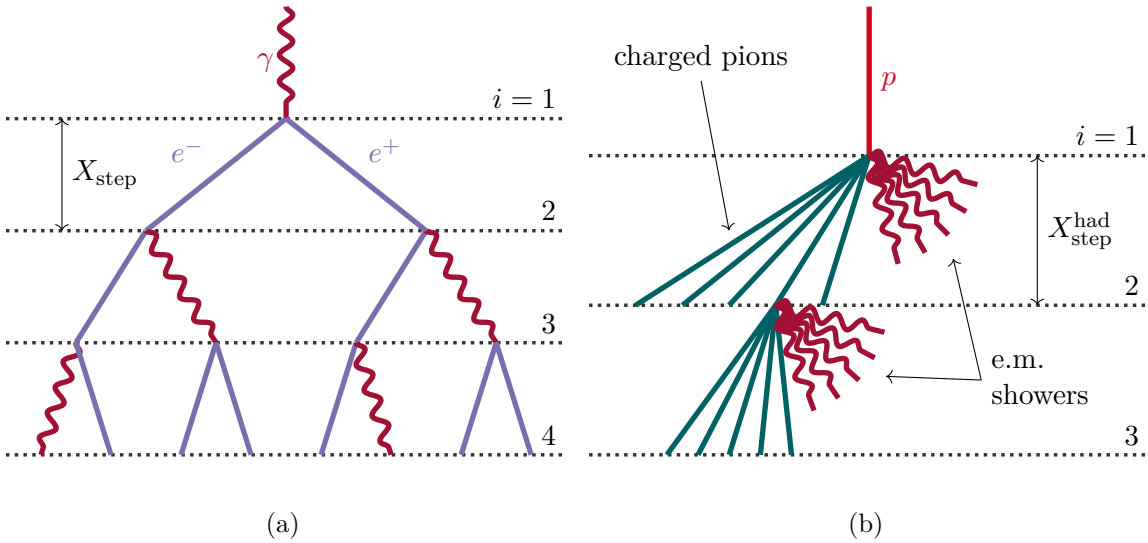

Figure 2.5: Schematic of the development of *(a)* an electromagnetic cascade according to the Heitler model and *(b)* the development of a hadronic cascade. In *(b)*, for simplicity only the interaction of one particle in the second generation is depicted and the electromagnetic showers are only indicated. Adopted from [39].

The traversed atmospheric depth at the shower maximum X_{max} can be calculated from the number of generations i_{max} necessary to produce N_{max} particles:

$$X_{\text{max}} = X_{\text{initial}} + i_{\text{max}} \cdot X_{\text{step}} \tag{2.28}$$

$$= X_{\text{initial}} + i_{\text{max}} \cdot \ln(2)\, \lambda_{\text{em}} \tag{2.29}$$

$$= X_{\text{initial}} + \ln\left(\frac{E_0}{E_c}\right) \lambda_{\text{em}} \tag{2.30}$$

$$\propto \ln E_0 \quad . \tag{2.31}$$

Here, X_{initial} is the atmospheric depth traversed before the first interaction takes place. An important quantity that can be determined from this result is the *elongation rate*, Λ, which is the change of X_{max} with energy:

$$\Lambda = \frac{\mathrm{d}X_{\text{max}}}{\mathrm{d}\,\log_{10} E_0} = \frac{\lambda_{\text{em}}}{\log_{10}(e)} = 2.3 \cdot \lambda_{\text{em}} \approx 84\,\mathrm{g/cm^2} \quad . \tag{2.32}$$

The Heitler model is a very simple description of an electromagnetic cascade. Nonetheless, it correctly describes three different characteristics [11]:

1. The number of particles N_{max} at the maximum of the air shower is proportional to the energy of the primary cosmic ray particle.

2. The depth of the shower at its maximum X_{max} is proportional to the logarithm of the primary energy.

3. The elongation rate Λ is proportional to the radiation length λ_{em}.

The Heitler model therefore is a good starting point to develop more involved models including a wider range of effects.

2.4.2 Extension of the Heitler model to hadronic showers

Modeling showers initiated by a hadron (typically a proton) is more complex than for pure electromagnetic showers. This is because of the higher multiplicity in the production of secondary particles in interactions and the fact that some fraction of the energy is transferred to an electromagnetic cascade. The electromagnetic cascade then develops independent of the hadronic shower. A simplified model similar to the Heitler model was proposed in [44]. A sketch of this model is shown in figure 2.5b.

The initial hadron is assumed to produce N_s secondary pions of which 2/3 are charged $\pi^\pm$ and 1/3 are neutral π^0. The energy is shared equally among all secondary particles. Neutral pions have a very short lifetime of $\tau_{\pi^0} = 8.5 \times 10^{-17}\,\mathrm{s}$ [13] and can be approximated to decay instantaneously into two photons which initiate electromagnetic cascades. The charged pions instead have a longer lifetime $\tau_{\pi^\pm} = 2.6 \times 10^{-8}\,\mathrm{s}$ [13]. At high energies, they thus are more likely to interact again after a distance $X_\mathrm{step}^\mathrm{had} = \ln(2)\,\lambda_\mathrm{I}$ than to decay. In the interaction, N_s secondary particles are produced as before. The energy contained in the hadronic and electromagnetic shower after the i-th interaction is given by:

$$E_\mathrm{had} = \left(\frac{2}{3}\right)^i E_0 \tag{2.33}$$

$$E_\mathrm{em} = \left(1 - \left(\frac{2}{3}\right)^i\right) E_0 \quad . \tag{2.34}$$

After 7 interactions a fraction of more than 94 % of the initial energy is transferred to the electromagnetic cascade. The number of electromagnetic particles in the shower maximum is then simply given by that of an electromagnetic shower (cf. eq. (2.26)) with initial energy E_em.

The energy per pion reduces after each interaction to

$$E_{\pi,i} = \frac{E_0}{N_\mathrm{s}^i} \quad . \tag{2.35}$$

The cascade stops if their energy falls below an energy E_dec, where the decay of charged pions into a muon and a neutrino[8] becomes dominant over the interaction process. For the atmosphere $E_\mathrm{dec} \approx 20\,\mathrm{GeV}$ is a good approximation [12].

The total number of generations can thus be derived from

$$E_{\pi,i_\mathrm{max}} = E_\mathrm{dec} = \frac{E_0}{(N_\mathrm{s})^{i_\mathrm{max}}} \Rightarrow i_\mathrm{max} = \frac{1}{\ln(N_\mathrm{s})} \ln\left(\frac{E_0}{E_\mathrm{dec}}\right) \quad . \tag{2.36}$$

For a primary particle with an initial energy of $10^{19}\,\mathrm{eV}$ and a multiplicity $N_\mathrm{s} = 15$, this results in ~ 7 generations. The multiplicity is energy dependent but the chosen value is a reasonable average [45].

The total number of produced muons N_μ can be derived assuming that all charged pions decay into muons as soon as their energy drops below E_dec. According to equation (2.36) $N_\mu = (N_\mathrm{ch})^{i_\mathrm{max}}$ with N_ch the number of charged pions produced in each interaction.

[8] The neutrino will be neglected in the model.

Replacing $i_{\max}$ in equation (2.36) and solving for N_μ yields:

$$N_\mu = \left(\frac{E_0}{E_{\text{dec}}}\right)^\alpha \quad \text{with} \quad \alpha = \frac{\ln(N_{\text{ch}})}{\ln(N_{\text{s}})} \qquad . \tag{2.37}$$

For typical values of $N_{\text{ch}} = 2/3 \cdot N_{\text{s}}$ and $N_{\text{s}} = 15$ it follows $\alpha = 0.85$. Compared to the number of particles in the electromagnetic cascade (cf. eq. (2.26)), the number of muons increases slower with the primary energy. For a primary proton with $E_0 = 10^{19}\,\text{eV}$, a total of $N_\mu \approx 2.5 \times 10^7$ muons and $N_{\text{em}} \approx 10^{11}$ electromagnetic particles is contained in the shower maximum.

The determination of the exact depth of the shower maximum in this model is rather involved because of the complexity of the cascade. A good approximation is to only consider the electromagnetic cascade which was initiated in the first interaction. It by far dominates the particle content of the air shower [39]. Then, $X_{\max}^{\text{had}}$ is given as:

$$X_{\max}^{\text{had}} = X_{\text{step}}^{\text{had}} + X_{\max}^{\text{em}}\left(\frac{E_0}{2N_{\text{s}}}\right) \overset{(2.30)}{=} X_{\text{step}}^{\text{had}} + X_{\text{initial}} + \lambda_{\text{em}} \ln\left(\frac{E_0}{2N_{\text{s}}E_{\text{c}}}\right) \tag{2.38}$$

The factor of 2 arises from the fact that each neutral pion decays into two photons with half the energy. The dependency on the initial energy is the same as for an electromagnetic shower. However, for primaries of the same initial energy E_0, the depth of the shower maximum is lower for the hadron induced case.

The hadron induced showers dicussed so far are initiated by a single particle, typically a proton. A simple extension for nuclei composed of many protons and neutrons is possible using the *superposition model*. The main assumption is that a nucleus with mass number A initiates A independent hadronic showers in the first interaction. These individual cascades consequently follow the model described in the previous paragraphs.

Each individual cascade has an initial energy of $E_{\text{h}} = E_0/A$. The content of muons and electromagnetic particles follows from equations (2.26) and (2.37):

$$N_{\text{em}}^A = A \cdot N_{\max}^p\left(\frac{E_0}{A}\right) = N_{\max}^p(E_0) \tag{2.39}$$

$$N_\mu^A = A \cdot N_\mu^p\left(\frac{E_0}{A}\right) \quad = A^{1-\alpha} \cdot N_\mu^p(E_0) \tag{2.40}$$

While the number of electromagnetic particles at the shower maximum is independent of the type of the primary, the number of muons increases with the mass number A. Assuming $\alpha = 0.85$ as before, a shower initiated by an iron nucleus with $A = 56$ contains about 80 % more muons than a proton initiated shower. The precise value depends on the value of α but the trend is noteworthy. A measurement of the muon content of the air shower can thus yield a good discrimination power between different types of primary particles.

The depth of the shower maximum reduces because of the lower energy of the individual showers:

$$X_{\max}^A = X_{\max}^p\left(\frac{E_0}{A}\right) < X_{\max}^p(E_0) \qquad . \tag{2.41}$$

The measurement of the shower depth also allows to discriminate different primary particles.

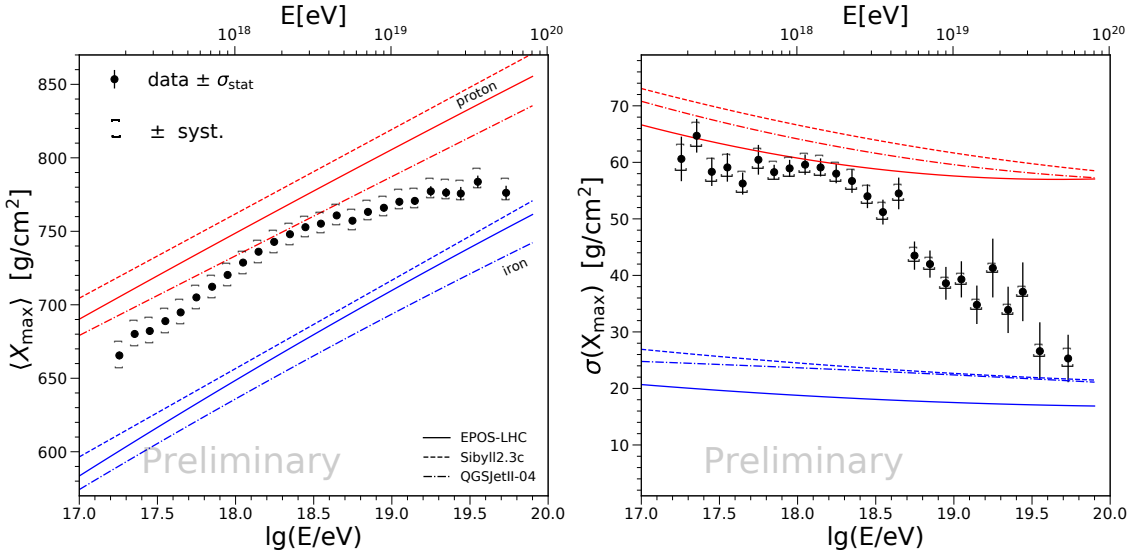

Figure 2.6: *Left* the mean depth of the shower maximum and *right* its standard deviation with respect to the energy of the primary particle as measured by the Pierre Auger Observatory. Lines indicate the expectation from simulations of air showers for a primary proton (red) or iron (blue). For each primary particle type, three different interaction models are used for the simulations to estimate systematic uncertainties. Taken from [38].

2.4.3 Towards measurements of the chemical composition

The chemical composition of cosmic rays at energies beyond the knee is still unclear but of great interest in order to discriminate different acceleration and propagation scenarios (cf. sec. 2.2.4 & 2.3.1). As mentioned in the previous paragraphs, the depth of the shower maximum and the number of muons at the shower maximum are crucial parameters for composition sensitive measurements.

All the calculations presented in the previous sections do not take into account the fluctuations of individual showers. These are significant and cause overlaps in the muon number and depth of the shower maximum of different primary particle types. Because of the superposition of individual hadronic showers in nuclei with $A > 1$, fluctuations decrease with increasing mass number. Monte Carlo simulation frameworks such as CORSIKA [46] take into account interactions and decays of individual particles in the atmosphere leading to more precise results. Due to the stochastic nature of the individual interactions, they also represent the shower-to-shower fluctuations.

In figure 2.6, a measurement of the Pierre Auger Observatory (for details see chapter 4) of the mean depth of the shower maximum and its standard deviation are shown [38]. Simulations of air showers for three different hadronic interaction models indicate the expectations for a pure proton or iron composition. Starting from intermediate $X_{\max}$ at $10^{17.2}$ eV the composition becomes lighter up to an energy of about $10^{18.3}$ eV. For higher energies, the composition becomes heavier again. The measurement of the width of the $X_{\max}$ distribution shows a similar trend. The interpretation is more complex than for the mean $X_{\max}$ because a mixed composition can also cause higher standard deviations than pure compositions of one primary particle type.

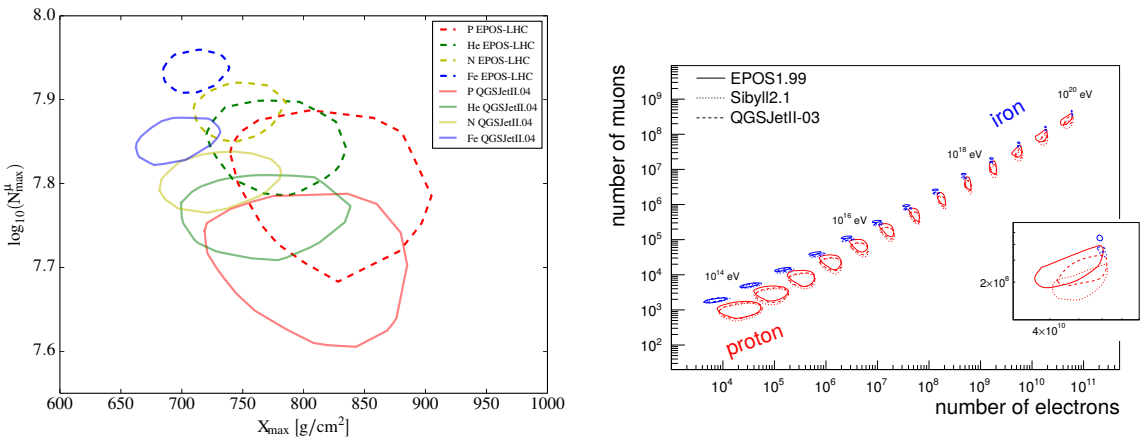

(a) Muon number with respect to depth of the shower maximum from CORSIKA simulations of air showers with a primary energy of $E = 10^{19}$ eV and zenith angle of $\theta = 38°$ for different primary particle types. Solid and dashed contours refer to different hadronic interaction models. Shown are the 1σ contours. Taken from [36].

(b) Muon number with respect to the electron number in vertical air showers observed at 800 g/cm^2 from CORSIKA simulations for different hadronic interaction models. Different energies of the primary particle between 10^{14} eV to 10^{20} eV have been simulated. Taken from [47].

Figure 2.7: Simulations of air showers describing possible observables to discriminate different cosmic ray primary particles.

The discrimination power for different types of primary particles can be improved by also determining the number of muons in the air shower. A corresponding simulation of the depth of the shower maximum and the muon number for different primary particles is shown in figure 2.7a. A clear trend with increasing A towards higher muon number and lower $X_{\max}$ is visible. The increase is about 40 % from proton to iron primary particles which is lower than the 80 % using the simplified model of the previous chapter. Reasons for the deviation of the simplified model can be the uncertainty in the multiplicity N_s or the fact that only a fraction of the energy might be passed to secondary particles in an interaction while the primary particle survives with lower energy.

Alternatively, the simultaneous determination of the muon and electron number in the air shower can yield a discrimination for the type of the primary particle type as shown in figure 2.7b. As expected from the previous calculations, heavier primaries have a larger number of muons compared to lighter ones while the electron number decreases.

The fluctuations decrease with increasing mass of the primary particle as expected. Still, a significant overlap between the different particle types is visible limiting the possibility for the measurement of the mass of an individual primary particle. The dashed and solid lines indicate different hadronic interaction models. They differ significantly leading to an additional systematic uncertainty in the measurements.

Good knowledge of the hadronic interactions is therefore crucial to correctly interpret the measurements. Current models suffer from the too low energy achieved at collider experiments compared to the center-of-mass energy reached when a UHECR particle interacts in the atmosphere. The Pierre Auger Observatory [7] tries to measure the muon content in very inclined air showers and the depth of the shower maximum. The resulting data compared to the simulations using different hadronic interaction models is shown in

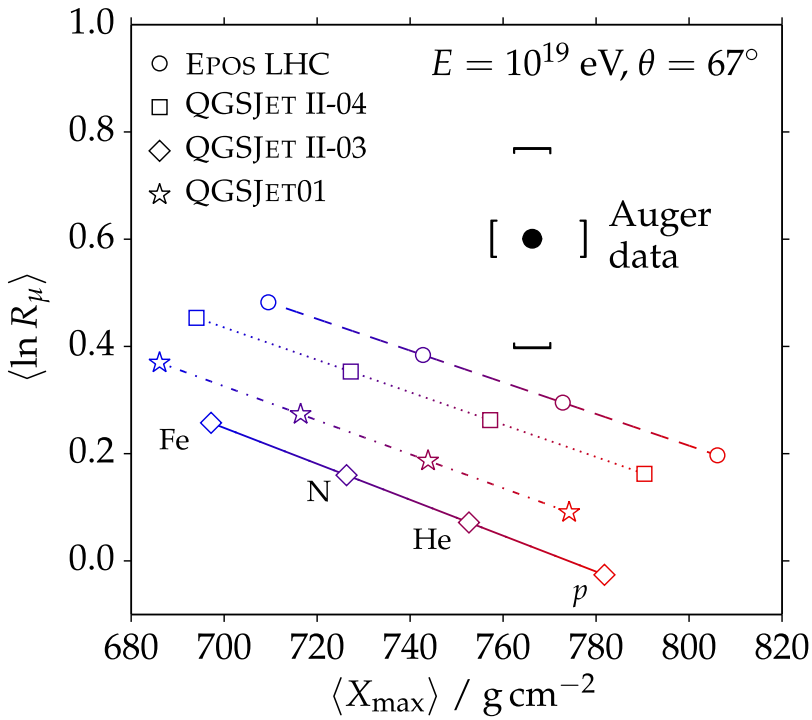

Figure 2.8: Measurement of the average muon content compared to the average depth of the shower maximum at the Pierre Auger Observatory. The variable R_μ is a measure for the number of muons in the air shower. The expection of four different hadronic interaction models is shown in the colored lines. The measurement clearly deviates from the expectation. Taken from [48].

figure 2.8. The measurement deviates from the expectation from different interaction models indicating a higher muon number in the data. The data is still subject to uncertainties on the energy scale and on the difficult determination of the number of muons. Improved detectors, such as AugerPrime (introduced in chapter 4.3), try to increase the capabilities of distinguishing between different shower components and to allow for better composition sensitivity.

2.5 Current status of the studies of UHECRs

One of the major questions concerning UHECRs are their sources. While the energy spectrum is determined with good precision, their origin remains unclear due to their deflection in magnetic fields. Key observables to discriminate different scenarios are the composition and possible anisotropies in the arrival directions as described in section 2.3.1.

Measurements of UHECRs with high statistics are performed by the Telescope Array (TA) experiment in the northern hemisphere and by the Pierre Auger Observatory in the southern hemisphere. The measured energy spectra around the cut-off are shown in figure 2.9. For this analysis, the energies of the two experiments are shifted with respect to each other to account for systematic differences in their energy scale [49]. The energy spectra match in a common declination band in equatorial coordinates where both experiments observe the same part of the sky. In the shown figure, the declination bands of the two experiments

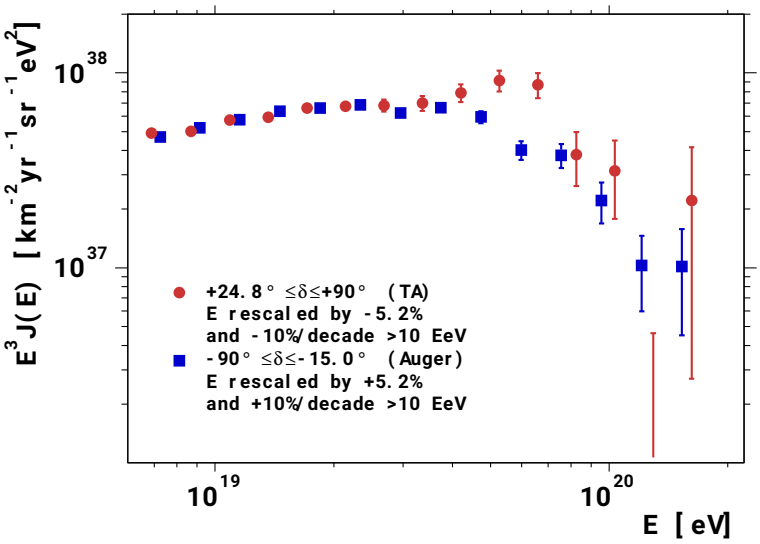

Figure 2.9: The energy spectrum scaled by E^3 as measured by TA and Pierre Auger around the cut-off. The shown spectra are taken in distinct declination bands. The energies are shifted such that the spectra agree in a common declination band. Taken from [49].

do not overlap and they show a systematic deviation around 5×10^{19} eV. The fact that the spectra agree in a common declination band but disagree in distinct regions of the sky might hint at an astrophysical origin producing different energy spectra over the sky [49]. This might for example be a nearby source of UHECRs that is only visible in the northern sky.

Tests for anisotropies in the arrival directions of cosmic-rays can be done on different angular scales. The Pierre Auger Observatory studied the correlation of the arrival directions of cosmic rays with known positions of Active Galactic Nuclei (AGNs) and Starburst Galaxies (SBGs) [50]. AGNs and SBGs are two promising candidates to produce UHECRs as can be seen from the Hillas plot in figure 2.3. The source catalogs have been obtained from the Fermi-LAT experiment [51, 52]. The distribution of the measured arrival directions of cosmic rays was fit to an isotropic background plus the sources. Two parameters were fit: a smearing of the source position and the fraction of cosmic rays that comes from these sources and not from the isotropic background. Best fit values yield a smearing of 7° (AGNs) and 13° (SBGs) and a fraction of 7 % (AGNs) and 10 % (SBGs). After scanning the energy threshold, the highest significance of disfavoring the isotropy scenario is 4σ for correlation with the SBGs above 39 EeV. The observed and modeled skymaps after subtracting the fit isotropic background are shown in figure 2.10. A clear correlation between the observation and the model is visible resulting in the high disfavoring of an isotropic scenario. It should be noted that coherent deflection in magnetic fields that would cause apparent shifts of the source positions are not taken into account in this analysis.

For the case of nearby sources of UHECRs an anisotropic arrival distribution of cosmic rays is expected (cf. sec. 2.3.1). Studies of large scale anisotropies such as dipole structures in the arrival direction allow to study this scenario. In [37], the Pierre Auger Observatory indeed reported the detection of a dipolar anistropy with an amplitude of $(6.5^{+1.3}_{-0.9})$ % in the direction in right ascension $\alpha = (100 \pm 10)^\circ$ and declination $\delta = (-24^{+12}_{-13})^\circ$. In figure 2.11, a

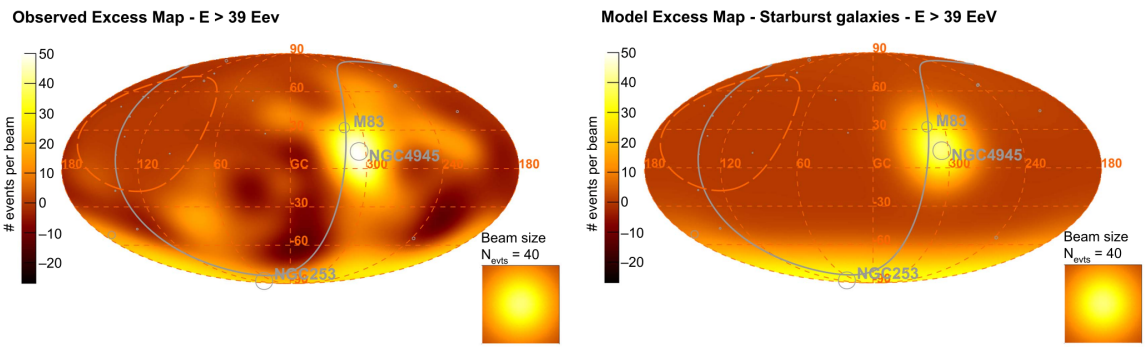

(a) (b)

Figure 2.10: Skymaps in galactic coordinates of *(a)* the cosmic ray flux observed by the Pierre Auger Observatory and *(b)* the flux modeled using a catalog of SBGs. The isotropic background is already subtracted. A gray line denotes the supergalactic plane and the red dashed line marks the limit of the field of view of the Observatory. Sources are smeared out with a beam size given in the bottom right. Taken from [50].

skymap of the measured particle flux is shown in galactic coordinates. The measured dipole is pointing away from the galactic center indicating an extragalactic origin of UHECRs. It is away by 55° from the dipole measured in the 2MRS distribution of galaxies [53] but taking into account the deflection in the magnetic field of the Milky Way leads to an improvement in the overlap.

The studies of cosmic ray anisotropies might be improved with future detectors able to discriminate the mass of the primary particles on an event-by-event base. The deflection angle of nuclei in the galactic and extragalactic magnetic fields is proportional to their charge Z [54]. Selecting a sample of light low charged cosmic rays can thus lead to lower smearing of source positions and better discrimination between different source candidates.

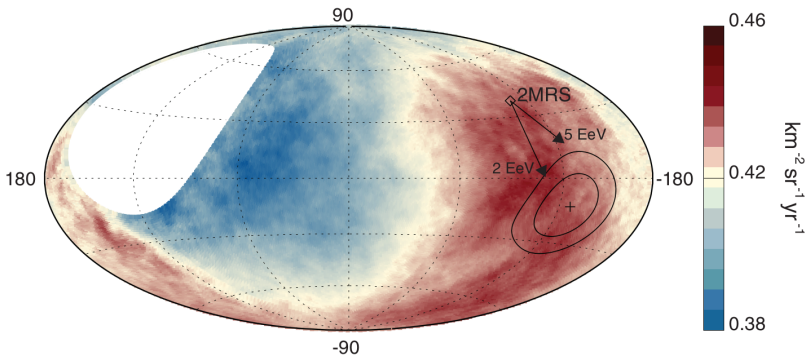

Figure 2.11: Skymap in galactic coordinates of the flux of cosmic rays with energies $E \geq 8\,\mathrm{EeV}$ smoothed by 45°. The direction of the dipole is marked by a cross and the contour lines mark the 68 % and 95 % confidence level regions. The diamond marks the direction of the dipole measured in the 2MRS galaxy distribution. Arrows indicate the expected deflection of cosmic rays in galactic magnetic fields with $E/Z = 5$ or 2 EeV. Taken from [37].

Chapter 3

Measurement of cosmic ray induced air showers

3.1 Types of air shower detectors

Typical measurements of air showers involve at least one of four main techniques:

1. Direct measurement of the particles in the air shower at ground level using particle detectors such as scintillators or water filled tanks exploiting the Cherenkov effect [55].
2. Measurement of the Cherenkov light produced by high energetic particles in the atmosphere using telescopes looking into the air shower.
3. Measurement of the fluorescence light emitted by atmospheric nitrogen when being excited due to the passage of the air shower.
4. Measurement of the radio signal produced in the air shower using antennas deployed at ground.

The different techniques have various advantages and disadvantages. Modern observatories therefore combine multiple subdetectors to improve the physics performance. In the following sections, a short overview of the different characteristics will be given based on [57] with focus on ground based arrays which the work of the author of this thesis is closely related to.

3.1.1 Arrays of particle detectors

Arrays of particle detectors have been used when air showers were discovered in 1939 [2]. The arrays evolved since those days and many experiments have used this detection technique (e.g. Volcano Ranch [59], AGASA [60], KASCADE [9]). Distributing many detectors triggered in coincidence allows for the detection of the shower front of an air shower as is sketched in figure 3.1. The distance of the detector stations determines the energy threshold of the array as a sparser grid of detectors requires a larger air shower for triggering. Separations can vary from a few meters up to more than one kilometer.

By determining the delay of arrival times in the different stations, the direction of the air shower can be reconstructed with a precision up to 0.5°. In order to achieve this precision,

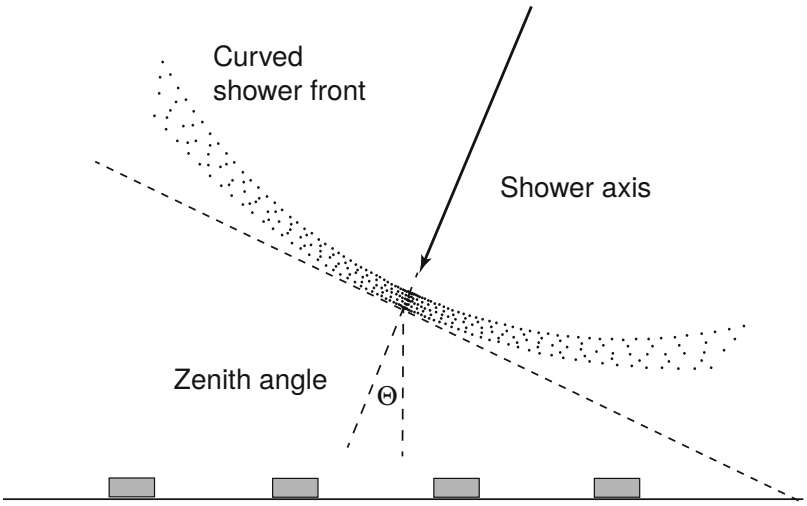

Figure 3.1: Principle of air shower measurements performed with arrays of particle detectors. Taken from [57].

systematics such as the curvature of the shower front or asymmetries produced in inclined showers need to be taken into account.

The energy can be reconstructed from the total signal measured in the stations by fitting a Lateral Distribution Function (LDF). The LDF describes the expected particle density with respect to the distance to the shower core. Using distinct detectors for the electromagnetic and muonic part of the air shower allows for sensitivity to the cosmic ray composition.

The main advantage of arrays of particle detectors is their duty cycle of $\approx 100\,\%$ which is typically independent of most environmental conditions. Their simplicity allows for instrumentation of large areas to achieve sensitivity around the cut-off of the spectrum. The main disadvantage is the fact that only a snapshot of the development of the air shower is taken at ground level. The lack of knowledge about the slant depth of the shower maximum compared to the atmospheric depth of the detector introduces uncertainties in the shower reconstruction.

3.1.2 Detectors of atmospheric Cherenkov light

High energetic charged particles emit Cherenkov light due to the refractive index of air $n_{\text{air}} > 1$. Even though mainly emitted by the secondary particles, also the light produced directly by the primary cosmic ray can be detected.

Imaging Air-Cherenkov Telescopes (IACTs), as the name states, measure an image of the Cherenkov emission of the air shower. Alternatively, an array of light detectors arranged similar to an array of particle detectors allows to determine the distribution of the light pool on ground.

The Cherenkov light is emitted at an angle of typically $< 1°$ limiting the size of the light pool on ground to a radius of $\sim 120\,\text{m}$. This small effective area reduces the ability of IACTs to detect UHECRs. The wavelength range of the emitted light is restricted to about 300 nm to 450 nm due to absorption in the atmosphere and suppression of emission of large wavelengths. In recent years, IACTs are mainly used to detect air showers induced by γ-rays in the GeV and TeV range (e.g. at MAGIC [61], H.E.S.S [62, 63], FACT [64]). The production of subshowers in the hadronic cascade initiated by nuclei leads to a fuzzy

image that can be well distinguished from the sharper image of a γ-ray induced air shower. The suppression of the hadronic background is therefore very good.

As the flash of produced Cherenkov light is very faint, observations are limited to dark cloudless nights. The duty cycle of such detectors is therefore around $\sim 10\,\%$ to $15\,\%$.

3.1.3 Detectors of fluorescence light

Charged particles of the air shower can excite the nitrogen molecules in the atmosphere. On deexcitation, they emit light in the wavelength range from 300 nm to 400 nm which can be detected by telescopes. In contrast to the emission of Cherenkov light, the emission of fluorescence light is isotropic and telescopes do not need to look into the shower. The telescopes instead can observe air showers in distances up to 35 km away depending on the primary particle energy. A large effective area can therefore be achieved with very few telescopes.

The amount of fluorescence light emitted is proportional to the ionization energy deposited in the atmosphere. Only a small fraction of $\lesssim 10\,\%$ is carried away by neutrinos or long living muons. Using fluorescence telescopes, a very precise estimation of the primary particle energy can therefore be achieved. The main uncertainty arises from the fluorescence yield which needs to be determined experimentally.

The angular resolution of a single telescope is of the order of a few degree but stereoscopic observation or additional information from a surface array allow to reduce it down to $\sim 0.6°$.

The highest energy cosmic ray particle that has ever been detected was measured using fluorescence telescopes. The Fly's Eye experiment reported an energy of $E = (3.2 \pm 0.9) \times 10^{20}\,\mathrm{eV}$ [65].

The main disadvantage of fluorescence light detectors is their low duty cycle of $10\,\%$ to $20\,\%$ and the relatively high energy threshold of about $10^{17}\,\mathrm{eV}$.

3.1.4 Detectors of the radio signal

Two different effects produce a charge separation in an air shower. First, the magnetic field of the Earth separates electrons and positrons in the air shower. Second, the overabundance of electrons over positrons in the atmosphere creates an excess of electrons in the shower front leaving positively charged nuclei behind. This charge separation leads to the emission of a pulse in the radio regime with frequencies $f < 100\,\mathrm{MHz}$. The emission is beamed similar to the emission of Cherenkov light.

It can be shown that the electric field is proportional to the energy of the primary particle. Very good energy resolution can thus be achieved using radio detectors [66]. Antenna arrays can be distributed on the surface to obtain an observational field of view of almost 2π and $100\,\%$ duty cycle.

Even though the detection of the radio signal succeeded already in the 1960's, it only became a feasible technique in recent years because of the more powerful electronics available.

3.2 Composition studies with ground based arrays

The current largest ground based arrays for the detection of UHECRs are Telescope Array (TA) and the Pierre Auger Observatory. Both distribute particle detectors (scintillator panels in the case of TA, water Cherenkov detectors in the case of Pierre Auger) on a grid on ground. These detectors measure the total signal produced by through going particles

but an individual signal produced by the muonic and electromagnetic shower components is not accessible. As described in section 2.4.3, these quantities might allow for a mass sensitivity for individual air showers.

In order to constrain possible designs to discriminate the muonic and electromagnetic shower components, the energy loss of particles in matter has to be understood. Good reviews on this topic can be found in [13, 67, 68]. The following introduction is based on these publications.

3.2.1 Energy loss of charged particles in matter

The energy loss of charged particles in matter can be described by three main contributions[1]:

1. Interaction with shell electrons of the material leading to excitation and ionization of the atoms.
2. Cherenkov radiation
3. Bremsstrahlung due to acceleration in the electric field of the nuclei of the medium

Energy loss of muons in matter

For heavy particles ($M \gg m_e$) such as muons, the contribution due to ionization and excitation processes is the dominant effect for energies below a few hundred GeV [67]. In this regime, the mean energy loss per traversed path length $\langle -\mathrm{d}E/\mathrm{d}X \rangle$ is then given by the Bethe-Bloch formula[2].

In figure 3.2, the energy loss of a muon in copper is depicted. For $\beta\gamma > 0.1$, the energy loss decreases until it reaches a minimum at around $\beta\gamma \approx 2$. Particles of this energy are called *Minimum Ionizing Particle (MIP)* as they experience the minimum energy loss by ionization. Even though the energy loss of a MIP is material dependent, its energy is not [69]. With increasing energy, the energy loss only weakly increases up to a $\beta\gamma \approx 1000$. At higher velocities radiative losses become the dominant processes for energy loss.

The Bethe-Bloch-formula describes only the *mean* energy loss of a particle in a medium. Statistical fluctuations of both the number of energy losses and the energy loss per collision can alter this value leading to a distribution of the deposited energy. The number of energy losses fluctuates according to Poisson statistics leading to a low relative uncertainty for dense material or very thick absorbers (in terms of the mean free path length).

The minimum energy loss per collision is determined from the possible excitations of the molecules in the traversed medium. The Most Probable Value (MPV) is usually only slightly higher [68]. In rare events, very large energies of almost the total energy of the incident particle can be transferred. This asymmetry in low and high energy losses leads to an asymmetric distribution of the energy loss in a medium. For thin absorbers and negligible change of the energy of the particle, the energy loss is described by the Landau distribution [70] shown in figure 3.3

$$\mathcal{L}(\lambda) = \frac{1}{\pi} \int_0^\infty e^{-t \ln t - \lambda t} \sin(\pi t)\, \mathrm{d}t \qquad . \tag{3.1}$$

[1] Other energy losses due to e.g. elastic scattering from nuclei or nuclear interactions are neglected here due to their small contribution.

[2] Only below a velocity $\beta \lesssim 0.1$ the Bethe-Bloch formula does not correctly describe the energy losses anymore.

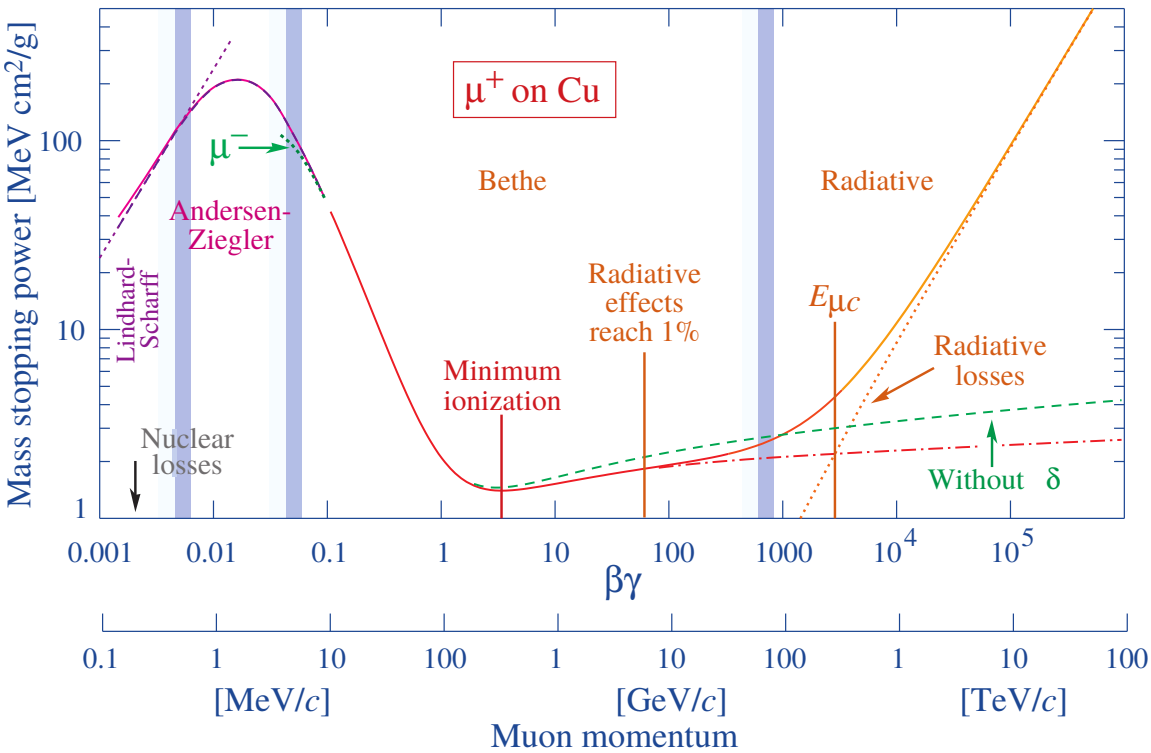

Figure 3.2: The stopping power or $\langle -\mathrm{d}E/\mathrm{d}X \rangle$ of a muon in copper. At intermediate energies, it can be described by the Bethe-Bloch formula. Only at energies above $\sim 100\,\mathrm{GeV}$ radiation processes become dominant. Taken from [13].

Due to the high skewness of the distribution, it is usually most feasible to measure the MPV instead of the mean. The mean is affected by large fluctuations due to outliers at very high energy losses. With increasing thickness of the absorber, the distribution gets less skewed but never approaches a Gaussian.

Typical measurements are affected by noise leading to a smearing of the Landau distribution. In many cases, a convolution of a Landau and Gaussian distribution thus describes the data better. This convolution leads to a shift of the MPV to higher values.

In air showers, most relativistic particles such as muons can be considered as MIPs [13]. They typically only deposit a fraction of their total energy inside the detector and fully traverse it.

Energy loss of electrons and positrons in matter

The energy loss of electrons and positrons[3] in collisions with electrons in the medium is similar to that of muons. Differences in the exact amount of the mean energy loss arise from the smaller mass of the electron and of the indistuingishability of the incident particle with the collision partner. These effects lead to slight modifications of the Bethe-Bloch formula that shall not be discussed here [67].

The major difference in the energy loss between electrons and muons is the contribution of radiation loss, especially through Bremsstrahlung. Due to the small mass of the electron, it is strongly affected by the electric field of the nuclei in the medium. These lead to a

[3]Electrons and positrons are referred to as electrons in the rest of this section.

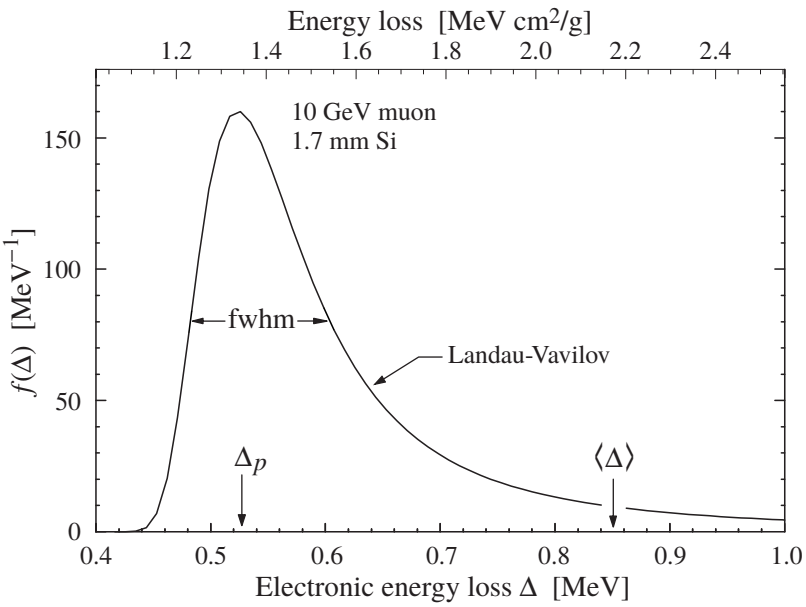

Figure 3.3: The Landau distribution for a 10 GeV muon traversing 1.7 mm of silicon. Δ_p is the MPV of the energy loss and $\langle\Delta\rangle$ is the mean energy loss that follows from the Bethe-Bloch formula. Modified from [13].

deflection of the electrons and hence to the emission of radiation. The cross section for Bremsstrahlung is proportional to $1/m^2$ where m is the mass of the incident particle. For electrons, this effect is therefore about 40 000 times stronger than for muons.

The critical energy E_c describes the energy above which radiation losses dominate over collision losses. It is material dependent but typically in the order of 10 MeV to 100 MeV for electrons [67]. The radiation length λ_em after that the energy of the electron due to radiation losses reduced to $1/e$ of the initial energy is therefore significantly lower than for muons. In water, for example, it is $\lambda_\mathrm{em} \approx 36\,\mathrm{g/cm^2}$ corresponding to a path length of $l \approx 36\,\mathrm{cm}$. Electrons, in contrast to muons, are therefore often absorbed inside the detection medium.

3.2.2 Energy loss of photons in matter

Photons lose their energy mainly in three different processes:

1. Photoelectric effect (dominant at low energies)
2. Compton scattering (dominant at intermediate energies)
3. Pair production (dominant at high energies)

The dominance of these three effects in the energy loss processes depending on the photon energy and the charge number of the absorber material is given in figure 3.4. In section 2.4.1, it was shown that the electromagnetic cascade of an air shower stops at a critical energy of $E_\mathrm{c} = 86\,\mathrm{MeV}$. This is the typical energy expected for the photons entering the medium and pair production dominates the energy losses in most materials. The resulting produced electron-positron pair then loses its energy according to the principles presented in the previous section.

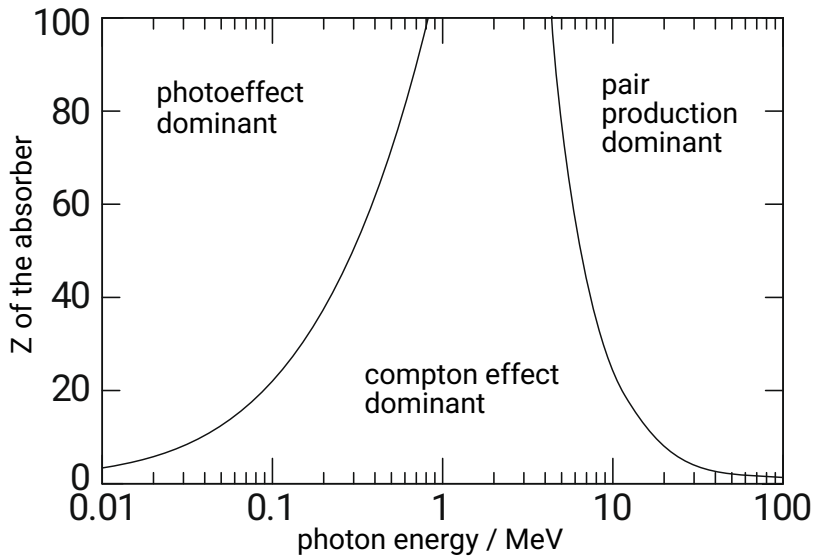

Figure 3.4: Areas in the (Z,E)-plane where the three different reactions leading to energy losses of photons are dominating. Modified from [68].

Photons have similar penetration depths as electrons and typically most photons get absorbed in cosmic ray particle detectors.

3.2.3 Measurement of the muon number in air showers

Exploiting that energy loss characteristics of muons and electromagnetic particles are very different, detectors can be designed to discriminate between the two components in air showers. This was done, for example, at the KASCADE-Grande experiment where parts of the detector were deployed underground [71]. The absorption in the soil above these detectors leads to a suppression of the electromagnetic contribution. This technique can yield precise measurements of the muon content of air showers but it is usually not feasible for the large detectors of UHECRs.

An alternative approach has been proposed in [72] where the characteristics of the energy deposit in Water-Cherenkov Detectors (WCDs) are studied. These are water filled tanks where charged particles are detected by measuring the Cherenkov radiation produced along their path. In figure 3.5, the amount of produced Cherenkov photons by electrons, photons and muons is shown for a WCD of 1.2 m height and 1.8 m radius. For muons, the amount of produced light is quite homogeneous over all the detector with a slight decrease to the bottom. For the electromagnetic particles instead, most light is produced at the top of the detector. The contribution at the right side originates from the inclination of the air shower.

If a layer is inserted into the water volume, the signals produced at the top part and in the bottom part can be extracted separately. In the top part, most light of the electromagnetic component is deposited while at the bottom part almost only the muonic component is visible. The signals in the top part S_{top} and bottom part S_{bot} can then be derived using

$$\begin{pmatrix} S_{\text{top}} \\ S_{\text{bot}} \end{pmatrix} = \mathcal{M} \begin{pmatrix} S_{\text{em}} \\ S_{\mu} \end{pmatrix} = \begin{pmatrix} a & b \\ 1-a & 1-b \end{pmatrix} \begin{pmatrix} S_{\text{em}} \\ S_{\mu} \end{pmatrix} \quad . \tag{3.2}$$

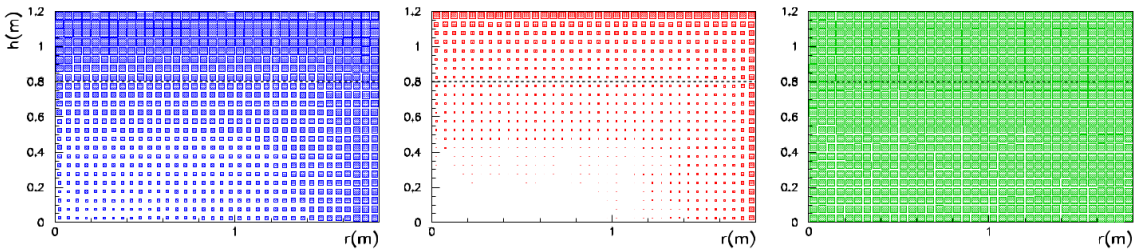

Figure 3.5: The distribution of the produced Cherenkov light in a WCD with 1.2 m height and 1.8 m radius. From left to right are given the contributions from photons, electrons/positrons, and muons. The simulated shower had a primary energy of 30 EeV and a zenith angle of 45°. Taken from [72].

Here, S_{em} and S_{μ} describe the contributions from electromagnetic particles and muons, respectively. The values of the coefficients a and b need to be determined from simulations and depend on the incident angle of the primary particle.

If the matrix can be inverted, the electromagnetic and muonic signals can be extracted:

$$\begin{pmatrix} S_{\mathrm{em}} \\ S_{\mu} \end{pmatrix} = \mathcal{M}^{-1} \begin{pmatrix} S_{\mathrm{top}} \\ S_{\mathrm{bot}} \end{pmatrix} \quad . \tag{3.3}$$

The uncertainty on these signals scales with the determinant of the matrix $\mathcal{M}^{-1}$. An ideal case would therefore be values of $a = 1$ and $b = 0$. In reality, this cannot be achieved. For the presented setup values of $a = 0.6$ and $b = 0.4$ were determined [72].

This simple approach is usually referred to as *matrix formalism*. It can be adopted to other setups where two different detectors have different response to the electromagnetic and muonic shower contributions. An example is the case of a scintillator detector that is placed below [73, 74, 75] or above a WCD [76]. The latter case will be realized in the upgrade AugerPrime of the Pierre Auger Observatory and introduced in section 5.

Chapter 4

The Pierre Auger Observatory

The Pierre Auger Observatory [7] is located in the Argentinean Pampas near the town of Malargüe at an altitude of around 1400 m. It is designed to detect UHECRs with energies above 10^{18} eV by measuring the induced air shower. With an instrumented area of 3000 km^2, it is the world's largest cosmic ray detector and thus allows for high statistics even in the regime of very low fluxes, near the cut-off at energies of around 5×10^{19} eV [77].

The Pierre Auger Observatory exploits a hybrid detection technique to allow for both precise measurements and calibration, as well as a high duty cycle. The Surface Detector (SD) [78] consists of 1600 Water-Cherenkov Detector (WCD) stations which are placed on a hexagonal grid with a spacing of 1500 m. Additional 60 WCD stations are added in a smaller area (referred to as *Infill*) of 23.5 km^2 to reduce the grid spacing to 750 m and thus the energy threshold. The SD is overlooked by 24 fluorescence telescopes located at four sites at the edges of the array. Three additional telescopes optimized for detecting low energy air showers overlook the Infill area (High Elevation Auger Telescopes (HEAT)). All fluorescence telescopes together compose the Fluorescence Detector (FD) [79].

A sketch of the layout is shown in figure 4.1. The FD and SD have complementary characteristics. The SD determines the shower footprint at ground. It allows for a precise determination of the position of the shower core and a good angular resolution of better than 1° above energies of $\sim 10^{19}$ eV [83, 84]. The SD has a duty cycle close to 100 % allowing for a high statistics data sample. Instead, the FD can only be operated during clear moonless nights, when it is dark but also clear enough to allow for the detection of the faint fluorescence light pulses produced by the particles of the air shower. The duty cycle is thus reduced to about 15 %. The FD can observe a large fraction of the shower development in the atmosphere. This allows for a precise determination of the deposited energy and thus a measurement of the energy of the primary particle with a resolution of $\lesssim$10 % [85] and a systematic uncertainty on the energy scale of 14 % [86], as well as the determination of the depth of the maximum of the shower development X_{max}. The FD and SD can be cross calibrated using showers measured in coincidence between the two. Thus, the energy measurement of SD can be calibrated using the good performance of FD.

A sketch of the layout and measurement principle of the two detector components is given in figure 4.2.

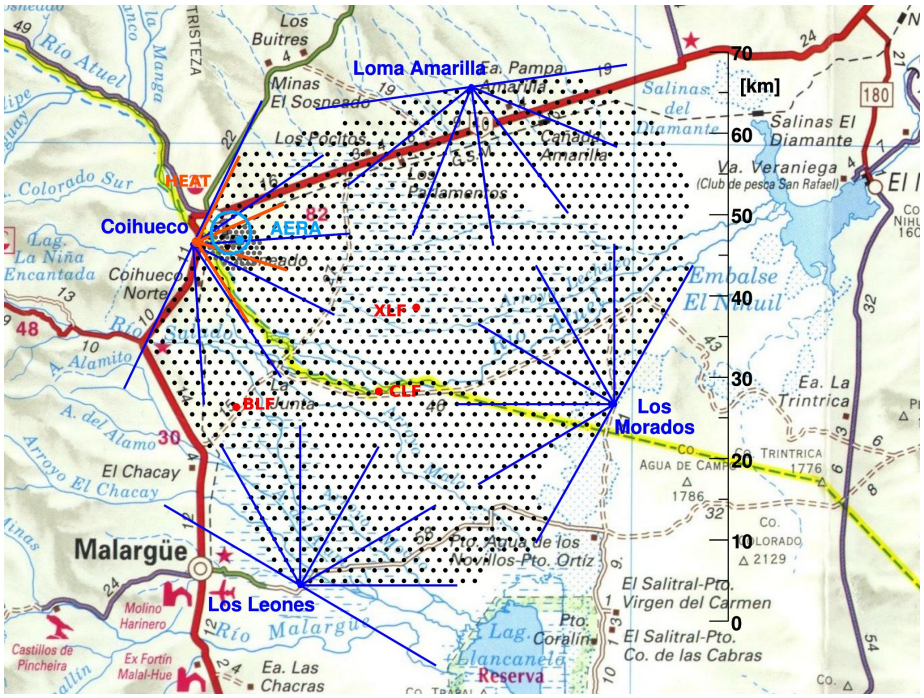

Figure 4.1: The layout of the Pierre Auger Observatory. Each black dot represents an SD station and the blue and red lines sketch the field of view of the standard fluorescence telescopes and HEAT, respectively. The red dots, labeled eXtreme Laser Facility (XLF) and Central Laser Facility (CLF) [80, 81], in the center of the array are the positions of lasers shooting into the atmosphere for calibration purposes. The Balloon Lanching Facility (BLF) was used to start weather balloons to study the atmosphere above the array [7]. AERA is an engineering array for the detection of the radio signal produced in air showers [82].

The site near Malargüe was chosen because of its suitable altitude, allowing an optimal air shower development in the atmosphere. The flatness of the site allows for wireless communication also over large distances. In addition, weather conditions are suitable for the detection of fluorescence light with clear nights and low light pollution [78].

The Pierre Auger Observatory started regular data taking in 2004, while construction was still ongoing. It was completed in 2008 and since then is continuously operated. The long operation time led to a good understanding of the detector and offers a perfect test area for new designs of air shower detectors. Especially, the measurement of radio signals produced in air showers using the Auger Engineering Radio Array (AERA) [82, 87] proved to be a competitive technique compared to traditional fluorescence or particle detectors.

Nowadays, the Pierre Auger Observatory is undergoing a major upgrade of its detector components. It will significantly improve the performance of the array and address major questions concerning cosmic rays. An overview of the upgrade will be given in section 4.3.

4.1 The Fluorescence Detector

The FD consists of 27 telescopes located at five sites. Four of these sites host six telescopes each. The telescopes are placed inside a building to protect them from environmental

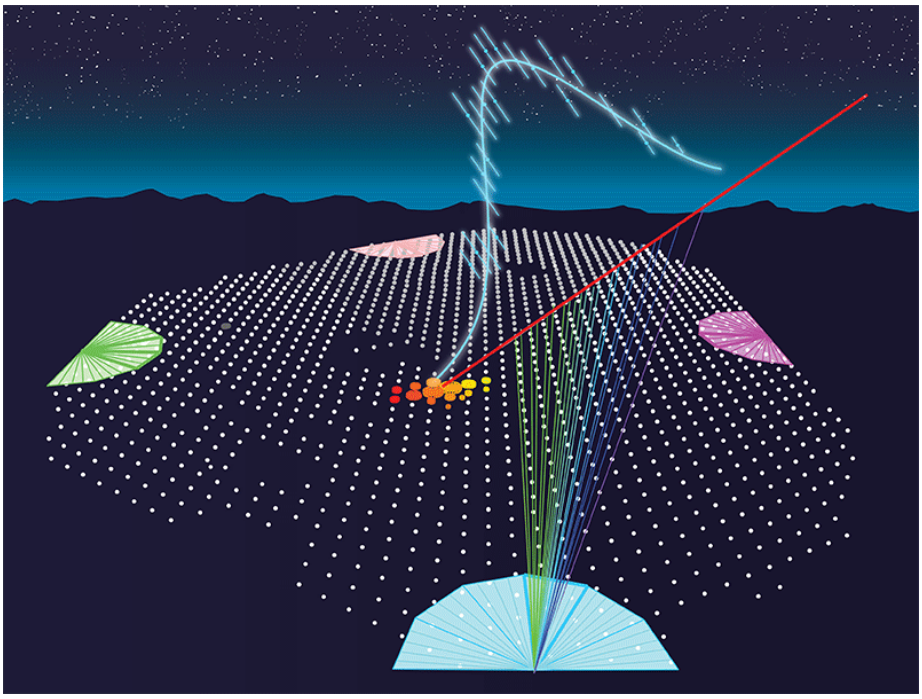

Figure 4.2: An overview of the measurement principle of the Pierre Auger Observatory. Each white dot represents one SD station while the colored triangles at the sites mark the field of view of the fluorescence telescopes. The SD measures the shower footprint at ground while the FD observes the longitudinal shower development.

influences such as rain, wind or light. During data taking, a shutter is opened to allow a free view for the telescopes into the atmosphere. The telescopes are arranged in a half circle, with each telescope observing a $30° \times 30°$ Field of View (FoV) in zenith and azimuth. Thus, the total FoV of one site is $180° \times 30°$. The vertical alignment allows for the observation from 1.5° up to 31.5° above the horizon. As can be seen in figure 4.1, the total FoV of all four sites together is optimized to observe the atmosphere over the whole surface detector array. A photograph of an FD building is shown in figure 4.3a.

At the fifth site, only three telescopes are located in three independent buildings, the HEAT detector. These buildings can be tilted upwards by 29° to observe a higher altitude part of the atmosphere. They are optimized for the observation of low energy showers as they have a lower X_{max}. When tilted upwards, they observe a range in elevation of 30° to 58°. As can be seen from figure 4.1, HEAT is located next to one of the regular FD sites. As HEAT and FD have a common FoV in azimuth, this setup allows for the observation of showers from 1.5° to 58° above the horizon.

All telescopes have the same optical properties. The general design is that of a modified Schmidt optics [88] and can be seen in figure 4.3b. A $10\,\mathrm{m}^2$ mirror focuses the incident fluorescence light on a 440 pixel camera. The pixels are arranged in 22 rows of 20 columns. Each pixel consists of a Photonis XP3062 Photomultiplier Tube (PMT) [89] with a cathode of hexagonal shape. An additional light concentrator placed in front of the cathode reduces the dead space between neighboring pixels. The total FoV of one pixel is $1.5° \times 1.5°$.

(a) A photograph of one of the FD buildings. Here, the shutters are opened and the aperture of the telescopes can be seen. Taken from [7].

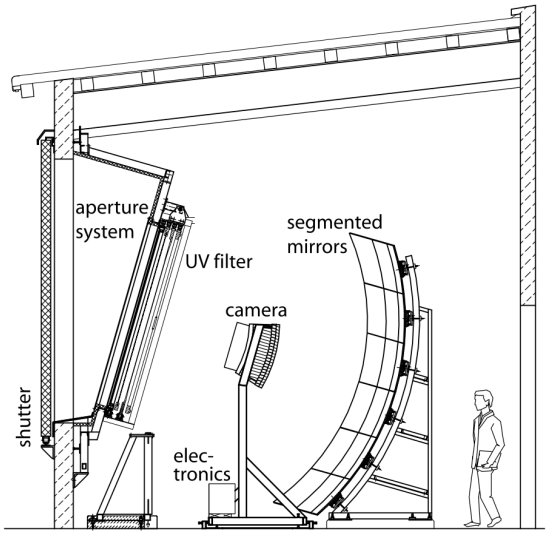

(b) A schematic view of an FD telescope. On the left, there is the aperture system that can also be seen in the left photograph. The segmented mirror focuses the light on the camera. Taken from [79].

Figure 4.3: Overview of the telescopes of the FD.

4.1.1 Calibration of the fluorescence detector

The conversion from the signal amplitude, measured in each individual pixel, to a light flux incident on the telescope has to be calibrated. Different components of the telescope influence the calibration. These include, e.g. the reflectivity of the mirror or the gain and quantum efficiency of the PMTs. Different calibration steps are executed [79].

An overall absolute calibration is achieved by using a light source at the telescope aperture that illuminates all pixels with the same light flux. This system has to be installed manually at the telescope and can only be performed very rarely. It therefore does not allow for monitoring changes that might affect individual nights.

An additional calibration system provides a measurement of the relative changes of the light yield of individual pixels. Three different light sources allow for the study of different components of the camera. One light source illuminates the camera directly from the center of the mirror. A second light source is mounted at the camera and directed to the mirror. It thus provides a measurement of the reflectivity of the mirror. The third light source illuminates a diffusive reflective sheet at the inside of the shutters. Thus, the reflected light traverses the full optical system of the telescope. All three calibration steps together provide a relative calibration of the full telescope and are performed each measurement night.

4.1.2 Reconstruction of air showers with the fluorescence detector

From the calibrated signals and their timing information, the air shower can be reconstructed. The geometry is reconstructed using the timing information in the pixels, while for a reconstruction of the shower profile and energy, also the calibrated signal sizes are of importance.

In figure 4.4 the reconstruction is illustrated. The fit of the shower geometry is performed

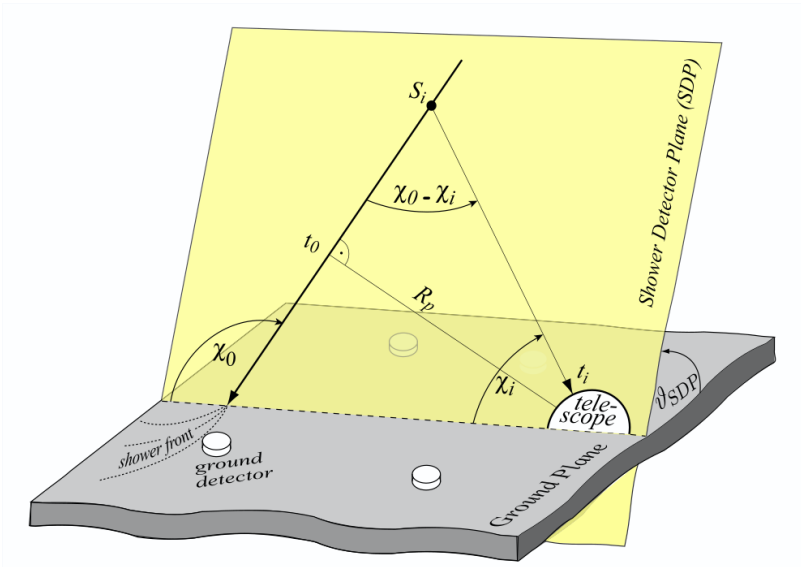

Figure 4.4: Sketch of the geometrical reconstruction of an air shower measured by the FD. Taken from [79].

using a χ^2 approach. For each modeled geometry, the expected arrival times of the light at the individual pixels is calculated. The sum of the squared difference between the prediction and the true arrival times, weighted with the timing uncertainty, is the χ^2 value. Minimization of the χ^2 yields the best prediction for the true geometry.

First, the Shower Detector Plane (SDP) is determined. It is the plane which includes the shower axis and the telescope which has seen the shower. It is given by the pointing directions of the triggered pixels. When the SDP is known, the shower axis can be characterized by the perpendicular distance R_p from the telescope to the shower axis and the angle χ_0 between the shower axis and a horizontal line in the SDP. The light arrival time t_i at a pixel i is then given by:

$$t_i = t_0 + \frac{R_p}{c} \tan\left(\frac{\chi_0 - \chi_i}{2}\right). \tag{4.1}$$

Here, t_0 is the time when the shower passes the point with the perpendicular distance R_p to the telescope and χ_i is the viewing angle of the pixel with respect to a horizontal line in the SDP. This function is fitted to the observed data and allows for a precise determination of the shower geometry. Only in the case of a low change in angular speed $d\chi/dt$, the accuracy is limited. This is typically the case when the observed track length is low. These reconstructions can be significantly improved by using also the precise timing information from the SD. An example of such a reconstruction is shown in figure 4.5. As the SD has an uptime fraction of almost 100 %, basically all showers which triggered the FD are reconstructed in hybrid mode.

With the geometry known, the amount of measured light can be converted into deposited energy in the atmosphere along the shower axis. In order to do so, the attenuation of the light in the atmosphere needs to be known and different sources of light have to be disentangled. These sources of light are the fluorescence light, direct and scattered Cherenkov light [90, 91], and multiple scattered light [92]. The resulting longitudinal shower profile is shown in figure 4.6. A Gaisser-Hillas profile [93] is fitted to the energy deposited

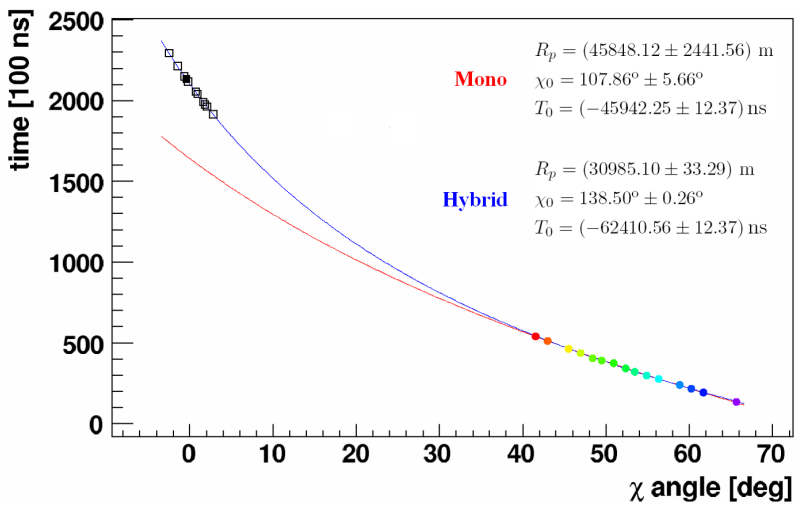

Figure 4.5: An example of the reconstructed arrival times of the light with respect to the viewing angle χ in the SDP. The reconstruction of the shower can be significantly improved using also timing information from the SD (blue line) compared to the FD only reconstruction (red line). Taken from [79].

per transversed matter density:

$$f_{GH} = \left(\frac{\mathrm{d}E}{\mathrm{d}X}\right)_{\max} \left(\frac{X - X_0}{X_{\max} - X_0}\right)^{(X_{\max}-X_0)/\lambda} e^{(X_{\max}-X)/\lambda} \quad . \tag{4.2}$$

Here, $(\mathrm{d}E/\mathrm{d}X)_{\max}$ is the maximum energy deposit along the profile at a slant depth of $X = X_{\max}$ and X_0 and λ are additional shape parameters. Integration of equation (4.2) leads to the total deposited energy. The total energy of the shower is then obtained by correcting for invisible energy that is carried away, by e.g. muons or neutrinos which are not visible to the FD [94]. The systematic uncertainty on the energy scale of the FD is 14 %.

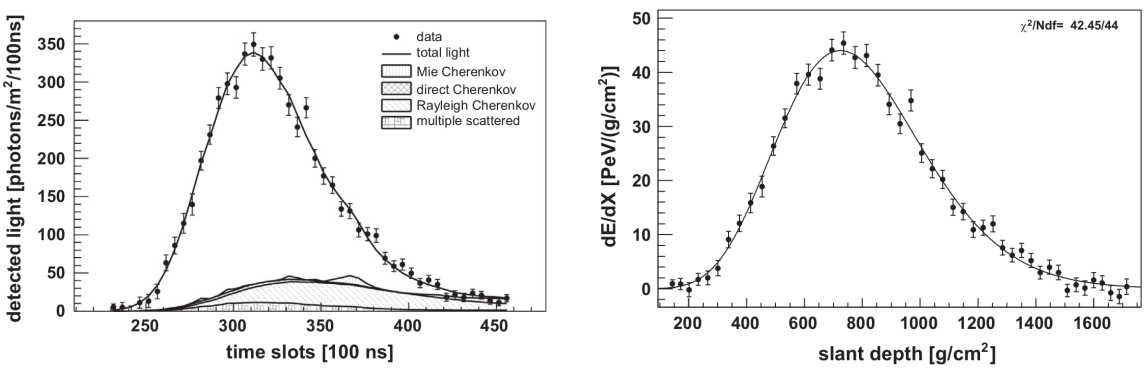

(a) The amount of detected light per time and area versus time.

(b) The energy deposited per transversed matter versus the slant depth.

Figure 4.6: Longitudinal profile of a shower measured with FD. Taken from [79].

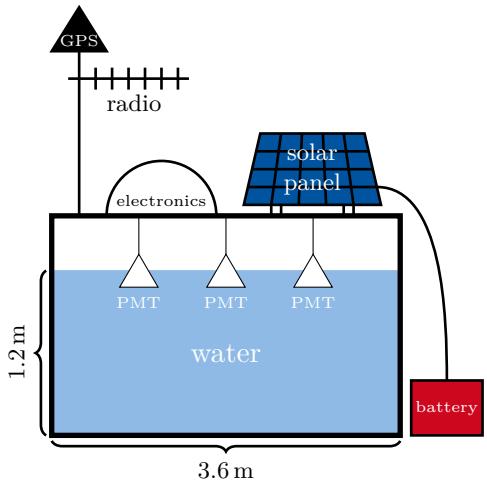

(a) A sketch of an SD station.

(b) A photo of a surface detector station in the field. Taken from [95].

Figure 4.7: The surface detector stations host 12 m^3 of purified water. Three PMTs detect the Cherenkov light produced by through-going charged particles. Signal digitization, calibration and monitoring is done at the station with the electronics installed under a protective cover. It is powered by a solar panel buffered with a battery. GPS is used for timing calibration and radio provides communication with the Central Data Acquisition System.

4.2 The Surface Detector

The SD is made up from 1600 detector stations located on a hexagonal grid with a spacing of 1.5 km. Additional 60 detector stations reduce the grid spacing to 750 m and even 433 m, lowering the energy threshold in this *Infill* region.

In figure 4.7, a sketch and a photo of a detector station are shown. Each detector station comprises a water tank of 3.6 m in diameter filled with 12 m^3 of purified water. To ensure a good light yield, the water is contained inside a sealed reflective liner.

High energy charged particles exceeding the speed of light in the medium traversed, produce Cherenkov light [55]. In the detector station, the Cherenkov light is detected by three 9” PMTs (Photonis XP1805 [96]) aligned on a circle with radius 1.2 m around the center of the tank. In addition, photons and electrons can initiate an electromagnetic cascade which also leads to a production of light in the water.

The detector stations are solar powered and equipped with an additional battery to bridge nights and cloudy days. The positioning as well as the event timing are done using a GPS antenna. All electronics is implemented on a Unified Board (UB) at the station and protected from environmental influence. It contains the GPS receiver, slow control for monitoring and controlling the station, the data acquisition with analogue to digital converters for each PMT, a processing unit, and a radio transceiver for communication. The total power consumption of one station is about 10 W.

The signals from the PMTs are picked-up from the anode and the last dynode separately and guided to the UB [97]. The dynode signal is further amplified by a factor of 32 [98] to achieve a high dynamic range. The signals are then digitized with a sampling rate of 40 MS/s by a 10 bit flash Analog-to-Digital-Converter (FADC).

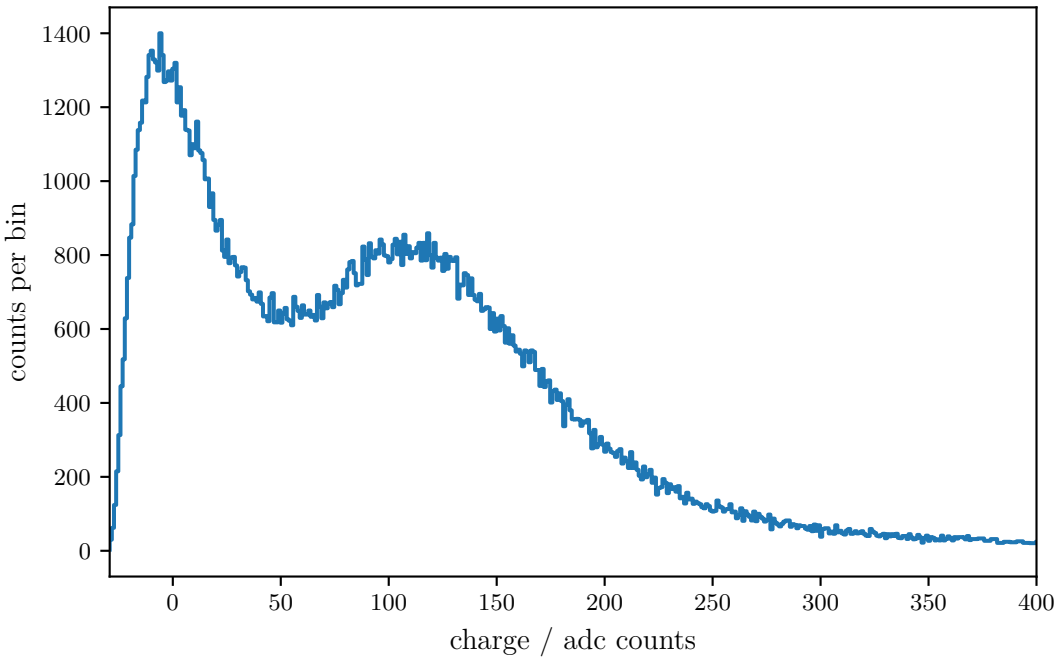

Figure 4.8: An example of a calibration histogram. The histogram is already baseline corrected so that the pedestal peak is at zero. The hump at a charge of about 120 adc counts is produced by the through going muons. The histogram is zoomed in, the full histogram extends to charge values of about 950 adc counts.

The detector stations implement two independent single station triggers [99]. A threshold trigger with a coincidence of all three PMTs allows for the detection of large signals. In addition, a time-over-threshold trigger with a coincidence of two out of three PMTs is optimized for the detection of also smaller signals. The two triggers have a total event rate of about 20 Hz. The station triggers are sent to the Central Data Acquisition System (CDAS) which builds the array triggers based on temporal and spatial coincidences of multiple stations. For events with a zenith angle below 60°, full trigger efficiency is reached at an energy of 3×10^{18} eV, regardless of the primary mass [99].

4.2.1 Calibration of the surface detector

The surface detector stations are calibrated in terms of the signal produced by a vertically and centered through-going muon (Vertical Equivalent Muon (VEM)) [98]. In order to obtain the signal of a VEM, a first rough estimate of the signals is achieved by measuring the trigger rates for different thresholds. Using this rough estimate, a trigger threshold for the individual PMTs of 0.1 VEM can be set. With a threefold coincidence of the PMTs, the rate is lowered such that an online processing of the events can be performed at the station. For each trace in total 20 bins (500 ns) around the trigger position are integrated. The corresponding charge is filled into a histogram for each PMT individually. In addition, a histogram of the amplitude and the average pulse shape are created.

An example charge histogram of an SD station is shown in figure 4.8. The position of the hump is produced by through-going muons. As the muons are omnidirectional and homogeneous, the actual VEM signal is lower. The calibration of the ratio between the

position of the hump and the VEM signal has been performed with a dedicated tank using a muon telescope to select vertical and centered muons [100].

The histogram is transmitted together with each full SD event and thus allows for precise calibration at the time when the event occurred. It is updated every minute.

4.2.2 Reconstruction of air showers with the surface detector

Different array triggers are implemented for the SD. They are based on spatial and temporal coincidence of multiple stations. More details can be found in [78] and [99]. In addition, the SD can also be triggered by the FD. Even if only one SD station has a signal, it can significantly improve the FD reconstruction (cf. sec. 4.1.2).

For a shower to be reconstructed by SD only, at least three neighboring stations must have had a trigger [7]. From the arrival times of the signals at the different SD stations, the direction of the air shower can be reconstructed. In contrast, the reconstruction of the position of the shower core, i.e. the region of highest particle density, relies on the signals measured at the SD stations. The reconstruction of the air shower depends on the zenith angle θ. While for vertical air showers up to $\theta \lesssim 60°$ the electromagnetic and muonic component can be measured, for higher incident angles, the electromagnetic component is absorbed. This dependency results from the different amount of traversed matter which scales approximately with $\cos^{-1}(\theta)$. Here, only the reconstruction for vertical events is discussed. For inclined air showers, the reconstruction procedure has to be adapted [101].

The Lateral Distribution Function (LDF) of the signals on ground is fitted using a modified Nishimura-Kamata-Greisen function (NKG-function) [7, 102, 103]:

$$S(r) = S(r_{\mathrm{opt}}) \cdot \left(\frac{r}{r_{\mathrm{opt}}}\right)^{\beta} \cdot \left(\frac{r + r_1}{r_{\mathrm{opt}} + r_1}\right)^{\beta+\gamma} \tag{4.3}$$

with r_{opt} the optimum distance, $r_1 = 700\,\mathrm{m}$ [104] and $S(r_{\mathrm{opt}})$ is a measure for the shower size. The value for the optimum distance r_{opt} depends on the geometry of the array. For the SD, it has been found to be $r_{\mathrm{opt}} = 1000\,\mathrm{m}$ [105]. At this distance, fluctuations of the expected signal $S(r_{\mathrm{opt}})$ are minimized and have only little dependence on the specific shape of the LDF. The signal at r_{opt} is thus referred to as S_{1000}. The parameters β and γ describe the shape of the LDF and are dependent on the zenith angle.

In figure 4.9, an example of a reconstructed LDF is shown. Besides the stations that are used for the reconstruction (*candidates* and *saturated recovered*), it also contains signals from stations which have been saturated, which did not trigger, or which triggered accidentally. For the station marked as *saturated recovered*, the signal saturates the Analog-to-Digital-Converter (ADC) and the measured signal would thus be smaller than the true signal. The true signal is estimated from the saturated signal.

The parameter S_{1000} is a measure for the size of the shower and thus used to reconstruct the energy of the primary particle. But, the shower size decreases with increasing zenith angle θ due to attenuation in the atmosphere. The dependence of the attenuation on the zenith angle can be determined using the constant intensity cut (CIC) method assuming an isotropic flux of primary cosmic rays [106, 7]. The attenuation curve $f_{CIC}(\theta)$ is described

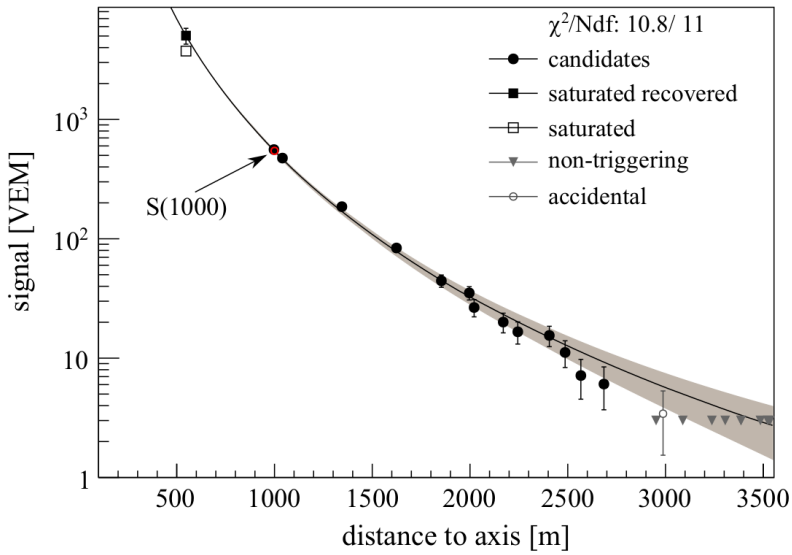

Figure 4.9: An example of a reconstructed LDF as measured with the SD for a single event. The figure also contains the signal of stations that have been saturated, that did not trigger, or that triggered accidentaly. Figure taken from [7].

as [107]:

$$f_{CIC}(\theta) = 1 + ax + bx^2 + cx^3 \tag{4.4}$$

$$x = \cos^2(\theta) - \cos^2(\theta_{\text{med}}) \tag{4.5}$$

$$a = 0.980 \pm 0.004 \tag{4.6}$$

$$b = -1.68 \pm 0.01 \tag{4.7}$$

$$c = -1.30 \pm 0.45 \tag{4.8}$$

with $\theta_{\text{med}} = 38°$ being the median of the zenith angle distribution. Thus, showers at this zenith angle are used as a reference. The signal size S_{1000} is converted for all showers to S_{38}, the expected shower size at 1000 m distance from the shower core at a zenith angle of $\theta = 38°$:

$$S_{38} = \frac{S_{1000}(\theta)}{f_{CIC}(\theta)} \tag{4.9}$$

To reconstruct the energy of the primary particle, the hybrid detection technique is of great advantage. The precise energy estimated using the FD is correlated with S_{38} and allows also the SD to have a good reconstruction of the primary energy. The systematic uncertainty on the energy scale originates from the FD as 14 %. The correlation of FD and SD reconstructed energies results in an energy resolution for SD reconstructed showers of 12 % to 16 % depending on the energy.

4.3 AugerPrime

The Pierre Auger Observatory has been operating successfully for more than a decade and achieved significant contributions to the study of cosmic rays (see e.g. [37, 108, 38]). Its performance has also shown the limitations of the current design and technology used.

With the experience from the operation and analysis of the Pierre Auger Observatory, a plan for an upgrade *AugerPrime* was developed in order to increase the performance of the Observatory [36].

Even though the understanding of UHECRs significantly improved in the last decades, a number of open questions still remains. An overview of these questions has been given in chapter 2. AugerPrime tries to address three of the major questions [36]:

1. The origin of the flux suppression at the highest energies is still unknown. It might originate from propagation effects as well as from the maximum energy particles can reach in the astrophysical sources.

2. The sources of the UHECRs are still unknown. Particles of the highest energies with a low mass, in particular protons, experience only small deflections in magnetic fields and can thus open a window for proton astronomy. Sensitivity for the mass of the primary particle is therefore necessary.

3. Hadronic interaction models nowadays suffer from a lack of knowledge of interactions at the highest energies. Current artificial accelerators are not able to reach the center-of-mass energies observed when UHECRs interact in the atmosphere. The Pierre Auger Observatory observes an excess of muons in air showers compared to simulations [48]. A better understanding of this systematic can help to constrain hadronic interaction models and also to investigate new physics phenomena such as Lorentz invariance violation or extra dimensions [36, 109, 110].

A key observable to address these questions is the number of muons observed in an air shower [111]. It allows for separation of measured air showers into a lighter and heavier sample and it can, at the same time, improve the measurements of hadronic interaction models.

AugerPrime includes various improvements to the current design of the Pierre Auger Observatory focusing on the mentioned physics goals:

1. An additional scintillator detector, the Scintillator Surface Detector (SSD), will be installed on top of the existing SD stations in order to improve the discrimination of the electromagnetic and muonic shower components.

2. An additional buried detector, the Underground Muon Detector (UMD), deployed in parts of the Infill area will allow for a dedicated measurement of only the muon component of air showers.

3. An additional Small PMT (sPMT) will complement the measurements of the three large PMTs of the WCD to extend the dynamic range to larger signals.

4. The UB of the SD electronics will be replaced with an upgraded version, the Upgraded Unified Board (UUB).

5. The duty cycle of the FD will be increased by extending the measurement also to periods with higher Night Sky Background (NSB).

6. An additional radio antenna will be installed on top of each SD station [112]. It will allow for the measurement of radio signals produced by the electromagnetic component of air showers.

The components 2 through 6 will be briefly introduced in the following paragraphs. The component 1, the Scintillator Surface Detector (SSD), will be introduced in more detail in a dedicated chapter 5, as the main work of the author contributed to this part of the upgrade.

The UMD

While the electromagnetic component of air showers is strongly absorbed in dense material, high energy muons can also penetrate them deeply. With a detector buried underground a very clear signal of the high energy muons can thus be measured. This type of detector has already been successfully developed at the Pierre Auger Observatory with the Auger Muons and Infill for the Ground Array (AMIGA) detectors [113, 114]. In total, 61 detectors will be distributed in the Infill region over an area of $23.5\,\mathrm{km}^2$. Besides their direct measurement of the muon component in this region, they will also allow for a cross calibration with the SD and SSD. The UMD is based on scintillator strips with a size of $4 \times 0.041 \times 0.01\,\mathrm{m}^3$ each. The light will be collected by fibers and guided onto a 64 channel Hamamatsu PMT. It will be operated as simple counters of muons, i.e. they count events whose signal exceeds an adjustable threshold.

The sPMT

For the sPMT, a 1” PMT (Hamamatsu R8619 [115]) was chosen [116]. It has a cathode area of only 1 % of the standard WCD PMTs. The number of detected photons is therefore lower and the produced signal is smaller. The saturation of the sPMT sets in only for a larger number of particles penetrating the WCD. The gain of the sPMT will be adjusted such that it has sufficient overlap with the standard WCD PMTs to be able to cross calibrate the signals from the two components. The increase of the dynamic range will allow for a more precise determination of the LDF close to the shower core.

The UUB

The UUB will be deployed at the SD stations in order to increase the data quality, but also to be able to operate the additional detector components which are going to be installed. A detailed description of the UUB can be found in [117].

The UUB has ten input channels. In contrast to the old UB, only the signal of the anode from the WCD PMTs is used. It is split into a High Gain (HG) and a Low Gain (LG) channel with an amplification ratio of 32. The signal from the PMT of the SSD is split into a HG and LG channel, with gain 32 and attenuation of 4, respectively. One additional channel digitizes the signal of the sPMT and another channel is used as a spare for possible future extensions. For each channel, a trace of 1024 samples with a dynamic range from 0 V to 2 V is digitized with a sampling rate of 120 MS/s at 12 bit resolution using an FADC.

All basic functions such as the readout of the FADCs, the trigger generation, clock generation, and GPS timing are implemented into a Field Programmable Gate Array (FPGA). An additional microprocessor running a LINUX system operates all high-level functions such as data handling and communication with the radio transmitter.

As the SD stations are operated remotely based on solar power only, the power consumption is crucial for the operation. It will be at the level of 10 W with the UUB, similar to the UB.

Increase of the duty cycle of FD

The air shower measurements using the FD provide most precise information on the shower characteristics by directly measuring the longitudinal shower profile. The main limitation is the low duty cycle of $\sim 15\,\%$ due to the restriction to clear moonless nights. The measurement periods are mainly defined by the NSB, particularly due to scattered moonlight but also due to twilight.

Extending the measurements also to periods with a large moon fraction will allow to increase the duty cycle of FD by about $50\,\%$ [36]. A crucial point is the performance and accelerated aging of the PMTs due to the higher light flux. Extensive tests of the PMT have been carried out in order to verify if an operation at high light fluxes is feasible when reducing the applied High Voltage (HV). They have shown that no negative effect on the performance of the PMTs is to be expected [36].

Test measurements have been carried out with one FD telescope during a period with high NSB [118]. They have proven that an extension of the measurement period can be performed at reduced gain with the current setup.

The impact of the higher NSB on the reconstruction efficiency has been evaluated by adding simulated NSB noise to measured FD events [36]. The results show that good quality data can be taken for events with energies above $10^{19}\,\mathrm{eV}$.

The additional radio detector

With AERA, the radio detection technique of extensive air showers has been studied in detail and with great success at the Pierre Auger Observatory. It has been shown that using the radio signal of air showers, an independent energy scale can be determined [66].

In case of horizontal air showers, the radio footprint at ground gets large, covering areas at the order of $100\,\mathrm{km}^2$. This effect is well proven by simulations [119] and measurements [120]. For horizontal air showers, the electromagnetic component is mostly absorbed in the atmosphere before reaching the SD and only the muons arrive at the stations. As the radio signal provides a measurement of the electromagnetic shower component, the radio array and SD together will be able to determine the relative contributions of the shower components in individual showers. Other detector components such as the UMD and SSD are only efficient for vertical showers making the radio array the ideal counterpart to increase the exposure.

Chapter 5

The Scintillator Surface Detector

The discrimination between the muonic and electromagnetic component of air showers is crucial for the success of AugerPrime. A high exposure is to be achieved in order to gain a large statistics data set of showers initiated by the highest energy primary particles. The full Pierre Auger Observatory should reach good discrimination sensitivity.

It will be achieved by adding a scintillator detector on top of the existing SD stations. This Scintillator Surface Detector (SSD) is easy to build and deploy and, together with the WCD, offers good discrimination power for the muonic and electromagnetic shower components. The signal of the SSD will be dominated by the electromagnetic shower component, whereas the WCD signal has a significantly larger contribution from the muonic component. This difference in the response allows for the discrimination between the two by using e.g. the matrix formalism that was introduced in section 3.2.3.

The SSD is complemented by the UMD and the radio array. The UMD has an excellent precision for muon measurements, but its installation by burying it underground is complex and time consuming. It is, therefore, not feasible for the full SD. The radio array, instead, is easy to deploy but suffers from the sparse grid of the SD. For vertical showers, the radio footprint is small but increases with zenith angle. It is thus the ideal counterpart to the SSD whose sensitivity lowers with increasing zenith angle.

5.1 Layout of the SSD

A detailed description of the SSD can be found in [121, 122]. In figure 5.1, a sketch of the layout of an SSD is shown and a photo of the SD station including the SSD can be seen in figure 5.2. Each SSD consists of 48 scintillator bars produced at the Fermi National Accelerator Laboratory in the USA [123] arranged in two detector halves. Each bar has a size of $1600 \times 50 \times 10\,\mathrm{mm}^3$ and holes along the long side with a distance of 25 mm from each other. The scintillator is coated with a TiO_2 reflective layer to increase the light yield, to mechanically protecting the bar, and to prevent cross talk between neighboring bars. The wavelength of the scintillation light is in the range of 330 nm to 480 nm but below 400 nm the scintillator becomes opaque. The active area of the detector is $3.8\,\mathrm{m}^2$.

In total 48 Wavelength Shifting (WLS) fibers (Kuraray Y11(300)M, S type [124]) with a diameter of 1 mm collect the light produced in the scintillator. Each fiber is pushed into one

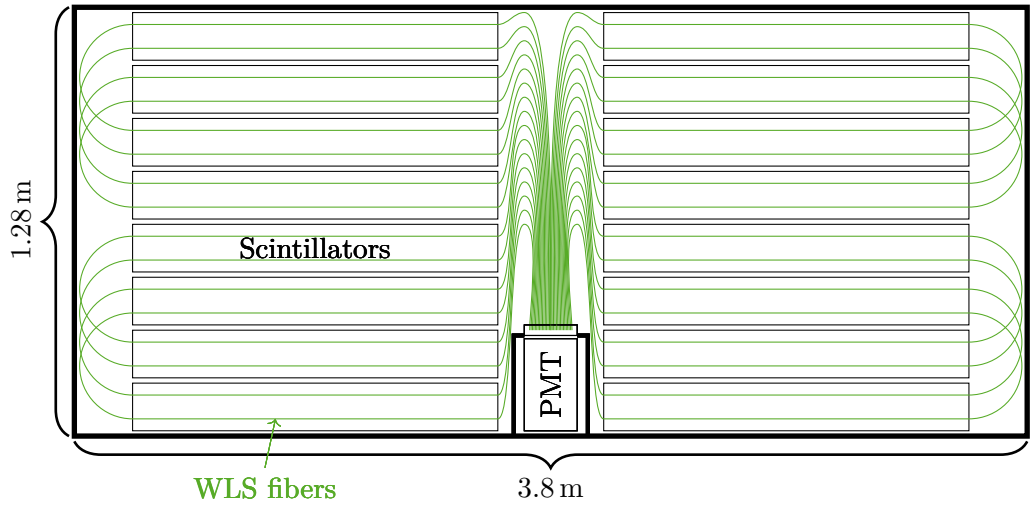

Figure 5.1: A sketch of the design of an SSD. The detector is split in two halves of scintillator bars. Optical fibers collect the light and guide it onto one central PMT. For reasons of clarity only eight instead of 24 scintillator bars are drawn per side. Sketch is not to scale.

Figure 5.2: A photo taken in the field of a station that already has an SSD installed. Image taken from [121].

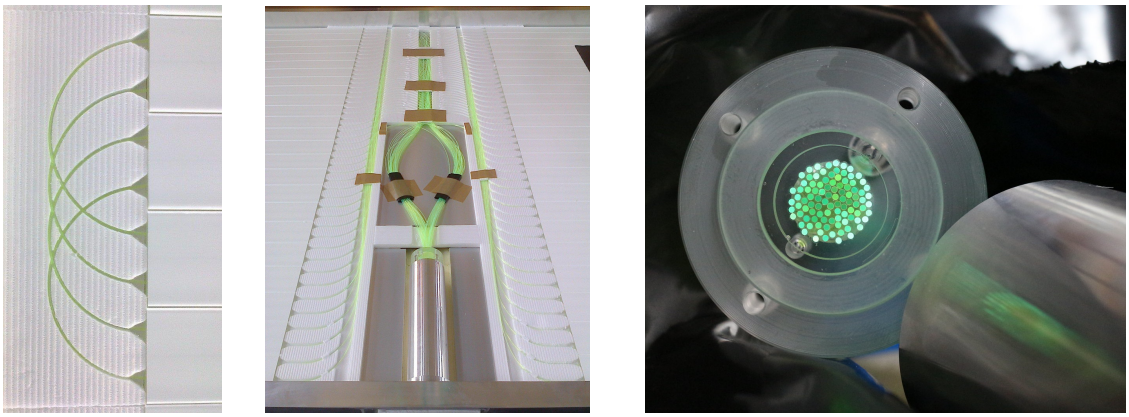

(a) (b) (c)

Figure 5.3: The routing of the WLS fibers in the SSD. At the ends *(a)*, they are routed in a U-turn and at the center *(b)* they are guided to a PMMA cookie. A cookie is shown in *(c)* before attaching it to the aluminum tube. The PMT is placed inside the aluminum tube at the bottom right of the image *(b)*. *(a)* and *(b)* taken from [121], *(c)* taken from [95].

hole of a scintillator, at the end routed in a U-turn and pushed back through the hole of another scintillator (cf. fig. 5.1). The absorption spectrum of the fiber matches the emission spectrum of the scintillator and is then shifted into the range 450 nm to 570 nm. All fibers have the same length of 5.9 m to guarantee the same amount of absorption for all fibers and avoid inhomogeneities in the detector. In addition, same fiber lengths ensure identical timing independent of the scintillator bar where the signal was produced. In order to avoid mechanical damage, the fibers are guided by plastic routers outside the scintillator bars.

The WLS fibers are guided to the space between the two detector halves where they are hold in place by a, so called, *cookie*. It consists of a round piece of Polymethyl Methacrylate (PMMA) with a hole of 13 mm diameter. A 6 mm thick PMMA window is placed in front of the fiber bundle and closes the cookie. The 96 fiber ends are fixed with optical cement (Eljen EJ-500 [125]). Before gluing, the fiber ends are melted to avoid light losses due to defects produced by cutting the fiber. The routing of the fibers is shown in figure 5.3.

One PMT of type Hamamatsu R9420 [126] is installed in the center of the detector. It has a cathode size of 1.5” and a quantum efficiency of about 18 % at 500 nm. It was chosen for its high dynamic range also when operated at low gain. The high dynamic range is required to allow for detection of single particles for calibration (cf. sec. 4.2.1) up to a signal of $\sim 2 \times 10^4$ MIP [116]. The HV is generated directly on the PMT base to avoid the need of long HV cables. The PMT is held inside a Polyvinyl Chloride (PVC) tube that can be pushed into the SSD from one side of the detector (cf. fig. 5.1), where it is hold in place by an aluminum tube. The PMT is pushed against the cookie with a spring and a silicone pad, between PMT cathode and the cookie window, ensures a good optical coupling and low mechanical stress on the PMT. The aluminum tube is closed with a light tight cable feedthrough but remains accessible throughout the whole lifetime of the detector.

The detector is enclosed by an aluminum frame with a length of 3.8 m, width of 1.28 m and a height of 8.3 cm. The scintillator bars are significantly thinner than the height of the detector. The remaining space is filled with polystyrene panels below and above the scintillators. They reduce the amount of air inside the detector and ensure a good mechanical

stability. The bottom and top of the detector are covered by 1 mm thick aluminum sheets. All corners and joints are sealed with glue to achieve a light tight frame. The total weight of one SSD reaches 120 kg.

5.1.1 Production of the SSD

The SSD was mainly designed at the Karlsruhe Institute of Technology (KIT) and twelve prototypes built there were deployed in the Argentinean Pampas in an early phase of the upgrade in the second half of 2016. After the validation of the design, the production of all 1500 detectors was distributed among six institutions: RWTH Aachen University, Laboratory of Subatomic Physics and Cosmology Grenoble, Karlsruhe Institute of Technology, Institute of Nuclear Physics Krakow, Italian National Institute of Nuclear Physics Lecce, and National Institute for Subatomic Physics Nijmegen. First institutions started production in 2017 and others followed consecutively until beginning of 2018.

The production at RWTH Aachen University started in March 2018 at a rate of about two detectors per week. It was finished in October 2019 with the completion of the 135th detector.

5.2 Testing of the SSDs produced in Aachen

As the production was distributed among six institutions, criteria for testing the detectors before shipment to Argentina were established to verify a good quality of all detectors [122]. These criteria include the hardware to be used for testing and the quantities to be measured.

The minimal requirement on the setup according to these criteria are two particle detectors working in coincidence to provide a trigger on atmospheric muons. These trigger detectors should have a sufficient area to test a representative part of the SSD (e.g. all scintillators have to be included in the measurement). If the trigger detectors are to small to achieve representativeness, different parts of the SSD can be measured consecutively. For the setup presented in this section, the two detector halves will be tested separately. The resolution of the Data Acquistion (DAQ) should suffice to determine the signal of a single Photon Equivalent (p.e.) and it should have a dynamic range large enough to determine the MIP signal at the same time.

There are two main quantities to be measured:

1. The average light yield of the detector for through-going MIPs
2. The lighttightness of the detectors.

At RWTH Aachen University, besides these quality criteria, the development of an easy-to-use test procedure was a main goal of the commissioning of the test stand. It should ensure that the tests can be carried out by different people without introducing systematic differences between the different testers and with only a short introduction needed.

A layout of the setup is shown in figure 5.4 and an image is shown in figure 5.5. All components will be described in detail in the following sections. In order to determine the light yield for through going MIPs, two MiniAMDs [75, 127, 73] have been placed above and below the detector under test. They are operated in coincidence and trigger the readout of the signal from the SSD PMT (Hamamatsu R9420 [126]), allowing for a pure muon signal measured with the SSD. The signal is digitized by a DRS4 evaluation board [128].

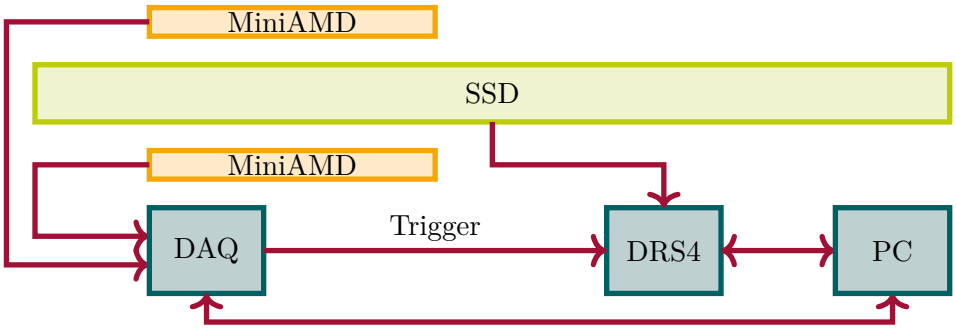

Figure 5.4: A layout of the test stand for the validation of the produced SSDs in Aachen. The two Mini Aachen Muon Detector (MiniAMD) detectors are operated in coincidence and trigger the readout of the SSD when a muon crossed both MiniAMDs. The MiniAMD DAQ consists of an EASIROC evaluation board and a mini PC which can be controlled through an ethernet connection. The SSD PMT signal is recorded with a DRS4 evaluation board.

Figure 5.5: A photo of the SSD test stand. Here, two SSDs are lying on the stand. Only the top one was tested.

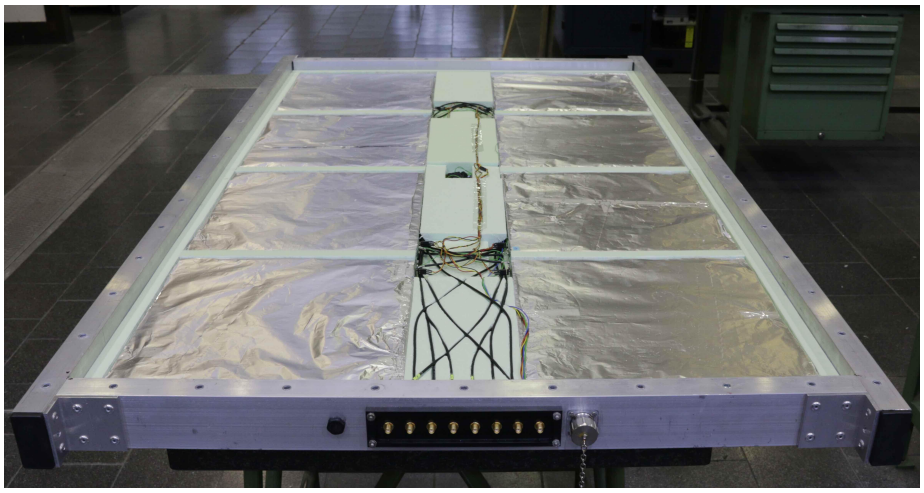

Figure 5.6: The interior of a MiniAMD. The space between the scintillator tiles is filled with Styrodur® and used for the routing of cables. Image taken from [73].

5.2.1 Mini Aachen Muon Detector

The MiniAMD had been developed in the scope of two doctoral theses [73, 74] and also a Master's thesis [129]. Here, only a summary of the main characteristics that are of importance for the presented test procedure will be described.

A photo of an open MiniAMD is shown in figure 5.6. It is made up by eight scintillator tiles with an area of $30 \times 30\,\mathrm{cm}^2$ and thickness 0.5 cm each. They are arranged in two rows of four tiles each with a gap of 18 mm between two neighboring tiles of a row. The two rows are separated by a distance of 120 mm. This arrangement results in a sensitive area of $0.72\,\mathrm{m}^2$.

The light produced by through-going particles in one tile is collected in a WLS fiber with a diameter of 1 mm which is clamped in a sigma shaped grove. One fiber end is mirrored using a highly reflective foil and the other end is guided to the edge of the scintillator tile. The light is detected by a Silicon Photomultiplier (SiPM)[1] (Hamamatsu S13360-1350PE [130]) of size $1.3 \times 1.3\,\mathrm{mm}^2$. The SiPM signal is processed by an Extended Analogue SI-pm ReadOut Chip (EASIROC) evaluation board [131]. One EASIROC board has 32 input channels and can thus operate up to four MiniAMDs.

The EASIROC allows for the implementation of various trigger algorithms and provides a trigger output. For the presented setup, a trigger was generated only if the two tiles which are directly above each other in the two MiniAMDs registered a signal. Only nearly vertical muons are selected like this, reducing a smearing of the MIP charge distribution due to the zenith angle distribution of atmospheric muons. For the given geometry of 1.4 m vertical distance between the two MiniAMDs, a maximum zenith angle of $\approx 17°$ is possible when the muon goes through opposite corners of the two tiles.

The MiniAMD data acquisition also hosts a single-board computer which allows for control of the EASIROC, including the trigger scheme and the SiPM voltages. Communication with the single-board computer is done via Secure Shell (SSH) through an ethernet connection. It allows for an easy starting and stopping of the trigger.

[1] Details on SiPMs will be explained in chapter 6.

As MiniAMD is smaller than the SSD, it is installed on a movable forklift to allow for easy change of the measurement position. Thus, each side of the SSD is measured separately. To ensure always the same position of the MiniAMD with respect to the SSD, the forklift is always pushed until it touches the SSD. The central position of the MiniAMD is verified with a custom made tube that can be used as a reference distance of the forklift with respect to the edge of the SSD (cf. fig. 5.5). The measurement is repeated with the MiniAMD placed on the other side of the SSD to test both sides of the detector.

5.2.2 DRS4 Evaluation Board

The Domino Ring Sampler of version 4 (DRS4) allows the digitization of up to 9 input channels at a sampling speed of 0.7 to 5 GS/s at an accuracy of 12 bit. For the presented setup, an evaluation board equipped with the DRS4 is used. It hosts four independent input channels with a dynamic range of 1 V peak-to-peak with a selectable median value of 0 V to 0.5 V. The input channels have an analogue bandwidth of 950 MHz. In total, 1024 samples can be digitized per channel per readout. A threshold trigger can be chosen for each channel independently and also an external trigger signal can be provided. The readout is triggered by an arbitrary AND/OR-logic of the four input channels and the external trigger input.

The conversion from ADC values to volts as well as the exact timing has to be calibrated for each sample of each channel individually. The manufacturer provides a software package that easily allows to perform these calibrations. The calibration is temperature dependent and therefore needs to be redone in case of significant temperature variations.

For the presented setup, the MiniAMD trigger signal has been used as a trigger input to the DRS4 evaluation board. No additional trigger conditions have been requested. As the PMT signals are very short ($\mathcal{O}$(ns)), a sampling frequency of 3 GS/s has been chosen to properly register them.

5.2.3 Data Taking Procedure

At RWTH Aachen University, 135 detectors were produced and had, consequently, to be locally tested. The design of the test stand and data taking procedure took into account this large number of detectors to be examined. Special focus was given to an easy-to-use data taking procedure. It would ensure that the tests can be carried out by several individuals, one at a time, without the need of extensive explanations or introducing systematic differences. In the following paragraphs the different steps of the data taking procedure will be explained.

The PMT

The PMT can easily be pushed into the aluminum tube of the SSD. A photo of the PMT inside its PVC tube together with the spring and flange is shown in figure 5.7. The PMT flange when installed in the SSD is displayed in figure 5.8. The flange is fixed with six screws to the SSD. A blue line on the PVC tube marks a position that is always placed at the top. This ensures that the PMT cathode always has the same orientation.

A Sub-Miniature-A (SMA) cable connects the PMT anode to the DRS4 signal input. The HV is supplied by a Nuclear Instrumentation Module (NIM) module with Safe High Voltage (SHV) type output connector. The HV throughput of the flange hosts a LEMO S Connector [132]. A short adapter piece is thus used in between a SHV cable and the throughput.

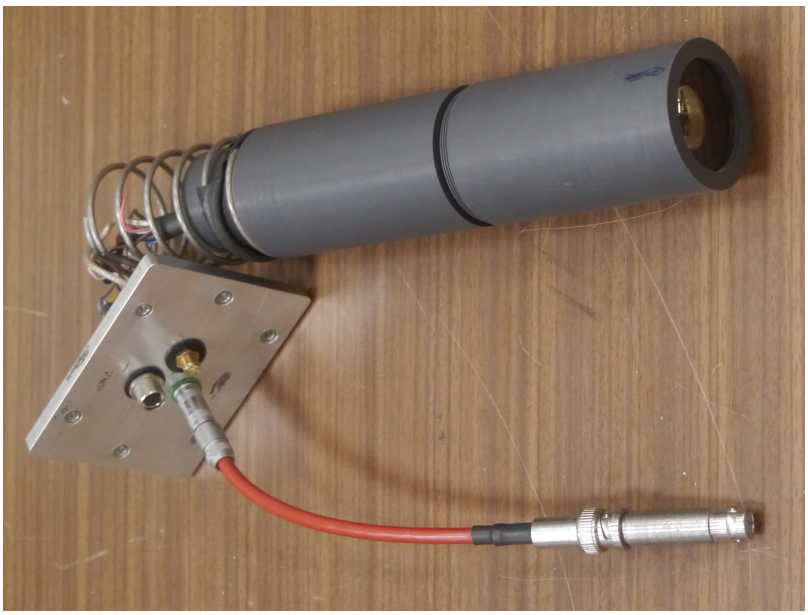

Figure 5.7: Photo of the SSD PMT inside the PVC tube connected to the flange with a spring in between. The flange has three cable throughputs: one for the HV supply, one for the signal and one for additional monitoring and slow control information. The last one is not used in the presented setup. The cable shown in the figure is the adapter piece for the HV.

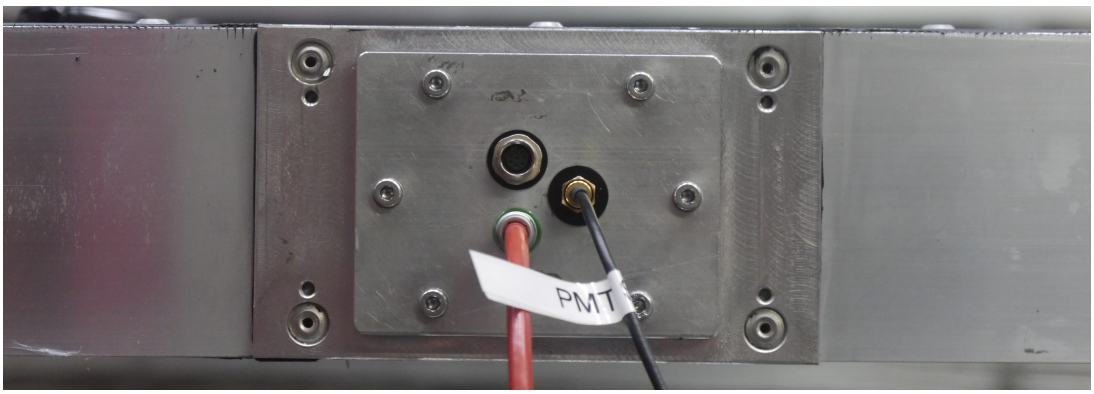

Figure 5.8: Photo of the SSD PMT flange when installed in the SSD. Six screws hold the flange in place. The PMT signal cable in black and the HV cable in red are connected. The third connector for transfer of slow control information was not used.

The HV and signal cables can be placed on hooks near the position of the PMT when unused to ensure a clean setup and quick installation.

The maximum HV allowed for the PMT is 1.5 kV. To achieve a sufficient signal-to-noise ratio also for single p.e. pulses, this maximum voltage is applied. It has to be ramped up manually at the HV supply.

The MiniAMD

The two MiniAMDs need three cables to be connected. Communication in between the PC and the MiniAMD is provided through ethernet and the trigger signals are supplied on a trigger output which has to be connected to the DRS4 with an SMA cable. The whole setup is powered by a standard power plug. As MiniAMD is movable, all these cables are available twice in the test stand in order to avoid significant rerouting of cables each time the position of MiniAMD is changed.

Again, hooks near the standard MiniAMD positions for the tests allow for convenient storage of unused cables. The connected trigger cable also has to be exchanged at the trigger input of the DRS4 evaluation board each time the position of the MiniAMD is exchanged.

The test software

The test software was designed to allow for as low user interaction as possible. To start a measurement, only the detector ID and the side that is being measured have to be indicated. The software then automatically starts the MiniAMD trigger system and sets up the DRS4 evaluation board correctly.

The ADC and timing calibration of the DRS4 evaluation board is checked for its applicability to the current settings and the current temperature. In case the temperature of the board is too low, the software waits for it to heat up. In case the temperature is too high or it does not heat up enough, the calibration has to be redone. For the calibration, all signal cables have to be disconnected. Thus, it cannot be done fully automatically but the tester is guided through the procedure. The temperature is monitored throughout the test run.

Data is automatically stored into ROOT-files [133]. The final file contains the raw traces triggered by the MiniAMD and additional software triggered traces that can be used to analyze the single p.e. pulses of the PMT. For each trace, the measurement time and the temperature of the DRS4 evaluation board are stored. In addition, the data is already processed during the measurement procedure and partial results are stored to the file. Details on the data analysis will be given in section 5.2.4.

The tester is provided with some plots showing the performance of the test. It is updated every 1000 muon triggered traces and allows to check for a proper performance of the testing. An example of such a status display is shown in figure 5.9. On the bottom right, one can see the charge distribution of the muon triggered traces and in the bottom center the charge distribution for the single p.e. pulses that have been found. The other plots will be explained in detail in section 5.2.4.

The test procedure can be finished by the tester or after a specified number of muon triggered events. Typically, a total of 250 000 events is taken. When the data taking is finished, the single p.e. charge and rate are determined as well as the MIP charge. These results are preliminary and checked in detail later. They allow the tester to discover any

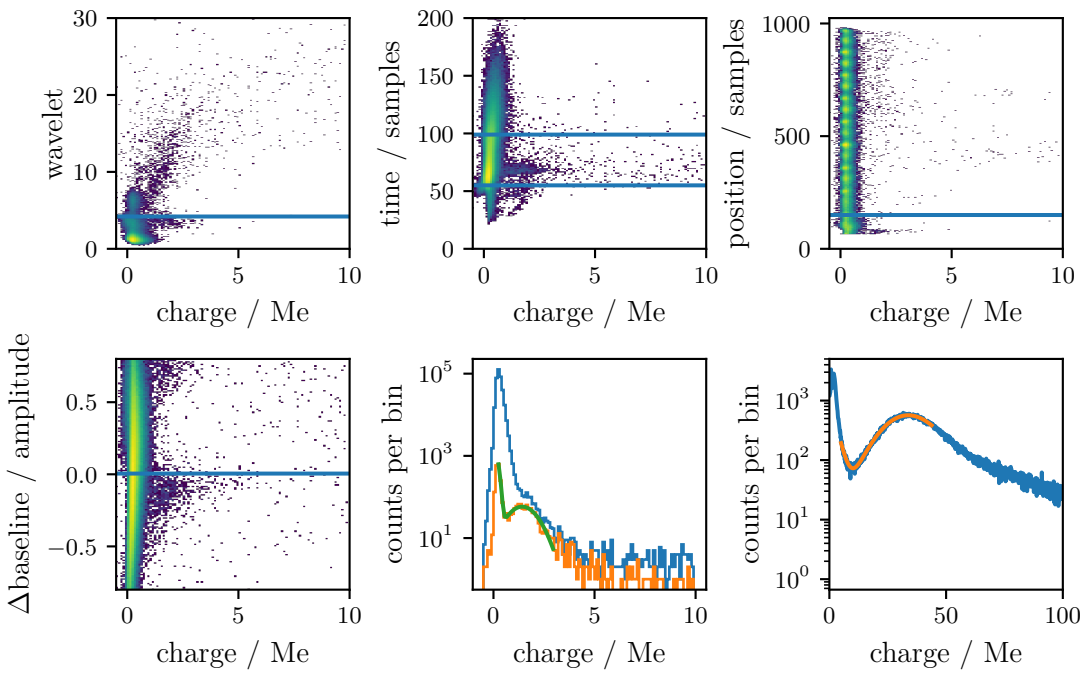

Figure 5.9: The status display as shown during the SSD test measurements. All charges are given in units of million elementary charges Me[2]. At the bottom right, the distribution of the muon triggered signals is shown. At the bottom center, the distribution of single p.e. signals can be seen before (blue) and after (orange) applying additional cuts. The curve after cuts is only shown at the end of a measurement. The performed cuts on the different variables are shown with blue lines. The cuts are preliminary and checked and potentially adjusted manually.

major problems, e.g. a too low HV value for the PMT. In case of problems, further action is taken depending on the specific kind of deviation from the expected result.

In addition, at the end of the test procedure, the MiniAMD trigger is stopped and its SiPM voltage ramped down. Afterwards, the mini PC is also shut down to allow for disconnection from power of the whole MiniAMD setup.

The tests have been carried out by four different people, mostly by a student assistant.

5.2.4 Analysis of the recorded traces

The analysis of the data taken during the test runs mainly separates in two different parts:

1. The determination of the charge produced by a through going MIP, typically a muon.

2. The determination of the single p.e. charge and rate.

With the single p.e. rate, the light tightness of the detector can be verified and the ratio of the charge of the MIP peak and the single p.e. is a measure for the light yield of the detector for through going muons.

[2]One Me is the charge of 10^6 electrons. Multiplying by the elementary charge $e = 1.602 \times 10^{-19}$ C converts the value to SI-units.

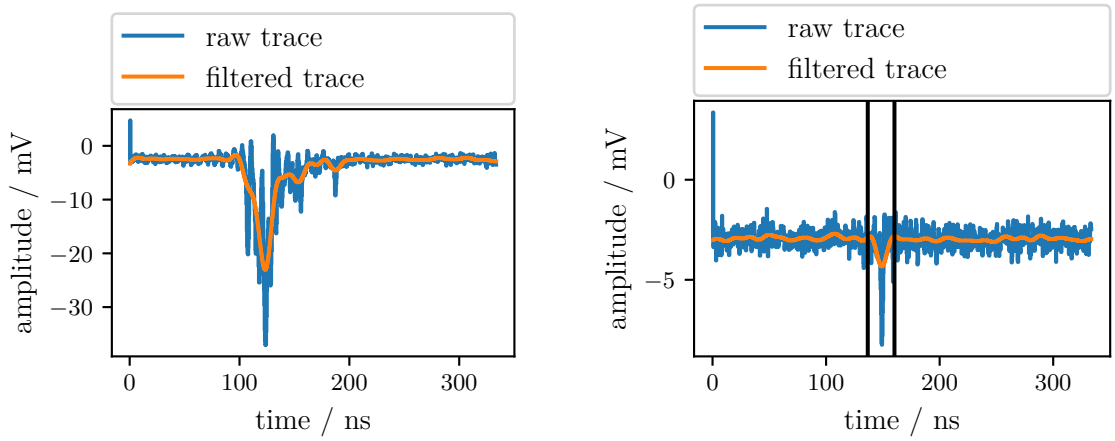

(a) A trace in the SSD triggered by MiniAMD due to a through going muon.

(b) A random triggered trace with a single p.e. pulse. The black lines mark the integration window.

Figure 5.10: Two example traces as measured with the SSD test setup. In both cases the raw trace and the trace after applying a 65 MHz filter are shown. The peak in the first bin is an artifact of the DRS4. It is excluded in the analysis.

In the following sections, the analyses of the different types of traces are described. In order to smooth the trace and remove high frequency noise, a fifth order Butterworth filter [134] is applied to the data. Its critical frequency where the gain drops by −3 dB is set to 65 MHz. This type of filter is also implemented in the UUB front end. Thus, the shape of the signals is the same as in the field in Argentina. A pulse finding algorithm is then applied to the filtered data and the found pulse is integrated to determine its charge.

All raw traces are stored into a file. A detailed analysis is only performed if the temperature of the DRS4 evaluation board is in a region of ±3 °C around its temperature during calibration.

Analysis of MiniAMD triggered traces

An example of a trace recorded for the muon triggered case is shown in figure 5.10a.

As PMT pulses are negative, in the following description, *lower* refers to a smaller value and thus to a *larger* amplitude. Vice versa *higher* refers to a *smaller* amplitude.

The pulse finding algorithm moves a sliding window with a length of five samples over the trace. If in five consecutive windows, the last sample is lower than the first sample, a pulse is considered to be found. As the baseline might vary, it is determined as the mean amplitude in the range of 30 to 5 samples before the beginning of the pulse. The sliding window is moved further along the trace to find the minimum of the pulse. It is considered to be found when the last sample of the window is higher than the first sample. The end of the pulse is the first sample after the minimum that exceeds the baseline in front of the pulse.

All samples in the found range are subtracted by the baseline and integrated. For convenience, the resulting sum of voltages is converted into the number of electrons in the pulse. The conversion factor results from the sampling rate $f = 3\,\mathrm{GHz}$, the readout resistor

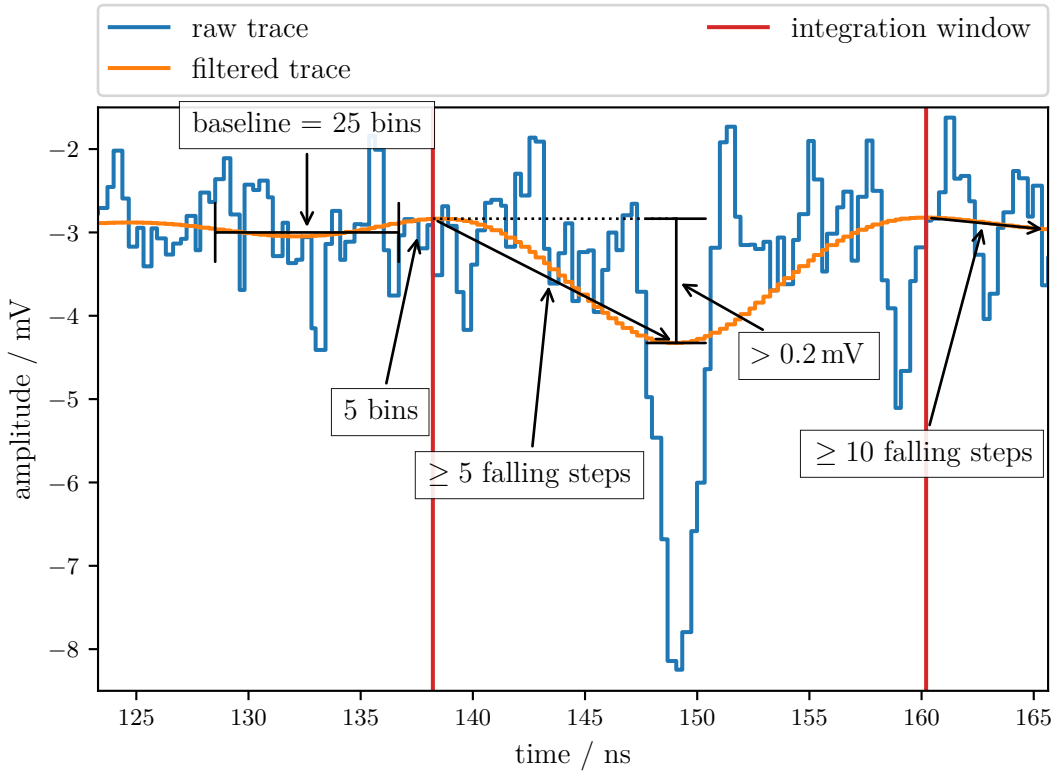

Figure 5.11: Schematic of the working principle of the algorithm to detect single p.e. pulses in the software triggered traces. Details are given in the text.

$R = 50\,\Omega$ and the elementary charge $e = 1.602 \times 10^{19}$ C:

$$Q_e = Q_\mathrm{V} \cdot \frac{1}{fRe} \tag{5.1}$$

With Q_e the charge in numbers of electrons and Q_V the sum of the samples in V. The resulting charge is filled into a histogram for later analysis. It will be described in section 5.2.5. Examples can be seen in figures 5.9 (bottom right) and 5.17.

Analysis of software triggered traces

In contrast to the signals triggered by the MiniAMD, the single p.e. pulses are very small and not triggered on. They can therefore occur at any position in the trace and are difficult to distinguish from background. The threshold for finding pulses is set very low and the pulse finding analysis is slightly different compared to the traces triggered by MiniAMD. A low threshold is important to avoid a bias in the extraction of the single p.e. charge. The size of the single p.e. pulses fluctuates due to noise and the small pulses resulting from underfluctuations need to be taken into account. Otherwise, a bias towards too high charges might occur.

In addition, various characteristics of the pulse are stored to be able to perform a posterior selection of the single p.e. events. A schematic is shown in figure 5.11 which is a zoom into figure 5.10b.

For this analysis, a pulse is considered to be found if more than five consecutively falling samples are detected in the waveform. In addition, the difference in amplitude of the first and last consecutively falling sample must exceed a threshold of 0.2 mV. The baseline is determined in the range of 30 to 5 samples prior to the beginning of the pulse. The end of the pulse is considered to be the beginning of the next *falling* edge that exceeds a length of ten samples. This way, small fluctuations are not taken into account. If the absolute difference between the baseline before the pulse and the last sample in the pulse exceeds 80 % of the amplitude, the pulse is discarded.

If the pulse fulfills all the criteria mentioned above, its characteristics are stored:

1. Its full charge, i.e. the sum of baseline subtracted amplitudes in the found range. It is converted to the number of electrons according to equation (5.1).
2. The length of the pulse, i.e. the number of samples from beginning to end of the pulse.
3. The position of the minimum of the pulse in the trace.
4. The difference in amplitude between the baseline before the pulse and the last sample divided by the amplitude.
5. A wavelet magnitude which is described in the following paragraph.

The distributions of these variables with respect to the charge of the pulse are shown in the status display for the tester (fig. 5.9).

The wavelet magnitude is determined by analyzing the raw trace (i.e. before applying the 65 MHz Butterworth filter) using a wavelet transformation. The wavelet transformation W is given by the integral of the product of a wavelet function $\psi(t)$ and the signal $S(t)$:

$$W(\mu, \sigma) = \frac{1}{\sqrt{\sigma}} \int_{-\infty}^{\infty} \psi\left(\frac{t-\mu}{\sigma}\right) \cdot S(t)\,\mathrm{d}t \tag{5.2}$$

with μ and σ the location and width of the wavelet function. The result is a two dimensional distribution in μ and σ which is a measure for the agreement of the wavelet with the signal for the given parameters. For the presented analysis a *Ricker wavelet* [135] is used. It has the functional form given in equation (5.3) and a 'Mexican hat' shape (figure 5.12):

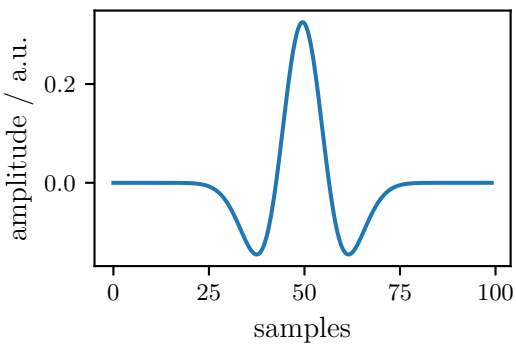

$$\psi(t) = \frac{2}{\sqrt{3\sigma}\pi^{1/4}} \left(1 - \left(\frac{t}{\sigma}\right)^2\right) e^{-\frac{t^2}{2\sigma^2}}. \tag{5.3}$$

Figure 5.12: The shape of the Ricker wavelet.

An example of the resulting spectrum is shown in figure 5.13 for the trace shown in figure 5.10b. At the beginning and end of the trace the wavelet magnitude is large. This is

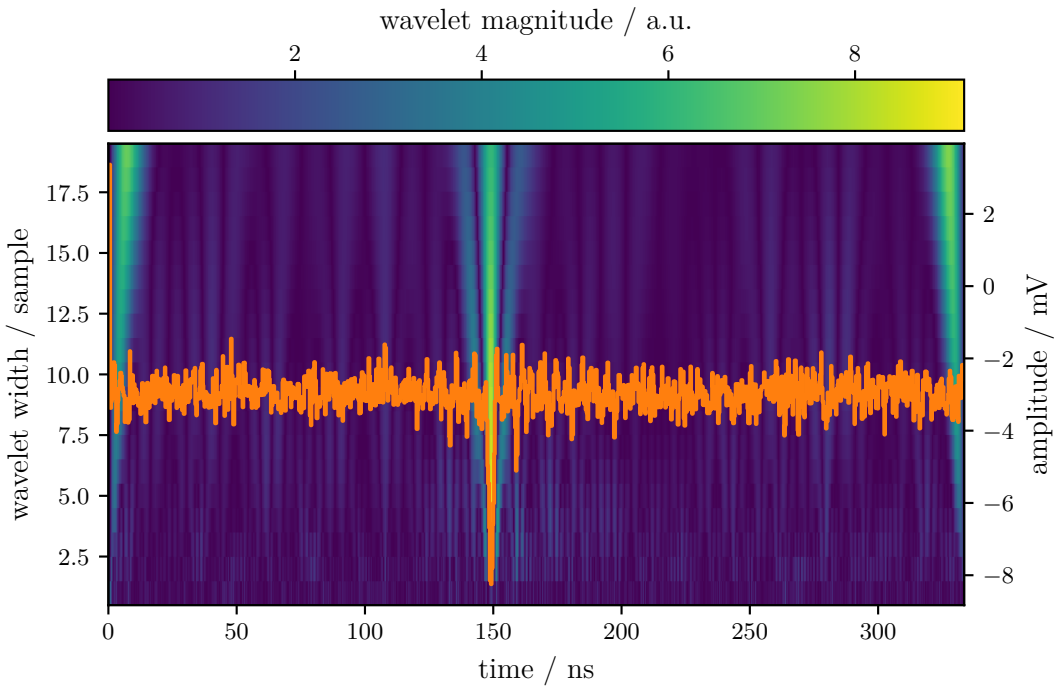

Figure 5.13: The wavelet magnitude as measured for different widths of the wavelet template for an example of a single p.e. pulse (orange). In the wavelet magnitude, there is a clear maximum visible at the position of the peak.

a result of edge effects. Therefore, if the peak of the pulse is in the first 20 ns or last 10 ns it is discarded. The region in the beginning is longer because of the determination of the baseline before the pulse starts. The largest wavelet magnitude in a region of ±5 ns around the maximum of the found pulse is also stored.

5.2.5 Determination of the light yield and light tightness of the SSDs

In the previous section, the analysis of the measured traces has been described. In order to determine the light yield and light tightness of the SSDs, the charge spectra need to be analyzed.

The analysis procedures for the different quantities to be characterized will be explained in the following paragraphs. For clarity, all results are shown together in section 5.2.6 in figures 5.19 and 5.20.

Determination of the single p.e. charge

From the two dimensional representation of the various characteristics of the single p.e. pulse candidates (cf. fig. 5.9), cuts can be determined that allow to reduce the background events while leaving the true single p.e. pulses unchanged. Two main features were observed to contribute to the background. One are artifacts from the DRS4 producing short positive peaks and the other contribution is an occasional ringing noise on the trace. The origin of the latter could not be determined. A detailed description of the different background contributions is given in appendix A.

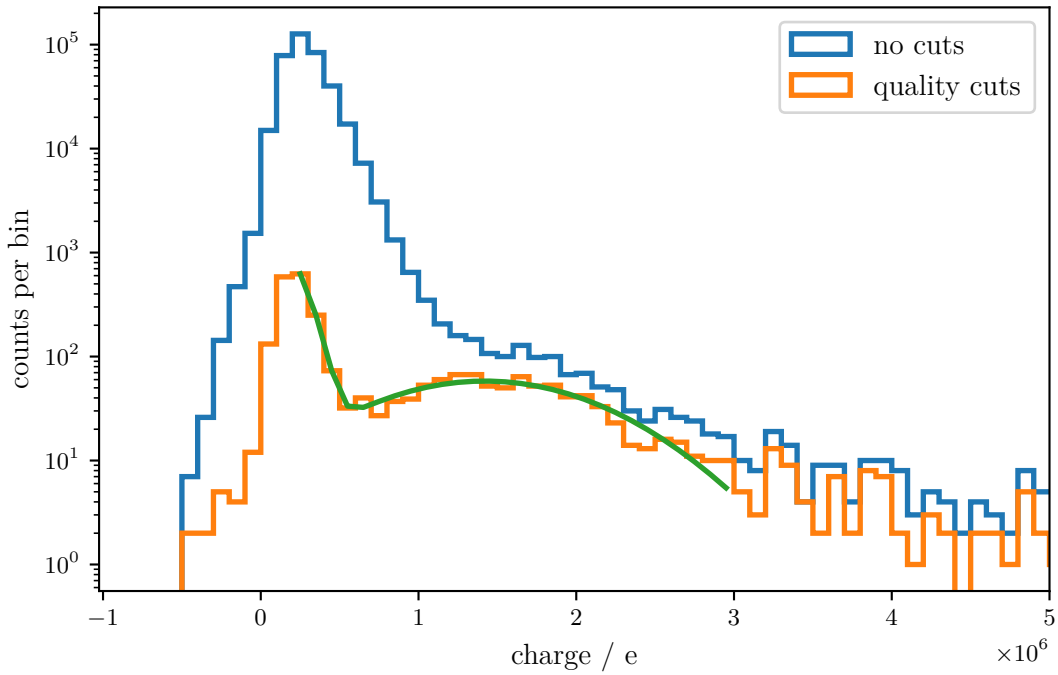

Figure 5.14: An example of the single p.e. distribution before and after cuts. The applied cuts significantly reduce the background and allow to properly determine the single p.e. peak.

The different cut values are determined for each SSD test individually due to variations in the background. Each measurement is checked manually and the cut values might be readjusted to achieve satisfying results.

In figure 5.14, an example of a single p.e. distribution before and after applying the cuts is shown. Even though the single p.e. pulse is difficult to distinguish from the background noise, it can be resolved well in this case. The distribution is fit with a sum of two Gaussian distributions. One describes the falling edge of the background and the second describes the single p.e. peak. The position of the second Gaussian corresponds to the average charge of a single p.e. pulse and the integral allows to determine the number of single p.e. pulses measured.

The precision of the determination of the single p.e. charge is expected to be rather low due to the significant contribution from background and the rather low number of single p.e. pulses that can be observed. For instance, for a rate of 10 kHz only a fraction of $\sim 0.5\,\%$ of the traces contains a single p.e. pulse. In principle, the rate of the software trigger could be increased to allow for a higher number of measured single p.e. pulses. But this would introduce a significant dead time and reduce the MIP rate. It is therefore not feasible.

In figure 5.15a, the distribution of the relative uncertainty of the measured single p.e. charges is shown. It clearly peaks around 5 % with a long tail. The tail originates mainly from measurements that could only be taken for a short time leading to very low statistics. The average uncertainty is at about 7.7 %, which is sufficient for the tests.

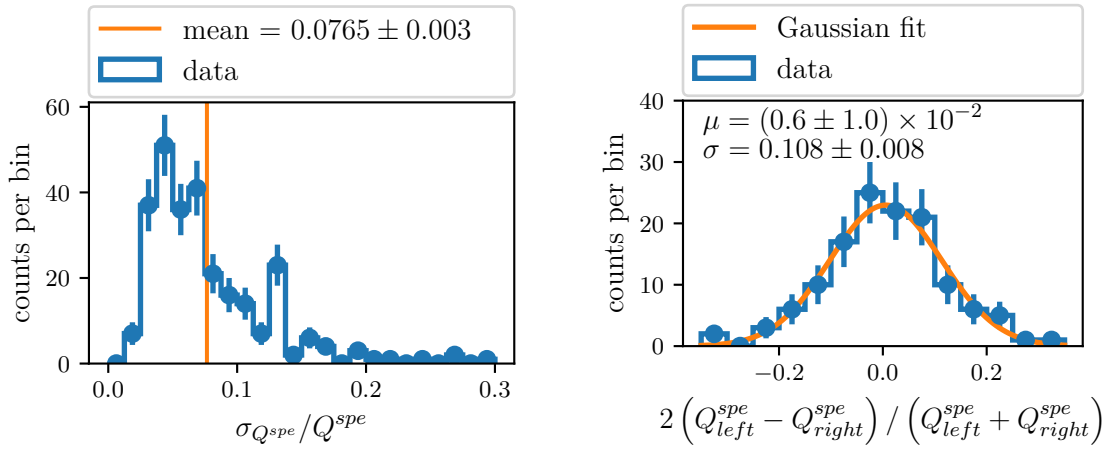

(a) The relative uncertainty of the single p.e. measurement.

(b) The relative difference of the single p.e. charge for two measurements of the same detector. The given μ and σ are the mean and width of the Gaussian distribution fitted to the data.

Figure 5.15: Comparison between two methods to determine the uncertainty on the single p.e. measurement.

The determination of the single p.e. and their uncertainty can be verified. For each detector, two measurements exist: one for its right side and one for its left side[3]. When switching between the two measurements, only the MiniAMD is moved but the PMT stays switched on. Thus, there are two measurements of the single p.e. charge for each detector. From the relative difference between the two measurements, the uncertainty of the determination of the single p.e. charge can be deduced. In figure 5.15b, the corresponding distribution is shown. It agrees well with a Gaussian fit. The relative uncertainty on the determination of the single p.e. charge is 10.8 %. It is slightly above the uncertainty that is determined from the fit directly. This effect might be explained by additional effects that change the single p.e. charge such as variations in temperature. As the effect is small and does not disturb the verification of the SSDs, it is not further investigated.

In figure 5.19 (5th row), the single p.e. charge is shown with respect to the detector ID. It varies between 0.76 Me to 1.6 Me. For all detectors, at least two data points are shown, for the measurements of the left and right side, respectively. There is no systematics visible in the measurement.

For detectors with ID 11 through 15, 20, 25, and 32, the single p.e. charge could not be determined. For the IDs 11 through 15 and 32 the proper determination of the single p.e. had not yet been implemented. As no sufficient software triggered data sample had been taken, a later analysis was not possible. The corresponding single p.e. charge is thus taken as the weighted average of all other measurements with the corresponding standard deviation. For the IDs 20 and 25, the applied voltage was 1400 V instead of 1500 V. At this lower voltage, the single p.e. could not be resolved. Here, the single p.e. charge was also taken from the weighted average and then corrected for the different applied voltage. The correction factor was taken from the datasheet [126] to be ≈ 0.70.

[3] *Left* and *right* side are defined from the perspective of a tester looking on the side of the PMT flange.

Determination of the single p.e. rate

The light tightness of the SSDs has to be verified. This can be done by measuring the single p.e. rate. In case of a light leak, the scintillator will be illuminated by ambient light and produce scintillation photons. These can be detected with the PMT and add to its dark noise.

From the integral of the Gaussian fit shown in the previous section and in figure 5.14, the single p.e. rate can be determined. The number of single p.e. pulses is given as the binned integral of the Gaussian. From the number of analyzed traces, the total measurement time is determined. The length of one trace is reduced by the excluded bins at its beginning and end.

The result is shown in figure 5.19 (bottom row). The single p.e. rate is similar for all detectors with an average of (8.61 ± 0.16) kHz for measurements during daytime and (8.67 ± 0.10) kHz during nighttime. They are in good agreement indicating that no systematic problem which affects the light tightness of all detectors is present. As the efficiency of the algorithm has not been determined, these values are not necessarily the true single p.e. rate and should thus not directly be compared to other measurements using different setups. However, the measurement will allow to identify outliers.

For the detectors 11 through 15, 20, 25, and 32, the shown rate is zero. As mentioned before, the detection of single p.e. pulses was not yet implemented for these detectors. Instead, the single p.e. rate was measured manually with an oscilloscope and no excess was found.

For detectors 23 and 95, the measured rate exceeds the average significantly. They have therefore been studied in more detail.

For detector 23, right after the measurement it was recognized that the PMT tube was not properly closed by the testing person. Light entered through a very narrow slit leading to the increased rate. The test was redone with a properly closed PMT tube. In addition, an inspection with a torch has been carried out. The noise rate was checked on an oscilloscope while illuminating consecutively all the joints of the detector. Again, no abnormal behavior was found and the detector approved.

Detector 95 was also checked using a torch and an oscilloscope. This way, a light leak was found at one bottom corner. No obvious misconstruction was visible by eye at this joint (fig. 5.16), meaning that the hole must have been tiny. It was closed by the mechanical workshop by milling a groove along the joint and filling it with additional glue. The detector was tested afterwards and showed standard behavior.

In the end, all detectors are verified to be light tight.

Determination of the MIP charge

The determination of the MIP charge is significantly simpler than that of the single p.e. due to the large signals that can be well separated from noise. In figure 5.17, an example of a MIP charge distribution is shown. In order to determine the position of the maximum of the peak produced by the through going MIPs, a fit is performed. It consists of an exponential contribution to describe the pedestal peak and a Landau function $\mathcal{L}$ convoluted with a Gaussian distribution G:

$$f(Q) = c_0 \cdot e^{-c_1 Q} + \mathcal{L}(Q, c_2, c_3, c_4) * G(Q, \mu = 0, \sigma = c_5) \,. \tag{5.4}$$

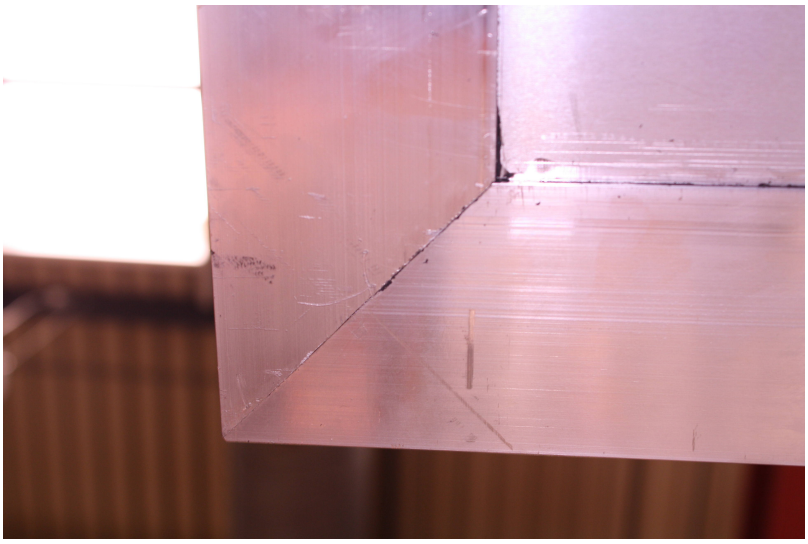

Figure 5.16: The edge at the bottom of detector with ID 95 where a light leak was detected before repair. The black parts correspond to the glue. No obvious issue is visible at the joint. It was sealed by the mechanical workshop.

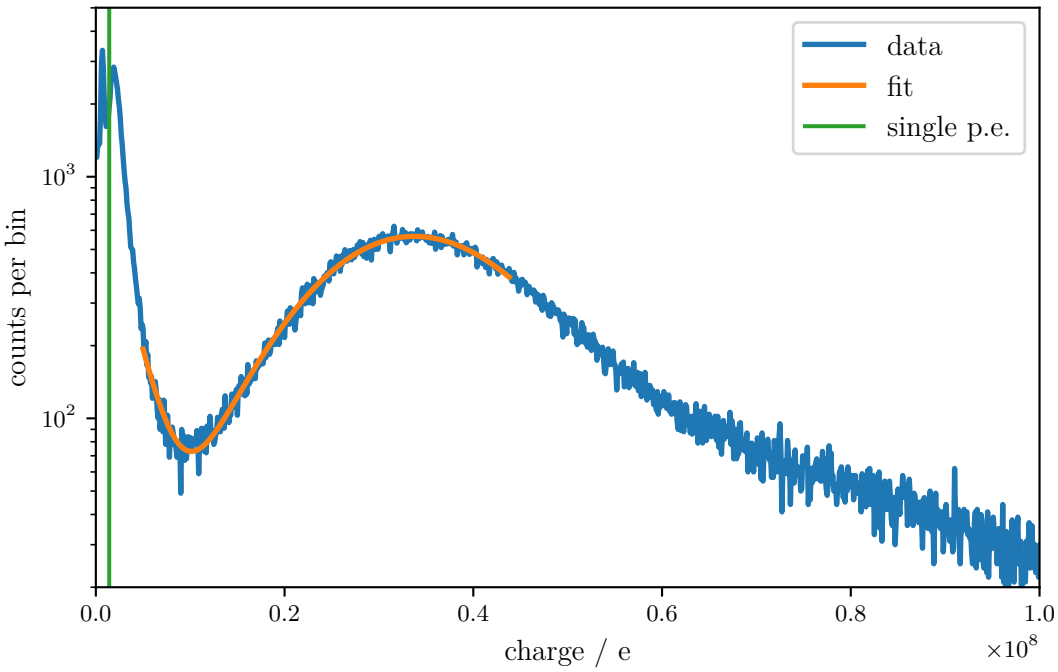

Figure 5.17: An example of a MIP charge distribution. The hump produced by the through going MIPs is well separated from the noise and the performed fit allows to determine the position of its maximum.

The parameters c_0 and c_1 describe the exponential background, c_2 through c_4 describe the normalization, MPV and width of the Landau distribution, respectively, and c_5 is the width of the convoluted Gaussian. The peak is expected to have a Landau shape (cf. sec. 3.2.1) but it is broadened by noise which can be described by a Gaussian. The function describes the peak very well and allows to determine its position and width.

The position of the peak is a fit parameter and can directly be extracted. As the width of the peak depends on both the width of the Landau and the width of the Gaussian in a non-trivial way, it is determined numerically. As standard Gaussian error propagation cannot be performed here, the uncertainty on the Full Width at Half Maximum (FWHM) was determined on a stochastic basis. Random values have been drawn for the coefficients of the fit according to the covariance matrix. For each of these sets of coefficients, the FWHM is calculated. The standard deviation of the distribution of FWHMs is a measure for the uncertainty.

The mean statistical uncertainty of the measurement of the MIP and FWHM is as low as 0.4 % and 0.9 %, respectively, due to the high statistics of typically around 250 000 triggers.

In figure 5.19, the charge of the MIP peak and its FWHM are shown with respect to the detector ID. There is a clear oscillatory pattern visible in the charge of the MIP and its FWHM. Such a pattern might arise from variations in temperature over the measurements resulting in a variation of the light yield of the scintillator. The workshop building where the tests were performed is temperature controlled and variations should be <5 °C. In addition, the tests have not been performed in order of their IDs but randomly for logistics reasons. In figure 5.20, the test results are shown with respect to the date of the test. In the representation with respect to the date of the test, the oscillatory pattern is significantly less pronounced. Thus, it is likely to result from differences in the production, e.g. due to different production batches of the scintillators or fibers which correlate with the detector ID. As the results are satisfying and prove that the detectors are working properly, this systematics is not investigated in more detail.

The light yield of the SSDs

From the measured single p.e. and MIP charge, the calibrated light yield of the SSDs in terms of p.e. can be determined. The resulting MIP and FWHM are shown in figures 5.19 and 5.20. The errorbars significantly increase compared to the uncalibrated result. It originates mainly from the large uncertainty on the determination of the single p.e. charge.

In figure 5.18, the distributions of the MIP charge and its FWHM are shown. A slight asymmetry due to a longer tail at high values can be recognized. A reason might be that the single p.e. can get underestimated when it comes to close to the background. This might happen when the HV was set too low.

The width of the distributions is around 10 %. For the single p.e. charge, an uncertainty of 7.7 % to 10.8 % was found while the uncertainty on the MIP charge or FWHM, respectively, is negligible. The remaining variation of about 0 % to 7.6 % thus is the intrinsic variation of the SSDs. These arise from differences in the scintillators, fibers or production quality.

5.2.6 Summary of the test results

All the test results with respect to the detector ID or the date of the test, respectively, are shown in figures 5.19 and 5.20. The determination of the single p.e. charge was carried out for each measurement individually with an uncertainty of 7.7 %. It also allowed to validate

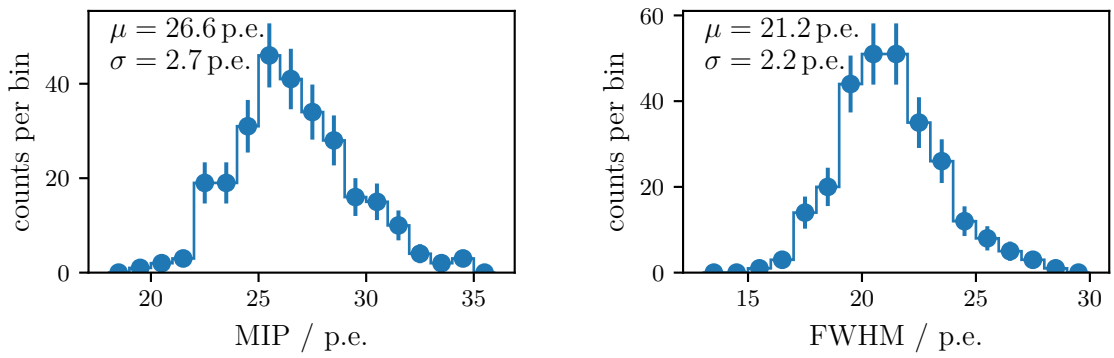

(a) (b)

Figure 5.18: The calibrated position of the MIP peak and its FWHM distributions. In both cases a slight asymmetry with a longer tail for large values is visible. This might result from an underestimation of the single p.e. charge in cases when it is rather low and thus difficult to be distinguished from background.

the light tightness of the SSDs by measuring the single p.e. rate. One detector has shown a light leak that could be repaired.

The light yield of the detectors has been measured to be 26.6 p.e. on average with a width of 2.7 p.e.. The main contribution to the uncertainty of the MIP charge originates from the single p.e. charge. Taking that into account, the overall spread in the light yield of the produced SSDs is below 7.6 %.

Two detectors have been measured at the KIT for cross checking. They have shown good performance there and these measurements allow for a precise comparison of the SSDs produced at RWTH Aachen University and at KIT. A conversion factor for the MIP signal determined in Aachen MIP_{AC} and the vertical MIP signal obtained at KIT $VMIP_{\mathrm{KIT}}$ was measured as $VMIP_{\mathrm{KIT}}/MIP_{\mathrm{AC}} = 0.837 \pm 0.038$. In addition, the measurement setup at KIT allows for a determination of the homogeneity of the response of the SSDs. The detectors produced at RWTH Aachen University have shown the same results as those of other production sites in terms of both light yield and homogeneity. A detailed description of these results is shown in appendix B.

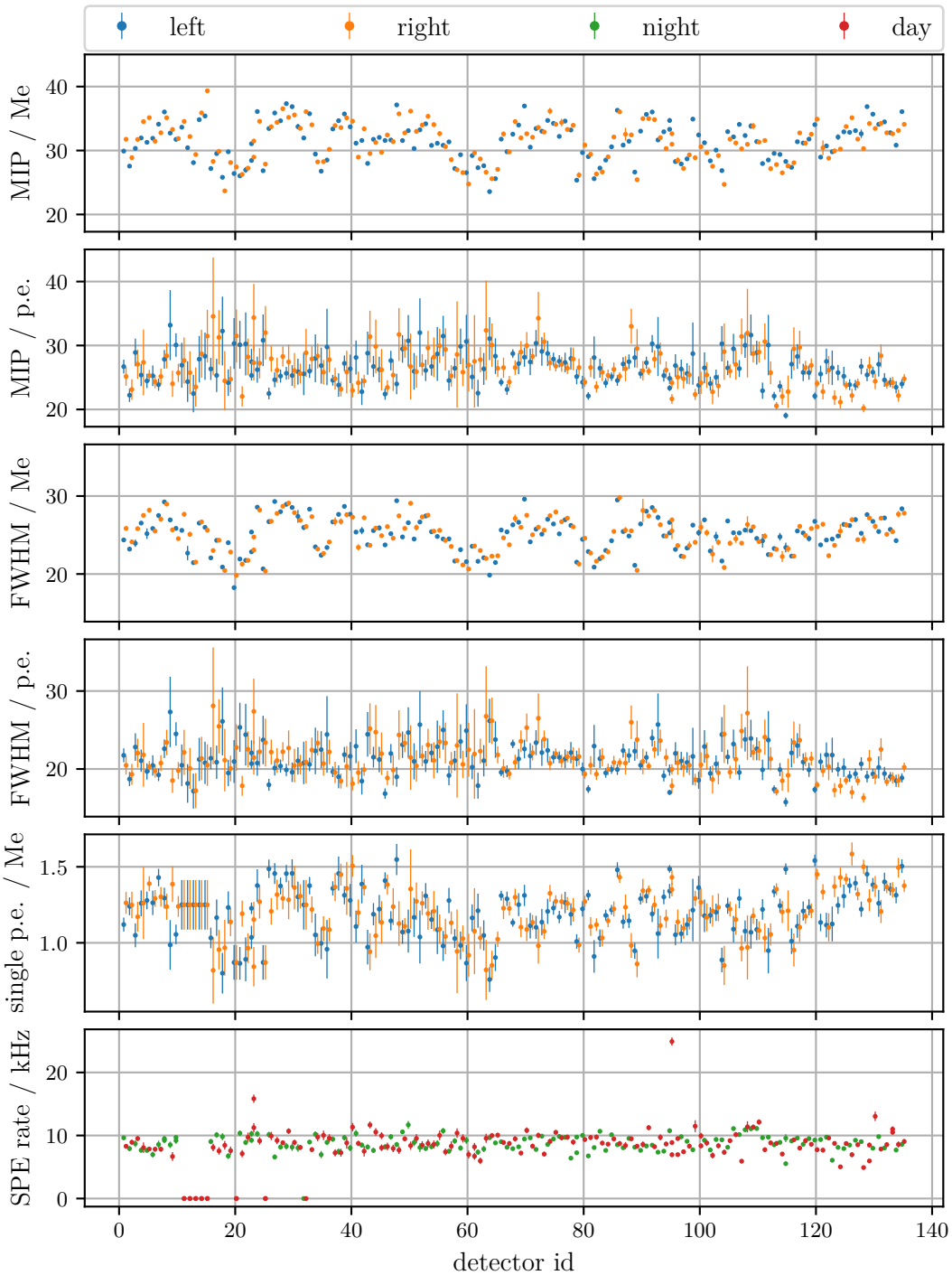

Figure 5.19: The SSD test results with respect to the detector ID. For each detector, two measurements (left and right side) have been performed. Points are slightly shifted to avoid overlaps.

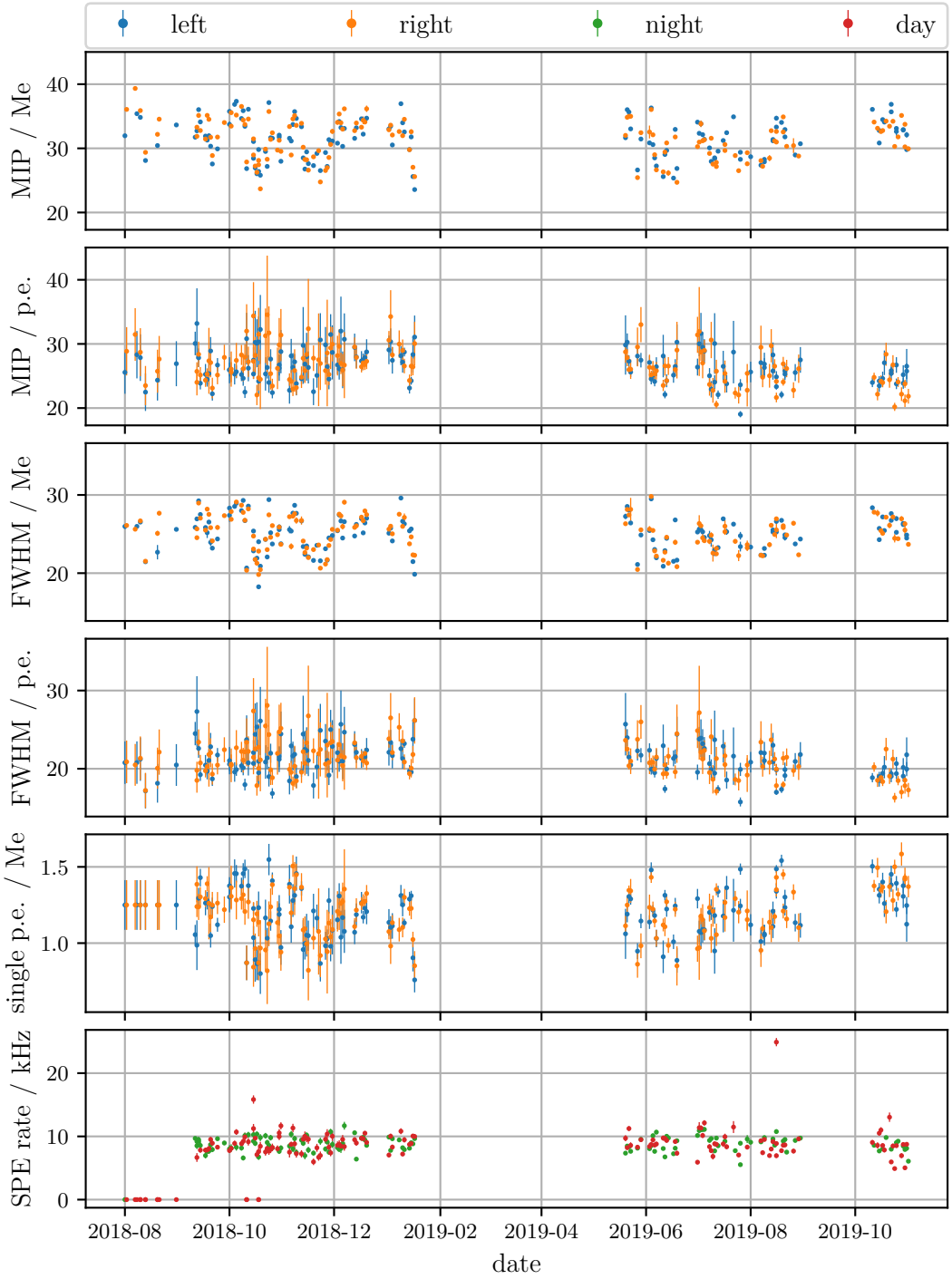

Figure 5.20: The SSD test results with respect to the date of the test. The large gaps result from periods where a lack of storage space prevented further measurements.

Chapter 6

Silicon Photomultipliers

SiPMs are light detectors based on semiconductor technology. While the development of solid state single photon detectors already started in the 1960's [136, 137], the first SiPMs were created at the end of the 1990's [138, 139]. Their development is a very active field of research and huge advancements have been made since their first operation [140] and they start to be used in many applications [141].

SiPMs are cell structured devices compiled of Avalanche Photodiodes (APDs) operated in Geiger-mode, so called Geiger-mode Avalanche Photodiodes (G-APDs) which will be introduced in detail in section 6.1.3. The cells are connected in parallel and only one summed output signal is generated. Typical cell sizes range from 10 µm to 75 µm with sensor areas of 1 mm^2 to 36 mm^2 [142, 143, 130]. This leads to a number of cells of $\mathcal{O}(10^2)$ to $\mathcal{O}(10^5)$. In figure 6.1, a photo of an SiPM is shown where the cell structure can be seen well. As each cell releases a fixed amount of charge when hit by a photon, the maximum output signal for simultaneously impinging photons is limited by the number of cells. This affects the dynamic range and will be further discussed in section 6.7.

In the following sections, an overview of the physics and characteristics of SiPMs will be given. An equivalent electronic circuit will be introduced and result in the implementation of a simple simulation of the response of SiPMs. The main goal of the development of the simulation is a precise understanding of the behavior of SiPMs in regimes of high light fluxes in order to extend the linear dynamic range.

6.1 The Geiger-mode Avalanche Photodiode

Geiger-mode Avalanche Photodiodes (G-APDs) are based on the working principle of a p-n junction, the boundary created when n-type and p-type semiconductors are brought together. In the following sections, the p-n junction and the transition to the G-APD will be explained. A good overview of different types of semiconductor devices can be found for example in [144, 145]. The information given in the following sections is based on these publications.

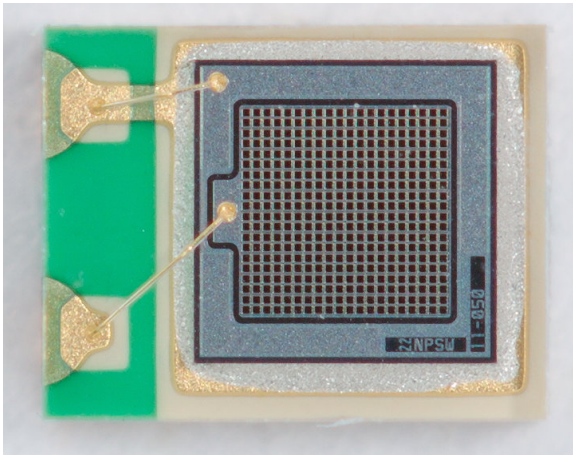

Figure 6.1: A photo of a Hamamatsu S12571-50C type SiPM. It has a cell size of 50 µm over an area of $1 \times 1\,\mathrm{mm}^2$. The single cells are well visible. Courtesy of L. Middendorf [74].

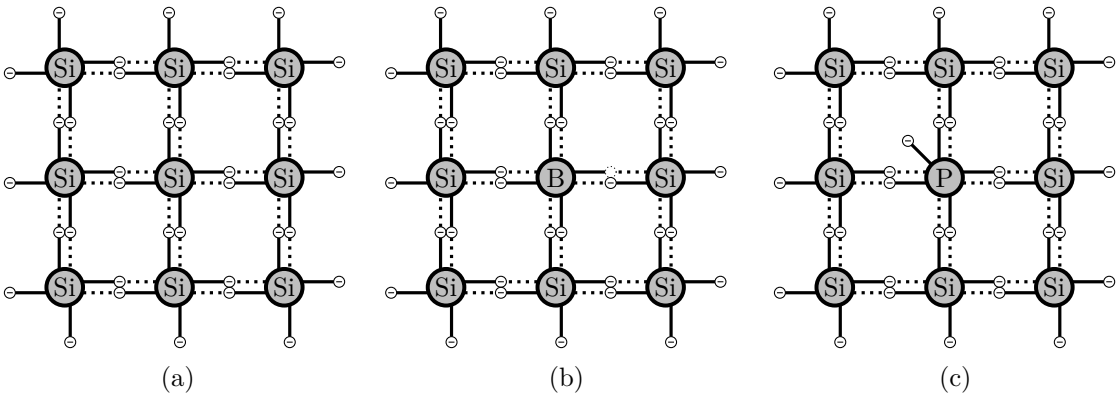

Figure 6.2: The lattice structure of silicon: *(a)* Undoped pure silicon. *(b)* *p-type* silicon doped with boron. One electron is missing in the lattice, a hole is created. *(c)* *n-type* silicon doped with phosphor. The additional electron is not part of a bond and can move through the lattice.

6.1.1 Doping of silicon

Silicon atoms have four valence electrons allowing for the creation of a regular lattice structure with each silicon forming four covalent bonds with its neighbors (fig. 6.2a). All valence electrons participate in a covalent bond and cannot move freely.

Adding a small amount of impurities of atoms with three valence electrons (e.g. boron or aluminum) will lead to a lack of electrons (fig. 6.2b). With this *p-type* doping, a positively charged hole is created which is often called *acceptor* because it can accept an electron.

For *n-type* doped silicon, atoms with five valence electrons (e.g. phosphor or arsenic) replace a silicon in the lattice (fig. 6.2c). The additional electron is referred to as a *donor* and does not have a partner to form a covalent bond and is only loosely bound.

The negative electron is donated to the conduction band while the positive hole is created in the valence band and can accept an electron to create a covalent bond [145].

6.1.2 The p-n junction

When a p-type and an n-type semiconductor are brought together, a *p-n junction* is formed. A schematic of such a junction is shown in figure 6.3. Electrons drift from the n-doped to the p-doped side of the boundary leaving a positive charge excess behind. At the n-doped side, they recombine with holes creating a negative charge excess. At the boundary, a sudden change from a negative to a positive charge excess occurs and an electric field is created. It counteracts the electron drift, resulting in an equilibrium when a sufficiently strong field is reached. The region where the recombination takes place is called *depletion region*.

At thermal equilibrium the resulting voltage V_{bi} over the junction is given by [145]:

$$V_{\mathrm{bi}} = \frac{k_{\mathrm{B}}T}{e} \ln\left(\frac{n_{\mathrm{D}} n_{\mathrm{A}}}{n_{\mathrm{i}}^2}\right) \tag{6.1}$$

with k_{B} the Boltzmann constant, T the absolute temperature, and e the elementary charge. The symbols n_{D} and n_{A} refer to the concentration of the donor and acceptor, respectively, and n_{i} is the intrinsic charge carrier density for an undoped semiconductor.

The width of the depletion region is given by [145]:

$$W_{\mathrm{d}} = \sqrt{\frac{2\epsilon_{\mathrm{s}}}{e \cdot n}\left(V_{\mathrm{bi}} - \frac{2k_{\mathrm{B}}T}{e}\right)} \tag{6.2}$$

with ϵ_{s} the permittivity of the semiconductor and n the concentration of charge carriers with $n \approx n_{\mathrm{D}}$ if $n_{\mathrm{D}} \gg n_{\mathrm{A}}$ and vice versa.

An additional reverse bias voltage V_{b} can be applied to increase the width of the depletion region. The additional positive voltage applied at the n-doped side pulls electrons to the cathode and holes to the anode, respectively. The additional voltage must be added to the intrinsic voltage when calculating the width of the depletion zone:

$$W_{\mathrm{d}} = \sqrt{\frac{2\epsilon_{\mathrm{s}}}{e \cdot n}\left(V_{\mathrm{bi}} + V_{\mathrm{b}} - \frac{2k_{\mathrm{B}}T}{e}\right)} \tag{6.3}$$

Increasing the bias voltage leads to a high field strength in the order of 10^5 V/cm in the depletion region [146]. At a specific voltage, breakdown phenomena occur leading to avalanche multiplication processes [145]. Above this *breakdown voltage* V_{bd}, free charge carriers undergo sufficient acceleration in the strong field to produce new charge carriers by impact ionization. An avalanche of charge carriers is produced leading to a high current through the p-n junction.

The breakdown voltage is temperature dependent due to an increasing probability of the charge carriers to excite optical phonons in the lattice with increasing temperature. The charge carriers loose energy through these processes and cannot further ionize atoms. The energy losses need to be compensated for by applying a higher electric field which corresponds to a higher breakdown voltage [145].

The initial free charge carrier can be created for example by thermal excitation of an electron in the valence band. An alternative possibility which is of special interest here is the creation by a photon. If a photon with sufficient energy impinges on the p-n junction, it can ionize an atom and the free charge carrier initiates the avalanche. This breakdown effect leads to a high amplification of the initially small signal of only one charge carrier.

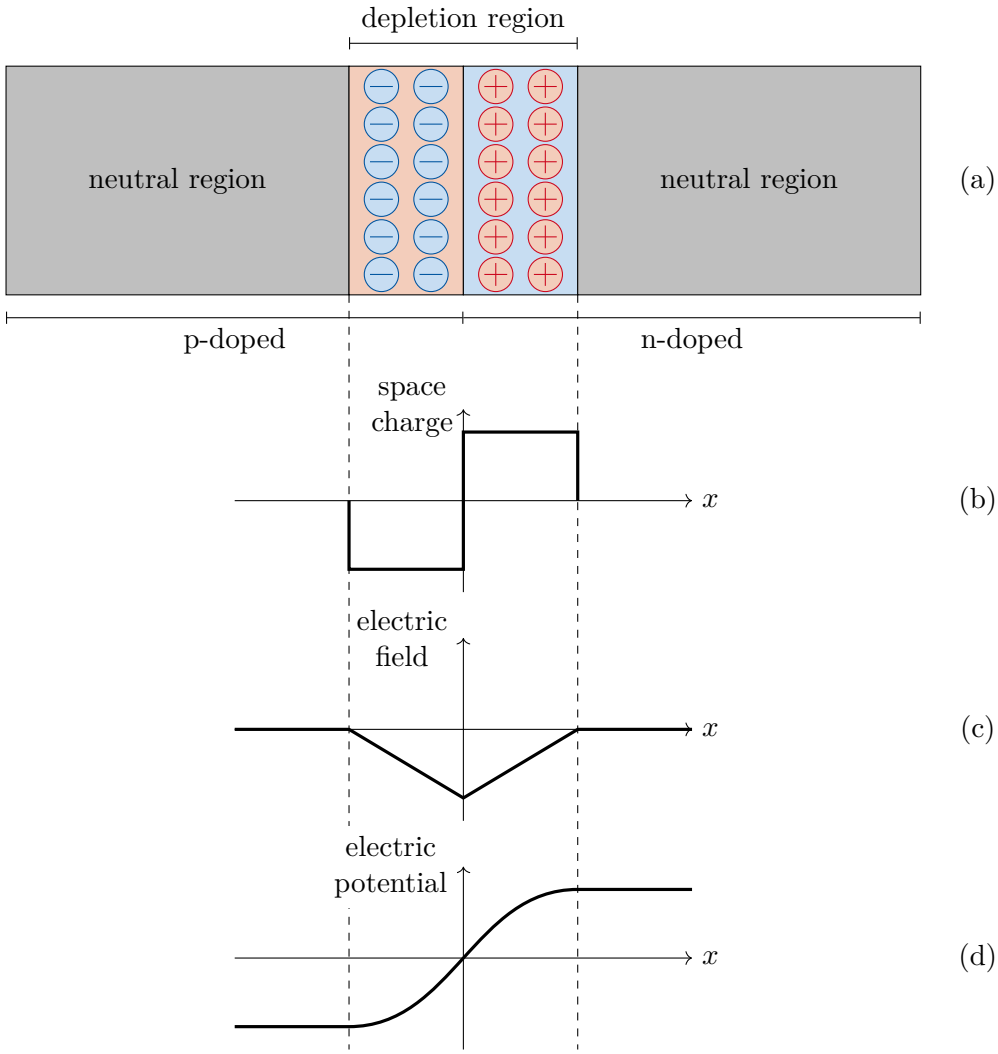

Figure 6.3: Schematic of the characteristics of a p-n junction. *(a)* Electrons from the n-doped region fill holes in the p-doped region creating an excess of negative charges. Vice versa, holes move from the p-doped region to the n-doped region. *(b)* The (idealized) distribution of the space charge over the p-n junction. *(c)* An electric field is created at the junction with a maximum field strength at the border of the p- and n-doped regions. *(d)* The electric potential changes from negative to positive over the junction.

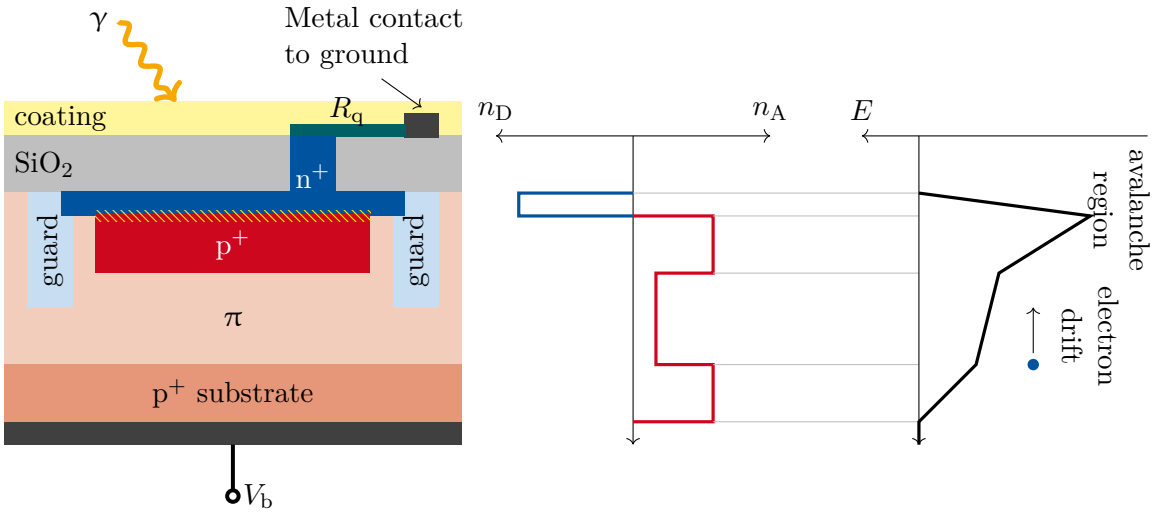

Figure 6.4: The sketch on the left depicts the vertical structure of a G-APD as used in modern SiPMs. The photon enters from the top where a protective coating (typically an epoxy resin or glass) is applied. It is followed by a transparent, insulating silicon dioxide layer with thickness of $\approx 0.15\,\mu m$ that separates the semiconductor from the metal contacts. Below, an $0.1\,\mu m$ to $1.5\,\mu m$ thick heavily doped n^+-layer is connected to the metal contact through the quenching resistor R_q. Together with the following heavily p^+-doped layer of a few µm thickness, they form a p-n junction with the depletion region hatched in yellow. The next $\approx 300\,\mu m$ thick lightly doped π-layer is the region where electron-hole pair creation takes place. The bottom heavily doped p^+-layer connects to the bias voltage through metal contacts. In the center and right plot, the density of donors n_D and acceptors n_A and the electric field strength E, respectively, are depicted. Adopted from [147].

6.1.3 Construction of the Geiger-mode Avalanche Photodiode

A Geiger-mode Avalanche Photodiode (G-APD) is a photo sensitive semiconductor device based on the p-n junction. It exploits the avalanche multiplication to achieve a high signal gain and must therefore be operated with a bias voltage above the breakdown voltage.

A schematic of a G-APD is shown in figure 6.4. Along the vertical structure of the G-APD, the doping concentrations n_D and n_A are not constant. Amplification only takes place in the very small depletion region ($\mathcal{O}$ (µm)). The thickness of the G-APD is dominated by a lightly positively doped π-layer ($\mathcal{O}$ (100 µm)). This is the region where impinging photons are absorbed and create electron-hole pairs. The large thickness results in a good Photon Detection Efficiency (PDE) (section 6.2.3) compared to the thin depletion region of a simple p-n junction only. The electric field in this region is too weak to allow for avalanche multiplication but sufficient to avoid recombination of the created electron-hole pair. The electron drifts towards the depletion region where the electric field strength gets strong and avalanche multiplication is initiated.

The produced current flows through the diode and the built-in series quenching resistor R_q leading to a voltage drop (section 6.6.1). Consequently, the voltage that is applied at

the diode junction decreases and eventually falls below the breakdown voltage. The electric field gets too low to sufficiently accelerate the charge carriers to create secondary ionizations. The avalanche is *quenched* and the G-APD recharges again.

The quenching always occurs at the same current flow. During the recharge of the cell, avalanches can in principle be initiated again. The resulting output signal will be smaller because the voltage across the diode did not reach its nominal value. For two instantaneously impinging photons only one avalanche is released and the output signal is identical to that from one impinging photon. Only after a sufficient waiting time (typically $\gtrsim 100\,\mathrm{ns}$, cf. sec. 6.6.8) the G-APD is fully recharged.

6.1.4 Arrays of G-APDs

An array of multiple G-APDs connected in parallel is referred to as Silicon Photomultiplier (SiPM). The G-APDs are also called *cells*. The behavior of the single G-APD remains the same as explained in the previous section.

Due to the parallel readout, the output current of the SiPM is the sum of the signals of the G-APDs. The SiPM is thus able to detect multiple photons at the same time as long as they impinge on different cells. This is typically the case in most applications. The number of cells limits the number of detectable photons. The consequences for measurements will be discussed in more detail in section 6.7.

6.2 Characteristics of SiPMs

A variety of characteristics of SiPMs has to be taken into account when considering their application. In the following paragraphs, the most important ones for usage in high energy physics experiments are introduced. Good overviews with detailed descriptions can for example be found in [140, 146].

6.2.1 The breakdown voltage

The breakdown voltage V_{bd} has already been introduced in section 6.1. When a reverse bias voltage V_{b} above the breakdown voltage is applied, amplification of the signal in Geiger-mode takes place. The voltage excess above breakdown is the overvoltage:

$$V_{\mathrm{ov}} \equiv V_{\mathrm{b}} - V_{\mathrm{bd}} \quad . \tag{6.4}$$

The value of the breakdown voltage can differ by up to 10 % for different SiPMs of the same type [130, 148]. Various techniques allow to determine the breakdown voltage for an individual SiPM. As the gain, i.e. the number of charge carriers released per avalanche, depends linearly on the overvoltage (cf. sec. 6.2.2), it can be measured for different bias voltages and be extrapolated to the voltage where it becomes zero. For this method the gain needs to be determined precisely which is sometimes difficult, especially when the gain is very low.

An alternative is to measure the dependency of the dark current on the bias voltage. The dark current flows even when the SiPM is not exposed to any light due to random triggering of avalanches. Details will be given in section 6.2.4. When the breakdown voltage is reached, the dark current rises steeply. The square root of the current becomes linear and determination of its intersection with the pedestal yields the breakdown voltage [149]. Such

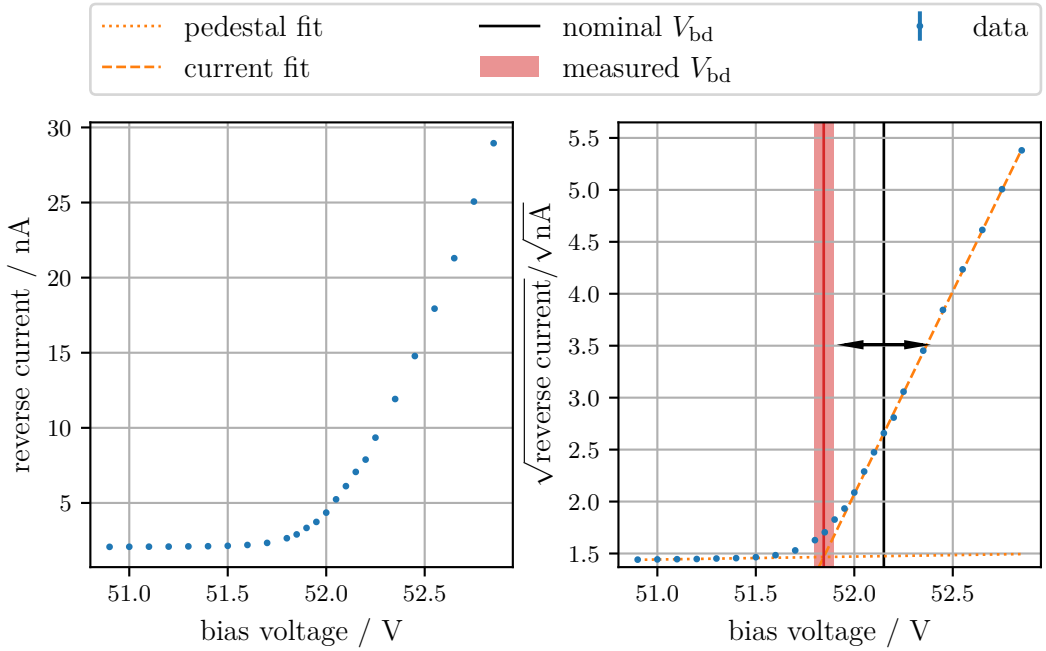

Figure 6.5: Measurement of the breakdown voltage of an SiPM of type Hamamatsu S13360-6025PE [130] using a method described in [149]. *Left:* The current with respect to the bias voltage. *Right:* The root of the current with respect to the bias voltage. The steep increase becomes linear. One linear fit is performed up to 51.5 V to determine the current pedestal and a second fit describes the steep increase above 52.05 V. The red line and shaded area show the breakdown voltage and its uncertainty, respectively. The black line indicates the datasheet value and the black arrow the uncertainty given by the manufacturer. The measurement was performed by the author of this thesis.

a measurement is shown in figure 6.5 for an SiPM of type Hamamatsu S13360-6025PE [130]. The bias voltage is generated by a Hamamatsu C11204 [150] power supply and the current is measured using a Keithley 6485 Picoammeter [151]. The ambient temperature was controlled to be 25 °C, the same as used by the manufacturer for determination of the breakdown voltage.

The measurement yields a breakdown voltage of (51.845 ± 0.048) V which is lower than the value of (52.15 ± 0.20) V stated by the manufacturer. Reasons might be different measurement techniques that can yield systematically different values. The manufacturer does not describe its definition of the breakdown voltage. It might also be that for the given breakdown voltage all sensors have the same gain at 5 V overvoltage. This is quite reasonable as in many applications a knowledge of the gain is more important than the breakdown voltage itself. In this case, the deviation originates from uncertainties in the manufacturing process.

The onset of the current is not abrupt but smeared out over a range of ~ 0.5 V. This smearing results from slight differences in the breakdown voltages of different cells due to manufacturing uncertainties. The steepening of the current therefore sets in at different bias voltages and produces the transition region.

Typically, the breakdown voltage is stated by the manufacturers for each device individually so that a characterization by the user is not necessary. Nonetheless, when multiple SiPMs are being operated, they should be powered independently with different bias voltages or SiPMs with similar breakdown voltages need to be selected to ensure homogeneous characteristics over all SiPMs.

Typical overvoltages applied are in the range of 1 V to 5 V [130, 148]. Most properties of the SiPM such as gain and PDE directly depend on the overvoltage. It is therefore crucial to achieve a precise bias voltage setting at the order of 10 mV for an accuracy in the gain of around 1 %.

The breakdown voltage depends linearly on the temperature (cf. sec. 6.1.2) with changes of $\beta = 20\,\mathrm{mV/K} - 60\,\mathrm{mV/K}$ [130, 148, 152] depending on the SiPM type and manufacturer:

$$V_{\mathrm{bd}}(T) = V_{\mathrm{bd}}(T_0) + \beta \cdot (T - T_0) \quad . \tag{6.5}$$

This corresponds to changes of the gain of $\mathcal{O}(1\,\%/\mathrm{K})$. To allow for stable SiPM operation, either the temperature needs to be kept stable or the bias voltage must be adapted according to the ambient temperature. As the former is not feasible in many applications, especially in high energy and astroparticle physics, the latter is mostly implemented. Dedicated power supplies designed for the operation of SiPMs allow for a correction of the bias voltage depending on the ambient temperature [150, 153].

6.2.2 Gain

The SiPM gain g is defined by the amount of charge carriers produced in the avalanche initiated by a single photon. It is in good approximation determined by the capacitances C_{d} of the diode and C_{q} of the quenching resistor and proportional to the overvoltage V_{ov} [146, 154]:

$$g = \frac{V_{\mathrm{ov}} \cdot (C_{\mathrm{q}} + C_{\mathrm{d}})}{e} \tag{6.6}$$

with e the elementary charge $e = 1.602 \times 10^{-19}\,\mathrm{C}$. Typical SiPM gains are in the range of $\mathcal{O}(10^5)$ to $\mathcal{O}(10^7)$ [130, 148]. The charge released in a single cell breakdown is specific for the type and operating conditions. It is denoted as one Photon Equivalent (p.e.).

Due to the high precision of the manufacturing process of SiPMs, the capacitances C_{d} and C_{q} are very uniform over the sensor. The result is a very good resolution of the photon number. In figure 6.6, example charge spectra of the signals measured by an SiPM are shown. The different peaks of this so called *finger spectrum*, correspond to different numbers of cells that have triggered. The distance of the peaks is directly proportional to the gain and their width depends on the electronics noise and the small variations in the released charge for each cell breakdown. The measurement was done using the optical module that will be presented in chapter 7. For the results in figure 6.6a, the SiPM was illuminated by a pulsed Light-Emitting Diode (LED). In figure 6.6b, only the dark noise is measured. Because of the crosstalk probability being low for the chosen SiPM type, the multiple p.e. peaks are not well separated from the tail of the 1 p.e. peak. Illumination with the LED yields a significantly better resolution. An overlay of the corresponding traces of the dark noise is given in figure 6.7. The used SiPMs have a comparably low gain of 7×10^5 [130]. With different SiPMs even better resolution can be obtained [73, 155].

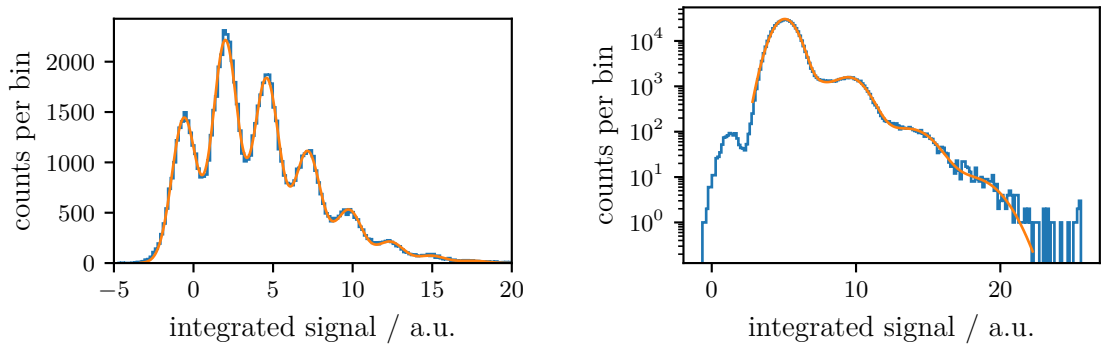

(a) Charge spectrum recorded when the SiPM was illuminated by a pulsed LED. The signal was integrated around the trigger region. The different peaks correspond to multiples of triggered cells.

(b) Charge spectrum recorded for an SiPM in darkness. The trigger threshold was set to an amplitude corresponding to ~ 0.5 p.e.. Because of the crosstalk probability being low, the peaks are not as pronounced as in *(a)*. An overlay of all triggered traces is shown in figure 6.7.

Figure 6.6: Example charge spectra of an SiPM of type Hamamatsu S13360-6025PE [130]. Note the different y-scales of the two graphics. Fits of correlated Gaussians describe the spectra and allow to extract information such as gain and crosstalk. The setup was cooled down to $\sim 5\,°\mathrm{C}$ to reduce the Dark Count Rate. The measurements were performed by the author of this thesis using the optical module that will be introduced in chapter 7.

6.2.3 Photon Detection Efficiency

The Photon Detection Efficiency (PDE) is defined as the ratio between the number of detected photons and the number of photons impinging on the detector. It is given as [146]

$$PDE\,(V_{\mathrm{ov}}) = QE \cdot P_{\mathrm{T}}\,(V_{\mathrm{ov}}) \cdot FF\,(V_{\mathrm{ov}}) \tag{6.7}$$

with QE the quantum efficiency, P_{T} the avalanche triggering probability and FF the geometrical fill factor.

The geometrical fill factor accounts for parts of the sensor that are not sensitive to impinging photons and is given as $FF = 1 - A_{\mathrm{inactive}}/A_{\mathrm{tot}}$ with A_{inactive} being the area where no avalanche can be triggered and A_{tot} the total area of the SiPM. A_{inactive} is given as $A_{\mathrm{inactive}} = A_{\mathrm{opaque}} + A_{\mathrm{boundary}} + A_{\mathrm{field}}$ with the different areas A_i being described in the following. The area A_{opaque} corresponds to regions where the SiPM surface is opaque for incident photons for example due to electrical wires. The contribution from a separation of the cells with optical trenches is summed in A_{boundary}. For smaller cell sizes, A_{boundary} usually increases because of the larger number of boundaries. The electrical field in a cell is not homogeneous and leads to parts of the cell that are insensitive [146]. This is accounted for in A_{field}. With increasing overvoltage, these areas get smaller wherefore also the fill factor is depending on the overvoltage.

The quantum efficiency quantifies the probability for a photon to reach and be absorbed in a depth of the SiPM where avalanche triggering is possible. This includes reflections at the surface and the absorption probability when entering the substrate.

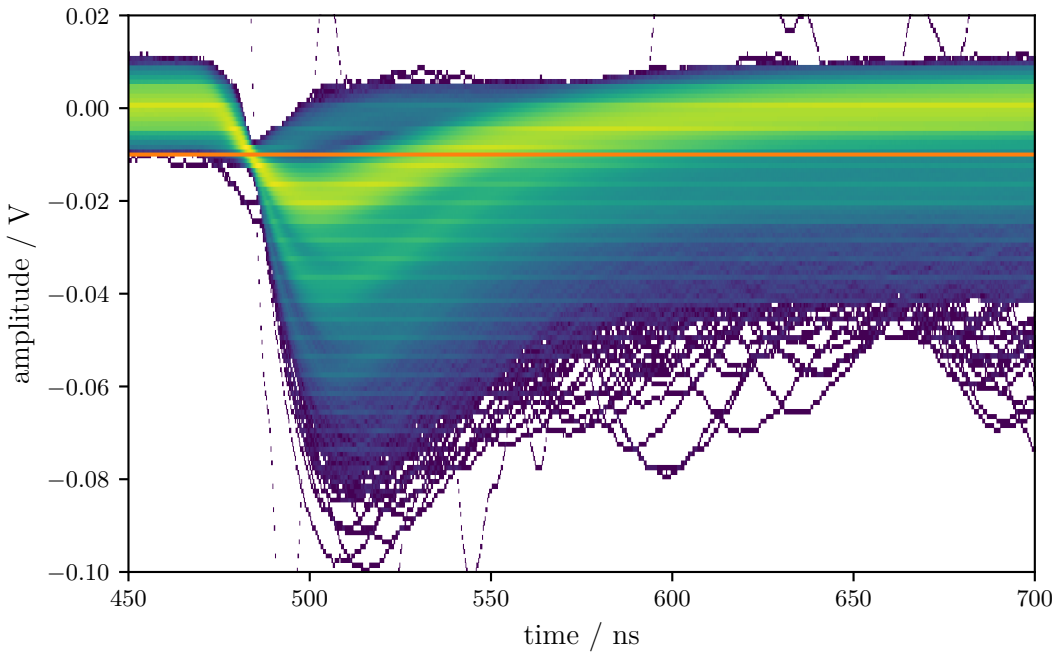

Figure 6.7: Overlay of traces triggered for an SiPM of type Hamamatsu S13360-6025PE in darkness with a trigger threshold at around 0.5 p.e. indicated by the horizontal line. In color, the logarithmic number of entries per bin is encoded. The discreteness of the pulses due to the breakdown of an integer number of cells is well visible. The resulting charge spectrum is shown in figure 6.6b.

Silicon has a very high refractive index of $n \approx 4.7 + 0.09i$ at 450 nm [156] leading to a high surface reflectivity. It is only slightly lowered by a glass or metal coating with $n \approx 1.5$ applied to the surface for protection. The reflectivity at the surface depends on the incident angle θ and on the refractive index of the medium surrounding the SiPM. The quantum efficiency is almost flat up to $\theta = 50°$ but reduces significantly at around $\theta \approx 70°$ [157, 158].

The avalanche triggering probability increases with the electric field and therefore with the overvoltage. It also depends on the energy or wavelength, equivalently, of the incident photon. This effect results from the different absorption depths and probabilities to create electrons or holes that initiate the avalanche process [159, 160].

SiPMs used in astroparticle physics experiments are usually sensitive in the wavelength range of about 300 nm to 800 nm with a peak sensitivity around 400 nm to 500 nm depending on the specific type [161].

The measurement of the absolute PDE is rather complicated as the precise number of photons impinging on the SiPM needs to be known. In addition, the SiPM noise has to be taken into account and corrected for [162]. This can be achieved using calibrated light sources or reference light detectors. A measurement of the relative change of the PDE with the overvoltage is simpler as the absolute light flux does not need to be known. The signal size S scales with gain g and the PDE as

$$S\left(V_{\mathrm{ov}}\right) \propto g\left(V_{\mathrm{ov}}\right) \cdot PDE\left(V_{\mathrm{ov}}\right) \tag{6.8}$$

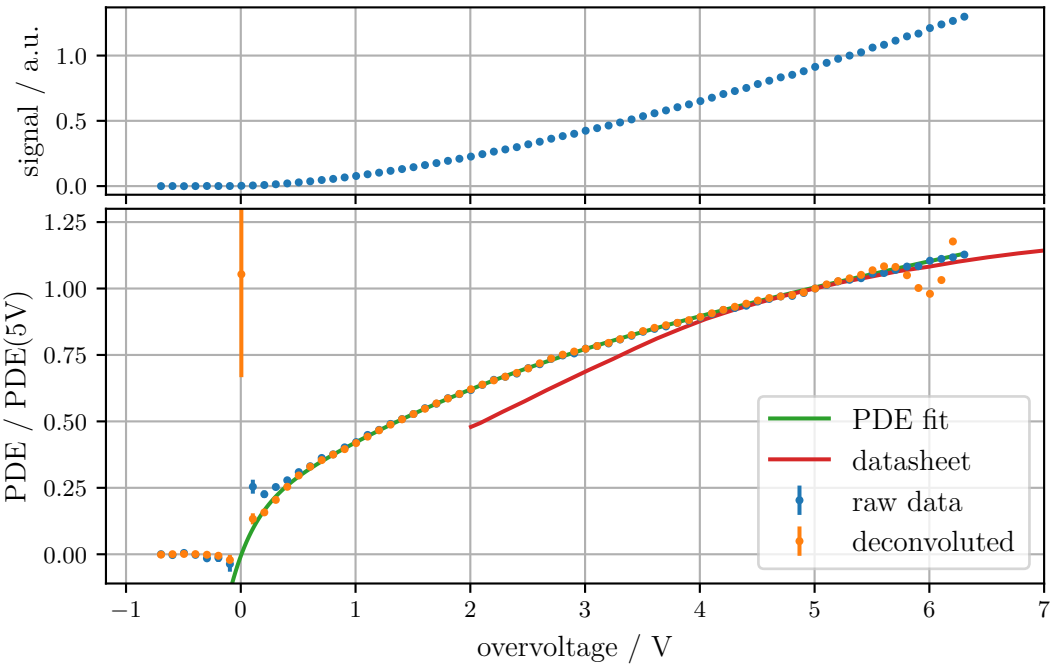

Figure 6.8: Measurement of the relative PDE with respect to the overvoltage performed by the author of this thesis. *Top:* The measured signal sizes. *Bottom:* The signal sizes divided by the overvoltage as indicated by equation (6.9). The PDE given by the manufacturer [130] is shown as well as a fit to the deconvoluted measurement. The fit is described in the text. All curves are normalized to a PDE of 1 at $V_{\mathrm{ov}} = 5\,\mathrm{V}$.

which allows to determine the relative change of the PDE with the overvoltage:

$$PDE\left(V_{\mathrm{ov}}\right) \propto \frac{S\left(V_{\mathrm{ov}}\right)}{g\left(V_{\mathrm{ov}}\right)} \propto \frac{S\left(V_{\mathrm{ov}}\right)}{V_{\mathrm{ov}}} \quad . \tag{6.9}$$

In figure 6.8, a measurement of the signal detected with the same SiPM of type Hamamatsu S13360-6025PE as was used in the measurement of the breakdown voltage is shown with respect to the overvoltage. The signal is produced by a pulsed LED and corresponds to a triggering of $\lesssim 10\,\%$ of the cells at $V_{\mathrm{ov}} = 5\,\mathrm{V}$. The rather low signal avoids double hits of cells which would spoil the measurement. At each overvoltage, 100 traces are recorded and the integrated signal is determined. A possible offset of the signals is corrected for by shifting the mean of the first four data points to zero. Comparing with figure 6.5, the assumption of no signal in that region is reasonable as it is already 0.4 V below the breakdown voltage.

The measured signal reaches zero below the breakdown voltage. This is a result of the different breakdown voltages of individual cells as explained in section 6.2.1. This smearing has to be corrected for before applying equation (6.9). Here, a Gaussian distribution of the breakdown voltages around the one measured in section 6.2.1 is assumed.

parameter	c_0	c_1 / V	c_2 / V	c_3 / V	c_4 / V	c_5
value	1.27	5.9×10^{-3}	1.62	15.3	0.191	0.838
σ_{c_i}	0.10	32.7×10^{-3}	0.12	1.9	0.035	0.010

Table 6.1: Resulting parameters and their standard deviation for the fit function given in equation (6.11). The corresponding function is shown in figure 6.8.

The measured signal is thus a convolution of the true signal $S_{\text{true}}(V_{\text{ov}})$ at a given overvoltage with the Gaussian distribution of breakdown voltages G:

$$S(V_{\text{ov}}) = S_{\text{true}}(V_{\text{ov}}) * G \quad . \tag{6.10}$$

In order to determine $S_{\text{true}}(V_{\text{ov}})$, a deconvolution has to be performed. The method used here is based on [163, 164] and a short review of the mathematical background will be given in section 6.8.2 of this thesis.

The width σ of the Gaussian is unknown and difficult to estimate. Therefore, several values in the range of $0.05\,\text{V} \leq \sigma \leq 0.2\,\text{V}$ have been tested. This range was chosen in accordance with the transition region that can be seen in figure 6.5 and extends over about 0.5 V. A value of $\sigma = 0.17\,\text{V}$ was observed to yield good results.

The relative PDE is determined by division of the deconvoluted signal with the overvoltage. A fit is performed to the relative PDE with the functional form:

$$PDE(V_{\text{ov}}) = c_0 \cdot \left(\tanh\left(\frac{V_{\text{ov}} - c_1}{c_2}\right) + 1\right) \cdot \left(1 - c_5 \cdot e^{-\frac{V_{\text{ov}} - c_1}{c_3}} - (1 - c_5)\, e^{-\frac{V_{\text{ov}} - c_1}{c_4}}\right) \tag{6.11}$$

with the resulting parameters given in table 6.1. The fit is only performed to the data points with overvoltages above 0.1 V and describes the data very well.

This is a rather simple method to determine the relative PDE over the whole overvoltage range as it only involves the measurement of the breakdown voltage and a pulsed light source.

6.2.4 The noise of SiPMs

SiPMs suffer from different sources of noise that are typically divided into *correlated* and *thermal* noise. Thermal noise effects can occur at any time and are independent of the impinging light. In contrast, correlated noise is associated with a triggered avalanche. The trigger might originate from an impinging photon or a thermal noise event.

Thermal noise

Thermal noise, as the name states, originates mainly from thermal excitations producing electron-hole pairs. An avalanche is initiated and the produced output pulse is indistinguishable from photon initiated signals.

It is typically measured as the Dark Count Rate (DCR), i.e. the pulse rate in darkness for a low threshold of 0.5 p.e.. The probability of a thermal excitation increases with temperature. The thermal noise is thus strongly temperature dependent. An often stated temperature increase for a doubling of the DCR is 8 K but depends on the specific device [140].

The dark count rate depends on the avalanche triggering probability from an electron-hole pair and thus increases linearly with the overvoltage (cf. sec. 6.2.3).

In addition, the DCR scales approximately linearly with the area of the SiPM and is almost independent of the cell size. While older types of SiPMs had very high DCRs of up to 1 MHz/mm^2 [165] at the type dependent recommended overvoltage it has significantly reduced in newer devices to 50 kHz/mm^2 [130].

Correlated noise

Correlated noise itself is divided into *optical crosstalk* and *afterpulsing*. Both types of noise only occur correlated with a triggered avalanche, hence the name.

Afterpulsing originates from impurities in the silicon lattice structure [146]. During the build up of an avalanche, charge carriers can be trapped in these impurities and do not propagate further. After some time delay, the charge carrier is released and initiates a second avalanche [140]. As the overvoltage at the cell depends on the time passed since last breakdown, afterpulsing strongly depends on time. The later the charge carrier is released, the larger is the produced afterpulse. For old types of SiPMs the effect of afterpulsing had a significant impact on measurements with probabilities of up to 40 % [165]. The advancements in semiconductor production in recent years lead to a significant improvement of the purity of the silicon reducing the afterpulsing probability to 1 % [148]. In most applications it can thus be neglected nowadays.

Optical crosstalk originates from secondary photons produced in the avalanche process due to recombinations of electron-hole pairs [146, 166]. Because of the isotropic emission, the produced photons can reach neighboring cells either through the silicon substrate or by reflections at the coating of the SiPM. A second breakdown might be induced at the neighboring cells resulting in an output signal equal to two p.e.. As also in the second breakdown secondary photons are produced, more cells can get triggered. Large pulses can thus be created only from a single initial breakdown triggered either by thermal noise or an impinging photon. The effect of crosstalk can be seen in figure 6.6 where pulses of a few p.e. are measured only from the dark noise.

The crosstalk probability is proportional to the amount of electron-hole pairs created in the avalanche and thus to the gain or overvoltage, respectively. As the reflectivity at the boundary between the coating and the surrounding medium depends on their refractive indices, the crosstalk probability is also affected by the materials optically coupled to the SiPM. This is for example the case when additional light guides are glued on the SiPM or when the SiPM is directly coupled to a scintillator [167]. The crosstalk probability stated by the manufacturers is typically given for surrounding air ($n \approx 1$).

For older SiPMs, the probability for producing a secondary avalanche can reach 40 % [142]. Newer SiPMs have trenches between the cells reaching deep into the silicon substrate. They separate the cells optically and reduce the crosstalk probability significantly [146, 168]. For recent devices, the crosstalk probability can thus even be reduced to 1 % [130].

6.3 Comparison of SiPMs and PMTs

For many decades, PMTs have been the device of choice when it came to the detection of very low light fluxes down to single photons. In recent years, SiPMs reached competitive performance allowing for the replacement of PMTs in many applications.

PMTs consist of an evacuated glass tube with a photocathode at the front window. When the photocathode is hit by a photon, an electron can be released. The electron is accelerated in an applied electrical field towards a dynode structure of typically 6 to 12

dynodes. Between two consecutive dynodes a voltage difference of $\mathcal{O}\left(10^2\,\mathrm{V}\right)$ is applied to accelerate the electrons. Due to the high kinetic energy, one electron can release a multiple of it when impinging on the dynode. This way an amplification is achieved and the signal can be picked up at the final anode.

Due to the small size of the dynode structure and its positioning inside the evacuated glass tube, its production is difficult. Small uncertainties in the relative position of the dynodes with respect to each other can lead to large uncertainties on the gain or linearity of the response. Thus, each PMT should be characterized individually.

In contrast, SiPMs being semiconductor devices are produced with great precision. Even though the breakdown voltage varies between different sensors, their characteristics only depend on the applied overvoltage. Using multiple SiPMs thus still produces a very uniform output [155].

PMTs are very sensitive when exposed to bright light. The high currents produced can damage the dynode structure and accelerate the aging of the PMT. In contrast, SiPMs do not suffer even under bright conditions. This is a feature which can significantly improve the performance of physics experiments, e.g. in the case of IACTs where observation time is mainly limited by too bright background conditions. With SiPMs observations also during bright moonlight are possible [169].

The same is true for mechanical stress such as vibrations. The dynode structure can easily be damaged while SiPMs are mechanically very robust. They are therefore also well suited for experiments where a significant mechanical impact is to be expected, e.g. for satellites during launch [170].

Inside PMTs, the electrons are accelerated over a large distance ($\mathcal{O}\left(\mathrm{cm}\right)$) in electric fields. When used in a magnetic field, the electrons can be significantly deflected leading to uncertainties in the behavior of the PMT. For SiPMs this is not the case so that they can well be operated e.g. at high-energy physics experiments such as CMS [171] or in medical imaging [172].

While PMTs are typically operated at high voltage of $\mathcal{O}\left(1\,\mathrm{kV}\right)$, the operating voltage of SiPMs is below 100 V. The precise operating voltage depends on the specific design of the SiPM. For Hamamatsu devices it is typically at 50 V to 60 V [130] while for ON Semiconductor devices it is usually only 20 V to 30 V [148]. These low operating voltages allow for a simple design and easy handling compared to PMTs.

The main advantage of PMTs compared to SiPMs is the possibility to achieve large sensitive areas. While SiPMs are only available up to sizes of $36\,\mathrm{mm}^2$, PMTs can reach up to 50 cm in diameter corresponding to an area of $8 \times 10^5\,\mathrm{mm}^2$. Thus, these are used e.g. in neutrino detectors such as Super-Kamiokande [173]. In addition, PMTs typically have a significantly lower dark count rate than SiPMs. While for PMTs, rates of $100\,\mathrm{Hz/mm}^2$ [126] and lower can be achieved, for SiPMs it is typically around 10 to $100\,\mathrm{kHz/mm}^2$ [130] (cf. sec. 6.2.4). As will be seen in section 6.7, the response of SiPMs is intrinsically non-linear and is usually approximated linearly for low light fluxes. In contrast, PMTs have a wide range of linear response which is often characterized for each device individually. This makes the interpretation especially of large signals simpler than for SiPMs where dedicated algorithms need to be applied to achieve a high linear dynamic range as will be described in section 6.8.

The completely different technology of PMTs compared to SiPMs also affects the dynamic range. The cellular structure of SiPMs results in an intrinsically non-linear response that can be linearly approximated for low light fluxes. On the other hand, the precise manufacturing of SiPMs make measurements also in the highly non-linear regime possible as will be seen

in section 6.7. The dynamic range of PMTs is linear up to a threshold current where it begins to saturate. The exact threshold as well as the behavior around the threshold is typically device and not only type dependent.

For many applications, SiPMs have superior performance compared to conventional PMTs. Their small size, low operating voltage and robustness make them an easy-to-use light sensor for both, physics experiments as well as laboratory measurements. Only when a large sensitive area and detection of single photons are necessary, SiPMs cannot replace PMTs yet.

6.4 SiPM equivalent electronic circuit

The behavior of SiPMs being parallel connected G-APDs shall be studied on the base of a simple electronic circuit. Starting from a single G-APD, the model will be extended to include parallel connections in arrays of G-APDs and their interaction with each other leading to a full SiPM simulation in section 6.5. In the following sections, the characteristics of this model will be investigated in detail.

Electronic models of a single G-APD have been proposed in [174] and later been extended to full SiPMs as being multiple G-APDs connected in parallel by [175, 176].

A circuit diagram representing the SiPM with one triggered cell is shown in figure 6.9. Here, only two cells are considered. One is the triggered cell and the other one represents all the other untriggered cells by assigning their total quenching resistance, quenching capacitance and diode capacitance. The two cells are connected in parallel.

A detailed analysis has been performed in [154]. The following description is based on this work and extends it to additional features. To understand the recharge behavior of the cells as discussed in section 6.1.3, the voltages V_o at the output and V' and V'' at the triggered and untriggered cells, respectively, are of interest.

The current I_d produced by the breakdown of the G-APD is assumed to be very short compared to typical recharge times of the cells. This is a valid assumption due to the negligible resistance of the diode compared to the quenching resistor. It can be shown that the total charge Q produced in the avalanche is given by [154, 146]:

$$Q = V_\mathrm{ov} \left(C_\mathrm{q} + C_\mathrm{d} \right) \tag{6.12}$$

resulting in an infinitely short diode current

$$I_\mathrm{d} \left(t \right) = Q \cdot \delta \left(t \right) \tag{6.13}$$

with $\delta \left(t \right)$ denoting the Dirac delta function.

The calculation of the time evolution of the system can be performed by converting from time domain (t-domain) to complex frequency domain (s-domain) using Laplace transformations [177]. The Laplace transformation of a function $f \left(t \right)$ is given by:

$$\tilde{f} \left(s \right) = \int_0^\infty f \left(t \right) e^{-st} \, \mathrm{d}t \qquad . \tag{6.14}$$

The diode current in equation (6.13) thus transforms to a constant:

$$\tilde{I}_\mathrm{d} \left(s \right) = Q \qquad . \tag{6.15}$$

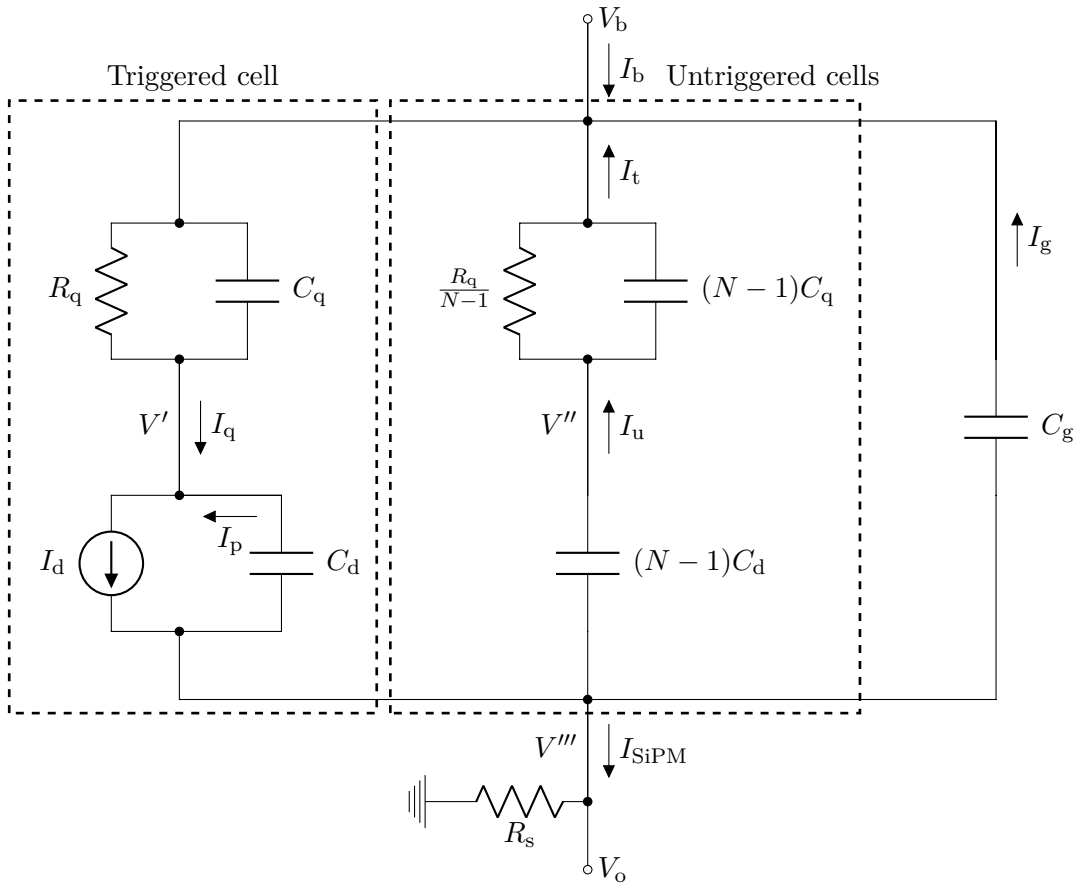

Figure 6.9: Equivalent circuit diagram of an SiPM with N cells of which one is triggered. The triggered cell is represented by the quenching resistor R_q with capacitance C_q connected in series to the diode. It is modeled by a capacitance C_d in parallel to a current source I_d which corresponds to the produced avalanche. All the $N-1$ untriggered cells are represented by only one cell which has the total quenching resistance $R_q/(N-1)$ with capacitance $C_q(N-1)$ and diode capacitance $C_d(N-1)$. The parasitic capacitance of the metal grid connecting the cells is given by C_g. Adopted from [154].

Similarly, the currents and voltages over a resistor or capacitor can be transformed:

$$I_R(t) = V_R(t)/R \tag{6.16}$$

$$\Rightarrow \tilde{I}_R(s) = \tilde{V}_R(s)/R \tag{6.17}$$

$$I_C(t) = C\frac{d}{dt}V_C(t) \tag{6.18}$$

$$\Rightarrow \tilde{I}_C(s) = s\,C\,\tilde{V}_C(s) - C\,V_C(t \to 0^-) \tag{6.19}$$

with $V_C(t \to 0^-)$ the voltage at the capacitor before $t = 0$. The advantage of performing calculations in the s-domain is that differential equations like in equation (6.18) are avoided. The result has to be transformed back to the t-domain using the inverse Laplace

transformation:

$$f(t) = \frac{1}{2\pi i} \int_{\gamma - i\infty}^{\gamma + i\infty} e^{st} \tilde{f}(s) \, \mathrm{d}s \tag{6.20}$$

where $\gamma \in \mathbb{R}$ has to be chosen such that the integral converges.

The details of this approach shall not be discussed here. The derivation follows the calculations presented in [154]. For a detailed understanding of the behavior of an SiPM, the time evolution of $V_\mathrm{o} = V'''$, V', and V'' will be evaluated. All calculations have been performed using the software *Mathematica* [178].

The currents at the different components in figure 6.9 can be calculated as:

$$\begin{aligned}
\tilde{I}_\mathrm{t}(s) &= \left(\tilde{V}'' - V_\mathrm{b}/s\right)\left(\frac{N-1}{R_\mathrm{q}} + s(N-1)C_\mathrm{q}\right) \\
\tilde{I}_\mathrm{q}(s) &= \left(V_\mathrm{b}/s - \tilde{V}'\right)\left(\frac{1}{R_\mathrm{q}} + sC_\mathrm{q}\right) \\
\tilde{I}_\mathrm{g}(s) &= \left(\tilde{V}''' - V_\mathrm{b}/s\right) sC_\mathrm{g} + C_\mathrm{g}V_\mathrm{b} \\
\tilde{I}_\mathrm{p}(s) &= \left(\tilde{V}''' - \tilde{V}'\right) sC_\mathrm{d} + C_\mathrm{d}V_\mathrm{b} \\
\tilde{I}_\mathrm{u}(s) &= \left(\tilde{V}''' - \tilde{V}''\right)(N-1)\, sC_\mathrm{d} + (N-1)\, C_\mathrm{d}V_\mathrm{b} \\
\tilde{I}_\mathrm{SiPM}(s) &= \tilde{V}'''/R_\mathrm{s}
\end{aligned} \tag{6.21}$$

Applying Kirchhoff's law relates the various currents to each other:

$$\begin{aligned}
\tilde{I}_\mathrm{SiPM} &= \tilde{I}_\mathrm{d} - \tilde{I}_\mathrm{p} - \tilde{I}_\mathrm{u} - \tilde{I}_\mathrm{g} \\
\tilde{I}_\mathrm{d} &= \tilde{I}_\mathrm{p} + \tilde{I}_\mathrm{q} \\
\tilde{I}_\mathrm{t} &= \tilde{I}_\mathrm{u} \\
\tilde{I}_\mathrm{q} &= \tilde{I}_\mathrm{t} + \tilde{I}_\mathrm{b} + \tilde{I}_\mathrm{g}
\end{aligned} \tag{6.22}$$

These equations can be solved for the voltages at the triggered and untriggered cells $\tilde{V}'$ and $\tilde{V}''$, respectively, and for the voltage at the output $\tilde{V}'''$. This results in:

$$\begin{aligned}
\tilde{V}'(s) &= \frac{V_\mathrm{b}}{s} - QR_\mathrm{q}\frac{1 + a_0 s + a_1 s^2}{1 + a_2 s + a_3 s^2 + a_4 s^3} \\
\tilde{V}''(s) &= \frac{V_\mathrm{b}}{s} + QR_\mathrm{q}\frac{b_0 s + b_1 s^2}{1 + b_2 s + b_3 s^2 + b_4 s^3} \\
\tilde{V}'''(s) &= QR_\mathrm{s}\frac{1 + c_0 s}{1 + c_1 s + c_2 s^2}
\end{aligned} \tag{6.23}$$

where the coefficients are given as:

$$
\begin{aligned}
a_0 &= c_1 - C_\mathrm{d}R_\mathrm{s} = C_\mathrm{d}\left((N-1)\,R_\mathrm{s} + R_\mathrm{q}\right) + C_\mathrm{g}R_\mathrm{s} + C_\mathrm{q}R_\mathrm{q} \\
a_1 &= c_2 - C_\mathrm{d}C_\mathrm{q}R_\mathrm{s}R_\mathrm{q} = R_\mathrm{s}R_\mathrm{q}\left(C_\mathrm{g}C_\mathrm{q} + C_\mathrm{d}\left(C_\mathrm{g} + (N-1)\,C_\mathrm{q}\right)\right) \\
a_2 &= b_2 = R_\mathrm{s}\left(C_\mathrm{g} + NC_\mathrm{d}\right) + 2R_\mathrm{q}\left(C_\mathrm{d} + C_\mathrm{q}\right) \\
a_3 &= b_3 = R_\mathrm{q}\Big(C_\mathrm{d}^2\left(NR_\mathrm{s} + R_\mathrm{q}\right) + C_\mathrm{q}\left(2C_\mathrm{g}R_\mathrm{s} + C_\mathrm{q}R_\mathrm{q}\right) + 2C_\mathrm{d}\left(C_\mathrm{g}R_\mathrm{s} + C_\mathrm{q}\left(NR_\mathrm{s} + R_\mathrm{q}\right)\right)\Big) \\
a_4 &= b_4 = R_\mathrm{s}R_\mathrm{q}^2\left(C_\mathrm{d} + C_\mathrm{q}\right)\left(C_\mathrm{g}C_\mathrm{q} + C_\mathrm{d}\left(C_\mathrm{g} + NC_\mathrm{q}\right)\right) \\
b_0 &= R_\mathrm{s}C_\mathrm{d} \\
b_1 &= c_0 = R_\mathrm{q}C_\mathrm{q}
\end{aligned}
\tag{6.24}
$$

Applying the inverse Laplace transformation (eq. (6.20)), yields the voltages in the time domain:

$$
\begin{aligned}
V'(t) &= V_\mathrm{b} - \frac{QR_\mathrm{q}}{N}\left(\frac{N-1}{\tau_\mathrm{q}}\mathrm{e}^{-t/\tau_\mathrm{q}} + \frac{R_\mathrm{s}C_\mathrm{g}}{c_2}\left(A_1\mathrm{e}^{-t/\tau_-} + (1-A_1)\,\mathrm{e}^{-t/\tau_+}\right)\right) \\
V''(t) &= V' + \frac{QR_\mathrm{q}}{\tau_\mathrm{q}}\mathrm{e}^{-t/\tau_\mathrm{q}} \\
V'''(t) &= \frac{QR_\mathrm{s}R_\mathrm{q}C_\mathrm{q}}{c_2}\left(A_2\mathrm{e}^{-t/\tau_-} + (1-A_2)\,\mathrm{e}^{-t/\tau_+}\right)
\end{aligned}
\tag{6.25}
$$

where the different constants are given as:

$$
\begin{aligned}
\tau_\mathrm{q} &= R_\mathrm{q}\left(C_\mathrm{d} + C_\mathrm{q}\right) \\
\tau_\pm &= \frac{2c_2}{c_1 \pm \sqrt{c_1^2 - 4c_2}} \\
A_1 &= \frac{1}{2} + \frac{2c_2/\left(R_\mathrm{s}C_\mathrm{g}\right) - c_1}{2\sqrt{c_1^2 - 4c_2}} \\
A_2 &= \frac{1}{2} + \frac{2c_2/\left(R_\mathrm{q}C_\mathrm{q}\right) - c_1}{2\sqrt{c_1^2 - 4c_2}}
\end{aligned}
\tag{6.26}
$$

The voltage V''' that is measured at the output shows two different exponential contributions $\tau_\pm$ corresponding to a short rising and long falling edge of the output pulse.

The voltages applied at the SiPM cells V' and V'' show an additional time constant τ_q. It originates from the recharge of the cell over the quenching resistor. V' and V'' only differ in the contribution of the exponential recharge τ_q. For V', the voltage drops to zero because of the flux produced at the diode. The consequent recharging current flows through the quenching resistor leading to the recharge with time constant τ_q. For V'', the increase of the output voltage V''' leads to a current flowing through the untriggered diode and consequently through the quenching resistor. Due to the large number of cells, this current is low and the voltage change at V'' is low as well. The consequent charge to be flowing through R_q is therefore lower at the untriggered cells than at the triggered cell.

The specific values of the recharge times τ_q and $\tau_\pm$ and their contributions to the total charge of the produced output pulse depend on the SiPM model. For Hamamatsu S13360-6025PE and S13360-6050PE (specifications given in appendix C, table C.1) this results in

SiPM	τ_q / ns	τ_+ / ns	τ_- / ns	A_1	A_2
S13360-6025PE	16.8	1.5	76.7	0.73	1.1
S13360-6050PE	30.9	1.8	95.6	0.52	1.7

Table 6.2: Recovery times as calculated for two different SiPM models for the readout circuit shown in figure 6.9 with $R_s = 50\,\Omega$.

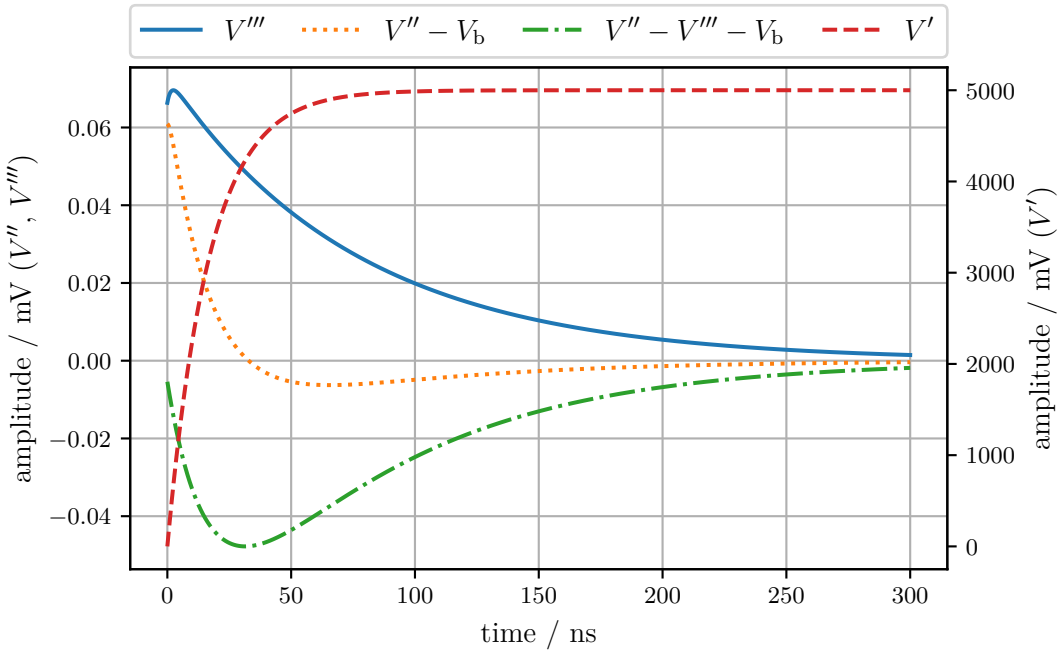

Figure 6.10: Time evolution of the different voltages as calculated using the model of the electronic circuit for the Hamamatsu S13360-6025PE after the triggering of one cell with $V_{ov} = V_b = 5\,\mathrm{V}$. The intrinsic parameters of the SiPM are given in appendix C and result in the time constants summarized in table 6.2.

the values given in table 6.2. The time constants are in the range between 1 ns to 100 ns. The amplitudes A_1 and A_2 describe the relative contribution of $\tau_\pm$ to the amplitude of the voltage drop at $t = 0$. A_1 is in the range between 0 and 1. As can be seen from equation (6.25), the resulting effect is a decrease of the voltages V' and V''. For V' the contribution from τ_q also produces a decrease of the voltage, while for V'' this contribution increases the voltage.

It should be noted that the voltage over the cells is given by the difference between V' or V'' and the output pulse V'''.

The output voltage V''' does not depend on the recharge of the cells through the quenching resistor. Only $\tau_\pm$ contribute to the output pulse. As the amplitude $A_2 > 1$ in the case of both SiPMs, τ_+ describes a fast rising edge while τ_- corresponds to a long falling tail.

In figure 6.10, the time evolution of the different voltages is shown for the Hamamatsu S13360-6025PE SiPM. The voltage V' at the triggered cell drops instantaneously close to zero and recovers to the nominal overvoltage. The voltage V'' increases but the voltage drop over the untriggered cells $V'' - V'''$ falls below V_{ov}. This results from the current

flowing through the readout resistor R_s resulting in a voltage $V''' = I_\mathrm{SiPM} \cdot R_\mathrm{s} \neq 0$. As V_b is constant, the voltage that drops over the whole SiPM is reduced.

The maximum drop in the voltage over the untriggered cells $V'' - V'''$ occurs only $\sim 30\,\mathrm{ns}$ after the breakdown of the cells. The output for a consequent photon impinging on a second SiPM cell will thus be lowest for this time delay between the two photons.

As can be seen from figure 6.10, this effect is only at the order of $\mathcal{O}\left(10^{-5}\right)$ compared to the overvoltage for a single cell breakdown. Given that large SiPMs can have $\mathcal{O}\left(10^{4}\right)$ cells, it can nonetheless become significant when many cells are triggered in a short time period $\tau \leq \tau_{-}$. It is crucial to properly understand this effect when exposing SiPMs to bright light fluxes. In section 6.7, the dynamic range of SiPMs is further discussed taking into account all the effects resulting from the presented model.

The reduction of the overvoltage due to the readout resistor can be avoided using active current-to-voltage conversion with transimpedance amplifiers [154]. As such a readout circuit is not used in any of the setups operated in the scope of this thesis, it will not further be discussed here.

6.5 Simulation of the SiPM equivalent electronic circuit

A good knowledge of the quantities of the SiPM equivalent circuit is crucial to understand the behavior in all possible situations such as an exposure to short but bright pulses or continuous illumination. An individual measurement of the intrinsic parameters is difficult and can suffer from significant uncertainties as will be seen for the case of the quenching resistor in section 6.6.1. The implementation of a simulation based on the equivalent circuit will be presented in this section. Dedicated measurements will allow for a fit of the SiPM parameters and yield the possibility to properly simulate the behavior of SiPMs in many situations.

In section 6.4, the time evolution of the voltages at the triggered and untriggered cells as well as at the output has been calculated (cf. eq. 6.25). A simulation of the SiPM needs to take into account these dependencies for each cell individually. Within the scope of this thesis, a simulation has been developed that deals with the behavior of each cell individually and accounts for previous hits in the same and other cells.

The basic design of the simulation is simple. For a photon impinging on a particular cell, the instantaneous gain and PDE need to be determined. The photon initiates an avalanche with a probability given by the PDE. For non-triggering of an avalanche, no charge is released. If an avalanche is triggered, the released charge equals the gain. Consequently, the voltages V', V'' and V''' change according to equation (6.25) with Q being the released charge. A crosstalk event resulting in an additional breakdown of a neighboring cell might be produced. The crosstalk probability is reduced if the applied voltages differ from their nominal values. Afterpulsing is neglected in this simulation due to its low contribution in the most recent devices.

The calculations performed in the previous section for the electronic circuit given in figure 6.9, are performed for only one avalanche being initiated. This is of limited use as for most applications multiple avalanches are triggered consecutively (with delays between consecutive triggers possibly being as low as $0\,\mathrm{s}$). The simulation being introduced here is therefore extended to allow for triggers of multiple avalanches (of one or more cells) at arbitrary times. The usage of V' for the voltage at the triggered cell and V'' for the voltage at the untriggered cells can therefore be ambiguous. In the following sections, V' will always

refer to the voltage that is applied at the cell that is being triggered. It can therefore already be influenced by previous hits of other cells according to the dependency given in equation (6.25) for V''. The variable V_{ov} will always refer to the nominal overvoltage that would be applied without any triggered cell.

6.5.1 The gain

The precise behavior of gain and PDE is determined by the datasheet. The gain is directly proportional to the voltage applied at the SiPM cell:

$$g^* = g \cdot \frac{V' - V'''}{V_{\mathrm{ov}}} \tag{6.27}$$

with g the nominal gain at the applied overvoltage V_{ov}. Thus, without any previous initiated avalanche, $V' = V_{\mathrm{ov}}$ and $V''' = 0$ the nominal gain is reached. The charge Q that is released at the triggered cell is scaled like the gain. From equation (6.25), the changes in the voltages V', V'' and V''' can be determined.

6.5.2 The PDE

As has been seen in section 6.2.3, the PDE is not linearly dependent on the overvoltage. The dependency was measured and can be implemented in the simulation using the fit of function (6.11) to the measurement.

The PDE is therefore precisely known for all voltages $V' - V'''$ applied over the cells. For a reduced voltage, the PDE is lower and the triggering of an avalanche becomes less likely. For the simulation, the PDE is always scaled to a value of 1 at the nominal overvoltage to reduce the number of photons to be simulated.

6.5.3 The optical crosstalk

As described in section 6.2.4, in the triggered avalanche photons can be produced due to recombination of an electron-hole pair. If these photons reach and trigger the neighboring cell, a crosstalk event is initiated. As the amount of electron-hole pairs scales with the gain, also the amount of produced secondary photons is proportional to the gain. The probability to trigger an avalanche in a neighboring cell is proportional to the PDE of that cell. The crosstalk probability depends on both the PDE of the neighboring cell and the gain.

6.5.4 Workflow of the simulation

In the previous sections, the behavior of gain, PDE and crosstalk dependent on the instantaneous overvoltage applied at the individual SiPM cells have been discussed. Together with the solutions for the behavior of the different voltages across the SiPM calculated in section 6.4, a simulation can be set up. The workflow of the simulation is depicted in figure 6.11. This schematic will be guided through in the next paragraphs.

When a photon impinges on a cell, the currently applied voltage at the cell needs to be determined. Its value originates from three different contributions:

1. The recharge of the voltage V' applied at the cell since its last breakdown.

2. The deviation from the nominal overvoltage due to the triggering of other cells in the SiPM given by $V'' - V_{\mathrm{ov}}$.

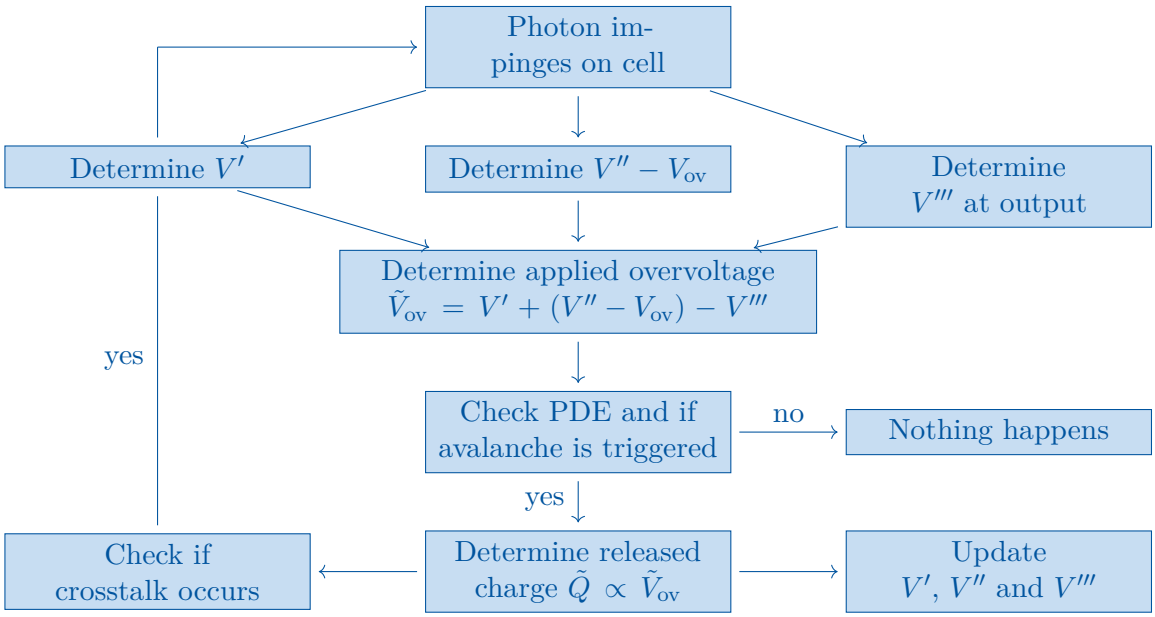

Figure 6.11: A schematic of the workflow of the SiPM simulation. Details are given in the text.

3. The voltage at the readout of the SiPM V'''.

The total instantaneous applied voltage over the cell $\tilde{V}_{\mathrm{ov}}$ is then given as:

$$\tilde{V}_{\mathrm{ov}} = V' + (V'' - V_{\mathrm{ov}}) - V''' \quad . \tag{6.28}$$

From the applied voltage, the PDE can be determined using the relation given in equation (6.11). A random choice is made according to the calculated PDE whether an avalanche is triggered. If no avalanche is triggered, nothing happens. If an avalanche is triggered, the instantaneous gain can be derived using equation (6.27).

From the gain, the effect on the voltages V', V'' and V''' is then calculated by scaling the released charge Q accordingly. The resulting pulses given by equation (6.25) are added to the current states of these voltages.

From the gain, also the probability of producing a crosstalk photon can be determined. It scales proportional to the gain. In a random process the decision on the production of a crosstalk photon is made. If a crosstalk photon was produced, the random process is repeated and a potential second crosstalk photon might be released or even more until the random process stops the production of new photons. For each crosstalk photon, a random direct neighbor is hit. Measurements have shown that the direct neighbors contribute most to the crosstalk [179] so that this restriction should be a valid simplification here.

6.5.5 Remarks

The simulation of the SiPM aims at giving reasonable results for a wide range of applications. This includes short faint pulses, high light fluxes or long lasting pulses, and it allows for a precise understanding over their full dynamic range. In some cases deviations from measurements can occur due to simplifications in the simulation.

In cases of only a few cells triggered, fluctuations in the released charge can occur, e.g. due to different breakdown voltages of individual cells. This is currently not included in the simulation, where each cell releases the same charge, but would be rather simple to be implemented. Additionally, random fluctuations of the released charge could also be added to improve the results.

For simulations of a high incident photon flux the reaction of the voltages at the cells are instantaneous whenever a cell was triggered. This is unrealistic as the signal transit time across the diagonal of a $6 \times 6\,\mathrm{mm}^2$ SiPM is $\mathcal{O}\,(10\,\mathrm{ps})$ to $\mathcal{O}\,(100\,\mathrm{ps})$. Thus, when the time difference between consecutive incident photons becomes significantly lower than these transit times, the time delay might need to be included in the simulation. A precise implementation can be difficult if the detailed wiring of the SiPM cells is unknown, and the computational effort can become enormous if the interactions of all individual cells with each other are simulated. Simplification by using an average delay might already improve results but is not tested here.

As will be seen in the next sections, the simulation as was implemented here achieves already precise results in different applications. Adding of the aforementioned extensions thus does only seem necessary in special cases.

6.6 Determination of the intrinsic SiPM parameters

A measurement of the intrinsic SiPM parameters is crucial for a proper understanding of its behavior. A measurement of the quenching resistor can be performed with a simple setup though it can still be subject to significant systematic uncertaintites. It will be introduced in section 6.6.1. The determination of the other parameters is more complex. A main observable feature resulting from the intrinsic parameters are the recharge times $\tau_\pm$ and τ_q according to equation (6.25). The measurement of these time constants is difficult but possible. An experimental setup that allows their determination will be discussed from section 6.6.2 onward.

6.6.1 Measurement of the quenching resistor

A measurement of the quenching resistance R_q can be performed by biasing the SiPM in forward direction. In this case, the G-APD becomes conductive with negligible resistance compared to R_q. The parallel connection of all G-APDs results in the total resistance of the SiPM

$$R_\mathrm{tot} = \frac{R_\mathrm{q}}{N} \tag{6.29}$$

with N the number of cells. A measurement of the forward current-voltage-curve (IV-curve) will therefore yield the quenching resistance.

Due to the possibly large number of cells, the total resistance R_tot of the SiPM can become small and parasitic resistances in the measurement circuit might need be taken into account. For instance, an SiPM of type Hamamatsu S13360-6025PE with 57 600 cells and a quenching resistor of $R_\mathrm{q} = 750\,\mathrm{k}\Omega$ has a total resistance of only $R_\mathrm{tot} \approx 13\,\Omega$.

For this measurement, a Hameg HMP4040 power supply [180] was used for biasing the SiPM. The current and voltage are read off from that device. An additional $50\,\Omega$ resistor was connected in series to avoid high currents. Two IV-curves have been taken. First, the SiPM has been replaced by a simple wire to determine the resistance of the measurement circuit without the SiPM. The result is given in figure 6.12a. From a linear fit a resistance

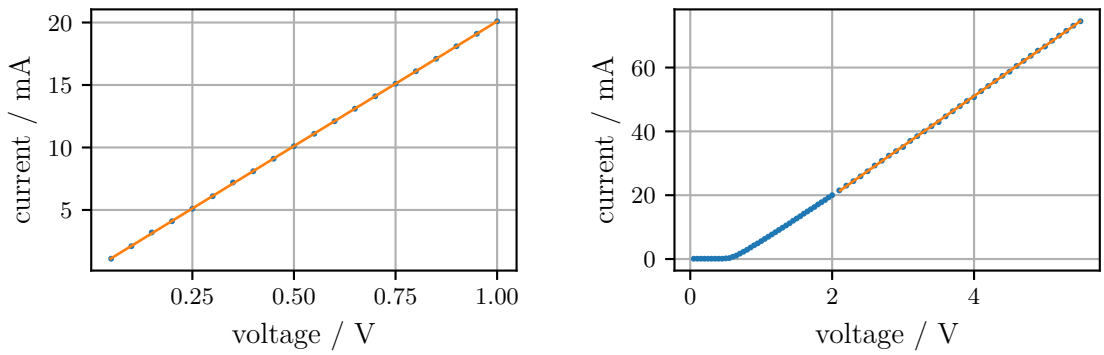

(a) (b)

Figure 6.12: IV-curves taken for the measurement of the SiPM quenching resistance with only a wire *(a)* and with *(b)* SiPM connected in the circuit. The orange lines denote linear fits to the data points.

of $R_{\text{bulk}} = (50.08 \pm 0.06)\,\Omega$ can be determined assuming an uncertainty on the current of 0.1 mA and on the voltage of 1 mV. These are the digitization precisions of the power supply.

When the SiPM is plugged into the circuit, a threshold voltage has to be reached before the current starts to flow. This is a result of the intrinsic voltage created in the p-n junction. Only when the applied forward voltage is sufficient to overcome the junction, it will become conductive. This can be seen in figure 6.12b. A linear fit can be applied to the region above 2 V to determine the total resistance of the circuit $R_{\text{tot,circ}} = (62.80 \pm 0.09)\,\Omega$. The quenching resistance is then given as

$$R_{\text{q}} = N \cdot (R_{\text{tot,circ}} - R_{\text{bulk}}) = (790.4 \pm 6.4)\,\text{k}\Omega \tag{6.30}$$

This value is well in the region of $R_{\text{q}} = (750 \pm 150)\,\text{k}\Omega$ stated by the manufacturer [181].

6.6.2 Exploiting the recharge times to measure intrinsic SiPM parameters

In order to determine also the other intrinsic parameters of the SiPM, two consecutive light pulses can be used to trigger the cells. The signal produced from the second pulse will be affected by the recharge times and can yield a measurement of their specific values.

Ideally, one cell is illuminated by two photons with a specific delay in time. From the probability of the second photon triggering an avalanche, the PDE can be determined and the size of the second pulse is proportional to the gain. Varying the time delay between the two photons allows to determine the time constants of the recharge behavior.

Obviously, the described measurement is experimentally challenging. A light source needs to be triggered with delays of $\mathcal{O}\,(\text{ns})$ producing on average only a single photon per pulse. The light must be focused on a single cell. Also this task is very difficult due to the small cell sizes of only some 10 µm. The output signal is the same as from the dark counts and additional electronics noise might spoil the output. Especially the possibly very tiny second pulse would be challenging to be detected.

Another more feasible measurement can be performed using large but short pulses illuminating the SiPM homogeneously. The first pulse triggers a fraction of the SiPM cells.

For the second pulse, the already triggered cells will have a reduced gain and PDE. Its output will therefore be reduced. The reduction will depend on the delay between the two pulses. The output of the simulation can be compared to the measurement and a fit yields the intrinsic parameters.

In order to obtain reasonable results from this kind of measurement, a proper selection of the used hardware is essential. The pulses should be short compared to the expected time constants of the SiPM voltage recharges (cf. tab. 6.2) leading to a required width of only $\mathcal{O}$ (100 ps). The size of the second pulse must be independent of the delay between the two pulses. This requirement is not fulfilled for many light sources as capacitors need to be recharged before a second pulse with full amplitude is released. Instead, two light sources triggered with a delay can be used. They must be arranged such that both illuminate the SiPM homogeneously. This imposes limits on the possible optical arrangement of the light sources and the SiPM. The light sources should be bright enough to trigger a significant amount of the SiPM cells. If too few cells are triggered, it is likely that the photons in the second pulse only hit cells that were not triggered by the first pulse. In this case, the visible effect would be small. For 50 % triggered cells per pulse, half of those cells will be triggered twice. Assuming that the signal originating from the double triggered cells is negligibly small, the total signal is dominated by the cells that are only triggered by the second pulse. The total signal of the second pulse is thus reduced by around 50 % compared to the signal that would have been measured without any cells being triggered by a first pulse. This effect should be measurable.

6.6.3 The measurement setup

For this setup, two pulsed light sources illuminate an integrating sphere. The homogeneous light output from the sphere is directed onto an SiPM. The SiPM is held inside a temperature stabilized setup. The pulses are triggered with a variable delay and the output from the SiPM is recorded with an oscilloscope. This configuration is sketched in figure 6.13 and an image is shown in figure 6.14.

The pulsers

For this setup, two mrongen picosecond pulsers [182] were used. One of them was a prototype provided by the manufacturer, and the other one was built by the electronics workshop of the Physics Institute III A at RWTH Aachen University. Each pulser drives a Vertical Cavity Surface Emitting Laser (VCSEL) emitting light of 850 nm wavelength. For this VCSEL, it was shown that the output pulse has a width of only $\sim$ 100 ps [182], which is well below the expected intrinsic time constants of the SiPM. A negligible trigger jitter of only $\sim$ 40 ps was measured for the light output [182]. The wavelength is not ideal because of the low PDE of most SiPMs in this regime. Different LEDs were tested by the manufacturer but they show longer pulses of up to almost 1 ns width. This is disadvantageous in the presented measurement. In addition, the light output for smaller wavelengths is lower as was tested during the preparation of the setup. The largest output signal of the SiPM could be achieved using the VCSELs.

Due to the different versions of the pulser, the mechanical structure was slightly different as indicated on the images given in figure 6.15. For one pulser, the VCSEL was installed inside a tube where an optical fiber could be attached which was not necessary here. This structure was soldered on the Printed Circuit Board (PCB) of the pulser (cf. fig. ¸6.15b).

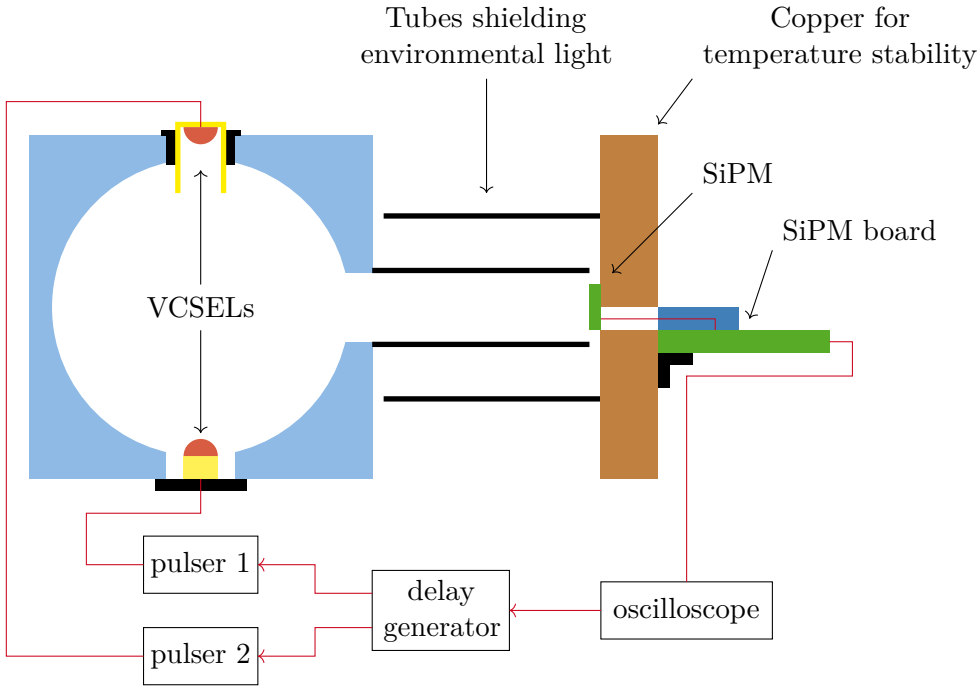

Figure 6.13: The setup used for the determination of some intrinsic SiPM parameters. The oscilloscope is used both for recording the signals produced by the SiPM and triggering a delay generator. The delay generator produces two output signals that serve as a trigger for the two pulsers. They drive the Vertical Cavity Surface Emitting Lasers (VCSELs) which produce a light output illuminating the integrating sphere. The mechanical shape of the holding of the two VCSELs is different because of different versions of the pulsers used. In the case of pulser 2, the VCSEL is directly soldered on the Printed Circuit Board (PCB), this is simplified in this sketch. The two VCSELs were not opposite to each other as indicated in the sketch. Instead an angle of 90° with respect to each other was between the two openings for the VCSELs and the opening where the SiPM was placed. This is simplified here because of the two dimensional representation.

For the second pulser, the VCSEL could be freely moved and was connected by a coaxial cable (cf. fig. 6.15a).

The delay generator

A Stanford Research Systems DG535 digital delay generator [183] is used to trigger the two pulsers. It produces two delayed output signals that trigger the pulse generation. The delay between the triggers can be chosen from 5 ps to 1000 s. The accuracy of the chosen delays is 1500 ps. This is rather large but a systematic uncertainty that affects all measurements. It can be calibrated by measuring the delay between the two generated output pulses. The time jitter of the output is < 100 ps which is negligible here. It is ideally suited for this measurement.

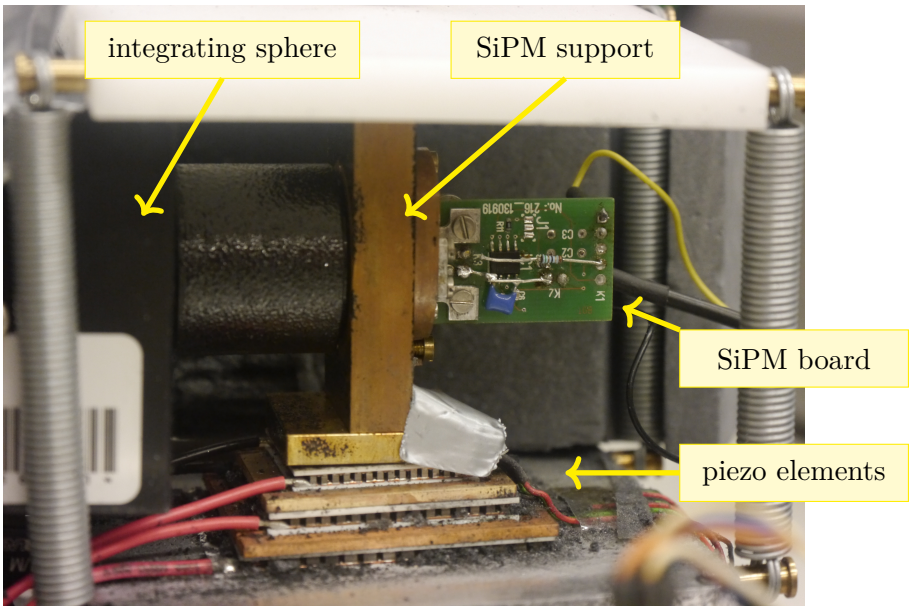

Figure 6.14: Image of the setup hosting the SiPM in a temperature stabilized environment. Here, one side is opened in order to take the photo. In standard operation, isolation is installed all around the copper block in the center.

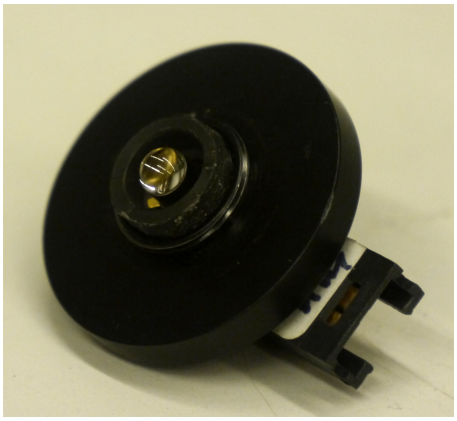

(a) The LED of pulser 1. The cable from pulser 1 is connected at the bottom right. The structure can be screwed to the integrating sphere.

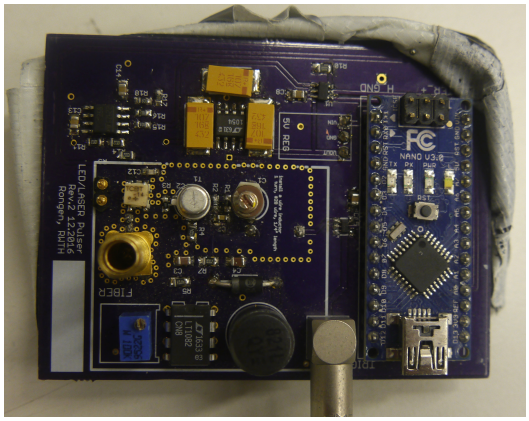

(b) The PCB of pulser 2 with the LED fixed inside the golden structure at the left. It is pushed into the integrating sphere through a rubber ring.

Figure 6.15: The two different versions of the pulsers used in the presented measurement.

The integrating sphere

The light produced by both VCSELs is emitted into an integrating sphere of type Thorlabs IS200-4 [184]. The ports of the integrating sphere have a diameter of $1/2'' = 1.27\,\text{cm}$. This is sufficient also for the largest available SiPMs with an edge length of 6 mm. The surface inside the integrating sphere has a high diffuse reflectivity of 99 %. The light is therefore reflected multiple times before possibly reaching the exit window. The exiting light is homogeneous and isotropic and ensures a homogeneous distribution of the light on the SiPM. The ports of the SiPM and the VCSELs are placed at angles of 90° with respect to each other to avoid the direct light to reach the SiPM from the VCSELs. The multiple reflections inside the sphere lead to a temporal broadening of the pulses. A dedicated simulation of the setup was performed to determine the amount of this effect. An exponential decay time of the output pulse of $\sim 3.44\,\text{ns}$ was found. The details of this simulation are shown in appendix D. The decay time is still below the expected intrinsic time constants of the SiPM. Therefore, the usage of the integrating sphere should be feasible.

The temperature stabilization of the SiPM

The SiPM is hosted inside a temperature stabilized environment. A dedicated setup was used that had been developed in the scope of another thesis [185]. Details can be found there. The SiPM is installed at a copper block. Its temperature is regulated through three piezo elements. The whole setup is thermally isolated and the targeted temperature can be set by the user and is kept automatically. In figure 6.14, an image of the setup is shown.

The setup was designed to use optical fibers to guide the light on the SiPM. This was not possible for the presented measurement as it would not guarantee a homogeneous light distribution on the sensor. Instead, the integrating sphere had to be placed as close to the SiPM as possible as indicated in figure 6.14.

Doing this, parts of the thermal isolation could not be properly placed. The room temperature around the setup was $\sim 20\,°\text{C}$ while the measurement temperature was $25\,°\text{C}$. The thermal insulation used should therefore be sufficient. The temperature of $25\,°\text{C}$ was the same the manufacturer uses to measure the datasheet values.

The readout oscilloscope

An oscilloscope of type Agilent Technologies DSO-X 3034A [186] is used for reading out the SiPM. The SiPM signal is directly fed into the oscilloscope without any pre-amplifiers in between. The oscilloscope readout is performed at an impedance of $50\,\Omega$. This setup represents exactly the schematics introduced in section 6.4. Readout is performed at a sampling rate of 4 GHz with an analogue bandwidth of 350 MHz and 20 000 samples per trace. The traces are transferred to a connected computer and stored to ROOT-files [133].

The oscilloscope also provides a waveform generator. It is used to trigger the delay generator which in turn triggers the pulsers. The readout of the oscilloscope is also triggered internally by its waveform generator.

6.6.4 Measurement procedure

The SiPM that was tested in this setup was of type Hamamatsu S13360-6025PE. This SiPM was chosen because it was also installed in the optical module that will be introduced in chapter 7. All measurements are performed at a temperature of $25\,°\text{C}$, the same temperature

as used by the manufacturer to determine the datasheet values. Ideally, all measurements only need to be performed for one SiPM of a specific type and the results can be used for all other SiPMs of the same type. In large scale applications of SiPMs this procedure will avoid characterization of each device individually. In order to study the feasibility of this approach, the breakdown voltage was taken according to the value given by the manufacturer.

The delays between the two consecutive pulses are chosen in a range between −100 ns to 2000 ns. Negative delays denote an inversion of the order of the two pulses. For large differences in the pulse sizes, changing the order of the pulses might yield different results. For differently sized pulses, the size of the output voltage V''' differs resulting in a changed reduction of the second pulse. In this section, pulse 2 or pulser 2 always refers to the pulse that is second for positive delays. For negative delays, the naming remains even though the order is reversed.

The chosen range is well above the expected time constants of the SiPM (cf. tab. 6.2). The largest delays of 500 ns to 2000 ns were taken to have two well separated pulses in the recorded trace. Determination of their start times allows to measure possible additional systematic delays in the circuit due to the delay generator, different cable lengths or trigger delays of the pulsers. The step size between two different delays was chosen between 1 ns around 0 and 500 ns at the highest delays.

For each delay, three different measurements were taken, with 100 recorded traces each:

1. One with only pulser 1 switched on producing a signal S_1 at the SiPM.
2. One with only pulser 2 switched on producing a signal S_2 at the SiPM.
3. One with both pulsers switched on producing a total signal S_{del} at the SiPM.

The first two measurements allow for the monitoring of significant changes in the amplitude of the produced pulses for example due to changes of the ambient temperature. From the third measurement, the relative reduction of S_2 due to S_1 can be determined. With an infinitely short recharge time of the SiPM voltages, the signal with both pulsers switched on would be given as $S_{\mathrm{del}}^{\mathrm{inf}} = S_1 + S_2$. The relative reduction of the signal of the second pulse due to the first pulse is then given by:

$$R_2 = \frac{S_{\mathrm{del}} - S_1}{S_2} \quad . \tag{6.31}$$

The measurement is repeated at different overvoltages. As gain, PDE and crosstalk show different dependencies on the overvoltage, its variation might help to discriminate different effects and to verify the correct implementation in the simulation.

6.6.5 Measurement of the offset in the delay

The offset in the delay is determined for each measurement series individually using all measurements with a set delay ≥ 500 ns. At these large delays, both pulses should be shaped well and not be deformed as the recharge time constants for the capacitors are significantly smaller (cf. tab. 6.2). In a first step, the delay was estimated to be 11 ns reading off the oscilloscope. This value was added to all delays in the subsequent measurements.

For a more precise determination of the delay, the leading edges of the pulses are detected and their separation is compared to the nominal delay. An example of a measurement at

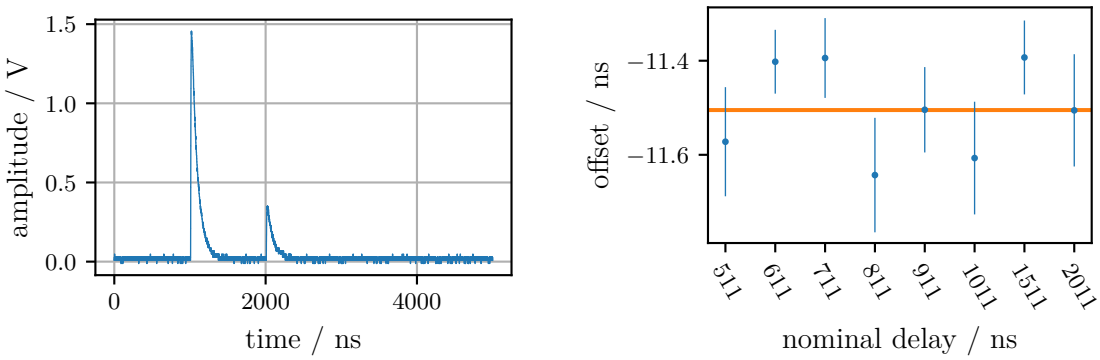

(a) An example trace of the double pulse as measured at a set delay of 1011 ns. The different pulse sizes result mostly from the different versions of the pulser used and not from the cell recharge.

(b) Differences between nominal and measured delay with respect to the nominal delay. The horizontal line denotes the median of the values.

Figure 6.16: Determination of the offset in the delay using the double pulses. These measurements were taken at an overvoltage of 5 V.

an overvoltage of 5 V with a set delay of 1011 ns is shown in figure 6.16a. The baseline is determined as the mean of the trace in the first 500 ns. A pulse search algorithm allows to detect the pulses. If at least seven consecutive samples are in increasing order, a pulse is considered being detected. The amplitude of the pulse is determined as the difference between its maximum and the baseline. A linear fit is performed in the range between the first sample that exceeds 5 % of the amplitude and the first sample that exceeds 50 % of the amplitude. These values have shown to provide good results. From the linear fit, the position of the baseline crossing can be extracted. The difference of the baseline crossing of the two pulses equals their delay. In figure 6.16b the difference between the nominal and measured delay is shown. The median of the distribution is taken as the offset in the delay of (11.50 ± 0.09) ns. The precision is better than 100 ps and negligible here. The delay is corrected for in all further analyses shown here.

6.6.6 Analysis of the double pulse measurement

An example trace of the double pulse as measured at an overvoltage of 5 V and a delay of 196 ns is given in figure 6.17. The baseline is determined as the mean in the first 875 ns of the trace. The signal is determined as the integral from 875 ns to the end of the trace. It includes both pulses. The second pulse is smaller than the first one because of the different versions of the pulsers. The measurement should not be affected.

This analysis is performed for all three kinds of traces, with only one pulser switched on or with both. The resulting reference signals when only one pulser is switched on are shown in figure 6.18. Both measurements are stable and no trend is visible. The widths of the distributions are 0.2 % and 0.9 % for S_1 and S_2, respectively. These fluctuations are negligible and for the further analysis only the mean of all $S_{1/2}$ weighted with their standard deviation is taken into account.

The resulting relative reduction of the size of the second pulse according to equation (6.31) is given in figure 6.19 for an overvoltage of 5 V with respect to the value of the breakdown

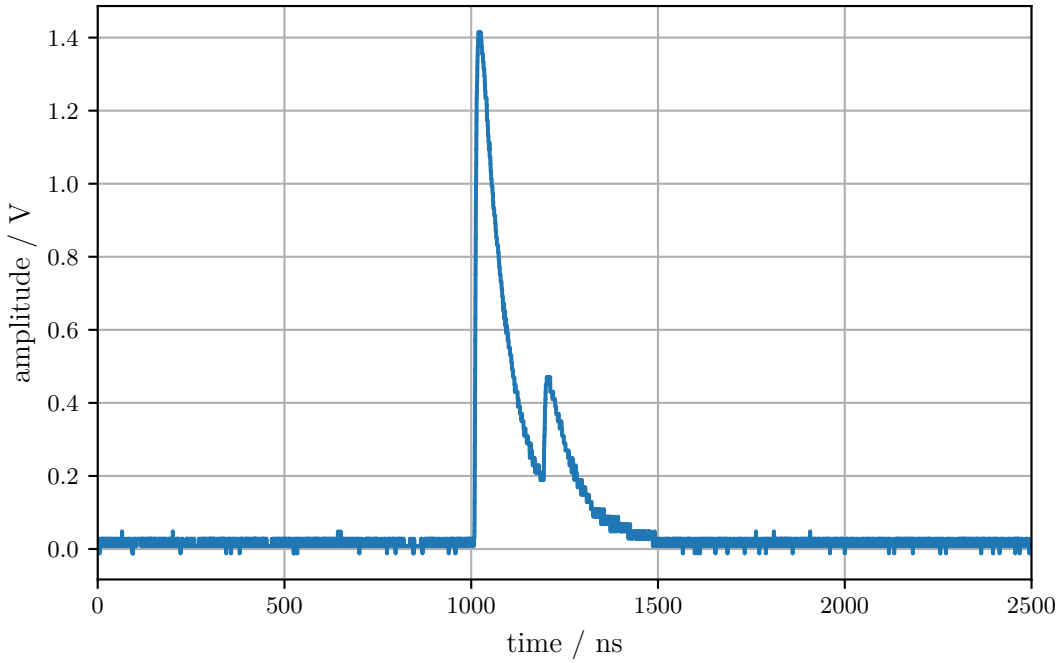

Figure 6.17: An example trace of the double pulses measured at an overvoltage of 5 V and a set delay of 196 ns. The trace is zoomed in, it extends up to 5000 ns.

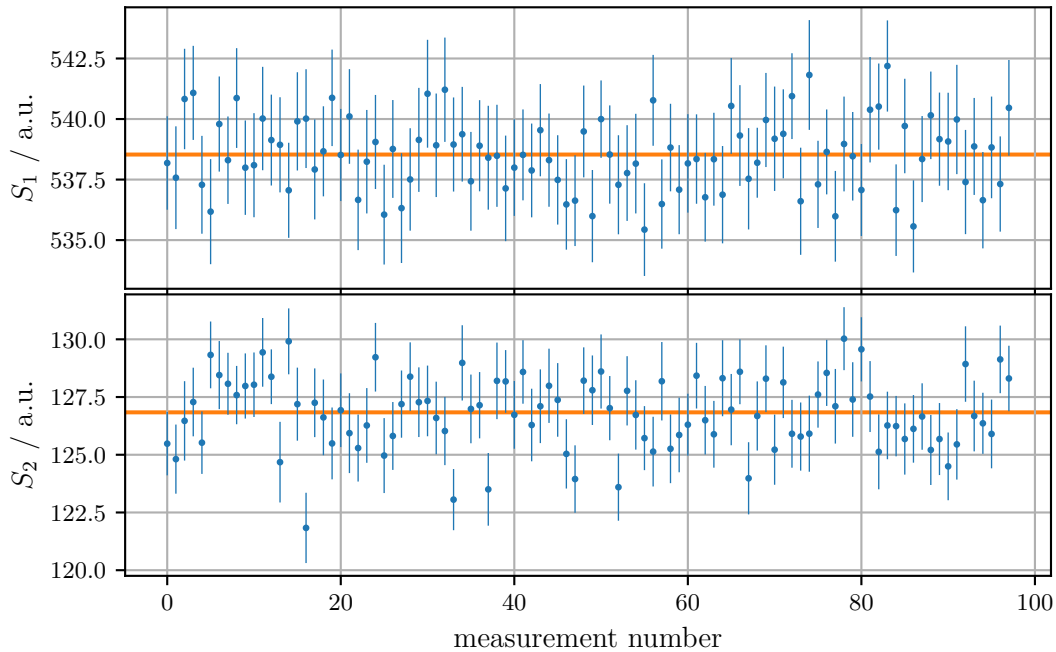

Figure 6.18: The reference signals S_1 and S_2 measured when only one of the two pulsers is switched on. The units of the signal size are identical for both so that relative signal sizes can be compared. The measurement number corresponds to the position in the chosen delays. The horizontal lines denote the weighted mean of all data points. Both measurements indicate a very stable operation.

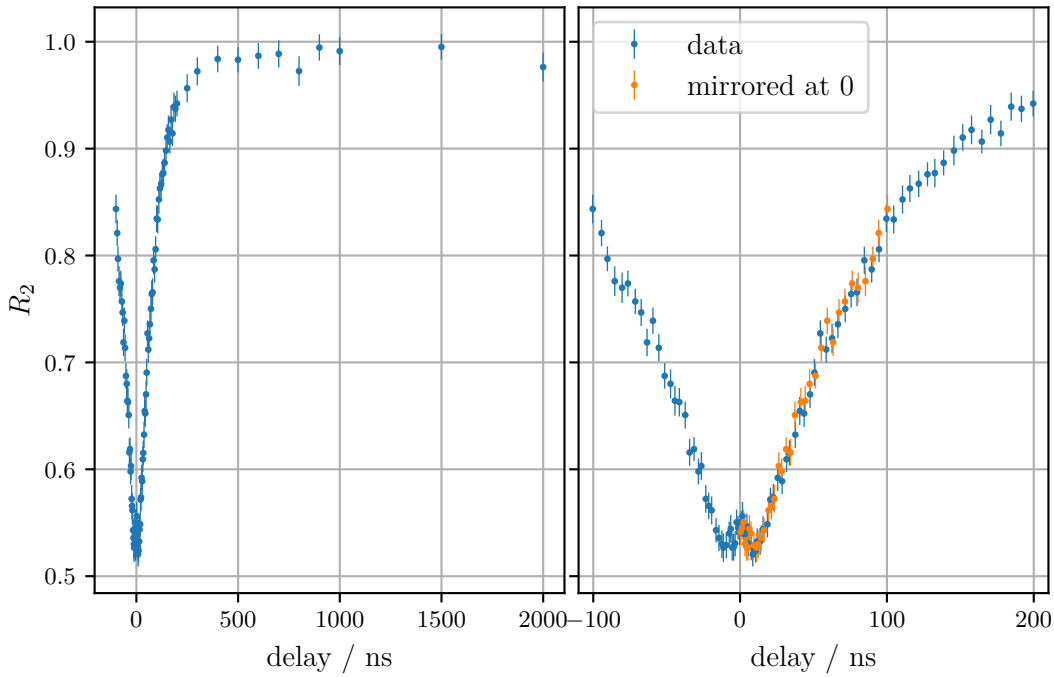

Figure 6.19: The measured relative reduction of the second pulse due to the triggering of avalanches by the first pulse according to equation (6.31). The delay is corrected for the measured offset. The right plot shows a zoom into the region around a delay of 0 ns. The orange data points are those with negative delay mirrored at zero. The distribution is symmetric.

voltage stated by the manufacturer. As expected, the signal of the second pulses reduces significantly for delays around 0 ns and the distribution is symmetric. The amount of reduction depends on the number of triggered cells. Here, almost 50 % reduction is reached which is significant and should suffice for further analysis. In the right plot of figure 6.19, the mirrored data points for negative delays are shown. They agree well with the positive ones meaning a symmetric distribution around 0 ns. The differently sized pulses thus do not have a significant impact on the result.

The measurement has additionally been performed at overvoltages of 3 V, 4 V and 6 V. The results are shown in figure 6.20. The amount of reduction of the second pulse increases with the applied overvoltage. It is a result of the increasing PDE which leads to more triggered cells. The errorbars increase for lower overvoltages due to the worse Signal-to-Noise Ratio (SNR).

The maximum reduction is not reached at a delay of 0 ns as might be naively expected. Instead it is at around 10 ns. This effect is caused by the delayed reduction of the applied voltage of the cells that were not triggered in the first pulse. This was shown in figure 6.10 for the datasheet values of the intrinsic parameters. The minimum of the dashed-dotted green curve is reached after ~ 30 ns. The discrepancy of this offset for measurement and simulation can result from deviations in the true intrinsic parameters of the SiPM. In addition, in the measurement a significant amount of cells will be triggered by photons of both, the first and the second pulse. In this case, the maximum reduction is at a shorter delay.

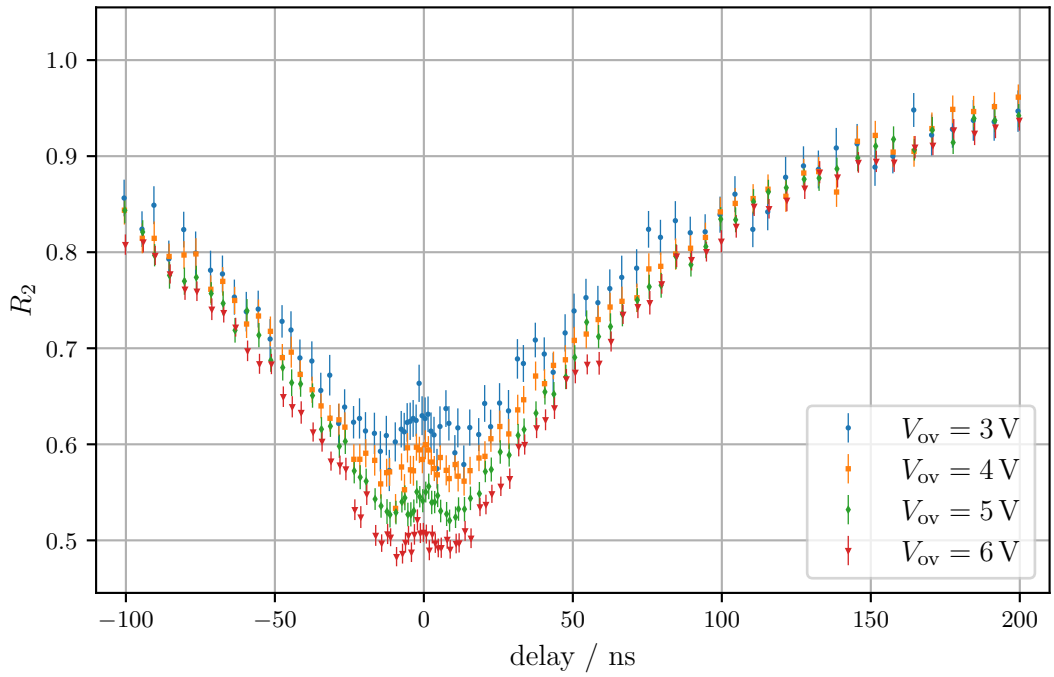

Figure 6.20: Comparison of double pulse measurements with different applied overvoltages. The effect of relative reduction of the second pulse increases with the overvoltage.

6.6.7 Simulation of the measurement

The simulation introduced in section 6.5 allows to determine an expectation for the result of this measurement. For each pulser an exponential time distribution for the arrival times of the photons on the sensor is randomly generated. The distribution follows the exponential time constant of $\tau = 3.44\,\text{ns}$ which was determined by the simulation of the integrated sphere as presented in appendix D.

The photons are time ordered and impinge on random SiPM cells. Each cell hit releases some charge that might be zero due to a low PDE. The total charge per pulse can be calculated for different configurations. Like for the measurement, references are determined for the charge released when only one pulser is switched on. The relative reduction of the second pulse due to the triggering by the first pulse can then be determined for different delays.

In order to perform a proper simulation of the measurement, the number of impinging photons per pulse needs to be known. This is a difficult task as already the output signal of a single pulse might be reduced because cells are hit twice. Only this reduced output signal is measured. The gain g of the SiPM at 5 V overvoltage is 7×10^5. The output signal in units of p.e. in the pulse is then given as:

$$\frac{N}{\text{p.e.}} = \frac{S}{R_\text{s} f_\text{s}} \frac{1}{e \cdot g} \tag{6.32}$$

with S the integrated signal in units of volts, $R_\text{s} = 50\,\Omega$ the readout resistor, $f_\text{s} = 4\,\text{GHz}$ the sampling frequency and e the elementary charge. The simulation should reproduce the same

output signal in units of p.e.. As one triggered avalanche of an untriggered SiPM produces a signal of 1 p.e., the output of the simulation can easily be calculated in units of p.e.. The number of incident photons is varied until the output signal matches the measurement.

The simulation is subject to fluctuations due to the random processes involved. Repeating the simulation and averaging the output can reduce the statistical fluctuations but it is computationally expensive.

6.6.8 Fitting of the simulation to the measurement

Performing the simulation of the measurement, optimal values for the intrinsic parameters of the SiPM can be obtained. The result of the relative reduction of the second pulse in the simulation is compared to the measurement by computing the χ^2-value for the agreement:

$$\chi^2 = \sum_i \frac{\left(R_{2,\mathrm{sim}}\left(t_i\right) - R_{2,\mathrm{meas}}\left(t_i\right)\right)^2}{\sigma\left(t_i\right)^2} \tag{6.33}$$

with $R_{2,\mathrm{sim}}$ and $R_{2,\mathrm{meas}}$ the simulated and measured relative reduction of the signal of the second pulse, σ the standard deviation of the measurement and t_i the i-th delay.

The statistical fluctuations of the simulation propagate to the calculation of the χ^2-value. It is not smooth as a function of the intrinsic parameters. Standard gradient based fitting routines like MIGRAD [187] will not succeed on these kinds of analyses. The gradients cannot properly be determined due to the fluctuations. Here, the *Nelder-Mead method* was used as it is a gradient free minimization algorithm [188]. A short introduction into its working principle is given in appendix E.

The simulation for a given set of intrinsic parameters is performed as follows:

1. The number of impinging photons reproducing the measured output signal is determined as described in the previous section. When a deviation of less than 0.1 % from the measured output signal is achieved, the accuracy is assumed to be sufficient.

2. For each measured delay between the two pulses, the simulation is performed using the number of impinging photons determined in the previous step. For each delay, the simulation is repeated until the uncertainty on the mean value of the output reduces to less than 0.1 %.

From the output of the simulation, the χ^2-value is determined.

The measurements for all four overvoltages are fit at the same time. Due to the computationally expensive function evaluation, for each overvoltage only every fourth data point is used in an alternating way. Nonetheless, one function evaluation takes $\mathcal{O}\,(\mathrm{min})$ when being evaluated on 48 cores due to the high precision to be achieved. Lower precisions were tested but did not yield satisfying results due to too large fluctuations in the χ^2-value.

The fit is performed in six variables: the quenching resistor R_q, the diode capacitance C_d, the grid capacitance C_g, an offset in the overvoltage ΔV_ov, the gain g at an overvoltage of $V_\mathrm{ov} = V_\mathrm{ov,nom} + \Delta V_\mathrm{ov}$ and the crosstalk probability p_x. An offset in the overvoltage is equivalent to fitting the breakdown voltage. It accounts for relative differences of the measurements at different overvoltages. As has been seen in section 6.2.1, figure 6.5, the values given by the manufacturer can significantly deviate from the correct value. The quenching capacitance C_q can be derived from the gain, the overvoltage and the diode capacitance using equation (6.6). The fit has been repeated multiple times in order to

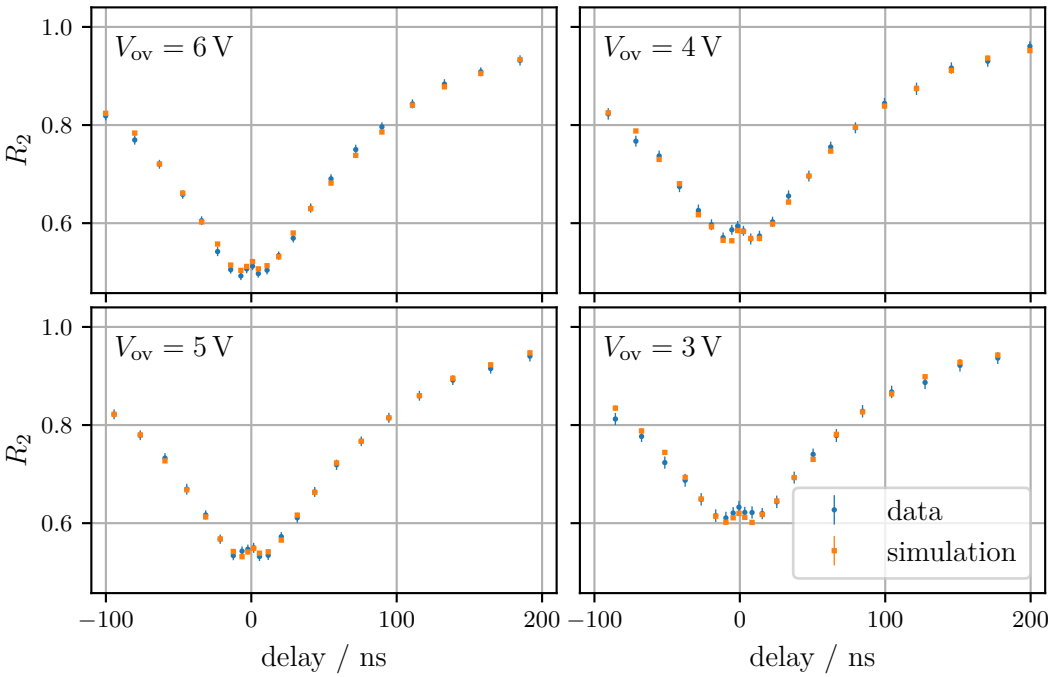

Figure 6.21: Result of the fit of the simulation to the data of the double pulse measurement. Both agree very well.

understand the impact of the statistical fluctuations of the function. The different initial simplices used are given in appendix E.

The result of the fit is shown in figure 6.21 for the average of all fits. Their individual results are indistinguishable from this one. The agreement between data and simulation is very good with a $\chi^2 \approx 60$ at 90 degrees of freedom. The final fit values are given in table 6.3. These values are in very good agreement with those determined by other measurements or the manufacturer. For the offset in the overvoltage ΔV_{ov}, a slight tension can be observed with the reference value. The agreement is around 1σ meaning no statistically significant deviation. Only the crosstalk probability shows a tension with the reference value. The measurement presented here is likely not very sensitive to this quantity as is indicated by the large uncertainty. In addition, a lower value of only 1 % can be found in the datasheet [130]. These deviations might result from different definitions of crosstalk or differences in the surrounding medium or the extraction technique (cf. sec. 6.2.4). The resulting recovery times and contributions to voltages V', V'' and V''' are given in table 6.4.

The determination of the uncertainty on the parameter values from this measurement is very elaborated. The accurate method for uncertainty estimation is to scan the χ^2-values when changing one parameter P_i. At each step, the other parameters have to be optimized to minimize the χ^2-value for the fixed P_i. The Gaussian standard deviation is then given for the value of P_i where the χ^2-value is increased by 1 compared to its minimum. For this method a huge amount of function evaluations needs to be executed because of the multiple minimization processes. In addition, the fluctuations of the χ^2-values make it difficult to determine an increase by 1 and is thus not feasible here. An alternative, widely used approximation is the calculation of the inverse Hessian matrix H, which is composed of the

fit	R_q / kΩ	C_d / fF	C_g / pF	g / 10^5	p_x / %	ΔV_{ov} / V
1	844	20.6	38.6	6.93	5.9	0.29
2	785	20.8	42.1	7.18	6.9	0.31
3	789	20.8	40.2	7.28	4.7	0.24
4	796	20.8	40.9	7.37	4.0	0.18
5	758	21.2	43.7	6.90	3.9	0.16
$\langle x \rangle$	794 ± 31	20.84 ± 0.22	41.1 ± 1.9	7.13 ± 0.21	5.1 ± 1.3	0.236 ± 0.066
ref.	790.4 ± 6.4	20.6 ± 2.1	41.1 ± 4.1	7	7 ± 0.2	0.305 ± 0.048

Table 6.3: Resulting values from five fits of the SiPM simulation to the measurement with different initial simplices. See text for details. The reference values in the last row are taken from the following sources: R_q and ΔV_{ov} have been determined in sections 6.6.1 and 6.2.1, respectively, of this thesis. C_d and C_g are given by the manufacturer [181] with an uncertainty of 10 % and g is given in the datasheet with unknown precision [130]. p_x was measured in [155]. The second to last row indicates the mean and Root Mean Square (RMS) of the fit results.

fit	τ_q / ns	τ_+ / ns	τ_- / ns	A_1	A_2
1	17.7	0.69	78.3	0.35	2.10
2	17.0	0.98	78.0	0.46	1.45
3	17.6	1.3	78.1	0.66	1.16
4	18.1	1.7	78.4	0.82	1.06
5	16.2	0.56	78.9	0.26	3.44
$\langle x \rangle$	17.3 ± 0.90	1.0 ± 0.5	78.3 ± 1.0	0.55 ± 0.22	1.4 ± 0.4
ref.	16.7 ± 0.2	0.8 ± 1.3	77.0 ± 0.7	0.4 ± 0.6	2 ± 4

Table 6.4: Recovery times and their contribution to the voltages applied at the SiPM cells as resulting from the measurement using equation (6.26). The values given in the rows $\langle x \rangle$ and *ref* are determined from the results given in the corresponding rows of table 6.3. The corresponding values calculated for the intrinsic values stated by the manufacturer have been given in table 6.2.

second partial derivatives of the χ^2-function with respect to the parameters. Estimation of the partial derivatives is challenging on a fluctuating function.

As these standard methods of uncertainty estimation are not feasible here, the fit is repeated multiple times as can be seen in table 6.3. Due to the fluctuations, for each fit procedure, a different minimum is found. From these multiple fits, the average and standard deviation for the individual parameters can be determined. The fluctuations from evaluating the χ^2-value with identical parameters are in the order of $\sigma_{\chi^2} \approx 4$. This is larger than the value of $\Delta\chi^2 = 1$ for the 1σ estimate making it plausible that multiple fits yield deviations that are in the correct order of magnitude for the uncertainty. The average values are given in row $\langle x \rangle$ of table 6.3.

6.7 Dynamic Range

As has been seen in the previous sections, the cellular structure of the SiPM has a significant impact on its response. For simultaneously incident photons, the output of a single cell is

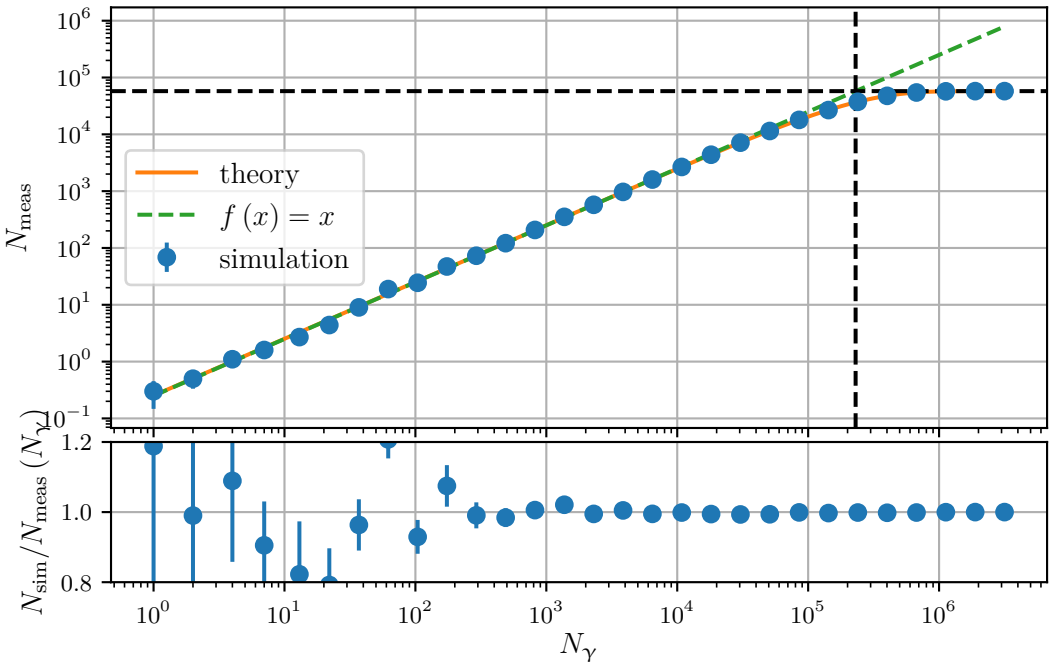

Figure 6.22: The dynamic range of an SiPM for simultaneously impinging photons. An SiPM with $240 \times 240 = 57\,600$ cells, a PDE of 25 %, crosstalk probability of 1 %, and negligible afterpulsing probability is assumed. These values correspond to the Hamamatsu S13360-6025PE [130]. The theory curve follows equation (6.34). The simulation is a simple toy Monte-Carlo and explained in the text. The simulation is repeated ten times for each point and the resulting mean and uncertainty are shown. The dashed lines denote the number of cells (y-axis) and number of cells divided by the PDE (x-axis).

either zero (if no avalanche process is initiated) or one p.e.. This effect limits the maximum output signal for simultaneous photons in terms of p.e. to the number of cells of the sensor.

This binary behavior of the SiPM cells for coincident impinging photons leads to a non-linear dynamic range. The relation between the incident number of photons and the output signal is then given by

$$N_{\mathrm{meas}}(N_\gamma) = N_{\mathrm{cell}}\left(1 - e^{-pN_\gamma/N_{\mathrm{cell}}}\right) \text{ p.e.} \tag{6.34}$$

with N_{meas}, N_γ, and N_{cell} the measured signal in p.e., the number of incident photons, and the number of cells, respectively. The detection probability can be approximated as $p \approx PDE(1 + p_{\mathrm{xt}} + p_{\mathrm{ap}})$ with the crosstalk and afterpulsing probabilities p_{xt} and p_{ap}, respectively.

The response of an SiPM is thus intrinsically non-linear. Nonetheless, for a low number of incident photons $N_\gamma \ll N_{\mathrm{cell}}$, a linear approximation $N_{\mathrm{meas}} \propto N_\gamma$ is feasible.

In figure 6.22, the measured number of photons N_{meas} versus the incident number of photons N_γ is shown. The simulation shown here is a simple toy Monte-Carlo where each SiPM cell releases a randomly chosen charge of either one or zero according to the PDE of 25 %. The theoretical curve and the toy Monte-Carlo simulation are in excellent agreement

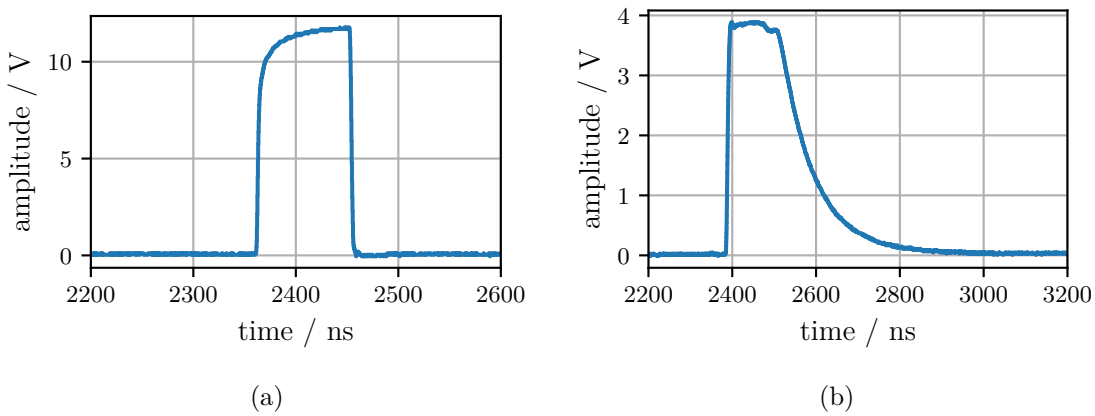

Figure 6.23: *(a):* Example pulse of the pulser to drive the LED. It is set to a width of 100 ns and an amplitude of 15 V. The amplitude is above the maximum the pulser can reach. *(b):* The electrical pulse $S(t)$ measured from the SiPM when being exposed to a light flash driven by the pulse in *(a)*. The measured integrated signal corresponds to around 10^5 p.e..

as expected. The deviation from linearity for this sensor reaches 10 % at a number of $N_\gamma \sim 50\,000$ incident photons producing a signal of $N_{\text{meas}} \sim 13\,000$ p.e.. This means that only one fourth of the 57 600 SiPM cells is triggered and only a fraction of the SiPM is actively contributes to the measurement. Considering that this SiPM is among those with the largest number of cells, the dynamic range of a single SiPM is limited to only $\sim 10\,000$ detected photons without correcting for the non-linearity.

In many applications, the assumptions of simultaneously impinging photons is not valid. For instance, the distribution of the arrival times of the muons in an air shower can spread over several 100 ns [73]. Additional broadening might arise from the detection medium such as scintillators or optical fibers. For these extended pulses, the SiPM cells might be triggered by multiple consecutive photons releasing only a reduced charge for the second one. The effect of the non-linearity is therefore reduced but depends on the time distribution of the incident photons.

The homogeneous response of the SiPM cells allows for a simple simulation of its response as has been seen in the previous section. This makes it plausible that a reconstruction of the number of incident photons can be achieved even in the highly non-linear regime. A corresponding algorithm will be presented in section 6.8.

6.7.1 Measurement of the SiPM dynamic range

The behavior of the SiPM when being exposed to bright, extended light pulses was measured in the same setup that was introduced in section 6.6.3 and sketched in figure 6.14. The identical SiPM of type Hamamatsu S13360-6025PE was used.

Pulser 1 was replaced by another pulser that was optimized for covering a high dynamic range and also allowed to vary the pulse length between 20 ns to 100 ns. It operated a LED of 390 nm wavelength. Different types of LEDs were tested with the LED used generating the highest signal on the SiPM. An example electrical pulse produced by the pulser when set to a width of 100 ns and an output pulse from the SiPM are shown in figure 6.23. It should be noted that the electrical pulse does not necessarily exactly correspond to the optical

pulse due to a possible slow reaction and decay of the LED pulse. The SiPM pulse has a plateau of $\sim 100\,\mathrm{ns}$ corresponding to the length of the light pulse. The output amplitude of almost 4 V is only about 1 V below the set overvoltage of 5 V. The gain and PDE of the cells are therefore highly reduced and the plateau results from this saturation effect.

The SiPM signal in terms of p.e., N_{meas}, was determined by integrating the measured traces:

$$N_{\mathrm{meas}} = \frac{\sum_i V_i}{R_{\mathrm{s}} e g R} \tag{6.35}$$

with V_i the voltage amplitude of the i-th sample, $R_{\mathrm{s}} = 50\,\Omega$ the readout resistor, e the elementary charge, $R = 4\,\mathrm{GHz}$ the sampling rate and g the gain of the SiPM. The first 7500 samples corresponding to a measurement time of 1875 ns are averaged for baseline subtraction and only the remaining 12 500 samples are used in the integration.

Pulser 2 was replaced by a photodiode of type Hamamatsu S2281-01 [189] that was used as a reference light detector. Its current I_{d} was measured with a Keithley 6487 Picoammeter [151]. The relative brightness S of the pulses is then given as:

$$S = \frac{I_{\mathrm{d}}}{R_{\mathrm{p}}} \tag{6.36}$$

where R_{p} is the repetition rate of the pulser. The repetition rate was varied as a function of the brightness. A lower rate is favorable for the SiPM to avoid saturation effects from consecutive pulses. At the same time, a low rate also results in a low current at the photodiode and a compromise has to be found. The rate was always adjusted such that the current was closely above 1 nA and the rate between 20 Hz to 300 kHz. The photodiode was not used as an absolute reference for the number of incident photons N_{ref}. Instead, the current was calibrated with the measured SiPM signal at measured signals of 10 to 1000 p.e. per pulse where the response is quasi linear. For linear response, the number of measured photons N_{meas} is therefore equal to the number of reference photons N_{ref} and the limited PDE is not taken into account. The true number of incident photons can be obtained by dividing N_{ref} by the PDE but is of no importance in this study. The resulting saturation curves for a 40 ns and 100 ns pulse width are shown in figure 6.24. The theory curve according to equation (6.34) is given as well for comparison.

For both pulse lengths, saturation effects become visible around 10^4 incident photons. For the shorter pulse, the response of the SiPM in the highly non-linear regime is lower than for the long pulse. This is expected due to the higher flux per time interval leaving the SiPM cells only short time for recovery. For the extended pulses it is clearly possible to achieve signals larger than the number of cells. This effect is in the literature sometimes referred to as *oversaturation*. As has been seen before, this behavior is expected due to cells being triggered multiple times and means that full saturation is not reached yet.

For both measurements, a step-like behavior is visible in the response curve in figure 6.24 at $N_{\mathrm{ref}}\,(T = 40\,\mathrm{ns}) \approx 1 \times 10^6$ and $N_{\mathrm{ref}}\,(T = 100\,\mathrm{ns}) \approx 2.7 \times 10^6$, respectively. The origin of this behavior is unclear. The shapes of the SiPM pulses below and above these positions have been investigated carefully but no systematic differences were found. The most plausible explanation is a saturation effect of the reference photodiode. This is supported by the fact that the number of photons per time for the position of the step differs by only $\sim 8\,\%$ indicating a threshold of the linearity of the device. The data points in these regions should therefore be considered with caution, but they are shown here for completeness.

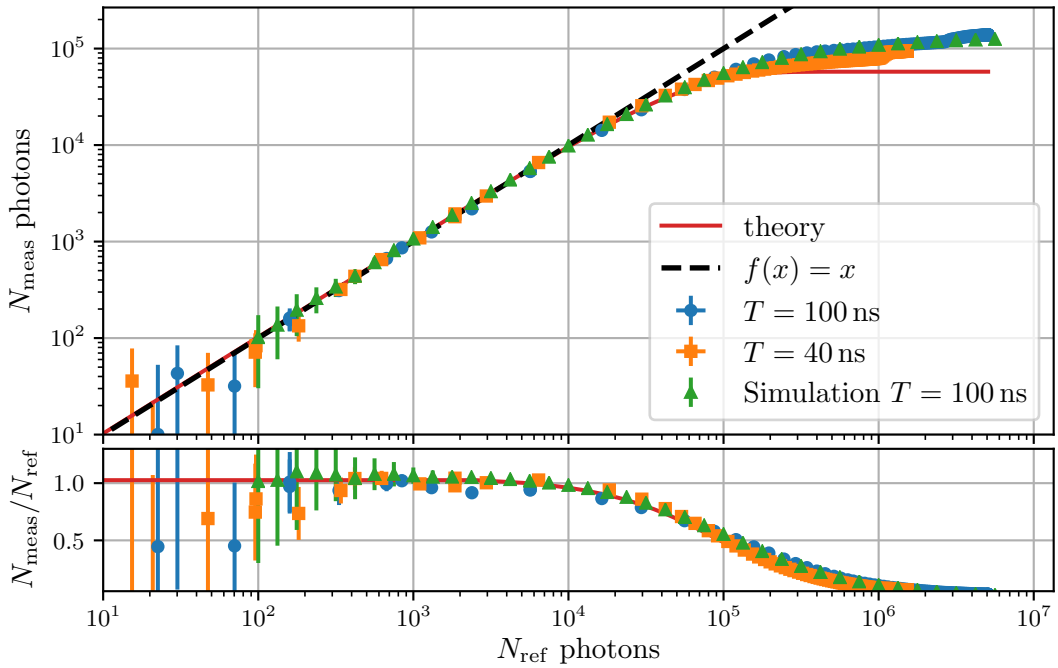

Figure 6.24: Two measurements of the response of the SiPM for input pulses with widths $T = 40\,\text{ns}$ and $T = 100\,\text{ns}$. For the shorter incident pulse, the deviation from linearity sets in a little earlier. The theory curve follows equation (6.34). The simulation will be introduced in section 6.7.2. It is in good agreement with the measurement of the same pulse width.

6.7.2 Simulation

In order to study the saturation behavior of the SiPM, a simulation of the measurement has been developed. It simulates the response of the SiPM in terms of released charge per incident photon and also the electric output pulse when being exposed to an incident light pulse. The SiPM simulation has been introduced in section 6.5. As in previous studies, a PDE of 100 % is assumed for fully recovered cells to reduce the simulation effort due to photons that do not trigger any cell[1]. The correct number of incident photons can always be obtained by division of the true PDE. Here, the parameters found in the double pulse measurement given in row $\langle x \rangle$ of table 6.3 are inserted. Each photon produces an electric output pulse $SPE(t)$ with an exponential rise and fall as

$$SPE(t) = c \cdot \frac{1}{1 + e^{-t/\tau_+}} \cdot e^{-t/\tau_-} \tag{6.37}$$

with an integral proportional to the released charge that can be adjusted by the normalization constant c. The time constants $\tau_\pm$ were determined in section 6.6.8 and are given in table 6.4.

[1]This simplification does not affect the average measured signal but the lower number of impinging photons has an impact on statistical fluctuations. As all pulses that will be considered in this section trigger at least some thousand cell breakdowns, the number of photons is large and the fluctuations small. It is therefore a valid simplification here.

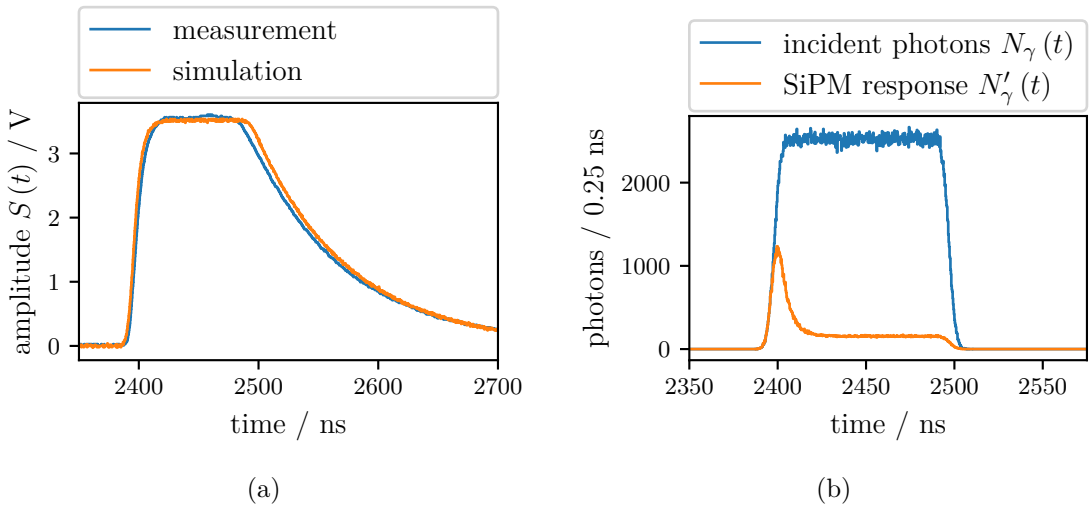

Figure 6.25: *(a):* Comparison of a simulated and measured trace $S(t)$, both for an incident number of 10^6 photons. Both show very similar characteristics. The differences in the shape likely arise from differences in the time distributions of the incident photons. *(b):* The simulated distribution of incident photons and the result when each photon is weighted by the released charge of the SiPM.

To achieve a good agreement between the simulation and the measurement, also electronic noise and digitization effects need to be taken into account. The simulated trace is thus also sampled at a rate of $R = 4\,\text{GHz}$. From the measurements, a RMS of the noise of $\sigma_{\text{noise}} = 9.9\,\text{mV}$ is determined. To each sample of the simulated trace is added a random value drawn from a Gaussian distribution with width σ_{noise}. The resulting voltage amplitudes are digitized in steps of 0.0201 V, the same as in the measurement.

In figure 6.25a, a comparison of a simulated and a measured trace $S(t)$ is shown. For the simulation, an incident uniform time distribution of 100 ns width is smeared by a Gaussian of 3 ns width. The traces are in reasonable agreement. The specific differences in the shape are likely to originate from deviations in the exact shape of the time distribution of the incident photons. For the measurement, the leading edge and the tail are longer than for the simulation. This might be attributed to a slow onset and afterglow of the LED.

The simulated incident photon distribution and the result when being weighted with the SiPM response is given in figure 6.25b. For the first $\sim 10\,\text{ns}$ both distributions agree. Then, the saturation effects of the SiPM set in and the maximum of the SiPM response distribution is only 40 % as high as the incident one. The peak is followed by a significant drop and a plateau. In this region, an equilibrium between the number of triggered cells and the photon flux is reached.

The simulated dynamic range has been shown in figure 6.24 together with the measurements. It is in good agreement with the measurement of the same pulse width of $T = 100\,\text{ns}$. A more detailed study of the dynamic range and the reconstruction of signals in the highly non-linear regime will follow in the next section.

6.8 An Algorithm to extend the linear Dynamic Range of SiPMs

The simplest approach to extend the linear dynamic range of an SiPM would be to measure its response over the whole range of incident photon numbers. A result similar to the one shown in figure 6.22 will be obtained and can be parameterized. The parametrization then allows to determine the incident number of photons for a given output signal.

As the size of the output signal does not only depend on the number of incident photons but also on their temporal distribution, this approach is not feasible in most applications. Typically, the temporal distribution can vary and is not known. For example, in air shower physics, the time distribution of the arriving muons depends on the energy of the primary particle and the distance to the shower core. A more general algorithm is therefore necessary to address a wide range of applications.

6.8.1 Overview of the chosen ansatz

The goal is to develop an algorithm that can be used if the time distribution of the incident photons is unknown. The main idea is to exploit the SiPM simulation developed in section 6.5 to find the time distribution of incident photons $N_\gamma(t)$ that produces the measured output signal $S(t)$. This is achieved in two steps:

1. An ideal SiPM is assumed which does not suffer from any saturation effects. Each impinging photon triggers an avalanche with charge equal to 1 p.e.. This corresponds to a PDE of 100 % and is used for simplification here. The correct number of incident photons can, in principle, be determined later by division by the true PDE. For this ideal sensor, the incident photon distribution $N'_\gamma(t)$ that produces the measured output voltage signal $S(t)$ is approximated.

2. For the real SiPM, the incident photon distribution $N_\gamma(t)$ that reproduces $N'_\gamma(t)$ when taking into account the saturation effects is determined. At this point, the knowledge of the time distribution is exploited by applying the SiPM simulation. Then, $N_\gamma(t)$ will also produce the measured output voltage signal $S(t)$ and the integral of $N_\gamma(t)$ is the total number of incident photons.

A schematic of the algorithm is shown in figure 6.26. In the following sections, this schematic will guided through in detail. The main advantage compared to the analysis presented in figure 6.24 is the usage of not only the integral of the measured pulse but also the time dependence of the signal $S(t)$. First studies have already been published in [190] where the author of this thesis has contributed significant parts.

6.8.2 Determination of the incident photon distribution for an ideal SiPM

In this step, an ideal SiPM is assumed where each incident photon triggers a breakdown of a cell. The corresponding time dependent voltage signal produced in one avalanche is given by $SPE(t)$ as given in equation (6.37) with the integral after proper conversion of 1 p.e.. Then, the measured voltage signal $S(t)$ is given as

$$S(t) = N'_\gamma(t) * SPE(t) + n(t) = \int_{-\infty}^{\infty} N'_\gamma(t') \cdot SPE(t-t')\,\mathrm{d}t' + n(t) \tag{6.38}$$

with $N'_\gamma(t)$ the time distribution of the incident photons and $n(t)$ time dependent noise. In the case of the measurements with an SiPM, the shape of the single p.e. pulse can be

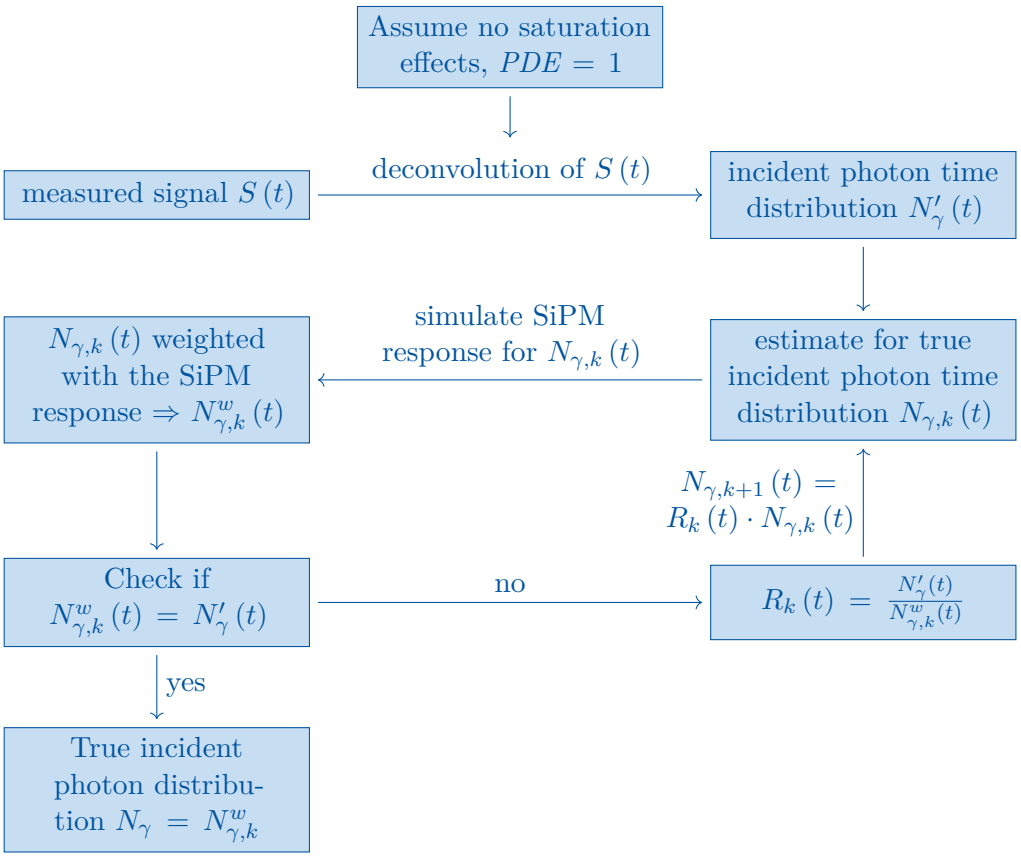

Figure 6.26: Schematic of the reconstruction of the incident photon distribution. From a measured voltage signal $S(t)$, the incident photon time distribution for an ideal sensor $N'_\gamma(t)$ is determined through a deconvolution of the signal. The SiPM response is considered in an iterative process. It finds the incident photon distribution $N_\gamma(t)$ that reproduces $N'_\gamma(t)$ when including the SiPM response. Details on the deconvolution are given in section 6.8.2 and the SiPM response is discussed in section 6.8.3.

well approximated using the results of the calculations performed in section 6.4. The pulse shape used here follows equation (6.37).

The determination of $N'_\gamma(t)$ corresponds to a deconvolution. The theory of deconvolutions is widely discussed in the literature for very different problems such as the determination of the energy spectrum of cosmic rays [191] or recovery of defocused images [192]. Depending on the specific problem different methods are favored. While often the smearing of the measurement (here by $SPE(t)$) is known or can at least be well approximated, the time dependent noise is usually unknown and can therefore not be subtracted. This can be a great challenge when solving equation (6.38) for $N'_\gamma(t)$.

Several algorithms such as Wiener filtering [193] or custom developed methods have been tested in the scope of this work. An algorithm based on [163, 164] was found to achieve very good results and will be introduced here based on these publications. It exploits Bayes' theorem and was originally developed for counting experiments. It allows for example to unfold the finite energy resolution from a measured energy spectrum of a cosmic ray experiment. Though at the first glance this might not be identical to the problem discussed

in this thesis, it is very much comparable. In contrast to the case of an energy spectrum or other types of counting experiments, the smearing of the photon distribution by the electric pulse $SPE(t)$ is not a probabilistic process. Nonetheless, the stochastic nature is negligible in the case of large event numbers making the two processes similar.

As the algorithm makes use of Bayes' theorem, $SPE(t|\tau)$ should be seen as a probability density function for an incident photon at time τ to produce a voltage signal V at a time t. For the rest of this section, greek τ will refer to times of incident photons while latin t corresponds to the time of the voltage signal produced at the SiPM. Neglecting the contribution of noise and assuming a discrete sampling of the signal $S(t)$, equation (6.38) can be rewritten as a matrix multiplication:

$$S(\mathbf{t}) = R\, N'_\gamma(\boldsymbol{\tau}) \qquad . \tag{6.39}$$

Here, $\mathbf{t}$ is the vector of all times where the signal is sampled. The same applies to $\boldsymbol{\tau}$. R is the response matrix with $R_{ij} = SPE(t_i|\tau_j)$. The negligence of the noise component $n(t)$ is justified here because of the focus on large signals where the signal-to-noise ratio is high. Nonetheless, the noise fluctuations still present in $S(\mathbf{t})$ can significantly spoil the result in the simple solution of equation (6.39) by inverting R. This is due to amplification of the noise when being divided by small values in the inverse of R.

Instead, a pseudo-inverse of R will be determined that avoids division by small values. Exploiting Bayes' theorem, the probability $SPE'(\tau_j|t_i)$ that a photon has hit the sensor at a time τ_j under the assumption of a measured voltage signal $S(t_i)$ at t_i is calculated:

$$SPE'(\tau_j|t_i) = \frac{SPE(t_i|\tau_j)\, P(\tau_j)}{\sum_k SPE(t_i|\tau_k)\, P(\tau_k)} \tag{6.40}$$

with $P(\tau_j)$ being the probability for a photon to hit the SiPM at time τ_j. Then, the incident photon distribution is given by

$$N'_\gamma(\tau_i) = \sum_j SPE'(\tau_i|t_j)\, S(t_j) \qquad . \tag{6.41}$$

The probability $P(\tau_i)$ for a photon to hit the SiPM at time τ_i is unknown but given by:

$$P(\tau_i) = \frac{N'_\gamma(\tau_i)}{\sum_j N'_\gamma(\tau_j)} \qquad . \tag{6.42}$$

Using an iterative approach the lack of knowledge can be compensated. From an initial prior distribution $P_0(\tau_i)$ the corresponding $SPE'_0(\tau_j|t_i)$ is calculated from equation (6.40) leading to a first estimate on $N'_{\gamma,0}(\tau_i)$ using equation (6.41). Assuming an initially uniform

prior yields:

$$P_0(\tau_i) = \frac{1}{N_{\text{samples}}} \tag{6.43}$$

$$SPE'_k(\tau_j|t_i) = \frac{SPE(t_i|\tau_j)\,P_k(\tau_j)}{\sum_m SPE(t_i|\tau_m)\,P_k(\tau_m)} \tag{6.44}$$

$$N'_{\gamma,k}(\tau_i) = \sum_j SPE'_k(\tau_i|t_j)\,S(t_j) \tag{6.45}$$

$$P_{k+1}(\tau_i) = \frac{N'_{\gamma,k}(\tau_i)}{\sum_j N'_{\gamma,k}(\tau_j)} \tag{6.46}$$

where N_{samples} is the total number of samples of the trace. A uniform initial prior represents the missing knowledge about the incident photon distribution. The iteration must be stopped when a satisfying result is obtained. Here, after each iteration the voltage trace resulting from $N'_{\gamma,k}(\tau_i)$ is calculated using equation (6.39). The χ^2-value is calculated for the agreement with the measured trace $S(\mathbf{t})$ in the bins that are at least 3σ above the noise level. Restriction to signals above the noise level is necessary to obtain a plausible result in the region of interest and not from just noise. If the χ^2 per number of degrees of freedom falls below 2 or if it only improves by less than 1 ‰ in one iteration, the iteration is stopped. Different stopping criteria have been tested as well. The chosen ones allow to obtain good results in a reasonable number of iterations.

Due to uncertainties in the involved distributions and the contribution of noise, small fluctuations will be present on the final result $N'_{\gamma,k}(\tau_i)$ leading also to negative values. This is unphysical for a number of photons and a smoothing is applied to remove these fluctuations. The details of this algorithm are described in appendix F.

In figure 6.27, the resulting photon distribution $N'_{\gamma,k}(\tau_i)$ is shown for a simulation of 10^6 incident photons according to section 6.7.2. The agreement between the originally simulated and the reconstructed trace is extremely good. In the photon distributions, a slight mismatch is visible in the falling tail and the initial peak is 5 % lower in the reconstruction. These differences are small and the reconstruction can be considered successful.

6.8.3 Reconstruction of the true incident photon distribution

The method described in the previous section assumes an ideal SiPM where a cell releases a pulse $SPE(t)$ for each incident photon. For a realistic SiPM this is not the case and the recharge of the SiPM cells needs to be taken into account. For each incident photon at time τ_i a charge corresponding to a fraction f_i of one p.e. is released. The goal is to find the incident photon distribution $N_\gamma(\tau)$ that reproduces $N'_\gamma(\tau)$ when each photon is weighted by f_i. This is done in an iterative approach.

As a starting point, photons according to $N'_\gamma(\tau)$ are put into the SiPM simulation introduced in section 6.5. For each photon, the fraction of the released charge f_i is obtained and the weighted distribution $N^{\text{w}}_{\gamma,0}(\tau)$ can be determined. Due to $f_i \leq 1$ in most cases (except for crosstalk events), $N^{\text{w}}_{\gamma,0}(\tau)$ will be below $N'_\gamma(\tau)$. Multiplying the time dependent ratio $R_0(\tau) = N'_\gamma(\tau)/N^{\text{w}}_{\gamma,0}(\tau)$ with the former input distribution allows to determine a

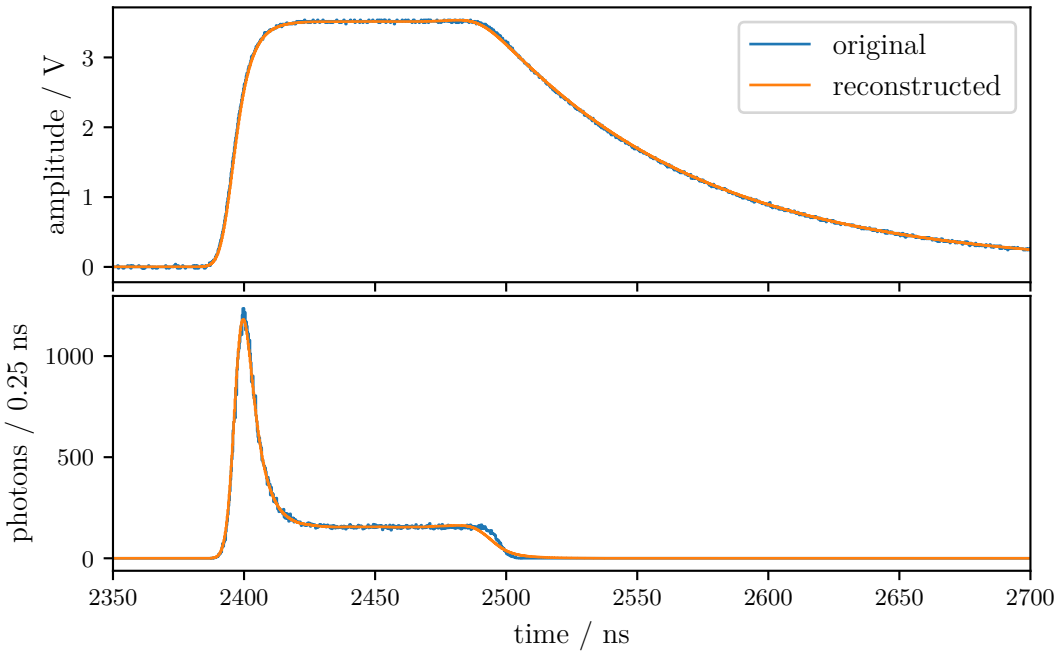

Figure 6.27: The originally simulated and reconstructed traces $S(t)$ (*top*) and the corresponding incident photon distributions $N'_{\gamma,k}(\tau_i)$ (*bottom*) for an ideal SiPM where each photon triggers a cell breakdown. The agreement is very good though some slight mismatch is visible in the falling tail. The incident number of photons is $N_{\mathrm{ref}} = 10^6$.

new input distribution whose output will be closer to $N'_\gamma(\tau)$. Iterating this process yields:

$$N_{\gamma,0}(\tau_i) = N'_\gamma(\tau_i) \tag{6.47}$$

$$N^{\mathrm{w}}_{\gamma,k}(\tau_i) = SiPM(N_{\gamma,k}(\tau_i)) \tag{6.48}$$

$$R_k(\tau_i) = \frac{N'_\gamma(\tau_i)}{N^{\mathrm{w}}_{\gamma,k}(\tau_i)} \tag{6.49}$$

$$N_{\gamma,k+1}(\tau_i) = R_k(\tau_i) \cdot N_{\gamma,k}(\tau_i) \tag{6.50}$$

with $SiPM(N_{\gamma,k}(\tau))$ being the response of the SiPM simulation when using $N_{\gamma,k}(\tau)$ as input photon distribution. The exact incident times of the individual photons are equally distributed within one time bin. The iteration has to be stopped when a reasonable agreement of $N^{\mathrm{w}}_{\gamma,k}(\tau)$ and $N'_\gamma(\tau)$ is achieved. For the presented algorithm, the relative deviation of the integrals of $N^{\mathrm{w}}_{\gamma,k}(\tau)$ and $N'_\gamma(\tau)$ is calculated. It is compared to the mean fraction of released charge $\bar{f}$:

$$\frac{\int_{-\infty}^{\infty} N'_\gamma(\tau)\,\mathrm{d}\tau - \int_{-\infty}^{\infty} N^{\mathrm{w}}_{\gamma,k}(\tau)\,\mathrm{d}\tau}{\int_{-\infty}^{\infty} N'_\gamma(\tau)\,\mathrm{d}\tau} < 0.005 \cdot \bar{f} \quad . \tag{6.51}$$

The dependency of the stopping condition on the mean fraction of released charge ensures similar accuracy for the incident photon distribution independent of the photon flux. For

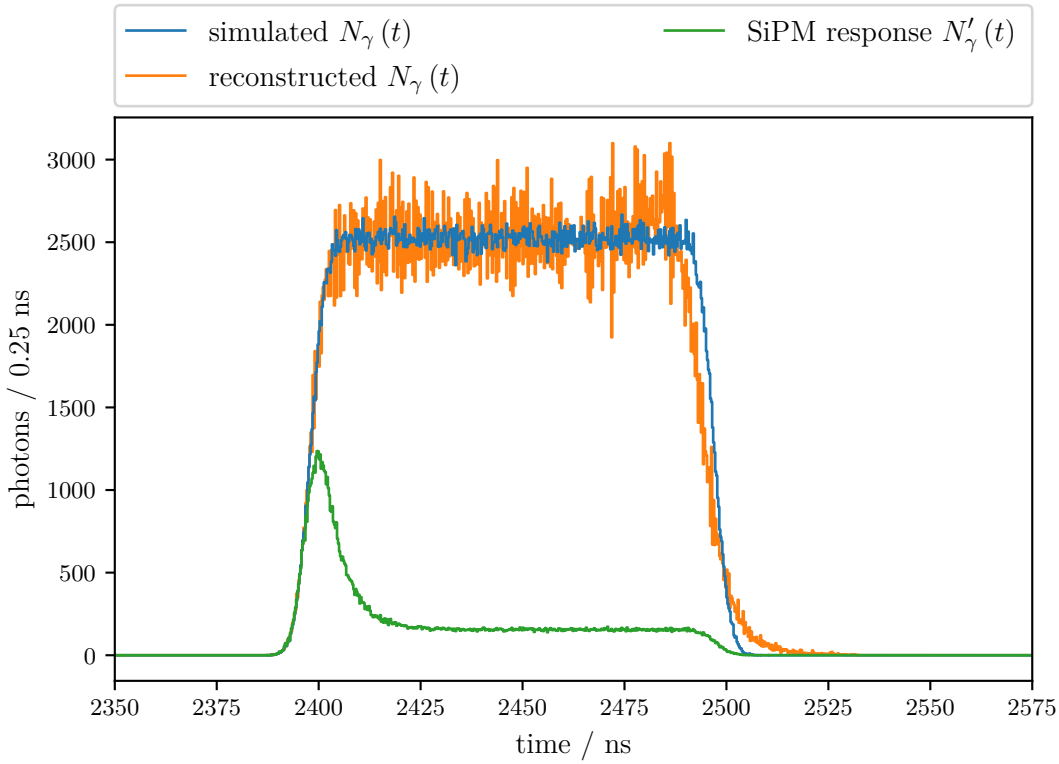

Figure 6.28: The originally simulated and reconstructed incident photon distributions for the same pulse as was shown in figure 6.27 with an incident number of photons $N_{\text{ref}} = 10^6$. The agreement between the two is very good though the reconstructed distribution has larger fluctuations. As before, the tail is longer in the case of the reconstruction. The distribution when taking into account the SiPM response differs significantly as expected.

high light fluxes, $\bar{f}$ gets low but large corrections need to be applied. Thus, a high accuracy on the output is needed.

An example of the initially simulated and reconstructed distributions is given in figure 6.28 together with the response of the SiPM for the same simulated pulse as was shown in figure 6.27. The raw SiPM response is significantly lower than the simulated distribution and not a good estimate for the incident photon distribution. Applying the reconstruction algorithm leads to a very good agreement between the originally simulated incident photon distribution and the reconstructed one. Only the tail deviates slightly as before, being longer for the reconstructed distribution. The total number of photons is lower by 0.6 % in the reconstructed distribution compared to one order of magnitude for the raw SiPM response as can be seen in figure 6.24 for $N_{\text{ref}} = 10^6$. This is a tremendous improvement of the linearity of the response.

6.8.4 Application on simulations

The algorithm for extending the linear dynamic range of SiPMs and reconstructing the number of incident photons in the highly non-linear regime can be applied on the simulations introduced in section 6.7.2. In figure 6.29 the resulting dynamic range is shown. For the

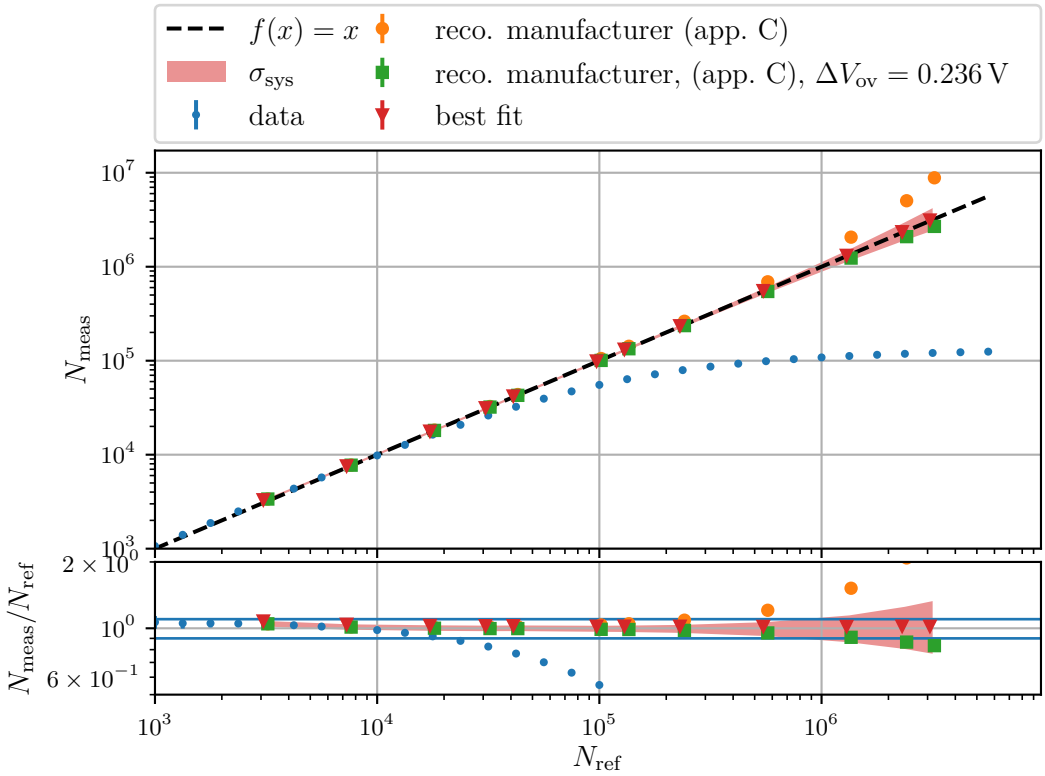

Figure 6.29: A simulation of the dynamic range and the reconstruction of the incident number of photons. The reconstruction is performed with three different sets of parameters. The *best fit* corresponds to the results from the double pulse measurement as given in table 6.3. These values were also used for the initial simulation. The systematic uncertainty on the *best fit* is indicated by a shaded band, for details see text. The values from the *manufacturer* used in the reconstruction are given in table C.1 in the appendix with $V_{\text{ov}} = 5\,\text{V}$. In an additional reconstruction, the overvoltage is shifted by 0.236 V to the one determined in the *best fit*. The horizontal lines in the bottom plot indicate 10 % deviation from linearity.

reconstruction using the same parameters as in the simulation, the linear dynamic range is extended over the whole range that was studied here up to 3×10^6 incident photons. This results in an improvement by at least two orders of magnitude compared to the uncorrected data where a deviation from linearity of 10 % is already reached at 2×10^4 incident photons.

The previous reconstruction involves perfect knowledge of the intrinsic parameters of the used SiPM. In applications where multiple SiPMs are operated, each needs to be characterized in detail to achieve this result. This might be possible in applications where only a few SiPMs are used but is not feasible when several hundred or even thousands of SiPMs are installed. This might be the case for example in IACTs where the cameras typically are equipped with more than 1000 pixels [64] or when a detector such as the SSD is read out with SiPMs. In these cases, a more feasible approach would be to use only the values given by the manufacturer.

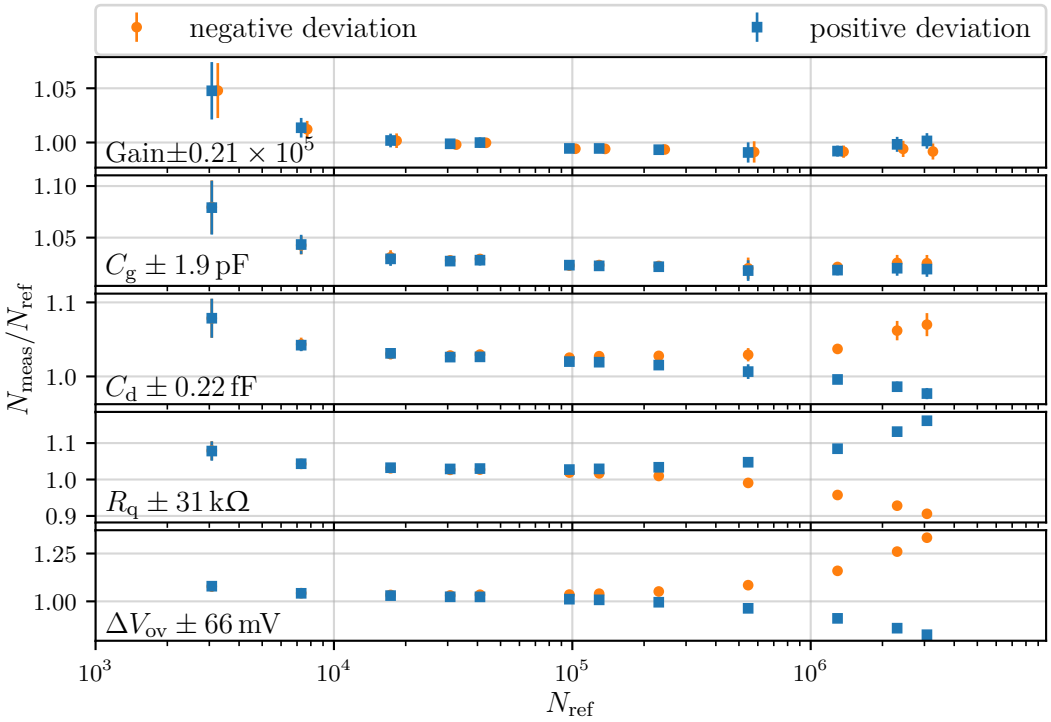

Figure 6.30: Impact of the uncertainties on the intrinsic parameters of the SiPM as determined in section 6.6.8. The *positive* (*negative*) deviation correspond to the results obtained when changing the corresponding parameter by one standard deviation in positive (negative) direction. Note the different y-scales.

In figure 6.29 a reconstruction using the values from table C.1 is given as well. It should be noted that for each new set of parameters also the time constants $\tau_\pm$ are calculated and the shape of the one p.e. pulse (eq. (6.37)) is changed accordingly. Its integral is always determined by the chosen gain. For these values, the reconstruction at a high number of incident photons clearly overestimates the true number. A deviation of 10 % from linearity is reached at 2×10^5 incident photons. The improvement compared to the uncorrected data is one order of magnitude which is still significant.

The measurement of the exact breakdown voltage as performed in section 6.2.1 is quite simple and could also be performed for a large number of SiPMs. Using the correct breakdown voltage significantly improves the reconstruction compared to using the one from the manufacturer as is indicated in figure 6.29. In this case, the deviation of 10 % from linearity is reached at 1.3×10^6 incident photons. The simple measurement of only the breakdown voltage of an individual sensor thus improves the reconstruction by a factor of 6 compared to the values from the manufacturer. This rather small effort might be worth to achieve a high dynamic range.

In order to understand the influence of the different intrinsic parameters, the reconstruction is repeated varying each one individually according to the uncertainties that have been estimated in table 6.3 on page 110. The resulting deviations from linearity are shown in figure 6.30. The highest impact originates from the uncertainty on the overvoltage reaching 30 % at 3×10^6 incident photons followed by the quenching resistor. The other parameters have only small influence below 10 % even at the highest photon fluxes. The total impact

of these uncertainties on the reconstruction by calculating their quadratic sum is shown as shaded band in figure 6.29 indicating the systematic uncertainty of the reconstruction. It should be noted that these values do not contain possible correlations between the different parameters. At 3×10^6 incident photons the systematic uncertainty is about 35 %. For small pulses below 10^4 incident photons, the deviation increases. This is an effect of the poor SNR, and improper treatment of the noise can lead to additional photons there. This is not further investigated here as it does not affect the results in the highly non-linear regime. A reconstruction for the small pulses is not necessary due to the still linear behavior.

The simulations indicate an excellent performance of the developed algorithm and promise to allow a significant extension of the linear dynamic range of SiPMs. The fact of the small impact of the variation of the intrinsic parameters also indicates a possibly good performance when being applied on data where knowledge is limited compared to the simulations.

6.8.5 Application on measurements

The same study as performed on simulations is done on the measurements presented in section 6.7.1. The measured dynamic range together with the reconstruction is shown in figure 6.31 and the propagated uncertainties from the best fit result of section 6.6.8 are given in figure 6.32. For the best fit results, a 10 % deviation from linearity is not reached within the studied range up to 4×10^6 incident photons compared to 1×10^4 for the raw data. An improvement of the linearity by more than two orders of magnitude is achieved. A slight systematic can be observed. In the range between 10^5 and 10^6 incident photons, an up to 5 % excess in the reconstructed photon number appears. For higher number of incident photons, the reconstructed number becomes too low with increasing deviation from linearity.

Reasons for this systematic can be of different kind. The most obvious is a systematic uncertainty in the best fit resulting in deviations of the intrinsic parameters. This could for example be an unknown series resistance due to bad connections. A small resistance of only 1 Ω would correspond to an uncertainty on the quenching resistor of 57.6 kΩ due to the large number of 57 600 cells. This is significantly larger than the statistical uncertainty of 31 kΩ. But, it should also be noted that a series resistor does not precisely have the same effect as a larger quenching resistor resulting in an additional uncertainty.

Another uncertainty originates from the precise shape of the single p.e. pulse used in the deconvolution process. The pulse might be distorted by the readout electronics. The tail has a very long time constant of 70 ns to 80 ns which should be well digitized by the electronics. The leading edge instead is very fast around 1 ns which could be differently shaped in the electronics. Nonetheless, due to the dominant tail, the precise shape of the leading edge is likely to have a small influence.

The total uncertainty originating from the fit to the double pulse measurement is 30 % at 4×10^6 incident photons and reduces to 12 % at 10^6. As was already seen in the simulation, the dominant contribution originates from the overvoltage.

Reconstructing the number of incident photons from the data given by the manufacturer results in a worse performance. The point of 10 % deviation from linearity is reached at around 10^5 corresponding to an improvement by one order of magnitude. Again, adding the information of the exact breakdown voltage can significantly improve the result by almost another factor of 10.

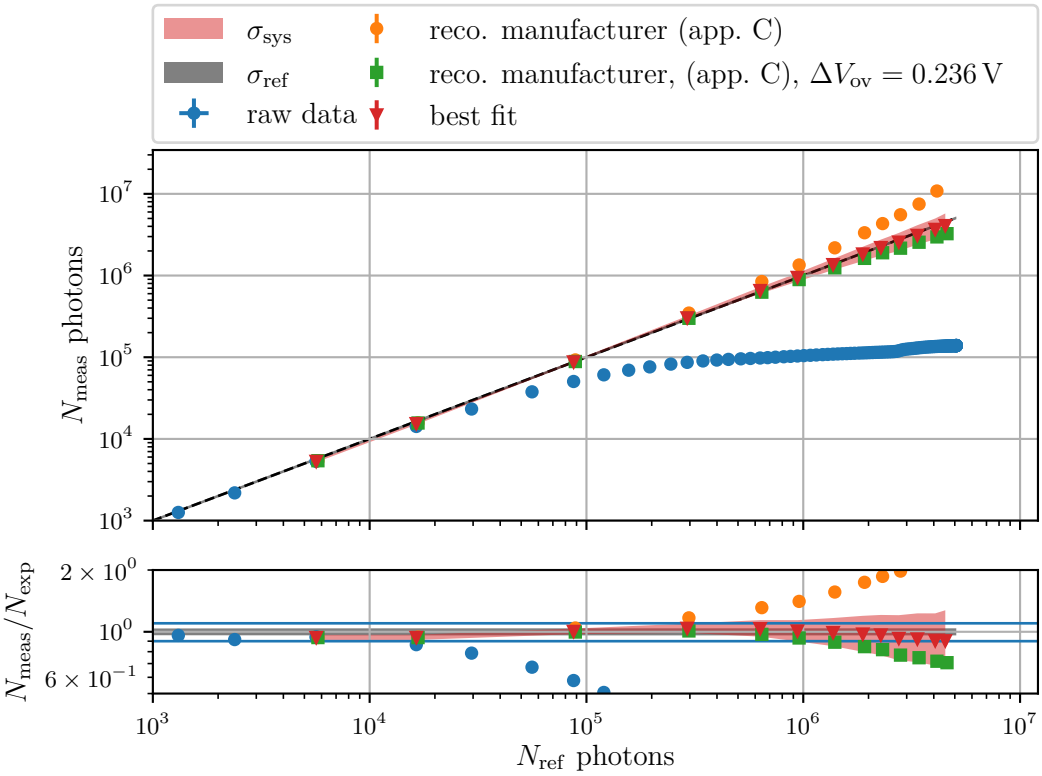

Figure 6.31: The reconstructed dynamic range for the measurement with 100 ns pulse width. Reconstructions were performed with the *best fit* values of section 6.6.8 and those given by the *manufacturer* with and without a shift in the overvoltage corresponding to the best fit. The black shaded area corresponds to the uncertainty originating from the determination of the reference number of photons. The red shaded area indicates the systematic uncertainty from the *best fit* results. The blue horizontal lines correspond to 10 % deviation from linearity.

Results achieved from the shorter 40 ns pulse are presented in detail in appendix G. It indicates similar results of an improvement in the linearity by at least two orders of magnitude compared to the raw signals. This is an important observation as a characteristic feature of this algorithm is its independency of the incident photon time distribution. The similar results for a pulse which is shorter than the longest recovery time of the SiPM and a longer one indicate that this goal is achieved.

6.8.6 Remarks

The precise manufacturing of SiPMs and the good knowledge of the evolution of the voltages across the SiPM cells even in regimes of high photon flux allow for an accurate simulation of its response. Exploiting this fact enables the extension of the linear dynamic range by two orders magnitude. SiPMs become a prime candidate in applications where a high dynamic range is needed from single p.e. resolution up to even millions of photons within some ten ns depending on the number of cells.

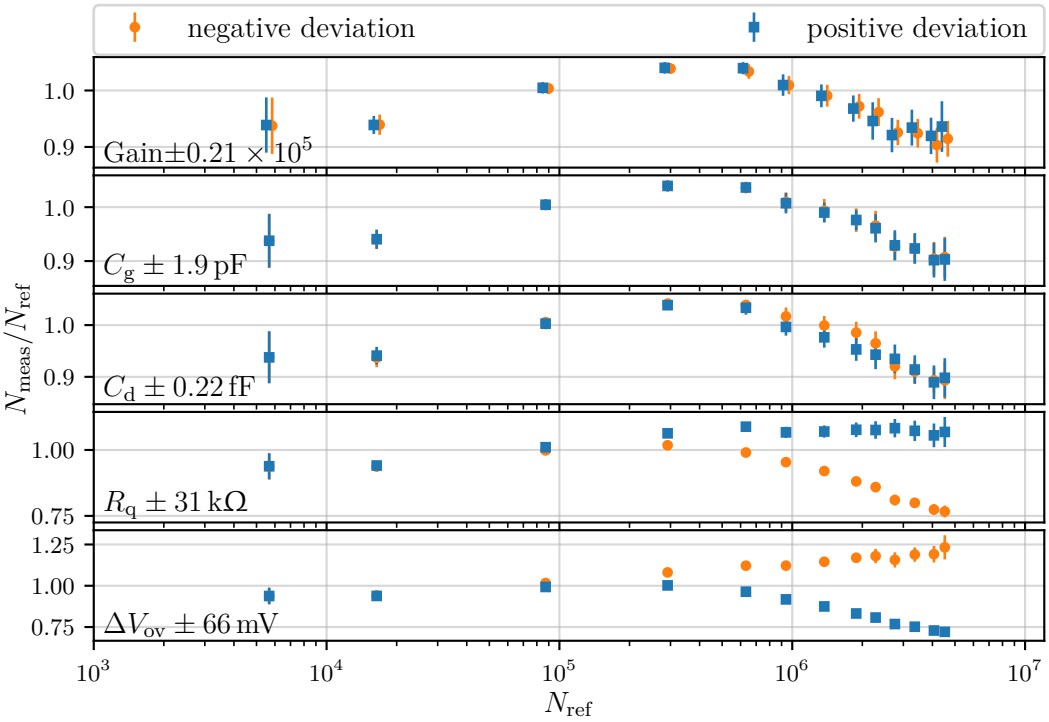

Figure 6.32: The impact of the uncertainties of the intrinsic SiPM parameters on the reconstructed number of incident photons. The *positive* (*negative*) deviation correspond to the results obtained when changing the corresponding parameter by one standard deviation in positive (negative) direction. Note the different y-scales.

Some questions were not addressed in the study here. The laboratory setup ensured a homogeneous light distribution on the SiPM. This must not necessarily be the case in physics applications where often optical elements are used creating inhomogeneous light distributions over the SiPM. Detailed simulations of the optical components can easily address this issue and be included in the reconstruction algorithm. Temperature dependencies of the intrinsic parameters might also introduce additional uncertainties. Especially the quenching resistor is known to have a temperature dependent resistance [185]. In old devices, values of 0.6 %/K were found [185] leading to a significant uncertainty when being exposed to typical environmental conditions. In newer devices the dependency has been reduced by a factor of 5 [194]. This reduces the systematic changes to the same order as the uncertainties studied here making the application of this algorithm to measurements realistic even without accounting for temperature variations.

Chapter 7

An SiPM based optical module for the SSD

The excellent performance of SiPMs has been proven in many lab measurements and also in a variety of physics applications, as has been presented in chapter 6. So far, no UHECR experiment exploited their advantages for making improvements to the study of cosmic ray air showers. In this chapter, an optical module will be introduced which was developed as an alternative for the conventional PMT in the SSD. It was studied in detail in laboratory measurements as well as in prototype SSDs deployed in the Argentinean Pampas.

SiPMs, in contrast to PMTs, offer an intrinsic resolution of the single p.e. signal that allows for photon counting. They do not suffer from aging effects and can be stably operated over many years [195]. These two characteristics allow for long term monitoring of the performance of the SSD. Changes of its light yield due to temperature variations can be studied as well as the aging of the scintillators and fibers. Their robustness and low operating voltage make them ideally suited for the application in the remotely deployed SSDs in the harsh environment of the Argentinean Pampas.

Besides two SiPMs of type Hamamatsu S13360-6025PE [130], the optical module hosts also the bias supply, digital control and pre-amplifiers. In the scope of this thesis, optical light guides have been developed to ensure optimal optical coupling to the cookie with the WLS fibers. The performance of the optical module has been characterized in various laboratory measurements. Three modules have been installed in prototype detectors in the Argentinean Pampas allowing the detection of cosmic ray induced air showers.

The optical module and partial results of the measurements have already been released in detail in [196]. Additional details will be given here. Some information can also be found in the publications [190, 197, 198]. The electronics of the module have been developed in the scope of another thesis [155]. Only a brief overview will be given here. The interested reader is referred to the other thesis for more information.

7.1 Requirements

The optical module was designed to be installed in the SSD. As the SSD was originally meant to be read out with a PMT, the optical module had to satisfy some requirements. Additional constraints arose from the readout electronics used at the Pierre Auger Observatory as well

as requirements set by the Pierre Auger Collaboration on the performance of the SSD. The following specifications had to be satisfied:

1. The mechanical and optical design should allow for a replacement of the PMT with as little modifications to the SSD as possible.
2. The output signals should be recorded using the UUB. Slight changes such as the gain of the amplifiers on the UUB were possible.
3. The signal measured for one Minimum Ionizing Particle (MIP) going through the scintillator should be well distinguishable from background.
4. The dynamic range should suffice to measure at least a signal of 12 000 MIPs.
5. A single p.e. resolution should be achieved to monitor the stability of the performance of the SiPMs.
6. The power consumption should be less than 500 mW.

In the following sections, the design of the optical module as well as its performance in the prototype SSDs will be introduced. As the author's work was related to the optical components of the module and not the electronics, his work was affected mainly by the requirements 1, 3 and 4.

7.2 Overview

Two SiPMs of type Hamamatsu S13360-6025PE [130] were chosen. Each of them offers an effective area of $6 \times 6\,\mathrm{mm}^2$ with a cell size of 25 µm, resulting in a total of 57 600 cells. The large number of $2 \times 57\,600$ cells results in a wide dynamic range and they offer a high peak photon sensitivity of 25 % at only 1 % crosstalk and negligible afterpulsing. The low gain of 7×10^5 makes a careful design of the pre-amplifiers necessary in order to achieve a good signal to noise ratio over the whole dynamic range from a single p.e. up to a breakdown of all cells.

Two SiPMs were chosen in order to achieve a sensitive area that is in reach of that of conventional PMTs. With $72\,\mathrm{mm}^2$, it is still rather small but, as the DCR scales with the sensitive area, the number of SiPMs was kept as low as possible. Solid PMMA light guides optimized for the application with WLS fibers are glued onto the SiPMs to increase the sensitive area.

A schematic overview and a picture of the optical module are shown in figures 7.1 and 7.2. The SiPM module consists of two PCBs. A round PCB hosts the two SiPMs with light guides and a temperature sensor. It is connected to the rectangular main PCB. It holds the Hamamatsu integrated circuit C11204-02 [150] for providing the SiPM bias voltage, slow control, pre-amplifiers, Universal Serial Bus (USB) connector for power and communication and three signal connectors. This mechanical layout with a round PCB at the front allows for easy replacement of conventional PMTs. For application in the SSD, the only modifications necessary affect the arrangement of the WLS fibers and the flange with cable feed throughs for closing the detector. Instead of one bundle, two bundles placed in front of the light guides are needed and a total of four cables needs to be guided out of the detector. This also means that an SSD built for the PMT cannot be equipped with the optical module presented here but the SSD has to be slightly modified during construction. The design of

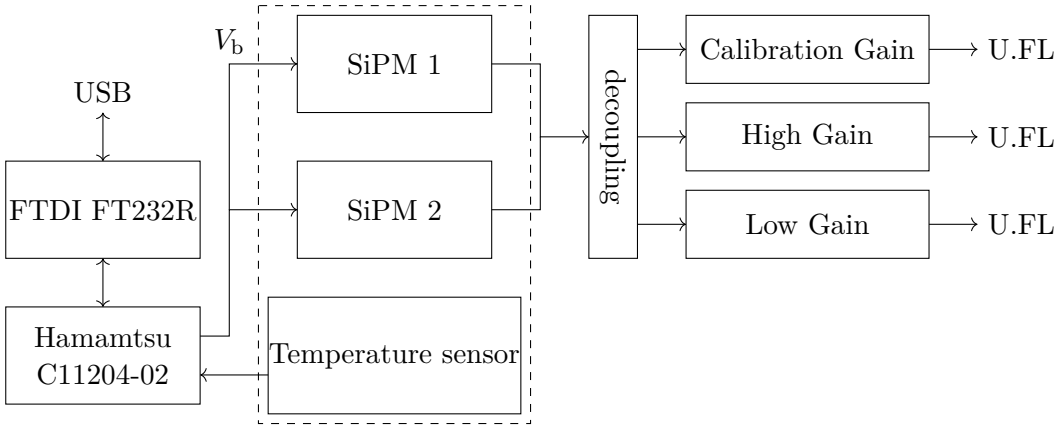

Figure 7.1: Schematic of the SiPM module. Power is supplied through a USB connection. A Hamamatsu integrated circuit C11204-02 generates the bias voltage for the two SiPMs corrected for the ambient temperature. The signal from the SiPMs is summed up, decoupled and split into three independent gain stages. Adopted from [196].

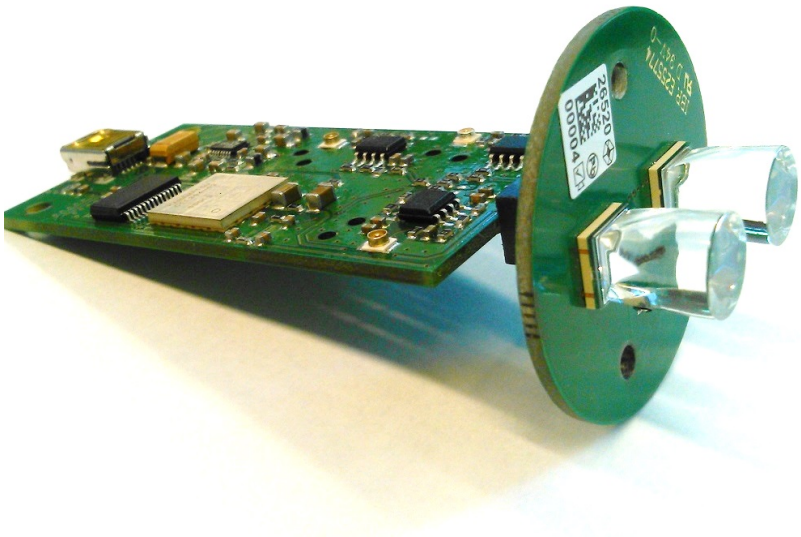

Figure 7.2: Picture of the SiPM module. It consists of two PCBs. The round PCB hosts the SiPMs, the light guides and the temperature sensor. The rectangular PCB is equipped with slow control, pre-amplifiers, bias voltage supply, USB and U.FL connectors. Taken from [196].

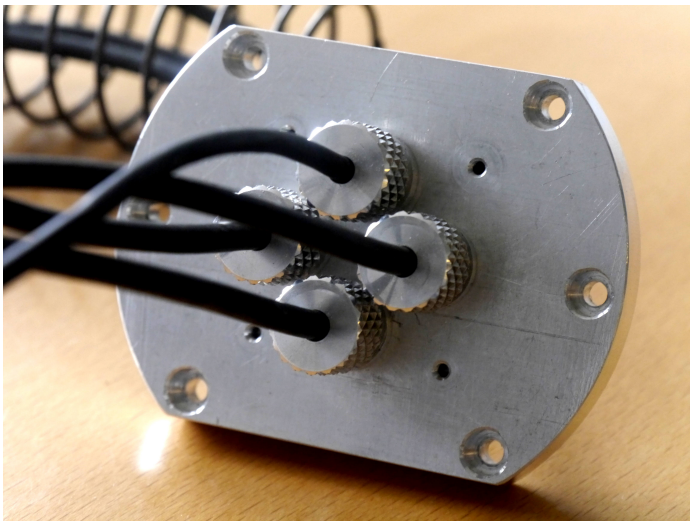

Figure 7.3: The flange designed for the optical module. Four feedthroughs allow to supply one USB and three signal cables.

an SiPM based optical module that can be used in a PMT SSD would not allow to meet other specifications such as dynamic range or single p.e. resolution. The module presented here therefore is a compromise of satisfying different requirements.

Details on the electronics and the optical design of the module will be given in the following sections.

7.3 Mechanical layout

The size of the optical module is chosen such that it can be hold by a PVC tube that is pushed into the aluminum tube of the SSD hosting the PMT in the baseline configuration. The two SiPMs are placed rotationally symmetric meaning that rotating the optical module by 180° exactly exchanges their positions. Three asymmetrically placed holes in the circular front PCB allow for a correct positioning in front of the cookie.

The flange for closing the aluminum tube of the SSD that hosts the optical module had to be modified in order to allow operation with the optical module. For power supply and slow control, one USB cable is needed and three signal cables must be connected to the UUB. A dedicated flange providing the feedthroughs for all four cables was designed by the Pierre Auger Collaboration. It is shown in figure 7.3.

7.4 Electronics

The electronics of the SiPM module had been developed in the scope of another thesis [155]. Only a brief overview necessary for the understanding of the following analyses will therefore be given here. The interested reader is referred to the aforementioned thesis for more details.

7.4.1 SiPM bias voltage supply

The bias voltage for the SiPMs is generated by a commercial integrated circuit of type Hamamatsu C11204-02 [150]. It is specifically designed for the application with SiPMs. The integrated circuit is powered by the 5 V of the USB bus and generates the bias voltage for the SiPMs of around 57 V. The temperature stability of the generated output voltage has been measured to be approximately 1.3 mV/K from −30 °C to 50 °C [196].

The output voltage is programmable via an on-chip Universal Asynchronous Receiver/Transmitter (UART) bus with a precision of 1.8 mV. The integrated circuit allows for a regulation of the output voltage according to a second order polynomial with respect to the ambient temperature which is measured by the temperature sensor on the SiPM PCB. This function corrects for the intrinsic temperature dependence of the SiPM breakdown voltage. The parameters of the polynomial can be programmed via UART and the output voltage is automatically corrected. This correction is always switched on during standard operation.

The bias voltage supply allows for monitoring of the applied voltage with a resolution of 1.8 mV and of the current drawn by the SiPMs with a resolution of 5 µA. The temperature can be read out with a resolution of 35 mK.

7.4.2 Pre-amplifiers

A proper design of the pre-amplifiers is crucial to achieve a good SNR for small signals down to a single p.e. up to a simultaneous breakdown of all cells. The dynamic range of 2 V and resolution of 12 bit of the UUB channels needs to be taken into account. All signals should be mapped on this range and be resolvable with the given resolution. These considerations led to the implementation of three channels with different gain (cf. fig. 7.1):

1. The *Calibration Gain (CG) channel* allows for resolution of the single p.e. signal. The channel saturates at ~ 3 MIP to allow for a calibration of the MIP signal in terms of p.e..

2. The *High Gain (HG) channel* is designed for physics calibration in terms of MIP. The lowest resolvable signal is $\lesssim 1$ MIP and saturation sets in at a few hundred MIP.

3. The *Low Gain (LG) channel* overlaps with the high gain channel allowing for cross calibration. It is designed for the detection of signals up to a breakdown of all cells.

The pre-amplifiers are installed on the optical module to be placed as close as possible to the SiPMs reducing pick-up noise. The UUB input channels have to be slightly modified to allow for reading out the optical module. The standard channels have amplifications of 30 dB, −12 dB and 0 dB and all need to be changed to 0 dB. This involves only replacing a few resistors and can easily be done.

7.5 Optics

The optical light guides designed in the scope of this thesis are optimized for the specific application in the SSD. This affects for example the specific WLS fibers being used, their number and arrangement as well as constraints on the homogeneity of the response and the targeted light yield.

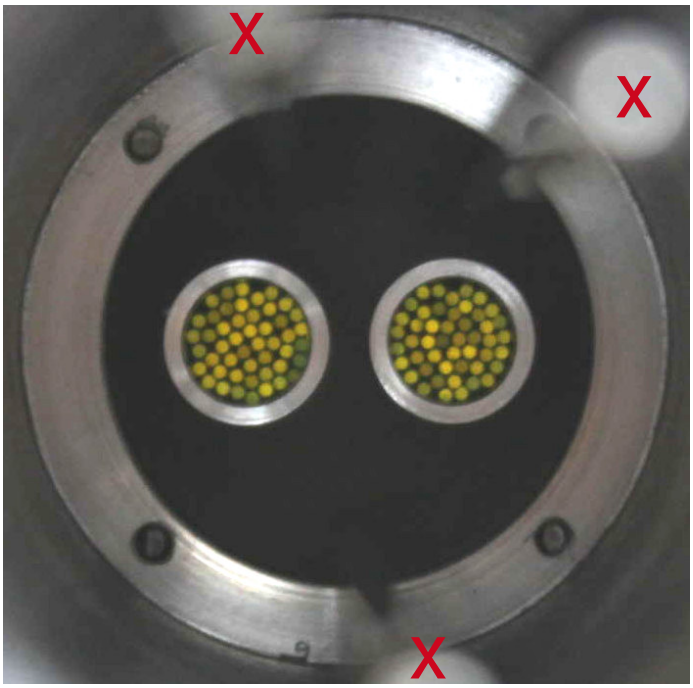

Figure 7.4: A photo of the cookie modified for the SiPM based optical module. Each fiber bundle is surrounded by a reflective aluminum ring. The three blurred pins marked by an x allow for a precise positioning of the optical module in front of the fiber bundles. Taken from [196].

For this application it was not necessary to achieve the optimal light guide but one that allows to satisfy all requirements. Given the short development time a variety of tests could only be carried out qualitatively, for example by comparing to the performance of a PMT SSD. It will be shown that the chosen light guides allow to achieve at least similar optical performance as the PMT.

Partial results presented in this section have already been published in [196]. All simulations and measurements shown here were performed by the author of this thesis and additional information is given here. No text is shared with that publication.

7.5.1 Modifications of the SSD

The optical design of the module was driven by the constraint to reduce the modifications of the SSD. Small modifications had to be made in order to distribute the light of the WLS fibers on the SiPMs. The fibers are not arranged in a single fiber bundle but in, two reflecting the arrangement of the SiPMs. Each of these two fiber bundles contains 48 fibers corresponding to one detector half (cf. fig. 5.3b & 5.3c on page 53). In figure 7.4, the modified cookie for the optical module is shown. Given the diameter of 1 mm per fiber, the diameter of one bundle reaches 8 mm (or an area of $\sim 50\,\mathrm{mm}^2$) which is more than the area of one SiPM of $36\,\mathrm{mm}^2$.

The fiber bundles are fixed in the cookie with Saint-Gobain BC-600 optical cement [199] and a 7.5 mm thick PMMA window of 9 mm diameter protects their ends. The window is surrounded by a reflective aluminum ring. It ensures that the light exiting the fibers is not spread over a large area but guided to the end of the window.

The light guides that can be seen on the module in figure 7.2 are optimized for the application with this design. The optimization process will be introduced in the next sections.

Three holes in the cookie allow to place aluminum pins which are the counter parts of the holes in the circular SiPM PCB described in section 7.3. These ensure a precise positioning of the light guides in front of the fiber bundles.

7.5.2 Design goals for the light guides

The design of the solid PMMA light guides depends on the size and shape of the entrance and the exit windows and on the angular distribution of the incident light. For the application in the modified SSD, they have to transform from a 9 mm round entrance window to a 6 mm edge length square. The angular distribution of the incident light is determined by the characteristics of the WLS fiber and the refractive indices of the surrounding media.

The response of the detector for through going particles should be homogeneous over the whole area. The transmission efficiency of the light guides should therefore be independent of the position of the fiber in the bundle. As described in section 6.7, the dynamic range of the SiPM depends on the number of illuminated cells. Therefore, the light distribution on the SiPM should be homogeneous to distribute the light over all cells.

7.5.3 Overview of the design of the light guides

The WLS fibers emit light in the green part of the spectrum. The light guides are made of PMMA, as it ensures good transmission in this wavelength region. It also allows for an easy production through milling or casting and, with a polished surface and without an envelope, provides total reflection. In order to transform from a round entrance window to a squared exit one, the shape of the light guides is given by the intersection of a round and squared geometrical body. For the round part, this can for example be a cylinder or truncated cone while the squared part can be given by a truncated pyramid with or without parabolic surfaces.

Surfaces described by tilted parabolas follow the shape of a Winston cone [200]. The squared pyramid with Winston shaped surfaces is referred to as *Winston pyramid* for the rest of this document. A Winston cone is a non-imaging light collector which perfectly transmits light with incident angles below a cut-off angle $\theta_{\max}$. Details on the construction of a Winston cone are given in appendix H.

Sketches of the resulting possible geometries are shown in figure 7.5. These geometries can be varied in length or cut-off angle, respectively. Their performance will be studied in detail in the next sections.

7.6 Simulation of the performance of the light guides

The study of different light guide geometries is based on simulations to achieve a good understanding of their performance in terms of light yield and homogeneity. In a second step, prototypes of light guides have been produced by a dental technician [201] and their light yield will be measured in a dedicated setup.

The simulations are implemented in Zemax Optical Studio 12 [202]. It allows for ray tracing of photons through media with varying refraction index and absorption length obeying standard laws of optics including scattering, reflection and transmission on surfaces.

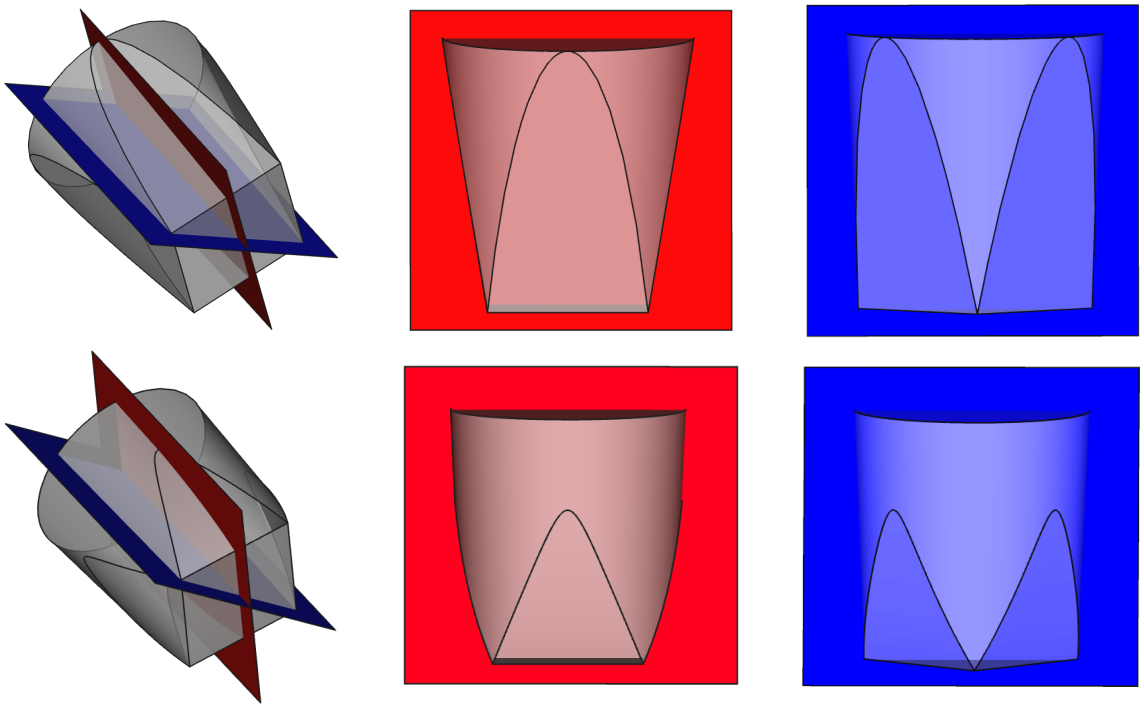

Figure 7.5: Example geometries of the light guides. The geometries to be studied are based on these two principle designs. *Top:* Three different perspectives of a ligh guides consisting of an intersection of a regular pyramid with a cone with a length of 1 cm. *Bottom:* The same perspectives for a light guide consisting of the intersection of a Winston pyramid and a cone with a cut-off angle of 39°. The parabolic shape of the Winston pyramid is well visible. Taken from [196]

Diffraction is not simulated but not necessary here, because all lengths are significantly above the wavelength of the optical photons.

For an optimization of the design of the light guides, one needs to know the spatial and angular distributions of the entering light. All components from the light exiting the fiber through the cookie, light guide and to the SiPM are therefore implemented in the simulation. The consideration of the optical effects of the SiPM is necessary due to the angular dependency of reflections at its coating. An overview of the implementation is shown in figure 7.6.

The cookie

Only one of the two fiber bundles is simulated, as their distance allows to assume them to be optically independent. A schematic of the cookie is shown in figure 7.7. It consists of a cylindrical piece of PMMA with a radius of 12.5 mm and a length of 12 mm. At the center, a 5 mm long cylinder with 4 mm radius made of BC600 optical cement is inserted. It hosts the light sources (described in the next section) positioned 0.5 mm away from the edge of the cookie. It is followed by a conical section that changes from 5 mm to 4.5 mm radius which is filled with BC600 optical cement. It connects to a 5.5 mm thick PMMA window of which 0.5 mm stick out of the cookie. The PMMA window and the conical section filled with optical cement are surrounded by a reflective coating. It represents the aluminum ring

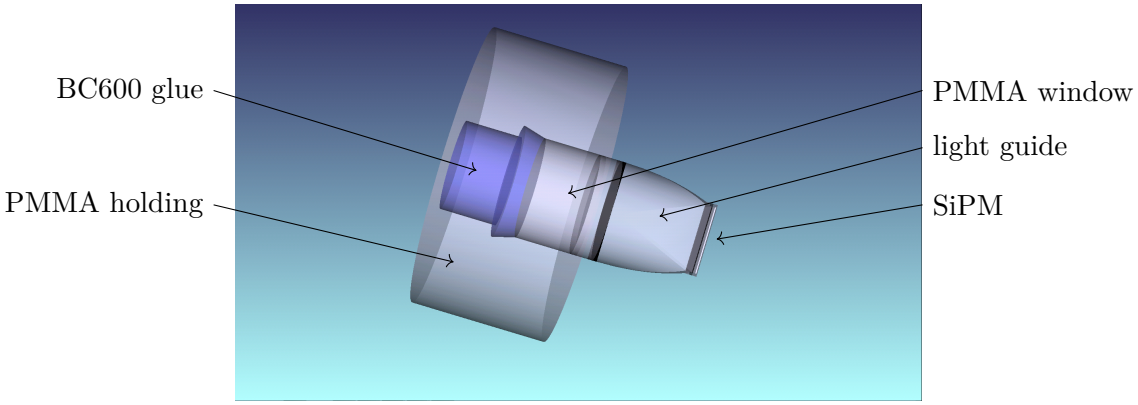

Figure 7.6: The basic layout of the simulation. All optical components from the light exiting the fiber to the SiPM are simulated. Only one fiber bundle is simulated. The distance between the two fiber bundles is large enough to assume them to be optically independent. Modified from [196].

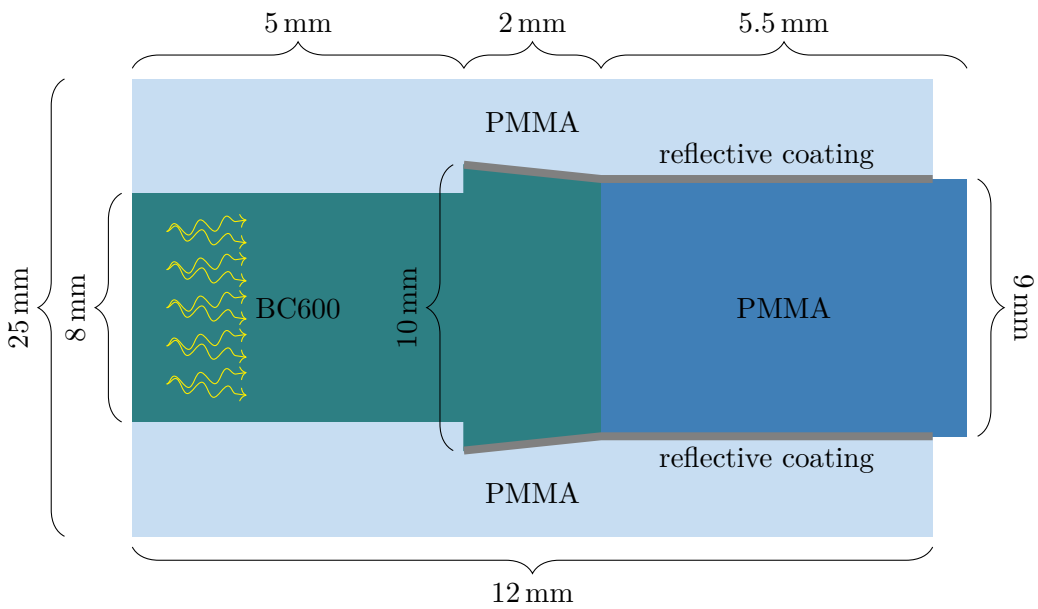

Figure 7.7: Sketch of the setup of the cookie. Light is emitted by the sources inside the BC600 optical cement on the left. At the right end, the light guide can be connected. The reflective coating represents the aluminum ring around the PMMA window. Not to scale.

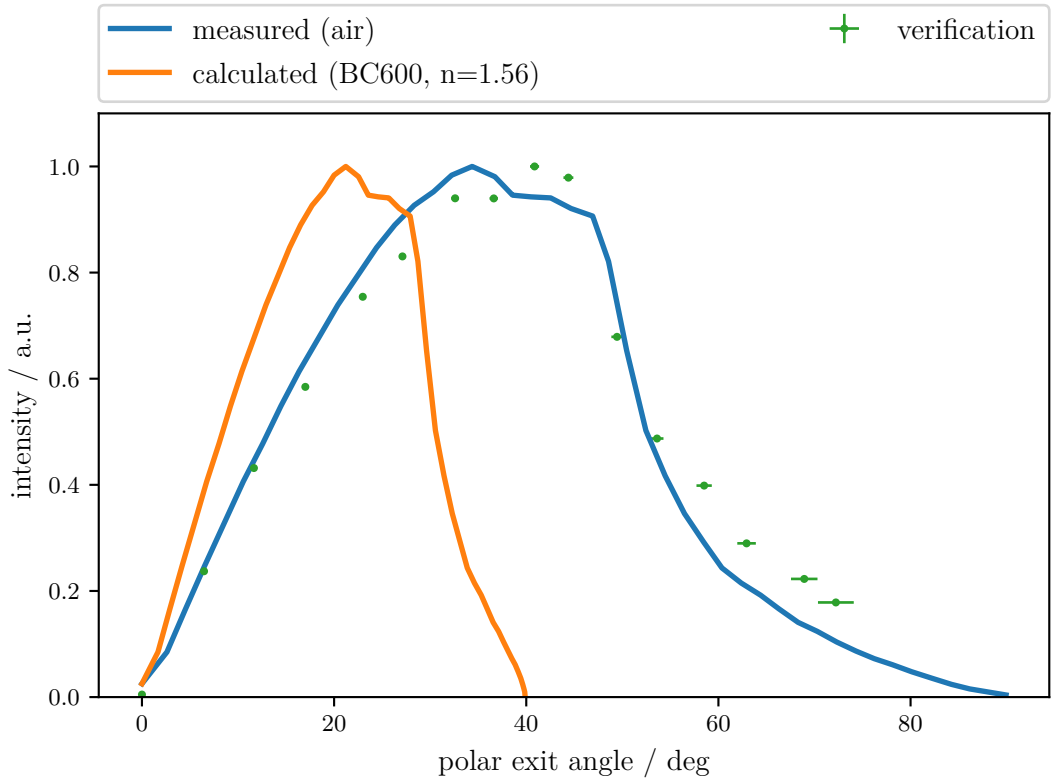

Figure 7.8: Angular distribution of the light output of an optical fiber in air. The measurements have been performed in the scope of a thesis [203]. The verification has been performed by the author. The differences might arise from systematic uncertainties of the measurement, for details see text. The orange line shows the distribution for a transition into BC600 optical cement calculated from the measurement in air using Snell's law.

introduced in the previous section. The characteristics of these reflections can be varied, for example in the amount of diffusive and specular reflection. At the end of the cookie window, the light guide will be placed.

The WLS fibers

The optical properties of the WLS fibers are not physically implemented into the simulation. Each fiber is instead represented by a round light source emitting light at a wavelength of 520 nm, corresponding to the peak of the emission of the WLS fiber after > 1 m absorption. The angular distribution of the emitted light given in figure 7.8 was measured in the lab in the scope of a previous thesis [203] and verified by the author of this thesis.

The measurement was performed in a dark room with the fiber end illuminated by a ultraviolett (UV) LED. The fiber had a length of about 15 cm and its exit window was polished. The light output was photographed with a commercial camera from different angles. From the images, the light intensity could be determined.

The measurement in the previous thesis was performed more rigorously, wherefore those results were taken for the further analyses. The verification measurement shows a similar

behavior. Differences might arise from systematic differences in the measurement, especially usage of different fibers of the same type. The deviations of the two measurements thus give an impression of the systematic uncertainty.

A difference between this measurement and the WLS fibers in the SSD is the surrounding medium. In the measurement, an optical transition from the WLS fiber into air ($n \approx 1$) occurred. In the cookie instead, a transition into BC600 optical cement ($n = 1.56$) [199] is realized. The angles from the measurement therefore have been transformed according to Snell's law.

This angular distribution is used in the simulation for the production of the initial photons. To simplify the simulation, a total of only 37 light sources of 1 mm diameter arranged on a hexapolar grid represents the fiber bundle compared to the correct number of 48 fibers[1]. The spacing between the light sources was chosen such that they fill the whole available space of 8 mm diameter in the cookie.

The light guide

The geometry of the light guide will be varied throughout the studies performed in this chapter. It is made of PMMA and directly attached to the cookie window. The exit window connects directly to the SiPM. All transitions are assumed to be perfect which means that no airgap in between is assumed. This corresponds to an ideal gluing of the light guide to the SiPM where the glue has the same refractive index as PMMA, is infinitesimally thin and does not contain any air bubbles.

The SiPM

The SiPM is composed of two layers. The bottom layer is the silicon with a refractive index of $n = 4.03$ at a wavelength of 520 nm [156]. It is protected by the second layer, made of epoxy resin with $n = 1.55$. The resin is in direct contact with the light guide.

In order to be considered detected, a photon needs to enter into the silicon. Only then it might trigger an avalanche. Effects like the fill factor (cf. sec. 6.2.3) are neglected, as it only influences the absolute number of detected photons but not the relative change between different types of light guides.

The correct implementation of the optical characteristics of the SiPM is crucial as it influences the angular dependency of the PDE. The angular distribution of the light exiting from the light guide might depend on its geometry and can therefore significantly influence the final result.

7.6.1 The geometries of the light guides

As mentioned earlier, the light guides are composed of a round and a quadratic part. In total, four different geometries have been considered:

1. Quadratic part: Winston pyramid; round part: cylinder
2. Quadratic part: Winston pyramid; round part: cone
3. Quadratic part: regular pyramid; round part: cylinder

[1] The arrangement of 37 light sources on a hexapolar grid was already predefined in the Zemax software and therefore allowed for a very easy implementation.

4. Quadratic part: regular pyramid; round part: cone

All these geometries can still be varied in their length or cut-off angle, respectively, and the sizes of the entrance and exit windows. The specific geometries are referred to by their length in the case of the regular pyramid or the cut-off angle for the Winston pyramid.

As is shown in appendix H, the size of the entrance window of the Winston pyramid is fixed if its cut-off angle and exit window size are fixed. Here, the light guide will be truncated if the parameter combinations yield a too large entrance window exceeding the size of the PMMA window of the cookie. This procedure does not preserve the cut-off angle meaning that light guides with smaller nominal cut-off angles might still perform better. For the rest of this section the cut-off angle should therefore rather be seen as a definition of a specific geometry than as a physically meaningful quantity.

The maximum allowed cut-off angle for an ideal Winston cone can be derived from the sizes of the entrance and exit windows with radii of $R = 4.7\,\mathrm{mm}$ and $r = 3\,\mathrm{mm}$:

$$\theta_{\max} = \arcsin\left(\frac{r}{R}\right) = 39.7^\circ \tag{7.1}$$

The slightly too large entrance window radius compared to the PMMA window of the cookie allows for some uncertainty in the placement of the light guide. Comparing with figure 7.8, this is the maximum angle of the light exiting the WLS fiber and for an ideal Winston cone all light is guided onto the SiPM. It should be noted that this geometry results in only a circle of 3 mm radius on the SiPM being illuminated. This is in contradiction with the goal of illuminating all SiPM cells homogeneously and therefore not feasible here.

In the simulation, the length or cut-off angle of the light guides are varied. Their performance is studied with respect to the transmission efficiency, the homogeneity of the light distribution on the SiPM and the efficiency for different positions of the fibers in the bundle. The effect of a varied size of the entrance window is studied as well.

7.6.2 Simulation of the transmission efficiency

The transmission efficiency is simulated with all 37 fibers emitting the same amount of light for different light guide geometries. The result is given in figure 7.9. The transmission efficiency is given for a photon penetrating the silicon layer. In the case of ideal surfaces (blue circles, orange squares), the transmission efficiency is between 78 % to 79 %. Only the very short light guide of 0.4 cm length shows a significant deviation compared to the others.

The worse performance of the very short light guide is expected, as for these light guides the angle between the incident photon and the surface exceeds the maximum angle for total reflection. Parts of the light are therefore transmitted out of the light guide. No difference between Winston and regular pyramids is apparent. These small differences between the different geometries result from the simulation of ideal surfaces. Even multiple reflected rays still reach the SiPM and light is only lost at optical transitions.

As a second step, a non-perfect polishing of the surfaces was assumed. It would result in a diffuse scattering of the incident photon instead of specular reflection. Here, 5 % of the photons is assumed to be Lambertian scattered when hitting a surface[2]. As expected, the transmission efficiency reduces by $\approx 5\,\%$. For the Winston pyramids, the result is almost independent of the cut-off angle with a slight improvement for large cut-off angles.

[2]Lambertian scattering is also described as perfect diffusive reflection. For a Lambertian radiator, the apparent brightness is independent of the angle of view.

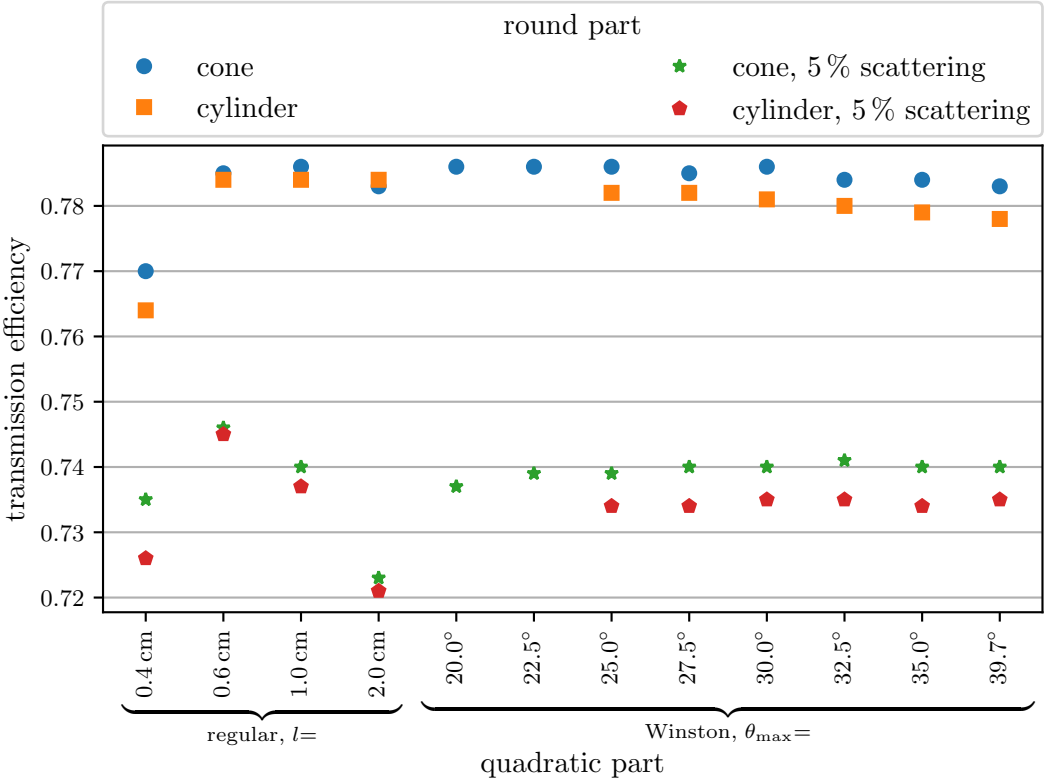

Figure 7.9: Simulated transmission efficiencies for the light guides. The light has to reach the silicon of the SiPM in order to be considered transmitted. The surface of the light guide has been simulated being ideal and with 5 % of the rays being scattered Lambertian. For four geometries a simulation with a cylinder was not possible due to issues with the Zemax software. Modified from [196].

For regular pyramids, short light guides perform significantly better than longer ones. The only exception is, as before, the shortest 0.4 cm long light guide. For long light guides, on average more reflections occur. This increases the probability of a random scattering leading to a loss of the photon. For Winston pyramids this effect is not as strong because the parabolic shape results in only one reflection before reaching the SiPM independent of the particular position on the surface.

As expected, a slightly better performance can be seen for light guides composed of a cone instead of a cylinder. All following simulations will therefore be performed with a cone as the round part.

A difficulty in the simulation is the contribution of local imperfections in the shape of the light guides which might result from the polishing. These affect only small parts of the surface making it a negligible effect compared to scattering. It is therefore not investigated here.

In the following sections, two light guides promising best performance, according to the previous findings, will be studied in more detail:

1. The intersection of a regular pyramid with a cone of 1 cm length: It shows a good transmission efficiency. At the same time it is significantly longer than the badly

performing light guide of 0.4 cm length. This margin accounts for possible systematic uncertainties in the simulation. It is named *regular-shaped light guide* in the following.

2. The intersection of a Winston pyramid with a cone and a cut-off angle of $\theta_{\max} = 39°$[3]: It has a good transmission efficiency being only negligibly lower than for the best light guide with $\theta_{\max} = 32.5°$. The light guide with $\theta_{\max} = 39.7°$ is the shortest possible light guide with Winston surfaces and is thus less affected by non-perfect polishing than the other light guides as was discussed in the previous paragraphs. Good performance also in the case of significant scattering can therefore be expected. It will be referred to as *Winston-shaped light guide.*

These light guides have already been shown in figure 7.5.

Photon detection efficiency of the full module

In the simulation no SiPM effects except its optical properties are implemented. The SiPM of type Hamamatsu S13360-6025PE has a PDE of $\sim 23\,\%$ at a wavelength of 520 nm according to the datasheet [130]. From the refractive indices of the protective resin and the silicon, a transmission efficiency from air into the silicon of $\sim 75\,\%$ for vertical incident light can be calculated. A photon that reaches the silicon therefore has a probability of 31 % of triggering an avalanche. According to the simulation, about 74 % of the photons are transmitted from the fibers to silicon. The total photon detection efficiency of the full optical system including the cookie and the light guide is thus given by $0.74 \times 0.31 = 23\,\%$. This is by chance similar to the PDE of the SiPM. Compared to the quantum efficiency of a conventional PMT of 13 % at 520 nm this is better by 75 %.

7.6.3 Dependency on entrance window radius

For the previous analysis, an entrance window size of 4.7 mm has been chosen to allow for some misalignment of the light guide in front of the cookie. The effect of a variation in the size of the entrance window and a misalignment is shown in figure 7.10. A misalignment might result from uncertainties in the mechanical production of the optical module or the cookie and some tolerance will be useful. An increase in the radius of the entrance window leads to a possible misalignment of the same magnitude without significant light losses. Increasing the entrance window size too much leads to a reduction of the transmission efficiency, even without a misalignment. Therefore, a choice of $R = 4.7$ mm is a good compromise between a good transmission efficiency and allowing for a small misalignment. Both light guide geometries show the same performance.

7.6.4 Dependency on fiber position

The homogeneity of the detector response depends on the variation of the transmission efficiency for different positions of the fiber in the bundle. This simulation is performed with only one fiber end emitting light and scanning its position. The results for the two previously introduced light guides are shown in figure 7.11. Both light guides show very similar performance with no strong dependency on the position of the fiber. The efficiency

[3] For $\theta_{\max} = 39.7°$ as shown in figure 7.9, the size of the entrance window cannot be increased anymore. A slightly smaller angle of $\theta_{\max} = 39°$ is therefore chosen here to allow also studies of different entrance window sizes.

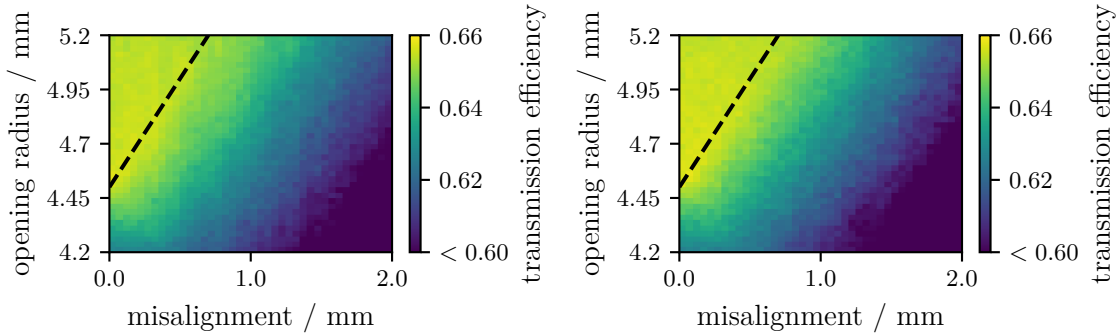

(a) The regular-shaped light guide (b) The Winston-shaped light guide

Figure 7.10: The radius of the entrance window with respect to the misalignment of the light guide. Below the black dashed line, parts of the cookie window are not covered by the light guide anymore.

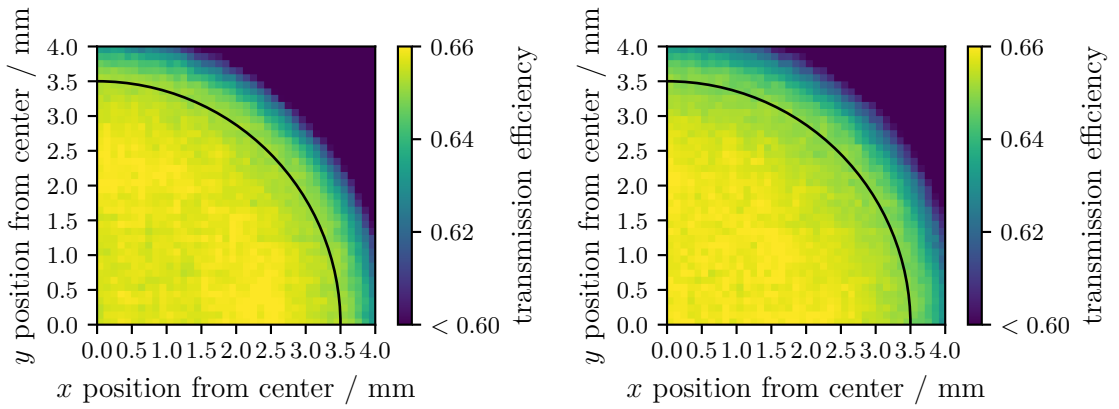

(a) The regular-shaped light guide (b) The Winston-shaped light guide

Figure 7.11: The dependency of the transmission efficiency on the position of the fiber in the bundle for two different light guides. The black line denotes the maximum position the 1 mm diameter fiber can have inside the 4 mm radius cookie. Taken from [196].

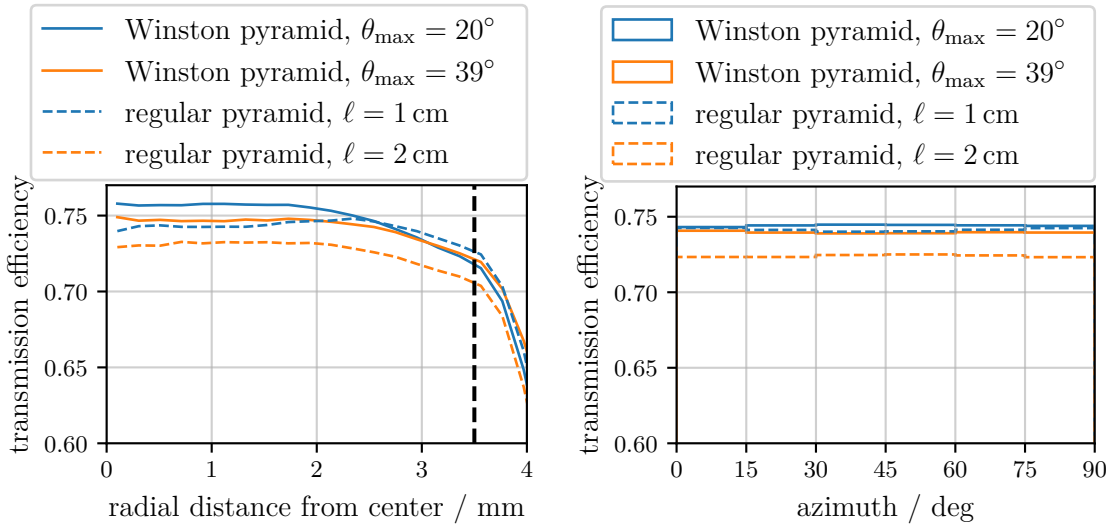

(a) Mean efficiency with respect to the radial distance from the center of the light guide. The dashed line denotes the maximum radial distance a fiber can have in the bundle.

(b) The mean efficiency with respect to the azimuth angle. Here, only radial distances up to 3.5 mm are taken into account.

Figure 7.12: Radial and azimuthal dependency of the transmission efficiency for four different light guide geometries. Taken from [196].

only drops when the fiber is moved outside the cookie which is, of course, not a realistic scenario.

The radial dependency for four different light guides is given in figure 7.12a. The mean value shows a dependency on the radial distance of only ±2 %. The only exception is the regular-shaped light guide with 1 cm length. Its variation is the smallest with only ±1 %.

Because of the azimuthal asymmetry of the light guides, also the dependency on the azimuth is studied. It is given in figure 7.12b. The distribution is flat for all geometries with a dependency on the azimuth below 0.5 %.

All light guides perform well in terms of the homogeneity with respect to the position of the fiber in the bundle. The regular-shaped light guide with a length of 1 cm compared to the other geometries shows a slightly smaller dependency on the radial distance from the center of the bundle.

7.6.5 Homogeneity of the SiPM illumination

As has been described in section 6.7, the dynamic range of an SiPM depends on the number of illuminated cells. In order to achieve a high dynamic range and allow for reconstruction of the signal in the highly non-linear regime, the light distribution on the SiPM must be homogeneous.

High light fluxes are achieved in the SSD when many particles penetrate the scintillator. Due to the large number of particles, their distribution can be assumed homogeneous resulting in an equal amount of light emitted by all fibers. The homogeneous distribution therefore must not be realized for a single fiber but only the combination of all. The simulation has been performed with all 37 fibers emitting an equal amount of light.

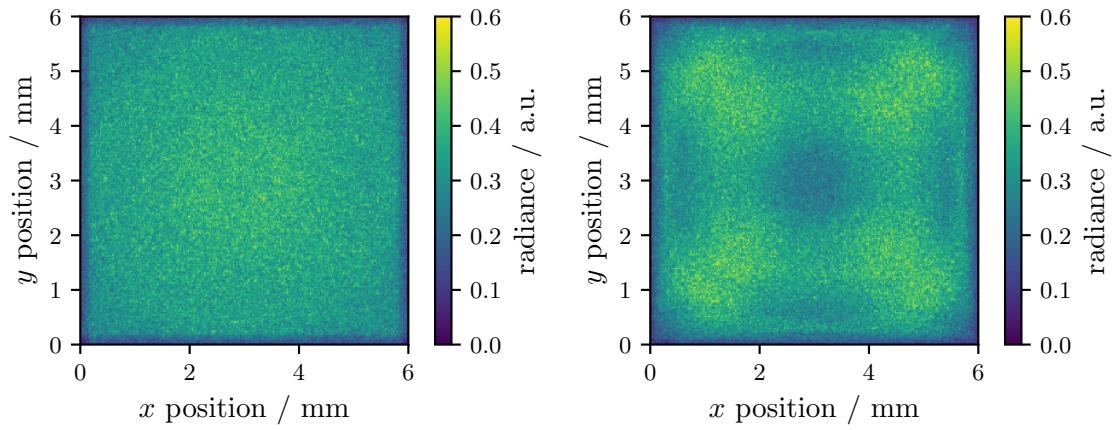

(a) The regular-shaped light guide

(b) The Winston-shaped light guide

Figure 7.13: The homogeneity of the illumination of the SiPM. For the regular-shaped light guide *(a)*, most light is concentrated at the center. In the case of the Winston-shaped light guide *(b)*, the light is rather concentrated closer to the corners. Taken from [196].

The resulting light distribution on the SiPM for the regular-shaped light guide and the Winston-shaped light guide is shown in figure 7.13. Both light guides show different patterns in the illumination of the SiPM. For the regular-shaped light guide, the radiance is highest in the center of the SiPM. About 13 % of the light is concentrated on the central $2 \times 2\,\mathrm{mm}^2$ while this corresponds to only 11 % of the total area. The distribution is thus slightly inhomogeneous. For the Winston-shaped light guide, the light is concentrated near the corners. A total of 45 % of the light is distributed in the four $2 \times 2\,\mathrm{mm}^2$ squares in the corners corresponding to 44 % of the area.

For both geometries, a narrow band of about 0.15 mm width along the edges is poorly illuminated. The width of the band might be reduced by increasing the size of the exit window. But, the band is advantageous as a slight misalignment of the light guide on the SiPM does not result in a significant reduction of the transmission efficiency to the SiPM. The size of the exit window is therefore retained.

In figure 7.14, the distribution of the illumination of the SiPM is given. For both light guides, the simulated flux is the same resulting in the same purely statistical fluctuations. The outer narrow band of low illumination with a width of 0.1 mm is excluded. Both distributions are well described by a Gaussian fit, which allows to determine the mean and width of the distributions. The distribution for the regular-shaped light guide is 4 % narrower compared to the Winston-shaped light guide meaning a more homogeneous distribution. This is likely a result of the focusing of the Winston-shaped surfaces which images the incident light on the focal points.

In terms of the homogeneity of the light distribution on the SiPM, the regular-shaped light guide, i.e. the intersection of a regular pyramid with a cylinder and a length of 1 cm, performs best.

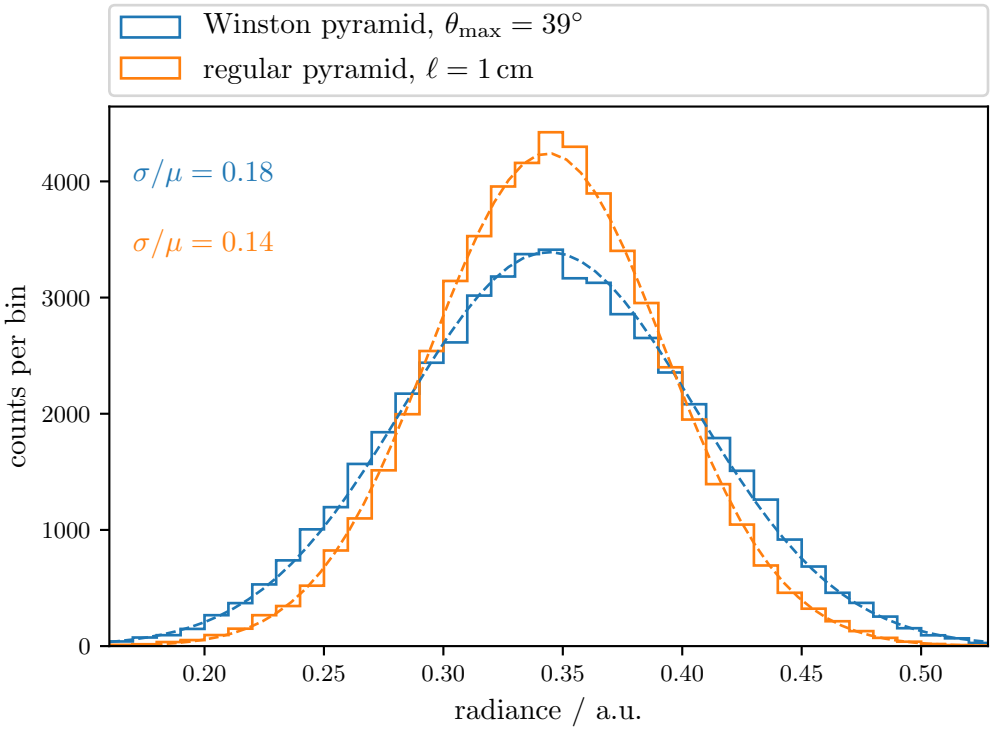

Figure 7.14: The homogeneity of the illumination of the SiPM for the two different light guide geometries. The corresponding two dimensional distributions are shown in figure 7.13. The simulation statistics is the same for both light guides. The variables μ and σ correspond to the mean and width of the Gaussian fits shown in the figure, respectively. Taken from [196].

7.6.6 Conclusion on simulations of the light guide

All light guides show a good transmission efficiency of around 74 % depending on the particular geometry. At a wavelength of 520 nm this corresponds to a photon detection efficiency of the full module including cookie, light guides and all SiPM characteristics of 23 %. Increasing the radius of the entrance window by 0.2 mm allows for a misalignment of the light guide in front of the cookie window without a significant reduction in the transmission efficiency.

In terms of a uniform light distribution on the SiPM as well as a homogeneous response for all fibers in the bundle, the regular-shaped light guide, i.e. the intersection of a regular pyramid with a cylinder and a length of 1 cm, performs best.

7.7 Measurement of the performance of the light guides

A measurement of the optical performance of the different light guide geometries is crucial in order to find the best geometry for the presented application. The determination of the light yield can be performed in a dedicated setup using optical fibers reproducing similar optical output characteristics as the cookie. For these measurements, prototype light guides have been produced by a dental technician [201]. They were milled from PMMA with hand polished surfaces.

In addition, the spatial homogeneity of a full prototype SSD was compared to that measured using a PMT.

7.7.1 Gluing of the light guides

In order to ensure good mechanical stability and optical transmission between light guide and SiPM, optical glue was applied between the two. The used glue was of type EPO-TEK 310M-2 [204] which has the same refractive index as PMMA and a high optical transparency. It therefore does not introduce an additional optical transition and was neglected in the simulations also because of its thinness compared to the SiPM coating or the length of the light guide.

It has a low viscosity that allows a small drop of glue to flow into all gaps between light guide and SiPM. Therefore, the amount of enclosed air bubbles in the glue is reduced. The glue consists of two components that need to be mixed before the application. Curing is performed at a temperature of 65 °C for 2 hours, which was realized in a standard oven. The glass temperature of the used PMMA is around 108 °C [201] and the maximum allowed storage temperature for the SiPM is 80 °C [130]. Both are not in contradiction with the curing temperature.

In order to test the gluing procedure, PMMA cubes with an edge length of 6 mm have been produced by the mechanical workshop of the Physics Institute IIIA of the RWTH Aachen University. They were glued on PMMA plates to test the handling of the glue. The final process is split into six steps:

1. The surface to be glued on and the light guide or test cube, respectively, are cleaned with a microfiber tissue.
2. The two components of the glue are portioned using a scale and mixed with a clean stick.
3. The glue rested for a few minutes to allow air bubbles to escape.
4. A small drop of glue was applied on the surface with a syringe.
5. The light guide was placed on the surface and slightly pressed. Due to the low viscosity of the glue it spreads over the full area. The light guide can be positioned correctly by carefully pushing from the sides.
6. The components are placed in a standard oven for curing.

An example of the result of these gluing processes is shown in figure 7.15. Some of the cubes were produced with a hole in their center. It was used to attach weights and test the strength of the glue after proper curing. The plate was turned upside down and weights were added consecutively. It was found that the cubes break off at weights of 5 kg to 7 kg. This is by far sufficient for the application in the presented optical module. It should also be noted that no tractive force is expected in the application in the SSD where the optical module is pushed to the cookie.

Additional tests involved temperature cycling between −30 °C to 50 °C and drowning the cubes in water for several days. Both tests could not reveal any issue in the gluing and it is considered to be suitable for the foreseen application. A gluing of two light guides on the SiPMs of the optical module is shown in figure 7.16. The quality of the gluing differs significantly as it was one of the first attempts of gluing the light guides on SiPMs. The

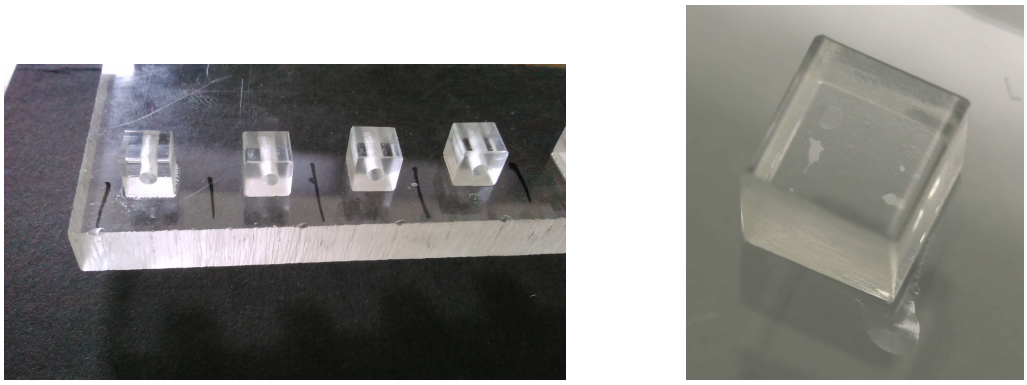

(a) (b)

Figure 7.15: Photos of the PMMA cubes glued on a PMMA plate. *(a)*: Four cubes with additional holes in the center which allow to attach weights to test the strength of the glue. *(b)*: Zoom of one cube with out hole. A few small light bubbles are still visible in the glue.

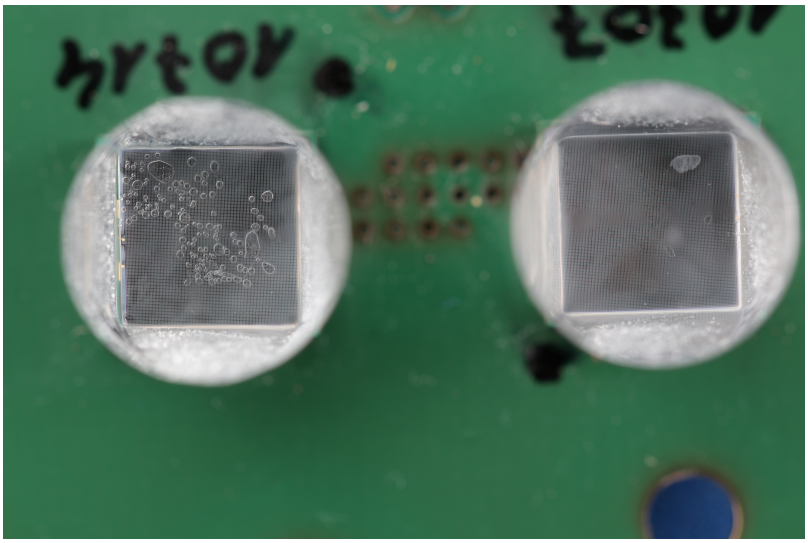

Figure 7.16: The gluing of two light guides on an optical module. It was one of the first gluing processes on SiPMs and the quality differs between the two. For the left light guide, many bubbles over a significant fraction of the area are visible. For the right one only one big bubble is apparent at the top right.

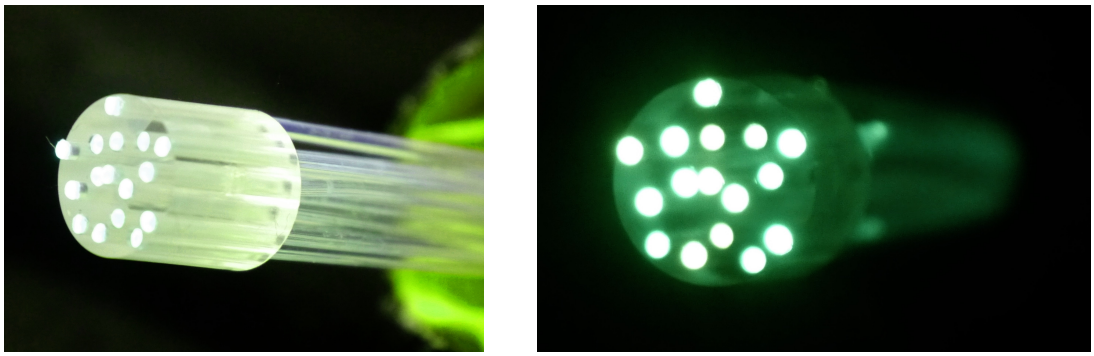

(a) (b)

Figure 7.17: Two images of the support structure for the WLS fibers. 16 holes are drilled in a solid PMMA cylinder and hold the fibers in place. *(a):* side view, two fibers are slightly sticking out. This is corrected when the setup is operated. *(b):* Front view in darkness, the WLS fibers are illuminated by a LED.

differences in the amount of air bubbles are well visible and allow for a check of the gluing by a simple visible inspection. The gluing process had been optimized by practicing such that later all gluings achieved a quality similar or better compared to the light guide shown on the right.

7.7.2 Light yield

When measuring the light yield of the light guides, the distribution of light must be as similar to the final application as possible, both in spatial and angular regime. A setup was designed that represents the SSD in many aspects. Eight scintillator bars of the same type as used in the SSD are read out by optical fibers. The 16 fiber ends are guided onto a support structure that allows for an arrangement that represents the radial light distribution of the cookie of the SSD with 48 fiber ends. A photo of this holding structure is shown in figure 7.17.

Additional scintillator tiles placed above the scintillator bars provide a trigger on through going muons. These scintillator tiles were designed for use in the Aachen Muon Detector (AMD) [75, 73], a precursor of the MiniAMD presented in section 5.2.1.

The setup is sketched in figure 7.18. The tests have been performed once with the light guides simply placed on the SiPM and again with the light guides glued on it.

Only very few prototypes of the light guides could be glued on the SiPM in order to properly test the final setup. Gluing is an irreversible process and only a limited number of SiPMs was available.

The scintillator tiles placed on top of the scintillator bars allowed for a triggering on through going muons. A coincidence between the tiles and the signal from the scintillator bars allowed for the suppression of background. The signal corresponding to a muon, the MIP signal, was measured with the SiPM for different light guides. When determining the gain of the SiPM from its finger spectrum, the light yield can be calibrated in terms of p.e.. An example of the distribution of the total signals is shown in figure 7.19. A pulse finding algorithm on the signal traces is used to also find single p.e. pulses from dark noise. In the histogram they produce the finger spectrum at the left which is fit with a function of correlated Gaussian distributions that was proposed in [205]. From this function the gain

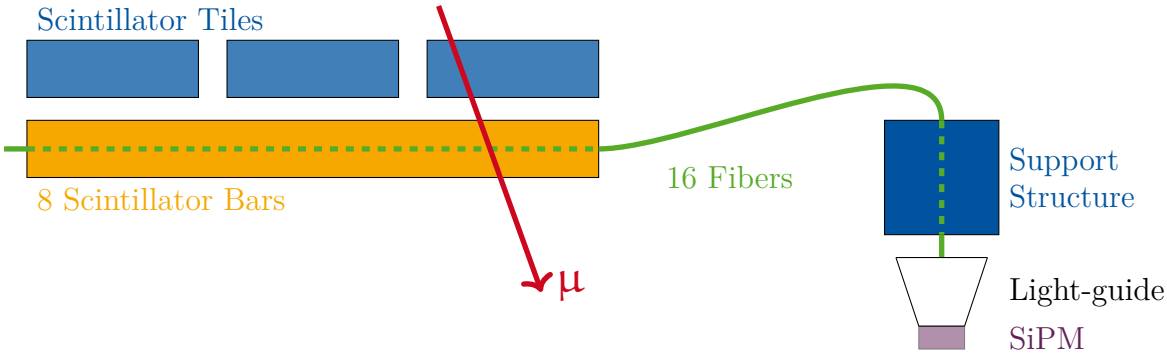

Figure 7.18: Sketch of the setup to determine the light yield of different light guide geometries. The light produced in the scintillator bars by through going mouns is collected by WLS fibers and guided through the holding structure on the light guide under test. The light is detected with an SiPM and its read out is triggered by external scintillator tiles. Modified from [196].

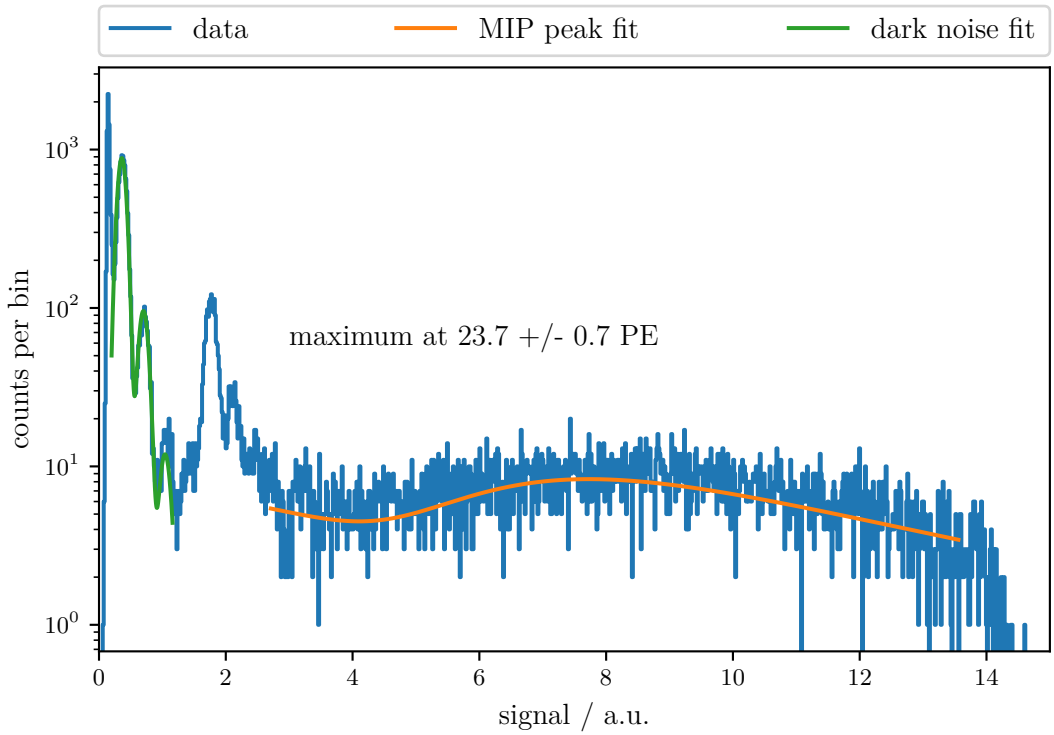

Figure 7.19: An example of a signal distribution as measured with the setup shown in figure 7.18. The peak at a signal of around 2 originates from the trigger threshold. Lower signals are found by a pulse finding algorithm. Both the dark noise spectrum with the single p.e. peaks and the MIP peak are well visible. The dark noise fit is composed of correlated Gaussian distributions and the MIP peak fit is a Landau distribution summed with an exponential to describe the background.

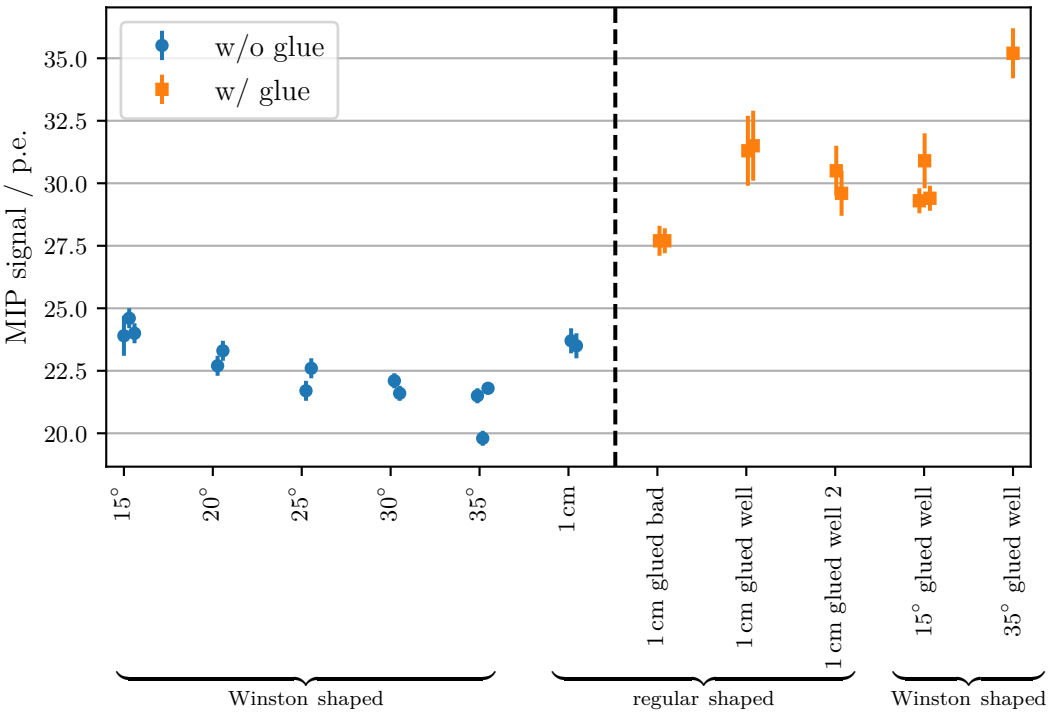

Figure 7.20: The light yield measured for different light guide geometries calibrated in p.e.. Measurements at the right of the dashed vertical line are performed with the light guides glued on the SiPM. For the measurements left of the dashed line, the light guide is simply placed on the SiPM. Different data points for the same light guide refer to independent measurements to study systematic uncertainties. Modified from [196].

of the SiPM can be extracted. The MIP peak can be determined from a fit of a Landau distribution summed with an exponential which describes the low signal background. The combination of both fits allows to extract the signal in terms of p.e. produced by through going muons for the light guide under test. The different light guides can then easily be compared.

The resulting light yield for different types of light guides is shown in figure 7.20. Light guides glued on the SiPM have a significantly higher light yield compared to those that are simply placed on it. The quality of the glue also plays a crucial role. For a badly glued light guide, the performance is measured to be worse by 12 % compared to the well glued ones. The badly glued light and the well glued light guide have been shown in figure 7.16. The amount of bubbles thus has a significant impact on the light yield and should be reduced.

The change in performance can be easily understood by the improved optical transition at the boundary of the light guide and the SiPM when glue is applied. For a light guide which is only placed on the SiPM, a transition first into air and then into the SiPM resin has to be taken into account. Using Fresnel equations, a total reflection for vertical incident light of 8 % can be calculated over this gap. At an incident angle of $\theta = 74°$ total reflection is reached.

For the Winston-shaped light guides a decrease of the efficiency with higher cut-off angles occurs. Higher cut-off angles lead to shorter light guides and thus to large incident angles

of the light at the exit window. As the reflectivity calculated in the previous paragraph increases with the incidence angle, more light is reflected. Gluing the light guide onto the SiPM, the reflectivity and its dependency on the incidence angle can be reduced. For the glued light guides, the light yield increases by 24 % to 67 % for cut-off angles of 15° and 35°, respectively. The larger increase for short light guides agrees with the expectations.

The regular-shaped light guide shows similar performance as the Winston-shaped light guide. The light yield increases by 30 % when being well glued instead of non-glued.

All light guides show sufficient performance for the application in the SSD. The signal induced by a through going muon can be well distinguished from SiPM noise. Shorter light guides are preferred because of lower absorption and a lower probability of a photon to hit a surface. Thus, surface imperfections have a lower impact on the performance. For further tests, the regular-shaped light guide of 1 cm length was chosen.

7.7.3 Spatial homogeneity of a full detector

The spatial homogeneity of a full SSD is affected by the characteristics of the light guides. In order to test their performance, an optical module has been installed in a prototype SSD. The light guides tested were the regular-shaped ones of 1 cm length. The measurement was performed at the KIT where the SSD was constructed and a dedicated facility to measure the spatial homogeneity of a detector was operative. The SSD was placed inside a muon tomograph which has been used as central tracker in the KASCADE experiment [206]. It has a positional resolution for through going muons of 1 cm and allows to determine a position dependent light yield.

The measurement has been performed twice: once with the presented optical module and once with a PMT reading out the same detector. Comparing the two measurements allows to exclude inhomogeneities that solely arise from the detector itself. This can be the case, for example, due to bad positioning of the fibers in the cookie or different production batches of the scintillators leading to differences in their light yield. The resulting light yields are shown in figure 7.21. The absolute scale of the signals measured with the SiPM based optical module and the PMT differs because of their different gains. The vertical stripe-like structure results from the different scintillator bars which show slight variations in their light yield. The response is mostly homogeneous, but especially for the bars at the right of the detector, some deviation is visible. It results from imperfections in the manufacturing of the cookie of this prototype detector.

In figure 7.22, a front view of the two fiber bundles of the cookie is shown. The fibers that correspond to the scintillator bars with a bad performance are all at the edges of the fiber bundle. In addition, they are slightly shifted away from the cookie window. This can lead to a loss of light to the sides of the fiber bundle where the light guide is not covering the area anymore. The aluminum ring of this detector was not polished and therefore only yielded diffuse instead of specular reflections. The light that impinges on the aluminum is therefore not necessarily reflected in the direction of the light guide but away from it. The light yield for fibers at the edges of the bundle gets reduced. The inhomogeneities are well explained by these effects. In future detectors, care should be taken in the production to avoid badly positioned fibers and to install a polished aluminum ring. Additionally, it should be ensured that a positioning of both fiber ends of one fiber at the edge of the bundle is avoided. The effect then averages out.

The right plot of figure 7.21 shows the ratio of the average signals measured with the SiPM module and with the PMT. The signals are scaled such that the mean ratio equals 1.

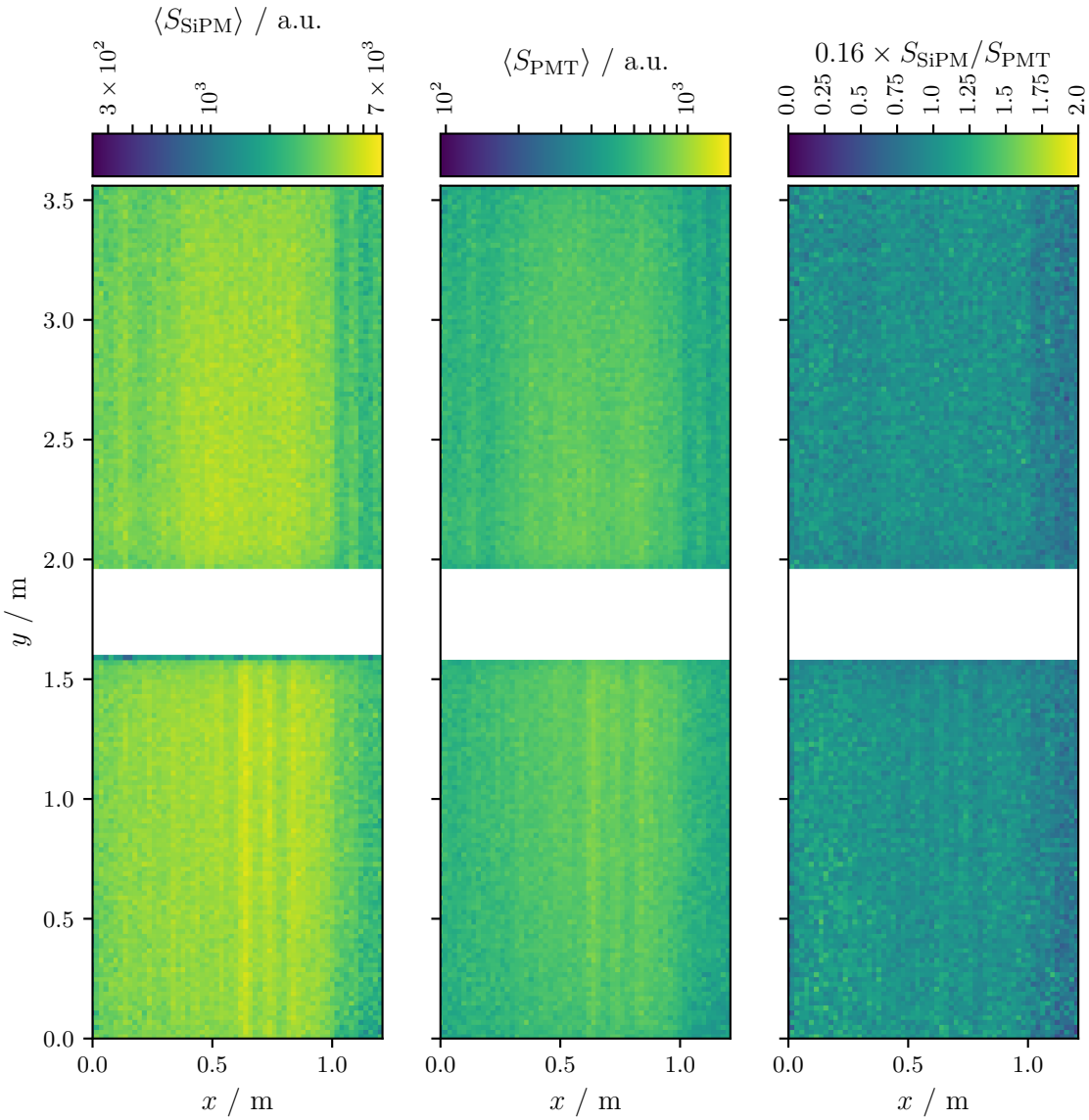

Figure 7.21: The position resolved light yield of the SSD measured on the muon tomograph at KIT. The bin size is chosen to be 1 cm in x-direction and 4 cm in y-direction as there is only a low dependence. *Left:* The measurement was performed with the SiPM module. *Center:* The measurement was performed with the PMT. *Right:* The ratio of the average signals measured with the SiPM and PMT. The SiPM signal is scaled such that an average ratio of 1 was achieved. The distribution is flat with only some slight deviation for the bars at the right due to production issues. See text for details. Taken from [196].

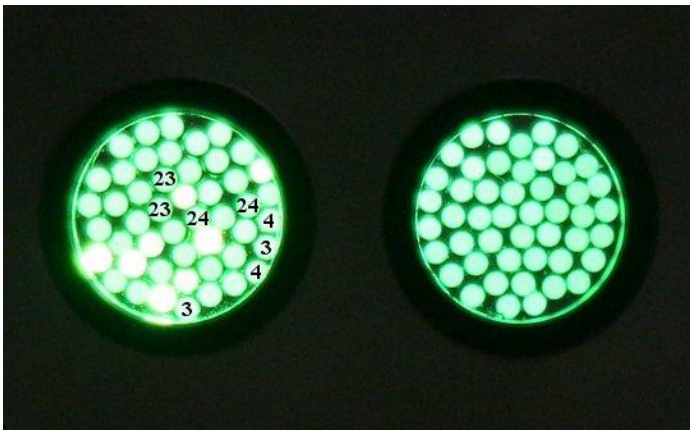

Figure 7.22: Front view of the fiber bundles of the detector shown in figure 7.21. The left bundle corresponds to the half of the detector with $y > 1.8\,\mathrm{m}$. The fiber ends labeled 3 and 4 correspond to the bars at the right of the detector. Those labeled 23 and 24 correspond to the left bars. Variations in the brightness of different fiber ends originate from inhomogeneous illumination. Taken from [196].

The distribution is very flat except for the previously mentioned scintillator bars at the right of the top half. It can be concluded that the impact of the poor positioning of the fibers is stronger for the SiPM module than for the PMT. The PMT has a large cathode area that extends significantly over the positions of the fiber bundles. Therefore, the PMT can still detect stray light.

The dependency of the light yield along the y-axis is low. This allows to study only the average signals for given values of x which corresponds to the light yields of the different scintillator bars. The resulting ratio of the SiPM and PMT signals is shown in figure 7.23. Even for the worst scintillator bars, the deviation stays below 10 % from the average value. The RMS of the distributions is low with only $\leq 4\,\%$. The light guides therefore only contribute to an inhomogeneity at the percent level.

7.7.4 Conclusion on the performance of the light guides

The chosen regular-shaped light guide of 1 cm length has proven to achieve good performance in the SSD. The light yield is sufficient to achieve a light yield for through going muons significantly above the SiPM noise. Simulations revealed a total optical efficiency that is better by 75 % than for the PMT. Measurements and simulations proved that a good homogeneity for the response of a full detector can be achieved. The light distribution on the SiPM was simulated to be mostly homogeneous with a slight concentration of the light in the center of the SiPM.

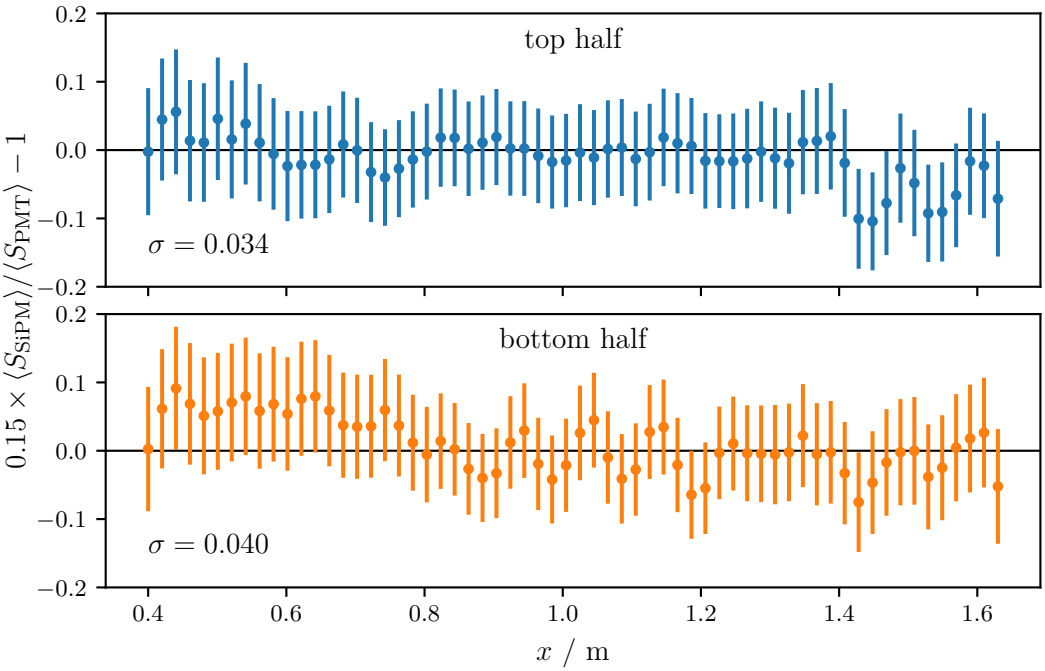

Figure 7.23: The signal ratio for the top ($y > 1.8\,\mathrm{m}$) and bottom ($y < 1.8\,\mathrm{m}$) half of the SSD. The RMS of the corresponding distributions is given in the plots. Taken from [196].

Chapter 8

Performance of the SSD in the field

The SiPM based optical module was installed in three prototype versions of the SSD. One of them had to be decommissioned for organizational reasons of the Pierre Auger Collaboration so that for two SSDs long term data could be taken. One of these two was used for the measurements on the spatial homogeneity presented in section 7.7.3. These SSDs were deployed in the array of the Pierre Auger Observatory in the Argentinean Pampas. A photo of such a station has been shown in figure 5.2 on page 52. The first commissioning was performed in September 2016. Results of those early measurements are published in [196].

The optical modules were replaced a few times. The main reasons were improvements in the electronics of the module [155] but also testing of SiPMs of type Hamamatsu S13360-6050PE with cell sizes of 50 µm instead of the baseline version with the Hamamatsu S13360-6025PE with 25 µm cell size. In addition, the detectors were moved to different places in the array. The results that will be discussed in the scope of this chapter were obtained in the final configuration with the electronics as described in the previous chapter and in detail in [155].

This chapter is structured in two parts. The first part up to section 8.5 is dedicated to the performance of the SiPM based optical modules in the field. In a second part starting in section 8.6, a first analysis of the performance of all SSDs is discussed.

8.1 Setup of the SiPM based optical modules in the field

Two SSDs equipped with the SiPM based optical module are deployed in the field at different locations where there is a running SD station:

1. One detector is located in the region named *AERAlet* in the center of a hexagon of SD stations with a spacing of only 433 m. This arrangement allows for a high trigger rate due to the lower energy threshold compared to the standard array. One standard SD station is 17 m apart and three additional PMT SSD stations were commissioned consecutively close by (cf. fig. 8.1a).

2. The second detector is placed in the standard array with a spacing of 1500 m. It is located at a distance of 15 m to a standard SD station and 10 m apart from an upgraded station with a PMT SSD (cf. fig. 8.1b).

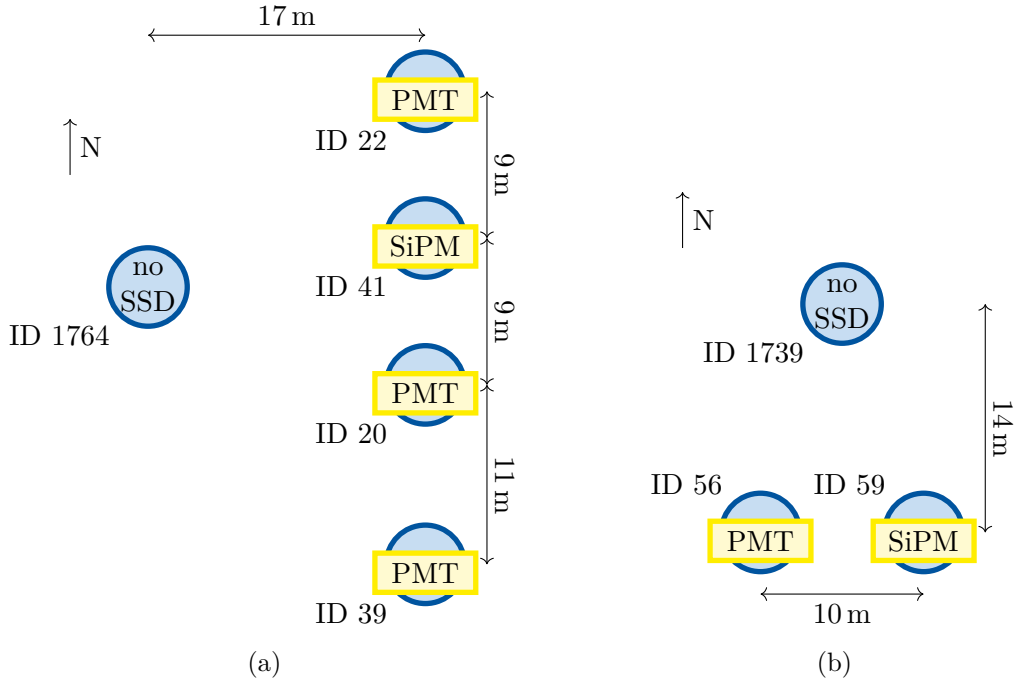

Figure 8.1: Locations of the SiPM SSDs with respect to the directly neighbored stations. In *(a)*, the distance to the next standard stations is 433 m from station 1764. These stations are not upgraded yet. In *(b)*, the next stations in the hexagonal grid are 1500 m apart. These surrounding stations are also upgraded and equipped with an SSD. Both maps are oriented to the north.

Sketches of the arrangements of the different detectors next to the SiPM SSDs are shown in figure 8.1. The close by positioning of SD stations that were not upgraded yet and of upgraded stations with a PMT SSD allows for a detailed comparison of their performance. It should be noted that the trigger on air showers is built by the information of the standard array stations. The upgraded stations are only placed additionally and readout whenever a trigger appeared but they do not contribute to it. The reconstruction of the air shower using the upgraded stations had been preliminary implemented by members of the Pierre Auger Collaboration, see e.g. [207, 208], into the *Offline* framework [209]. Offline is the standard software for reconstruction and simulation of data of the Pierre Auger Observatory. This also includes a proper calibration of the SD and SSD signals measured with the stations following the same principles as for the old stations (cf. sec. 4.2.1). The calibration of the SiPM SSDs was not performed in that scope because of slight differences that will be explained in the course of this section. The author of this thesis implemented the calibration of the SiPM signals to allow for a proper comparison to the PMT SSDs.

For both SiPM based optical modules, the bias voltage is set to 5 V above the breakdown voltage stated by the manufacturer at 25 °C. The bias voltage is corrected according to the ambient temperature with 57 mV/K.

For station 59, data starting on July 17, 2018 is used. Station 41 was only properly running starting from November 27, 2018. For both stations, data taken until March 31, 2020 is used. In station 41 an occasional saturation of the ADC of the LG channel was

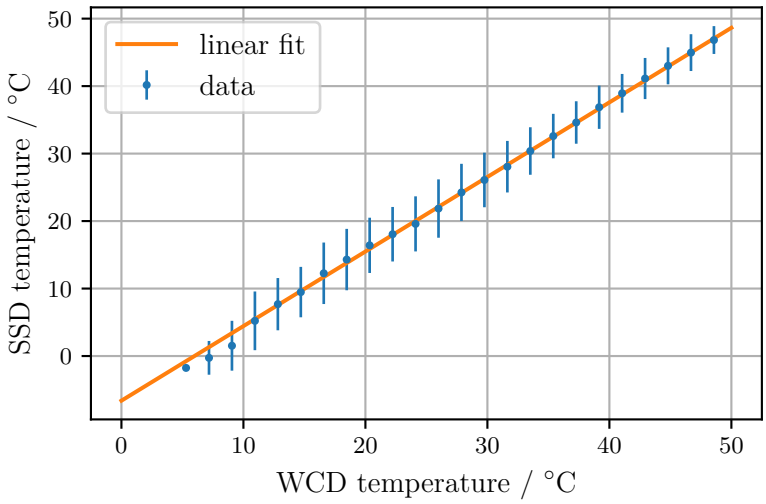

Figure 8.2: Correlation of the temperature measured at the WCD PMTs and at the SSD of station 59. The distance of the data points corresponds to the ADC resolution of the temperature sensor. The errorbars denote the RMS of the distributions.

observed. Therefore, the overvoltage of this module was lowered to 2.5 V starting from April 15, 2019 to reduce the signal sizes.

The UUBs operating at the two stations with an SiPM SSD are of different versions. The one installed at station 41 suffers from a high baseline noise which will also be seen later in this chapter.

Temperature dependency

The optical module has a temperature sensor that, in principle, allows for monitoring the temperature at the SiPM board. The transmission of this information in the standard data stream suffered from unresolved software issues and was only available for station 59 from August 16, 2018 until March 4, 2019. This time period can be used to cross calibrate with the temperature sensors of the WCD PMTs as is indicated in figure 8.2. The clear correlation between the two can be reasonably described by a linear fit. This correlation is used whenever no temperature measurement from the SiPM module is available. It is also used for station 41 as no temperature data was transmitted for that station. Since both stations are identical in their orientation and not exposed to any shadow, a similar correlation is expected.

Temperature data is transmitted regularly roughly every 5 minutes but not necessarily associated with a specific event. Therefore, the times of the events and the times for the temperature measurements differ. A linear interpolation between the two neighboring temperature measurements is therefore performed.

8.2 Calibration histograms of the SiPM SSDs

As has been explained in section 4.2.1, calibration histograms are taken during standard operation of the observatory. Here, slight differences arise from the upgrade to the UUB with its increased sampling rate compared to the UB and some modifications have been

implemented for the special case of the SiPM based optical module as will be explained in the following.

The events used for the production of the calibration histograms are triggered by the WCD on through going single muons. The signal from the SSD (WCD) is summed in a time window of 167 ns (417 ns) corresponding to 20 (50) samples around the trigger. The different windows were chosen by the Pierre Auger Collaboration because of the shorter pulses from the SSD PMT compared to the WCD PMTs. The obtained signals are filled into a histogram. The histogram is renewed every 61 s. When a shower trigger was detected, the calibration histogram is transmitted and stored with other information about the event such as the arrival time and signal traces. For the PMT SSDs, the histogram is obtained at the HG channel as it provides single MIP resolution.

For the SiPM, both the CG and HG channel are of interest to provide single p.e. resolution and the standard MIP calibration. The standard data format used at the Pierre Auger Observatory is limited to sending only a single calibration histogram. Therefore, the two histograms are transmitted alternating for each event. The MIP calibration from the HG channel is, thus, only available for every second event. In order to obtain information for the missing event, data from the CG channel can be used, the value for the MIP signal can be interpolated between neighboring events or one exploits the temperature dependency of the MIP signal (cf. sec. 8.2.2). More details will be given in the next sections.

8.2.1 The CG calibration histograms

An advantage of the histograms taken at the CG channel is the single p.e. resolution. It allows for studying the performance of the detector by e.g. determination of the gain. Throughout this section, the gain is defined as the integrated signal obtained from one single p.e. pulse.[1]. As the MIP signal is also visible, the number of photons detected per MIP can be determined. In figures 8.3 and 8.4, examples of histograms of the two SiPM SSDs are given.

The MIP peak is well separated from the pedestal and can be precisely determined. At the pedestal, multiple shoulders originating from the single p.e. resolution can be seen. Exploiting the single p.e. resolution, the MIP signal can be calibrated in terms of p.e. as will be shown in the following section. In order to extract information from the histograms such as the SiPM gain or the MIP peak, dedicated fits have been developed that account for the data taking algorithm.

Fitting the MIP peak

The position of the MPV of the MIP signal is determined from a parabolic fit, as indicated in figures 8.3 and 8.4. It is also used in the standard Offline calibration and sticking to the same function here avoids introducing systematic uncertainties.

The MPV of the MIP signal is given in figures 8.5 and 8.6 with respect to temperature. For both stations, the raw signal is stable except for some outliers with a lower signal at low temperature for station 41. When being calibrated with the gain of the SiPM, this feature disappears. Details on the determination of the gain will be given in the next section as

[1] In chapter 6, the gain was defined as the number of charge carriers produced in one cell breakdown. As no amplifiers were used in the measurements presented there, the gain could be directly calculated from the integrated signal of a single p.e. pulse by equation (6.32). Here, the signal is also amplified on the SiPM based optical module and at the UUB with a factor that is not precisely known. The conversion to a number of charge carriers produced in one cell breakdown is therefore not possible.

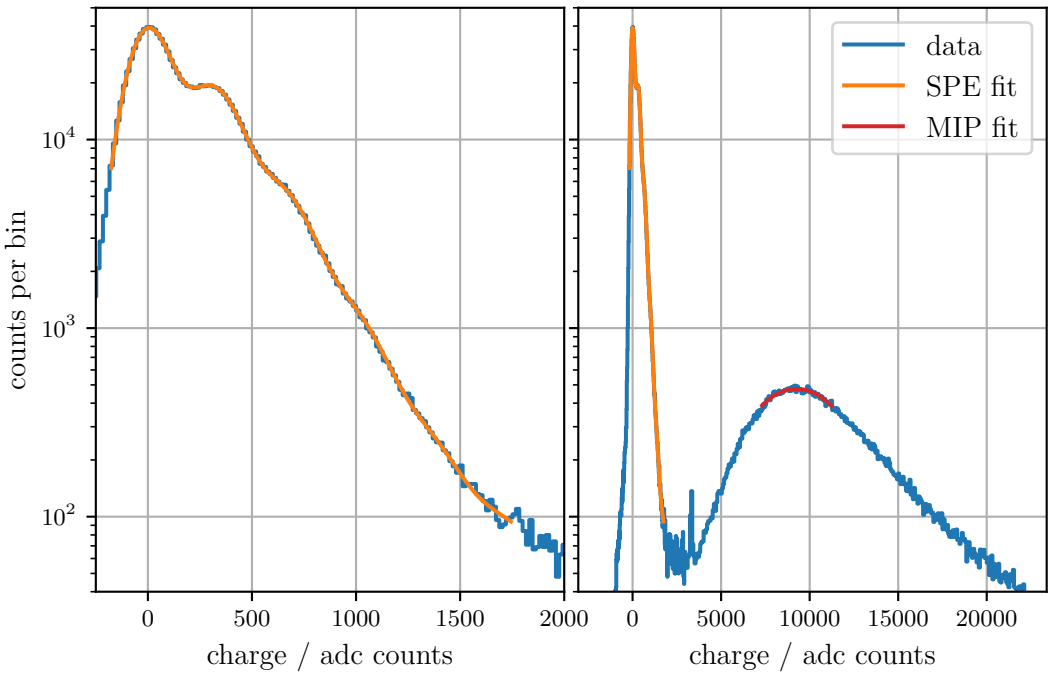

Figure 8.3: Example of a calibration histogram measured at station 41. *Left:* Zoom into the pedestal region. Details on the fit are given in the text. *Right:* The full histogram. The peak around a charge of 3500 adc counts originates from noise of the DC/DC converter of the UUB.

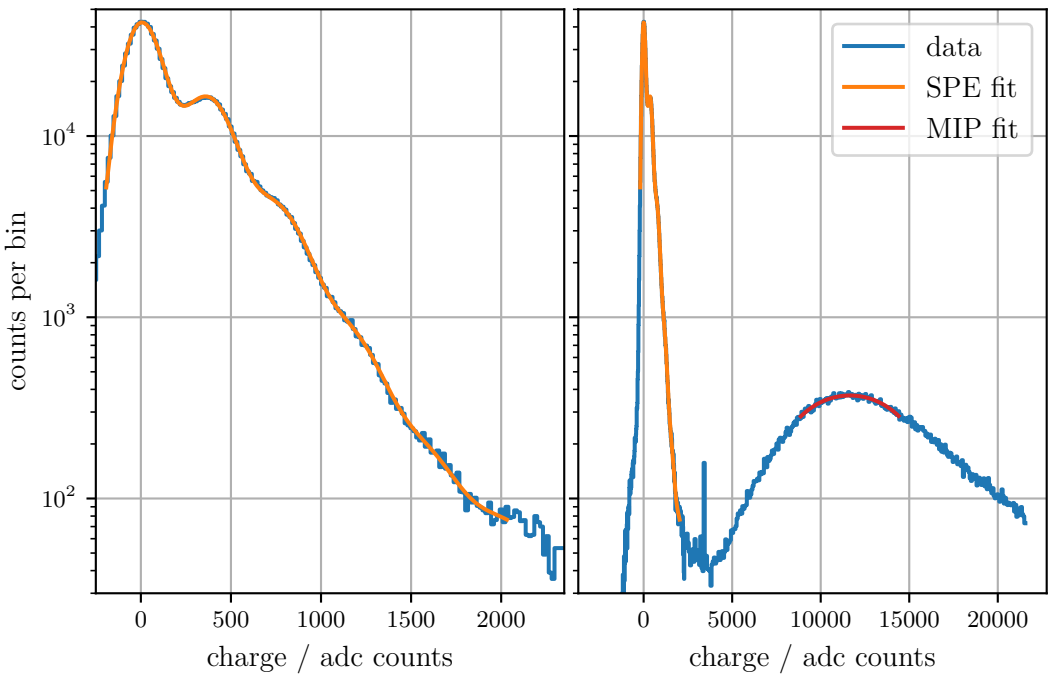

Figure 8.4: Same as figure 8.3 but for station 59.

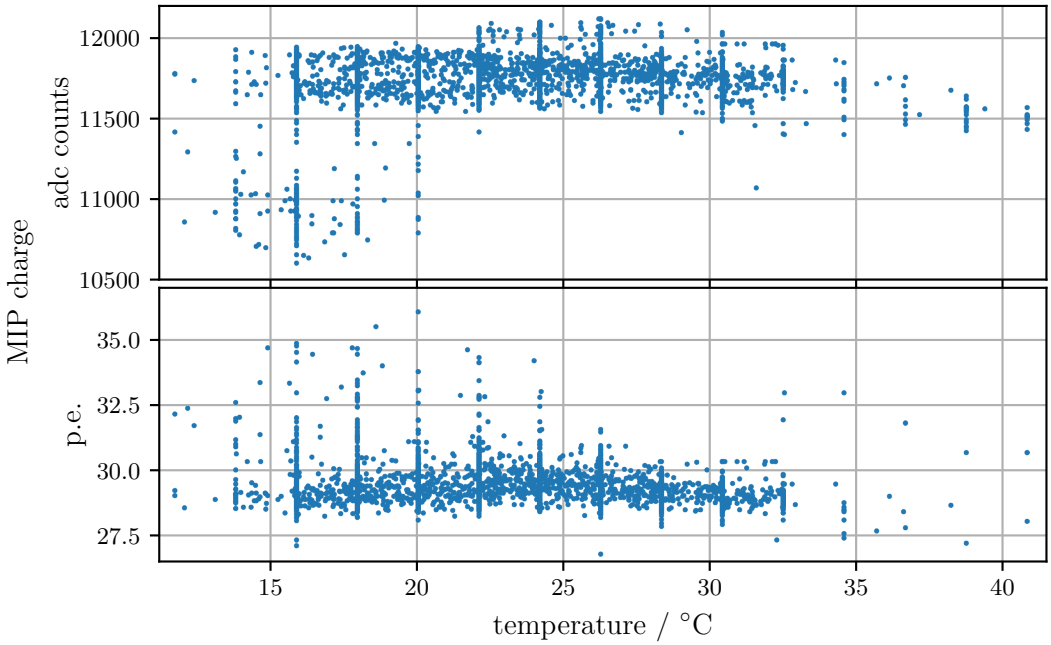

Figure 8.5: The position of the MIP peak with respect to temperature for station 41. The vertical lines originate from the poor temperature resolution of the sensor of the WCD PMT. *Top:* the raw signal as determined from the calibration histograms. *Bottom:* The raw signal divided by the gain of the SiPM. Details are given in the text.

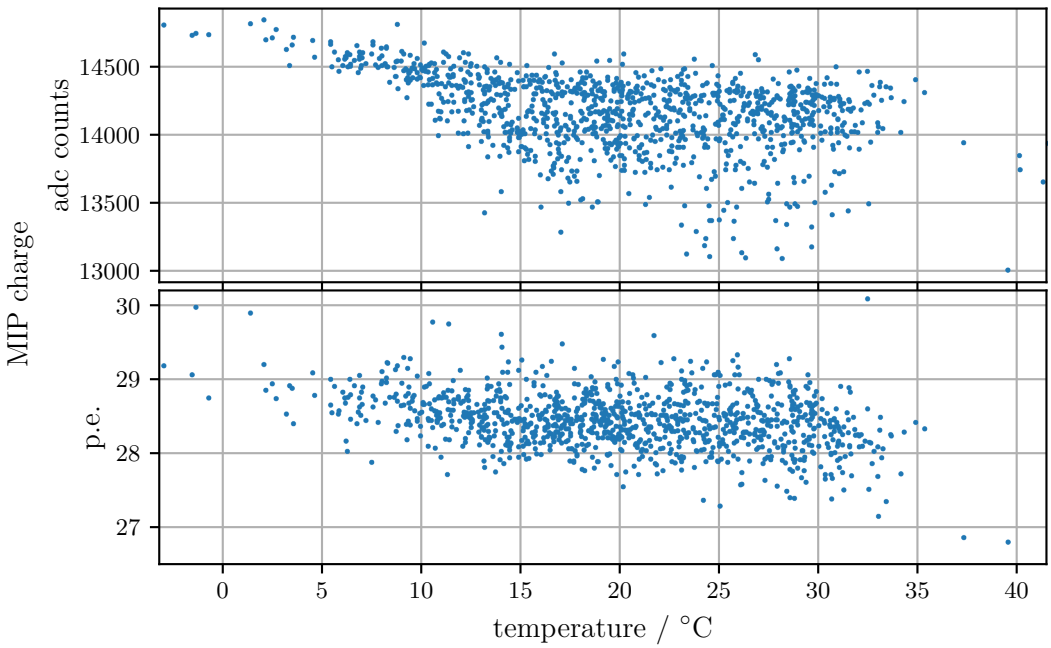

Figure 8.6: Same as in figure 8.5 for station 59.

well as the interpretation of these outliers. The statistical uncertainty on the determination of the MPV is only around 2 % for both stations.

A function to describe the single p.e. spectrum

In typical applications, the single p.e. spectrum is recorded by triggering on the small pulses with thresholds around 0.5 p.e. (cf. sec. 6.2.2) or dedicated algorithms search and integrate the dark noise pulses (cf. sec. 7.7.2). These approaches ensure a full integration of the dark noise pulses and, hence, result in a clear single p.e. spectrum. The algorithm used for the creation of the calibration spectra at the Pierre Auger Observatory was designed for the determination of the MIP signal. The trigger is generated by the WCD for crossing muons and the signal measured at the SSD is integrated around the time of the trigger. It ensures that the MIP signal is contained in the integration window.

For the measurement of the single p.e. spectrum, this algorithm is disadvantageous because of the random nature of the dark noise. The pulses do not necessarily lie fully inside the integration window but fractions of it might reach outside. In addition, the high DCR can result in multiple independent dark noise pulses in the integration window of which a fraction might only be contained partially. These effects smear the Gaussian shape of the peaks in the single p.e. spectrum and a fit of correlated Gaussians as was used in previous analyses of this thesis (cf. sec. 6.2.2 and 7.7.2) does not describe the data well.

A fit function has been developed that takes into account these effects and allows for a proper extraction of features such as the gain. This function will be introduced in the following.

The general idea is to calculate the probability for obtaining a charge q when integrating a measured trace in a region of fixed length T at random position. Assuming only dark noise pulses from the SiPM (i.e. no physics signal from e.g. muons was triggered) and no electronics noise, three cases can be distinguished:

1. No pulse is in the integration window and the integrated signal q is zero.

2. One pulse is, at least partially, in the integration window. The integrated signal q is in the range 0 to n p.e., with $n \in \mathbb{N}$, and follows a Probability Density Function (p.d.f.) $\hat{Q}_n(q)$ that needs to be determined. Values of $n > 1$ can occur due to crosstalk.

3. In total $M > 1$ pulses are, at least partially, in the integration window. The pulses must not be at the same position and might have different sizes. They will contribute differently to the integrated signal q which can be any positive real value. The p.d.f. $\hat{Q}_{\mathrm{tot},M}(q)$ for measuring a charge q if M pulses are in the integration window needs to be calculated.

It should be noted that the notion of a pulse being *in the integration window* is a bit vague. As typical pulses have an exponentially falling edge, they extend to infinity and all pulses that were produced before the start of the integration window are at least partially in the integration window. Here, pulses that start in a piece of trace with length $\tau > T$ and $\tau > \tau_{\pm}$, the exponential rise and fall of the SiPM pulse, are considered to be in the integration window. The probability for the different cases to occur is then given by a Poisson distribution with mean $\lambda = (T + \tau) \cdot R$ with R the DCR.

A schematic of the construction of the function is shown in figure 8.7 that will be guided through in the next paragraphs. The goal is to calculate the p.d.f. $\hat{Q}_{\mathrm{dark}}(q)$ for a charge q

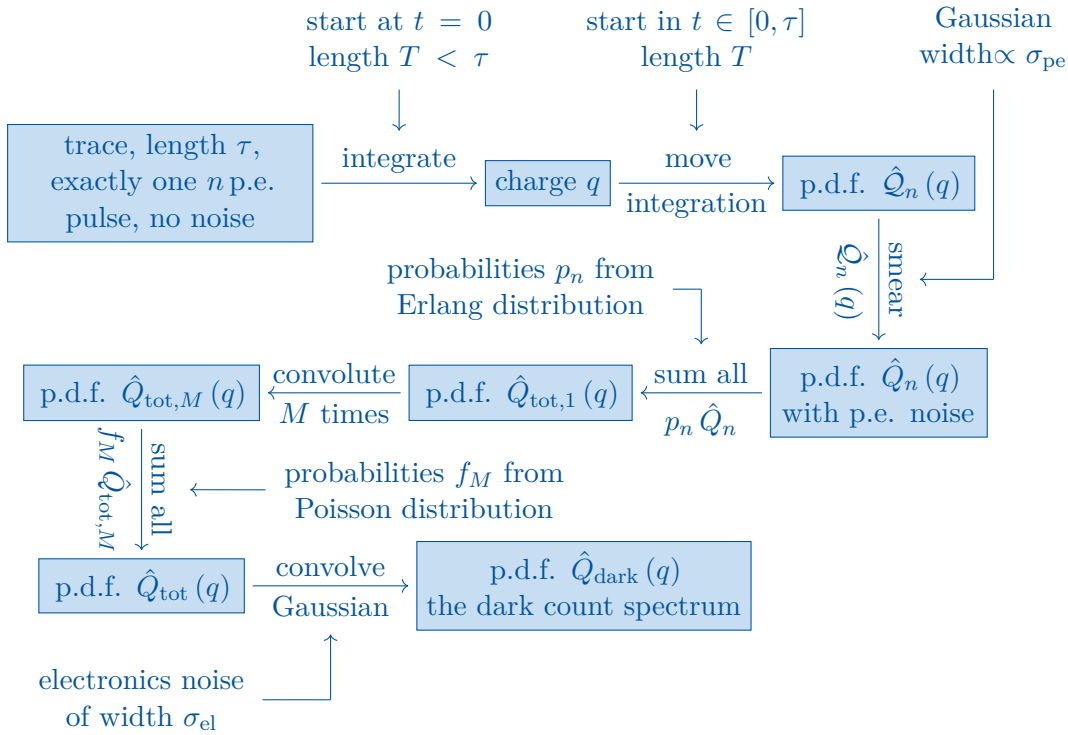

Figure 8.7: A schematic of the construction of a function that describes the single p.e. spectrum. All steps are explained and motivated in detail in the text.

to be measured from dark noise. It should include noise from the electronics and the noise due to slight variations in the released charge of a single cell breakdown.

As a starting point, a trace of length τ with exactly one pulse of size n p.e. is considered. The shape of the pulse $SPE(t; \tau_{\pm})$ is given by equation (6.37) on page 114. The parameters $\tau_{\pm}$ are well known from the results obtained in section 6.6.8. The exponential time constants of the pulses are therefore fixed to values of $\tau_{-} = 78.3\,\mathrm{ns}$ and $\tau_{+} = 1.0\,\mathrm{ns}$. An example is shown in the top graph of figure 8.8. An integration window with fixed length T is moved over the trace. Depending on the position, the resulting integrated signal q varies as is shown in the bottom left plot of figure 8.8 for the case of $n = 1$. The distribution $\hat{\mathcal{Q}}_n(q)$ of the obtained charges q is given in the bottom right plot of the same figure, again for $n = 1$. After normalization it corresponds to the p.d.f. for obtaining a charge q if exactly one n p.e. pulse is in the trace.

The distributions $\hat{\mathcal{Q}}_n(q)$ do not take into account noise. Electronics noise σ_{el} will be added later. Here, the noise originating from slight variations in the released charge of a cell breakdown will be taken into account. It is assumed to be Gaussian distributed with a width σ_{pe}. It occurs, for example, from uncertainties in the manufacturing process resulting in slight variations in the characteristics of different cells. For n simultaneous breakdowns, the individual uncertainties need to be summed quadratically and are given as $\sigma_{n,\mathrm{pe}} = \sqrt{n}\sigma_{\mathrm{pe}}$. This kind of noise causes a relative variation of the integrated charge q by:

$$\frac{\sigma^{q}_{n,\mathrm{pe}}}{q} = \frac{\sigma_{n,\mathrm{pe}}}{n\,\mathrm{p.e.}} \quad . \tag{8.1}$$

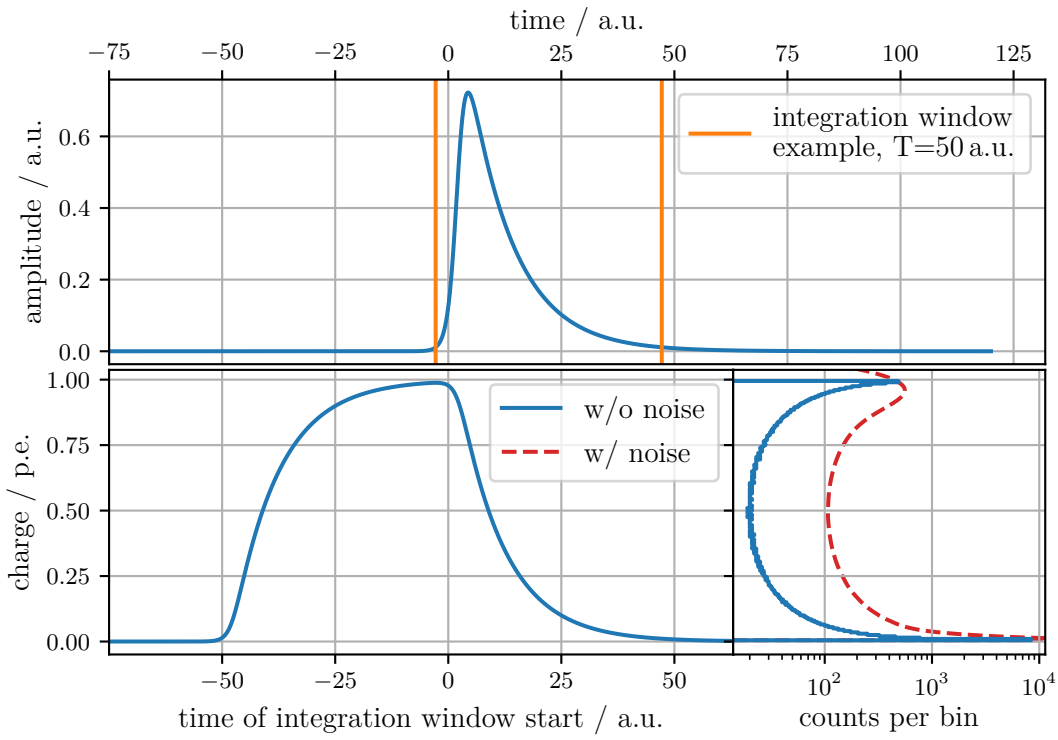

Figure 8.8: The determination of the p.d.f. to obtain a charge q when integrating a single p.e. pulse over an arbitrary region of fixed length T. At the top, the pulse is shown together with the integration window at an exemplary position. At the bottom left, the integrated charge q is shown as a function of the start time of the integration window. At the bottom right, the distribution $\hat{\mathcal{Q}}_1(q)$ of the integrated charges q is given. Assuming a noise of $\sigma_{\mathrm{pe}} = 0.05\,\mathrm{p.e.}$, the distribution is smeared out. For details see text.

To account for this noise, each bin of the distribution $\hat{\mathcal{Q}}_n(q)$ is smeared by a Gaussian distribution of width $\sigma^q_{n,\mathrm{pe}}$. The result for the case of $n = 1$ and $\sigma_{\mathrm{pe}} = 0.05\,\mathrm{p.e.}$ is shown in the bottom right of figure 8.8. After this smearing, $\hat{Q}_n(q)$ corresponds to the p.d.f. for obtaining a charge q if exactly one pulse of size n p.e. is contained in the trace of length τ.

Obviously, the size of the pulse that is measured is not known a priori. As a next step, the probability p_n of the occurrence of a pulse of size n is taken into account. It will result in the p.d.f. $\hat{Q}_{\mathrm{tot},1}(q)$ of measuring a charge q if exactly one pulse of unknown size is in the trace. It is given by the sum of all $\hat{Q}_n(q)$ weighted with their probability of occurrence p_n:

$$\hat{Q}_{\mathrm{tot},1}(q) = \sum_{n=1}^{N} p_n \hat{Q}_n(q) \qquad . \tag{8.2}$$

The values of p_n can be obtained from the dark count spectrum that has been studied in detail in other works [205]. They found that a modified Erlang distribution allows for a good description:

$$p_n \propto \frac{\left(p_{\mathrm{xt}} e^{-p_{\mathrm{xt}}} \cdot i\right)^{i-1}}{\left((i-1)!\right)^{\nu}} \qquad , \tag{8.3}$$

with p_{xt} the optical crosstalk probability and ν an additional shape parameter. The value of N in equation (8.2) can, theoretically, be the number of cells of the SiPM. Due to the low crosstalk probability of only a few percent, all effects from N larger than a few breakdowns can be neglected. Here, $N = 5$ is used because the fit does not extend further as can be seen in figures 8.3 and 8.4.

Still, the possibility of more than one pulse to occur in the trace is not included. For more than one pulse in the trace, the resulting p.d.f. can be calculated by convolutions of $\hat{Q}_{\mathrm{tot},1}$. For exactly M pulses, the p.d.f. is given as:

$$\hat{Q}_{\mathrm{tot},M}(q) = \underbrace{\hat{Q}_{\mathrm{tot},1}(q) * \ldots * \hat{Q}_{\mathrm{tot},1}(q)}_{M \text{ times}} \quad . \tag{8.4}$$

For the case of no pulse in the trace, the integrated signal q is always zero and $\hat{Q}_{\mathrm{tot},0} = \delta(0)$ with $\delta(q)$ being the Dirac δ-function.

This result can be extended to also include the probabilities f_M for M pulses to occur in the trace. The resulting p.d.f. $\hat{Q}_{\mathrm{tot}}(q)$ is the probability to measure a charge q from the random dark noise where multiple pulses of different sizes occur:

$$\hat{Q}_{\mathrm{tot}}(q) = \sum_{M=0}^{M_{\mathrm{max}}} f_M \hat{Q}_{\mathrm{tot},M}(q) \quad . \tag{8.5}$$

Assuming random dark noise with a DCR of R, a length of the integration window T and a length of the trace τ, $f_M = f_M(T, \tau, R)$ is a function of the length of the integration window T, the length of the trace τ and the DCR R. It is obtained from a Poisson distribution with mean $\lambda = (T + \tau) \cdot R$. Theoretically, M can reach the number of cells. In order to simplify calculations, the sum can be restricted to low $M \lesssim 3 \cdot \lambda$. For the studies presented here, $\lambda < 2$ is always the case and $M_{\mathrm{max}} = 5$ is chosen.

In order to include also electronics noise, $\hat{Q}_{\mathrm{tot}}(q)$ is convoluted with a Gaussian $G(\sigma_{\mathrm{el}})$ of width σ_{el} to obtain the dark count spectrum $\hat{Q}_{\mathrm{dark}}(q)$:

$$\begin{aligned}\hat{Q}_{\mathrm{dark}}(q) = A \cdot G(\sigma_{\mathrm{el}}) * \Bigg[& \sum_{M=0}^{M_{\mathrm{max}}} f_M(T, \tau, R) \\ & \cdot \Bigg(\underbrace{\sum_{n=1}^{N} p_n(p_{\mathrm{xt}}, \nu) \hat{Q}_n(q; \sigma_{\mathrm{pe}}) * \ldots * \sum_{n=1}^{N} p_n(p_{\mathrm{xt}}, \nu) \hat{Q}_n(q; \sigma_{\mathrm{pe}})}_{M \text{ times}} \Bigg) \Bigg]\end{aligned} \tag{8.6}$$

with A being a normalization constant that depends on the number of events that were measured. So far, q was assumed to be given in units of p.e.. In order also include the gain g, it can be replaced by $q = \tilde{q}/g$ with $\tilde{q}$ being the measured charge in arbitrarily chosen units that also the gain shall be measured in. The function has a total of 9 parameters: the normalization A, the gain g, the length of the trace τ, the length of the integration window T, the DCR R, the p.e. noise σ_{pe}, the electronics noise σ_{el}, the crosstalk probability p_{xt} and the shape of the modified Erlang distribution ν. Usually it is reasonable to also allow for an offset in the charge Δq such that $q \to q + \Delta q$. As mentioned before, the values for M_{max} and N need to be chosen depending on the specific case. Here, $M_{\mathrm{max}} = N = 5$ was set because the spectrum was not fit for larger pulses.

The measurements performed in the field at the Pierre Auger Observatory do not contain the pure dark count spectrum. Additional contributions arise from the physics events. As these contributions are triggered on, the pulses should always be well contained in the integration window such that the whole math described for the dark count spectrum does not need to be applied here. The contribution from real events corresponds to a sum of correlated Gaussians G being modulated with a physics function $s(n)$:

$$\hat{Q}_{\text{phys}}(q) = \sum_n s(n)\, G\left(q; \mu = n, \sigma = \sqrt{n}\sigma_{\text{pe}}\right) \quad . \tag{8.7}$$

The exact shape of the function s depends on the particular measurement. In other works [155], exponential functions were found to yield a good description of the measurements at low signals. This is sufficient here because only the background pedestal shall be described. A sum of two exponential functions is used:

$$s(n) = a \exp(b \cdot n) + c \exp(d \cdot n) \quad . \tag{8.8}$$

For the description of the measurement, both the dark count spectrum and the physics contribution need to be taken into account by calculating their convolution

$$\hat{Q}_{\text{meas}}(q) = \hat{Q}_{\text{phys}}(q) * \hat{Q}_{\text{dark}}(q) \quad . \tag{8.9}$$

This function can yield a full description of the measured spectra. It allows to extract the gain, the DCR or the p.e. and electronics noise.

Fitting the single p.e. spectrum

The function given in equation (8.9) shall be fit to the pedestal region of the spectra shown in figures 8.3 and 8.4. The number of parameters to be fit can be reduced exploiting some knowledge of the system. The length of the integration window T is 20 samples corresponding to 167 ns in the case of the UUB. The shape of the SiPM pulse $SPE(t; \tau_{\pm})$ is known from the measurements in section 6.6.8. The length of the trace τ should significantly extend the length of the pulse and is fixed to $\tau = T + 5\tau_{+} + 5\tau_{-} = 563.5\,\text{ns}$. This reduces the number of parameters by 2. The total number of parameters then is 12, 8 for Q_{dark} in equation (8.6) and 4 for Q_{phys} in equations (8.7) and (8.8).

Examples of the fit were presented in figures 8.3 and 8.4 for both SiPM SSDs. The data are well described and the fit allows a proper extraction of parameters of interest.

Results from fitting the single p.e. spectrum

From the fits performed in the previous section, the performance of the SiPMs can be evaluated. A major concern is the temperature dependency of the breakdown voltage which needs to be corrected for to allow a stable operation of SiPMs over a wide temperature range. As the gain is directly proportional to the applied overvoltage, its determination allows for the prove of the correct compensation. In figure 8.9, the gain with respect to the temperature is given. The stability is very good and better than 3 % on a temperature range of 40 °C. The average uncertainty on the gain is 2 % for station 59 and 3 % for station 41 due to the higher baseline noise of the UUB there.

For station 41, several outliers with a reduced gain are visible at low temperatures. The origin is unclear. They are also visible in the MIP signal (cf. fig. 8.5) meaning that these

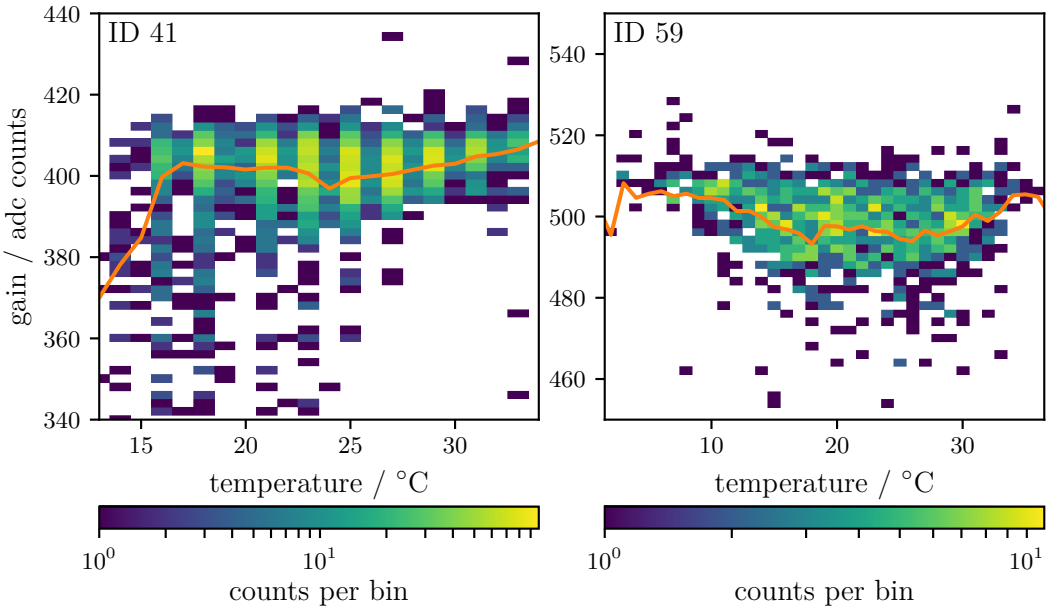

Figure 8.9: Determination of the stability of the gain of the SiPMs with temperature. The orange line indicates the median of the distributions. The gain is stable at better than 3 % over a temperature range of 40 °C. The vertical lines apparent for station 41 originate from the temperature measurement using one of the WCD PMTs with only poor resolution.

are not only failed fits. Different issues might cause this effect. The temperature sensor on the optical module might fail, leading to a wrong temperature measurement and thus to a wrong overvoltage. Alternatively, bad connections might result in a reduced signal. This could be between the main board of the optical module and the SiPM board or at the cables from the optical module to the UUB. The former two effects would affect the DCR as well, while the latter does not. The events with low gain can hence be investigated in more detail by studying the DCR. The fact that such outliers are not visible for the optical module in station 59 strongly supports a technical issue over systematic failures. The optical module of station 41 nonetheless delivers good data as the calibration is always possible.

The DCR can also be extracted from the fit and yield valuable information about the proper understanding of the performance of the SiPMs. It is sensitive to changes in the overvoltage and the temperature. It might therefore give additional information on the reasons for the peculiar behavior of station 41. In figure 8.10, the DCR is given with respect to the temperature at station 41. The events where the gain is reduced are marked. These events have a significantly lower DCR compared to the rest. This observation favors a reduced overvoltage applied at the SiPM over an issue with the connection between the optical module and the UUB. The latter would only affect the signal sizes but not the rate.

In figure 8.11, the DCR is given with respect to temperature for both SiPM SSDs. The typical statistical uncertainty from the fitting is 2 % to 3 %. The distributions are both in good agreement with an exponential function as is expected. The manufacturer gives a rate of 1.6 MHz to 5 MHz at 25 °C for a single SiPM [130]. Here, two SiPMs are operated in parallel, so that the double of these values is expected. The results in the field of

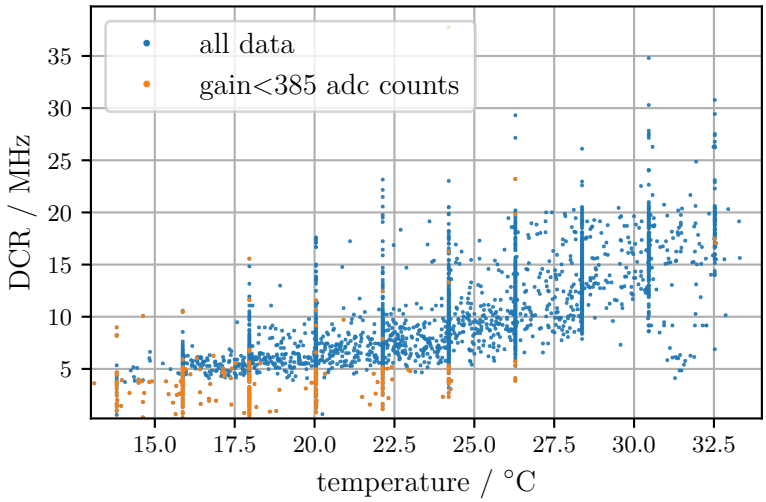

Figure 8.10: The DCR with respect to temperature for station 41. The events with a gain below 385 adc counts are marked. They show a significantly reduced DCR. The vertical lines originate from the poor resolution of the temperature sensor of the WCD PMT.

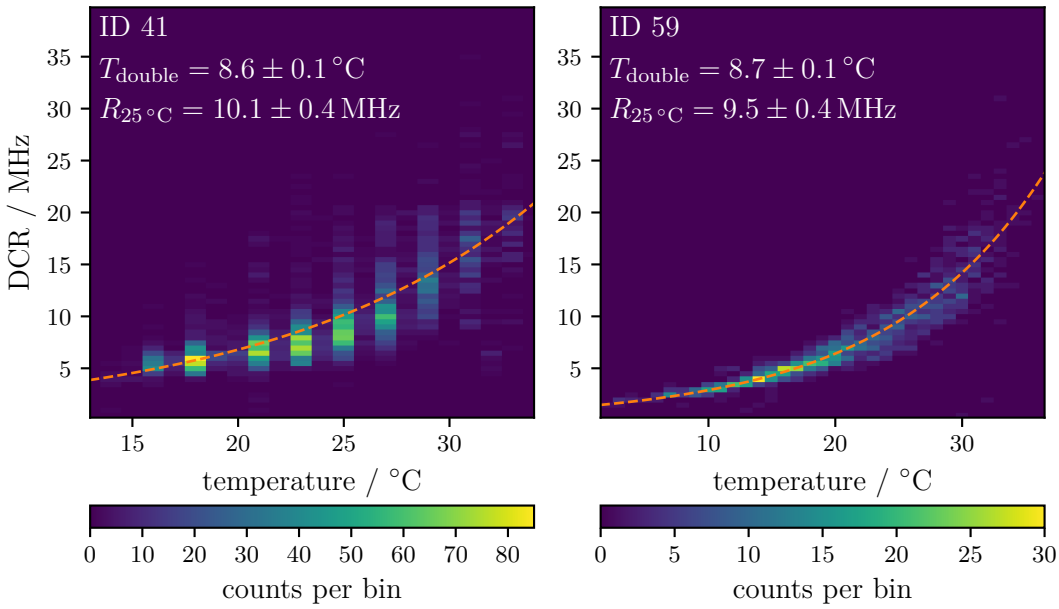

Figure 8.11: The DCR with respect to temperature for both SiPM SSDs. A fit of an exponential function denoted by the dashed orange line yields the rate at 25 °C and the temperature difference for a doubling of the rate.

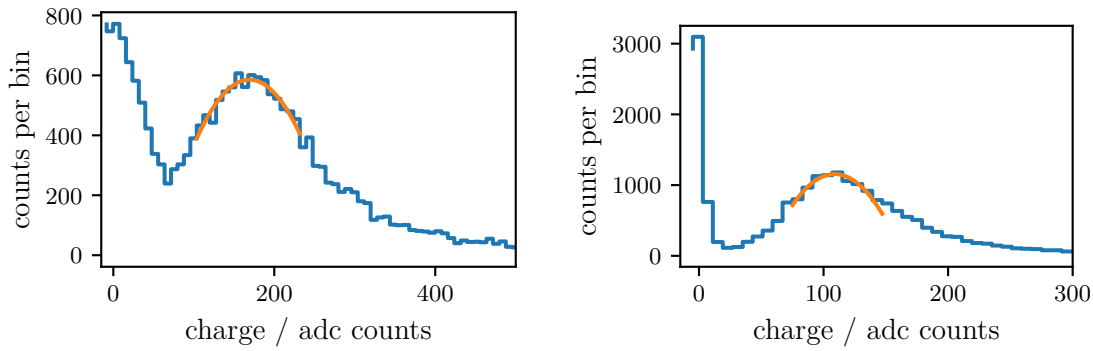

(a) ID 41

(b) ID 59

Figure 8.12: Examples of the calibration histograms measured at the HG channels with the SiPM SSDs. The orange line denotes a fit of a parabola to the data as in done in the standard calibration of the Pierre Auger Observatory. The histograms are zoomed in and extend to the right. For details see text.

$R_{25} = (10.1 \pm 0.4)$ MHz and $R_{25} = (9.5 \pm 0.4)$ MHz for stations 41 and 59, respectively, are at the upper end of this range but in agreement. The DCR might be increased due to additional photon noise from the scintillator. In the literature, a temperature change of $T_{\text{double}} \approx 8\,°\text{C}$ to $10\,°\text{C}$ for the doubling of the DCR is found [140, 149]. This is a rather rough estimate and in good agreement with the values of $T_{\text{double}} = (8.6 \pm 0.1)\,°\text{C}$ and $T_{\text{double}} = (8.7 \pm 0.1)\,°\text{C}$ for station 41 and 59.

Determination of the number of photons per MIP

As the gain of the SiPMs is known in units of adc counts, the raw MIP charge, as shown in figures 8.5 and 8.6, can be calibrated in units of p.e.. These values are also given in the figures. For both detectors a value of 28 p.e. to 29 p.e. is found. As can clearly be seen, the outliers of station 41 at low temperatures disappear due to the low gain. This calibration is a unique feature from the application of SiPMs, which would not have been possible with conventional PMTs. Thus, the reduced signals can be attributed to the optical module and are not a defect of the scintillators or WLS fibers.

These results prove the excellent understanding of SiPMs. Though these measurements were performed with a simple algorithm during standard data taking they yield fruitful information on the performance of the detector. This is usually impossible with conventional PMTs due to the lack of single p.e. resolution.

8.2.2 The HG calibration histograms

The histograms created from the signals measured with the HG channel allow for a calibration of the MIP signal. Examples measured at the two different stations with SiPM SSDs are shown in figure 8.12.

To determine the position of the MPV of the MIP signal distribution, a fit is performed. The standard calibration of the Pierre Auger Observatory uses a parabolic fit. In order to avoid any systematic bias when comparing calibrated signals from the SiPM and PMT SSDs, this is also done here.

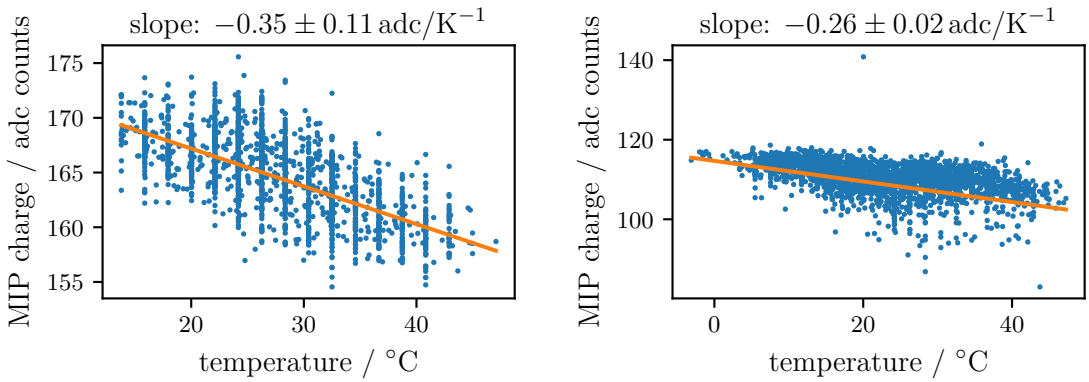

(a) ID 41

(b) ID 59

Figure 8.13: The dependency of the MIP signal on the temperature. A clear decrease with increasing temperature is visible. Uncertainties on individual MIP signal measurements are not shown for clarity but used for the displayed fit. Note the different y-axis scales.

For both SSDs, the fit is in good agreement with the data and the peak position can be extracted. For station 59, the pedestal is significantly narrower compared to station 41. This is due to the different versions of the UUB used in the two stations. The one installed at station 41 suffers from a higher baseline noise, leading to the increased width of the pedestal. For both SSDs, the MIP peak is well separated from the pedestal and therefore allows for a precise calibration of the MIP signal. The uncertainty on the individual determination of the MIP signal is $\approx 9\,\%$ for station 59 and $\approx 20\,\%$ for station 41, due to the worse separation of the peak from the pedestal.

In figure 8.13, the MIP peak is given with respect to temperature, as in the previous section. For station 41, calibration using the histograms from the HG channel is only possible for the period where the overvoltage was set to 5 V. For the lowered overvoltage, the peak is not separated from the pedestal anymore and calibration is only possible with the CG channel or through the correlation with temperature.

A clear temperature dependency can be seen for both stations. The values are in agreement within the uncertainties. The weighted average dependency is found to be $(0.27 \pm 0.02)\,\mathrm{adc/K}$.

8.2.3 Correction to the MIP signal

The algorithm running on the UUB for extracting the integrated signal produced by a through going MIP was optimized for the signals produced by the PMT. The PMT signals are significantly shorter than those produced by the SiPMs. The integration window is 20 samples long, corresponding to 167 ns. The tail of the SiPM signals with decay times of $\sim 76\,\mathrm{ns}$ is therefore not fully contained in this window. In order to correct for this effect, average traces are used. These are determined from signals that correspond to about 3 MIP during normal data taking. They are transmitted together with the calibration histograms for every event.

An example is given in figure 8.14. The pulse is significantly longer than the integration window. A correction factor is determined by integrating the full trace and relating the result

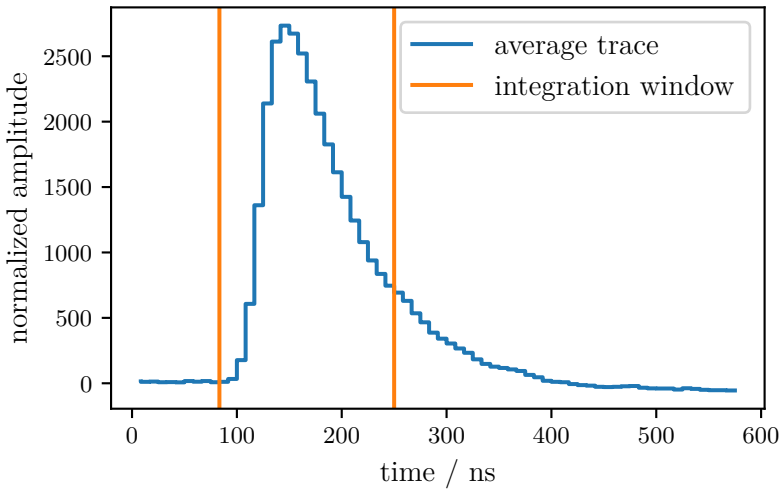

Figure 8.14: Average signal shape of the SiPM based optical module for signals of ~ 3 MIP. The integration window is significantly shorter than the pulse.

with the integral over only the standard integration window. An average of 1.24 ± 0.04 is found for station 41 and 1.14 ± 0.02 for station 59. This factor is applied to all MIP signals. The given uncertainty originates from the standard deviation over all events.

8.3 Signal extraction

The extraction of the measured signal is performed using the algorithm implemented in the standard calibration of the Pierre Auger Observatory. This is done to avoid systematic deviations between the PMT and SiPM SSDs. Nonetheless, the different shapes of pulses generated by the SiPM based optical module demand slight modifications of the parameters to be used. Compared to the PMT, the pulses from the optical module have a lower amplitude but are longer. In addition, the baseline noise of especially the HG channel of station 41 is higher than in other stations which also has to be taken into account. The details of the signal extraction algorithm are given in appendix I, together with the implemented modifications for the optical module presented here.

The algorithm was also implemented for the CG channel of the two stations in order to allow for cross calibration of the channels of the optical module. In further analyses, like reconstructions of air showers, this channel is not contained because of limitations of the Offline framework for using the additional channel.

Examples of signal traces for all three channels of both stations are shown in figure 8.15 together with the determined baseline and the regions where a signal was found according to the algorithm presented in appendix I. All events were triggered by multiple neighboring WCDs in coincidence as was described in section 4.2. These traces are not from the same events and selected in the sense that a medium sized pulse was taken for each channel. Multiple signals might be found for each channel by the algorithm.

The signals show an undershoot after the pulse. The baseline extraction algorithm corrects for this effect and additional pulses can be detected also in that region. For large pulses, the undershoot of the CG channel can hit the lower end of the allowed range of the ADC. For these signals, no information from the CG channel is used any further analysis.

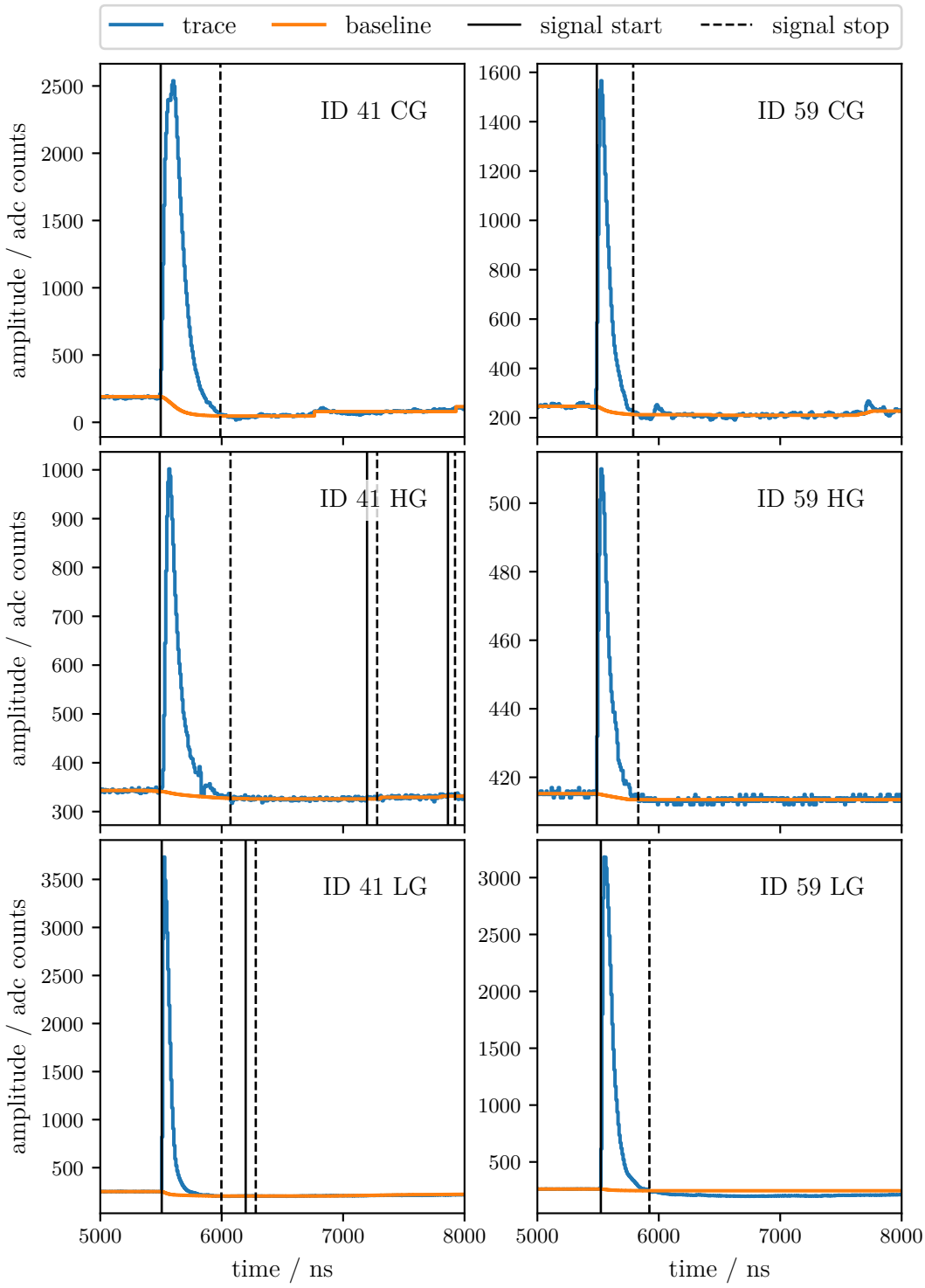

Figure 8.15: Examples of traces measured with the different channels of the two SiPM SSDs. Note the different y-scales.

The algorithm extracting the total signal only considers ranges where the measured trace is above the baseline. The minimum signal is thus zero if no proper pulse was found.

8.3.1 Cross calibration of channels

The conversion of the signals measured at the different channels is performed in the overlapping regions. The correlations are given for both stations in figure 8.16. A good correlation is visible and a linear fit allows for the conversion of signals between the different channels. Several quality cuts were applied to select only reasonable events. None of the two channels must be saturated and the undershoot must always stay above the lower limit of the ADC range. In addition, signals must be larger than zero to discard events where pulses were not found accidentally or the baseline was badly determined. For the case of the conversion from the CG channel to the HG channel of station 41, the lowest allowed signal for the CG was 22 000 ADC counts. For lower signals the fluctuations around the mean value are not symmetric anymore because of the restriction to purely positive signals in the pulse finding algorithm.

The found conversion factors are used in all following analyses.

8.4 Comparison with neighboring PMT SSDs

As can be seen in figure 8.1 on page 158, the stations where an SSD with the SiPM based optical module is installed are neighbored by a standard PMT SSD. Due to the small distances of $\sim 10\,\mathrm{m}$, both stations measure the same shower at almost the same distance to the shower core. This feature allows for a comparison of the measured signals for the same air showers. The signals should be strongly correlated though systematic differences might arise if the shower cores are near the stations resulting in a steep LDF.

It should be noted that, for most of the events used in this analysis, a reconstruction of the shower parameters is not possible. The events were just sufficient to generate a trigger of the readout to be saved. A discussion of reconstructed air showers will follow in section 8.4.1. In figure 8.17, the correlation of the signals is shown.

For the stations 59 and 56, which are located in the regular array, a total of 796 events shows a very good correlation. Due to the sparse spacing in the regular array, the trigger rate is rather low and the average distance to the shower core is large. Only a low number of events therefore contains large signals. For the largest events around 10 000 MIP, the non-linear response of the SiPMs results in a reduction of the signal. This effect might be corrected for using the algorithm presented in chapter 6.8. For this analysis, the effects on the signals due to the electronics of the optical module and the UUB needs to be known. This study could not be done here due to a lack of a UUB for laboratory measurements.

The stations 41 and 22, being located in the AERAlet, show a significantly higher trigger rate resulting in 80 187 coincident events, due to the triggering on lower energetic air showers. A clear correlation of their signals is evident. For signals < 200 MIP, the distribution is well centered around the ideal line as expected. As for station 59, the non-linearity of the SiPM becomes visible at around 10 000 MIP. The PMT pulses saturate the ADC before any saturation effect from the PMT itself can be observed. For signals > 200 MIP, the SiPM based optical module shows on average a larger signal than the PMT. This effect can be seen in detail in figure 8.18. The large signals measured in these stations originate from low energetic air showers with a shower core close to the stations. Therefore, the steepness of the LDF has a significant influence on the relative differences in the signals between both

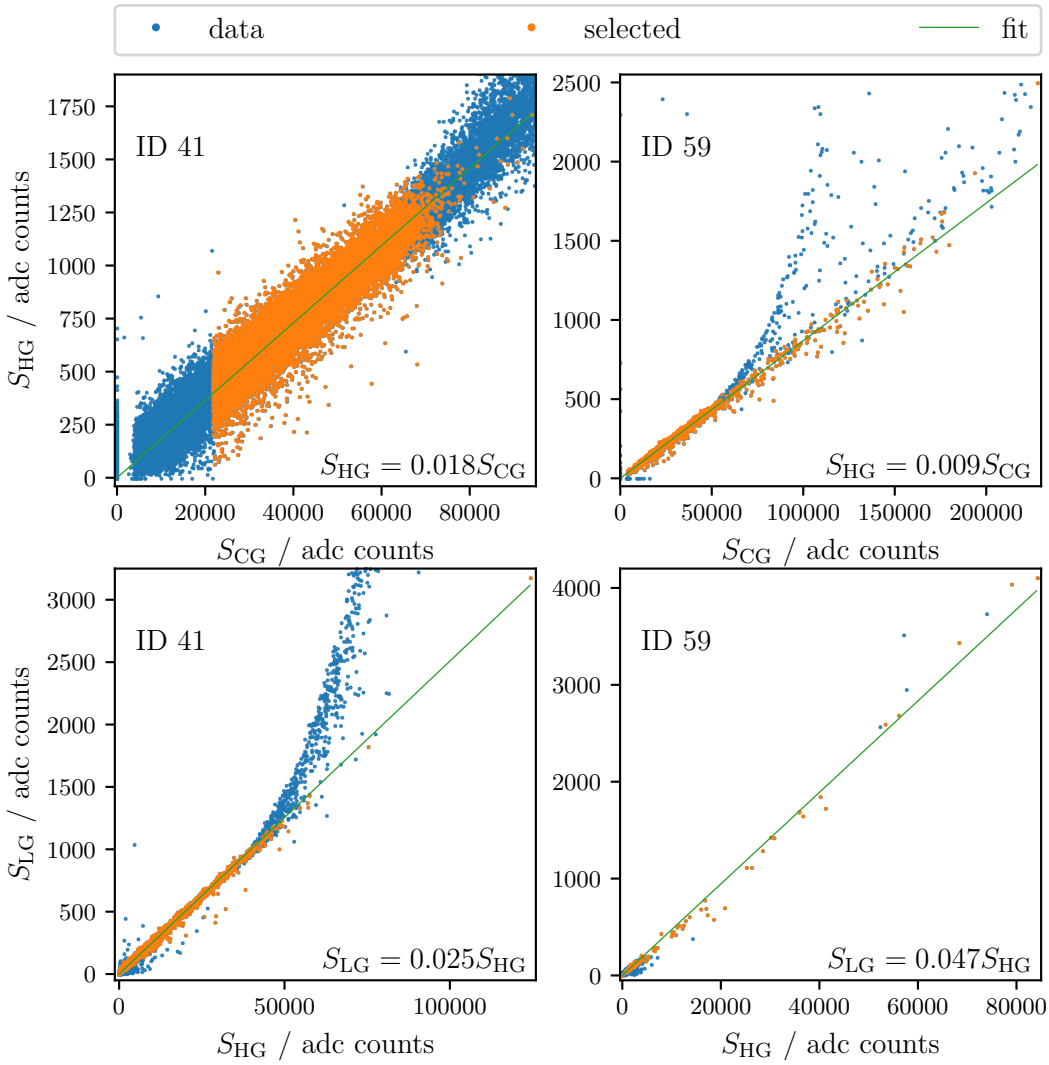

Figure 8.16: Cross calibration of the channels of the optical module. The fits are performed on the *selected* data. The main criterion for data to be *selected* is that non of the two channels is saturated. Additional quality cuts are described in the text.

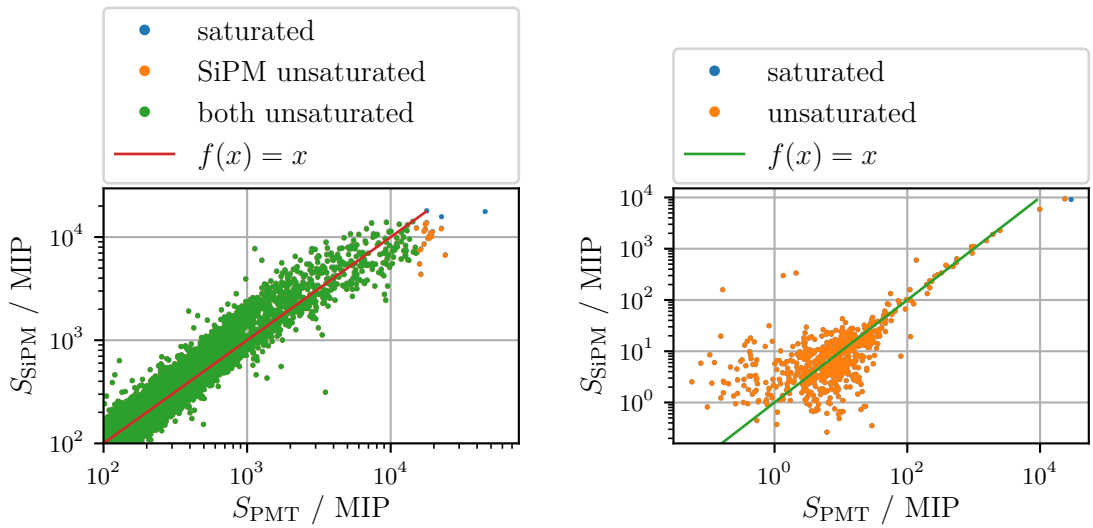

(a) stations 41 & 22

(b) stations 59 & 56

Figure 8.17: Comparison of the signals measured in the SSDs equipped with the SiPM based optical module and a neighboring PMT SSD. *(a):* In this representation it can clearly be seen that the PMT signals saturate the ADC at lower signals than the SiPM signals. A 2D-histogram is shown in figure 8.18. Note the different axis scales in the two figures. *(b):* A clear correlation of the signals is visible. For the event labeled *saturated*, the voltage amplitude exceeds the dynamic range of the ADC in both stations.

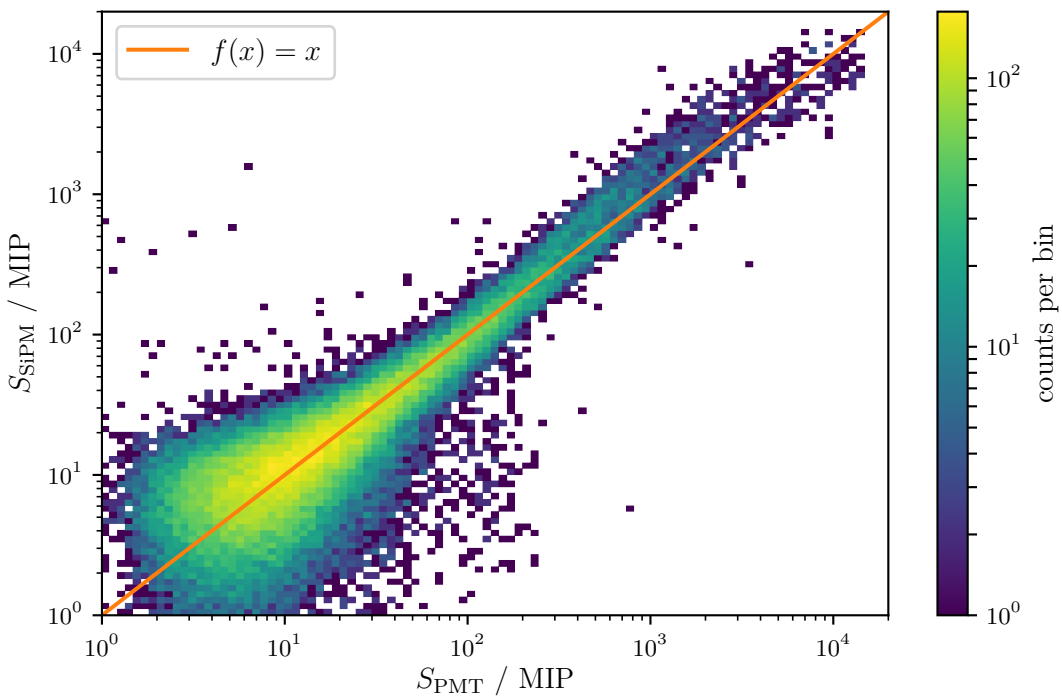

Figure 8.18: Correlation of the signals measured in the SSDs of station 41 and 22.

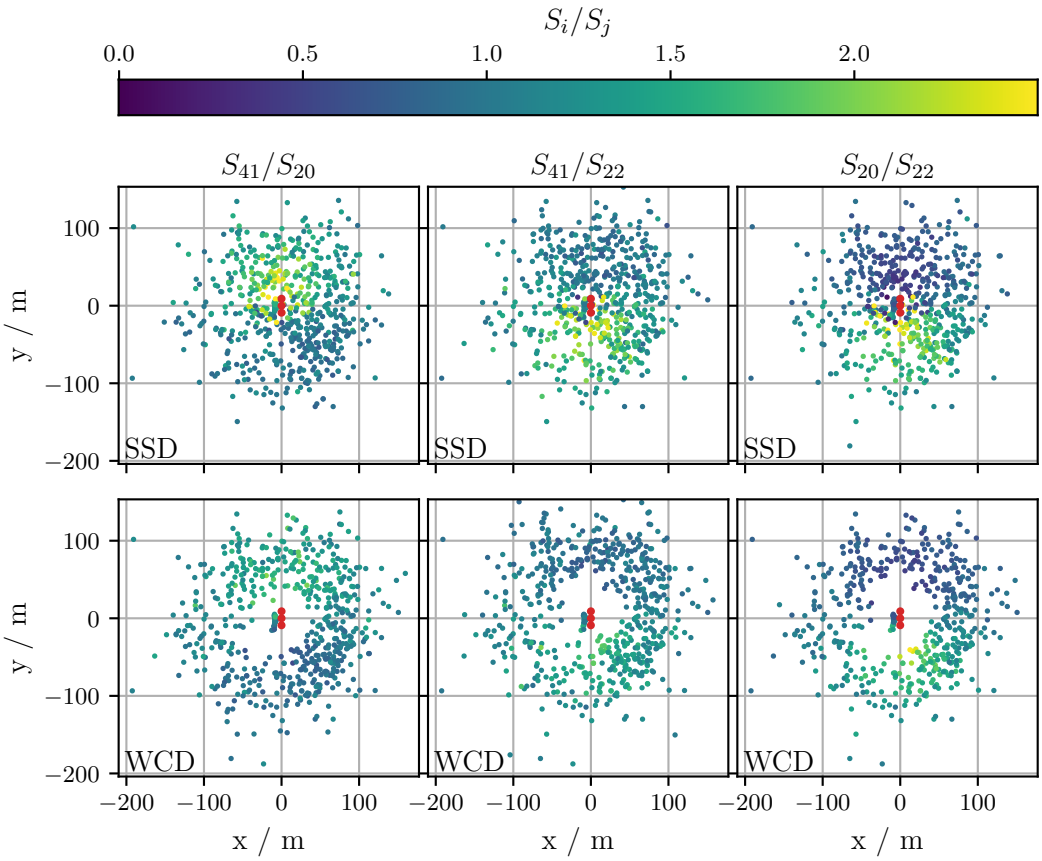

Figure 8.19: The signal ratios measured in the SSDs and WCDs of stations 20, 22, and 41 with respect to the position of the shower core. Only events where the SSD or WCD have, in both compared stations, a signal above 200 MIP or VEM, respectively, are selected. The three red points mark the stations 22, 41, and 20 from top to bottom as can also be seen in figure 8.1a. The ring like structure for the WCDs originates from saturation when the shower is too close.

stations. In contrast, for stations 59 and 56 in the regular array, the distance to the shower core is larger meaning a locally flat LDF.

The effect is studied using air showers that have a proper reconstruction of the position of the shower core. The reconstruction allows for a determination of the spatial distribution of the air showers around the stations of interest. In figure 8.19, the ratio of the measured signals in the SSD or WCD, respectively, of stations 20, 22, and 41 is given with respect to the location of the shower core.

A clear asymmetry is visible for all compared stations. The station that is closer to the shower core also shows a larger signal, as expected. This is the result of the steep LDF close to the shower core. The ratios show similar behavior for the SSD and WCD. The asymmetry is stronger for the SSD due to the steeper LDF of the electromagnetic part of the air shower compared to the muonic part.

In figure 8.20, the distributions of the determined signal ratios are shown. It is clearly visible that the distributions of the comparison of station 41 with the other two deviates from the comparison of station 20 with station 22. The effect is the same in the WCD

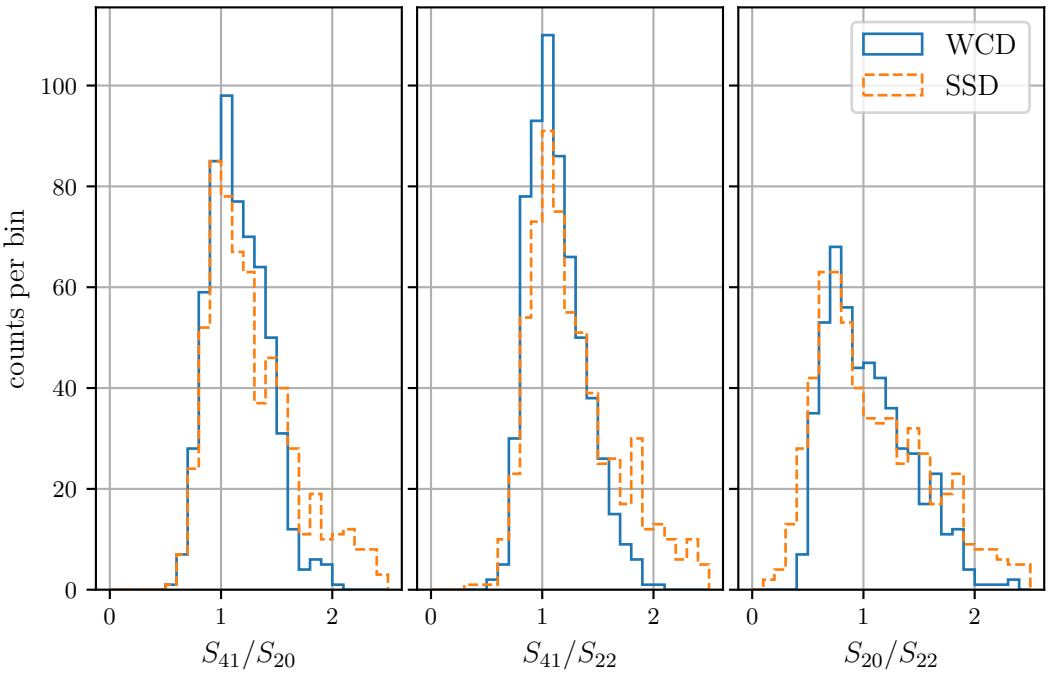

Figure 8.20: The distribution of the signal ratios for the WCD and SSD given for the signals shown in figure 8.19.

and in the SSD. The on average larger signal measured in the SSD of station 41 therefore seems to be an effect of the station and not of the SiPM based optical module. At these low distances from the shower core, local effects of the air showers become very important and inhomogeneities in the distribution of the core positions can have a significant impact on the measurement. The trigger is driven by the old station 1764 in coincidence with the surrounding stations which are 433 m apart. Station 1764 is the closest to station 41 and has similar distances to the stations 20 and 22, making plausible an effect of the trigger to produce such an inhomogeneity. The statistics are too low to properly study possible inhomogeneities of the positions of the shower core.

8.4.1 Comparison of reconstructed air showers

For a fraction of the events shown in the previous section, a reconstruction of the parameters of the air showers is possible. The analysis is restricted to showers with a reconstructed zenith angle $\theta < 32°$, as was also used in other analyses [208]. This reduces systematic effects due to attenuation in the atmosphere for highly inclined showers. For the data used here only a proper determination of the LDF using the signals of the WCDs is requested. The status of the reconstruction using the SSDs is not used.

For the AERAlet, the sample contains 95 470 events of which 19 462 have a signal in station 41. For the regular array, it is 816 events of which 54 contain a signal in station 59. The standard reconstruction using the WCDs already allows to draw conclusions on the signal in the SSD with respect to the distance to the shower core. The reconstruction used in the AERAlet where station 41 is located is optimized for the fine grid and therefore

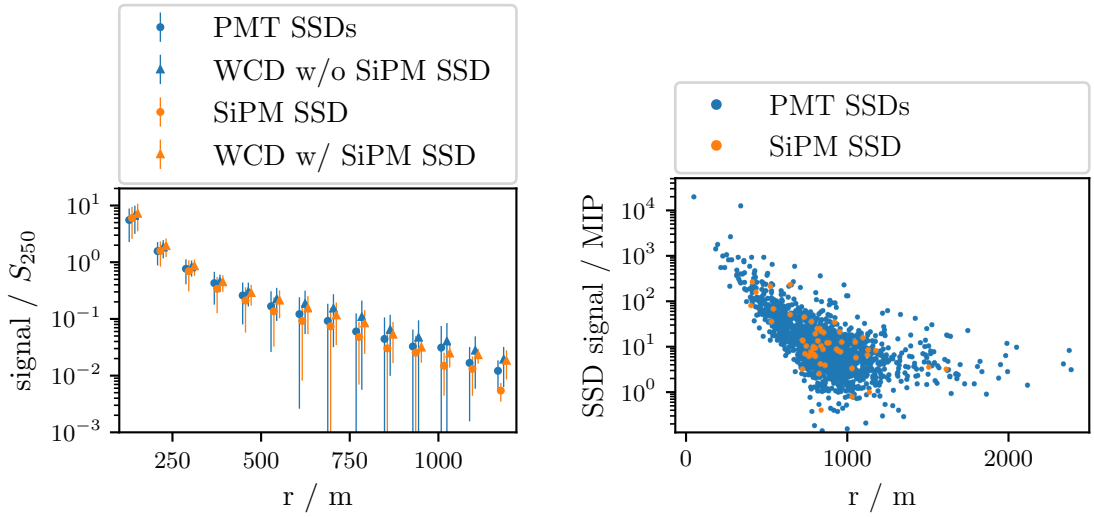

(a) station 41

(b) station 59

Figure 8.21: The lateral distribution of the signals measured in the SSD. *(a):* A profile of the signal distributions measured in the WCDs and SSDs. The signals are divided by the shower size to compensate the different energies of the primary particle. The errorbars represent the widths of the distributions. A good agreement can be observed. Data points are slightly shifted horizontally to improve visibility. *(b):* For station 59 only 54 events are found such that a determination of a profile as in *(a)* is not meaningful. The distributions of the PMT and SiPM SSDs are in agreement.

not directly comparable to the reconstructions in the standard array used for station 59. Especially, the different energy ranges can cause significant deviations.

In figure 8.21, the measured signals in the SSD with respect to the distance to the shower core are shown using all shower events. All PMT SSDs are combined resulting in a significantly higher statistics compared to the SiPM SSDs.

For the AERAlet with station 41, a profile of the signals divided by the shower size determined from the reconstruction using the WCDs is shown. The profile of the SiPM SSD is in good agreement with the result from the PMT. The signal drops slightly faster for the SSD compared to the WCD. This is a result of the decreasing contribution of the electromagnetic component to the signal far from the shower core.

For station 59 in the regular array, statistics are too low to study the profile. The events are in good agreement with the measurements of the PMT SSDs.

A more detailed study on reconstructed events with focus on physics conclusions will be given in section 8.6.

8.5 Conclusion on the SiPM based optical module

The SiPM based optical module shows the same behavior as the PMT. No systematic differences were observed. At signals of around 10 000 MIP, saturation effects of the SiPM become significant. As had been shown in section 6.8, this effect can be corrected for and an improvement of the linearity by at least one order of magnitude seem plausible. This

brings the dynamic range into a regime where no events were detected with the presented setup.

The single p.e. resolution of the SiPMs allows for a precise calibration of the response of the detector. At the same time it will be possible to monitor long term effects such as a decrease in the light yield of the scintillators or WLS fibers during regular operation. This is not possible with conventional PMTs, due to the lack of single p.e. resolution.

The SiPM based optical module is a mature alternative compared to the conventional PMTs. It achieves at least equal performance and is well suited for physics measurements.

8.6 Towards a composition study with the SSD

The main goal of the installation of the SSD at the Pierre Auger Observatory is the improvement of the sensitivity of the surface detector on the mass of the primary particle. As has been described in detail in section 3.2, the possibility for discrimination between different primary particles originates from the differences in the relative contributions of the electromagnetic and muonic shower components. As showers initiated by heavy particles have a large number of muons, these should also show a comparably larger signal in the WCD. Analyses using only the signals from the WCD cannot disentangle the signals originating from the muonic and electromagnetic shower components.

In this short analysis, the effect is studied based on simulations and data in order to understand if this goal can be achieved with SSD. The data is based on the Preproduction Array (PPA), a part of the Pierre Auger Observatory where 77 SSDs were installed in the regular array with 1500 m spacing. The data taking started in March 2019 using the UB because the new UUB was not available yet. One of the WCD PMTs was disconnected and replaced by the SSD PMT. Due to the relatively large size of this array, reasonable statistics could be collected to allow for first analyses.

The stations in the AERAlet are not surrounded by upgraded stations. The reconstruction of the LDF using only the SSDs around station 1764 (cf. fig. 8.1a) is not reliable due to their small spacing. The high event statistics from this sub-array can therefore not be used in this analysis.

The reconstruction of the LDF measured with the SSDs was implemented in the scope of another thesis [208]. Details can be found there and will not be discussed here. An example of a reconstructed LDF of both the SSDs and the WCDs is shown in figure 8.22. It also involves the SiPM SSD of station 59. The different shape of the LDF measured with the SSDs compared to that from the WCDs is well visible. This difference can be used to study the composition.

In order to improve data quality, for selected events the LDF had to be successfully reconstructed using at least three SSDs. The maximum zenith angle is $\theta = 56°$ as other studies have shown poor reconstruction efficiency for higher zenith angles [208].

8.6.1 Simulations

For a proper interpretation of the measurement, simulations need to be performed. For this analysis, the response of the Pierre Auger Observatory on air showers simulated with the CORSIKA software [46] is simulated and the air shower is reconstructed. The CORSIKA showers are taken from libraries generated for the Pierre Auger Observatory [210] using the EPOS-LHC hadronic interaction model [211]. The simulation of the response and reconstruction of the observatory was performed in the scope of another thesis [212].

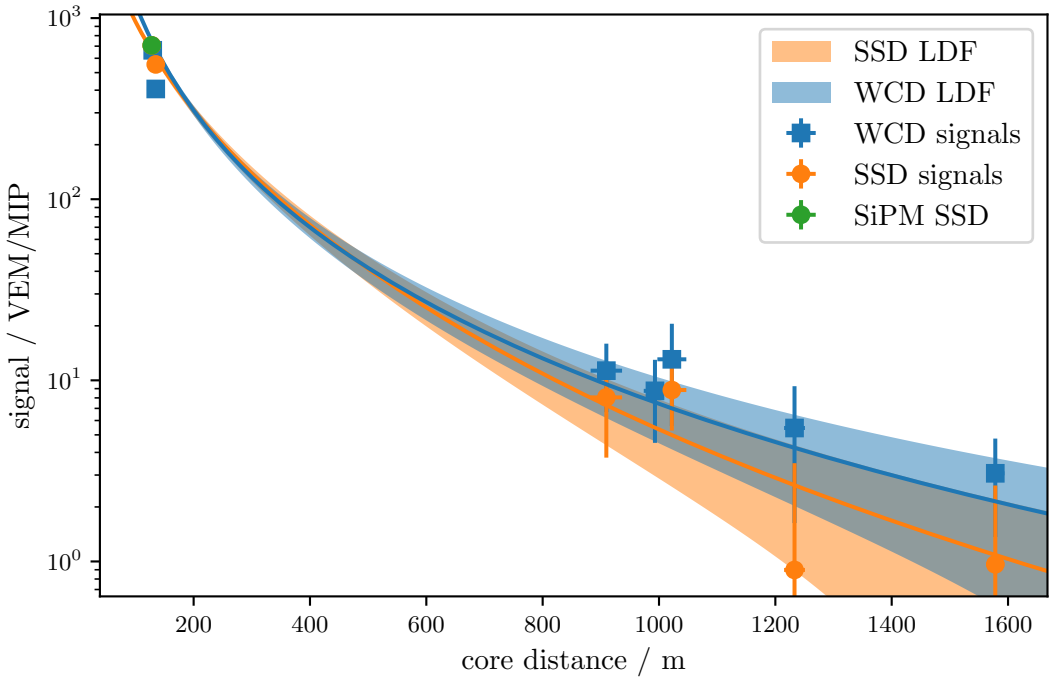

Figure 8.22: An example for the LDFs measured for one event with the SSD and WCD. A clear difference in the shape of the two is visible.

For the simulations, iron and proton primaries in the energy range of $10^{17.5}\,\mathrm{eV} < E < 10^{20.2}\,\mathrm{eV}$ with a spectral index $\gamma = 1$ are used. They are reweighted to represent the measured spectrum with $\gamma = 2.7$. The set is split in energy bins of width 0.5 in the logarithmic energy. A total of around 5000 air showers is simulated per bin for proton and around 2500 for iron. The differences in the number of simulated air showers are taken into account in the further analysis by weighting each air shower with the inverse of the total number of air showers of that primary in that energy bin. Each shower is reconstructed five times with different random locations of the shower core. For the rest of the analysis, only reconstructed variables such as the energy are used.

The simulated energy spectra are shown in figure 8.23 together with the spectrum as measured with the WCDs only. The simulations are scaled to match the integrated flux of the measurement over the shown energy range. The agreement between data and simulation is very good for both primary particles. Events with reconstructed energies below $10^{18}\,\mathrm{eV}$ are excluded from the analysis. Full efficiency of the array is only reached around $E = 10^{18.5}\,\mathrm{eV}$ so that even the first bin should be taken with caution. As the spectrum agrees well between data and simulation also in that bin it is still considered for this analysis.

8.6.2 The reconstructed LDFs

The main impact of the mass of the primary particle on the development of an air shower is expected to be in the relative contribution of the electromagnetic and muonic components. Due to the different response of the SSD and WCD to these two components, also different relative signals are expected. A first step is therefore to study the ratio of the signals.

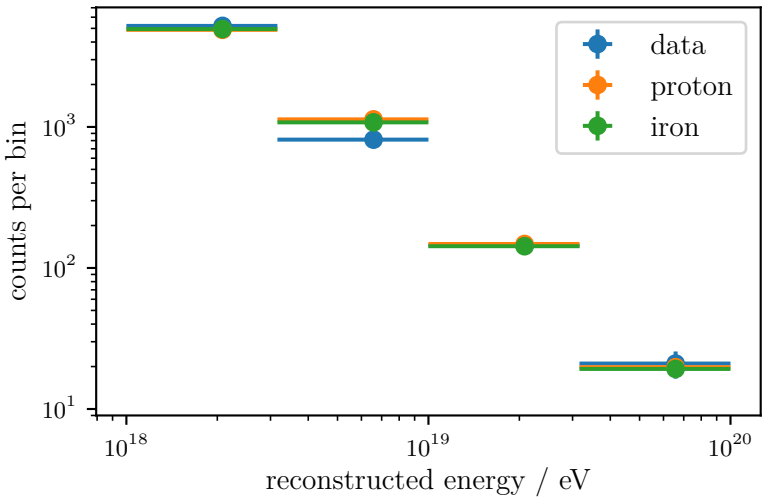

Figure 8.23: Comparison of the measured and simulated energy spectra. They agree well in the studied energy range. The errorbars along the energy represent the width of the bins of the histogram.

For individual stations, the signal ratio might suffer from significant fluctuations. It seems more feasible to use the reconstructed LDFs as it considers the information of all triggered stations. In figure 8.22, an example of the reconstructed LDFs of an air shower is shown. The different shapes can well be seen.

In order to study the characteristics of the LDFs, their average over the whole energy range is calculated in dependence of the distance to the shower core. The different energies are taken into account by dividing the LDFs by S_{1000}^{WCD}, the signal at a distance of 1000 m to the shower core of the LDF of the WCD. The resulting average LDFs are shown in figure 8.24, together with their ratio. The LDFs reconstructed using the WCDs lie on top of each other due to the scaling with S_{1000}^{WCD}. The LDFs of the SSDs reveal a slight difference between the simulations with proton and iron primaries. In the ratio, this difference becomes more evident though the distributions have significant overlap. The average LDF from the measurement is in good agreement with the iron simulation.

8.6.3 The merit factor

The feasibility of separating between proton and iron induced air showers is determined by calculating the merit factor MF as a function of the distance with

$$MF = \frac{|\mu_1 - \mu_2|}{\sqrt{\sigma_1^2 + \sigma_2^2}} \tag{8.10}$$

with $\mu_{1,2}$ and $\sigma_{1,2}$ the mean and standard deviations of the distributions to be compared. The results separated in four bins in the reconstructed energy are shown in figure 8.25. The distance of the highest merit factor varies from 630 m to 1300 m with only a low dependency of a few percent over several hundred meters. The merit factor is clearly best at the highest energies but still low with a maximum value of $MF = 0.42$. Other more complex studies based on simulations presented in [36] found a value of $MF = 1.54$ which

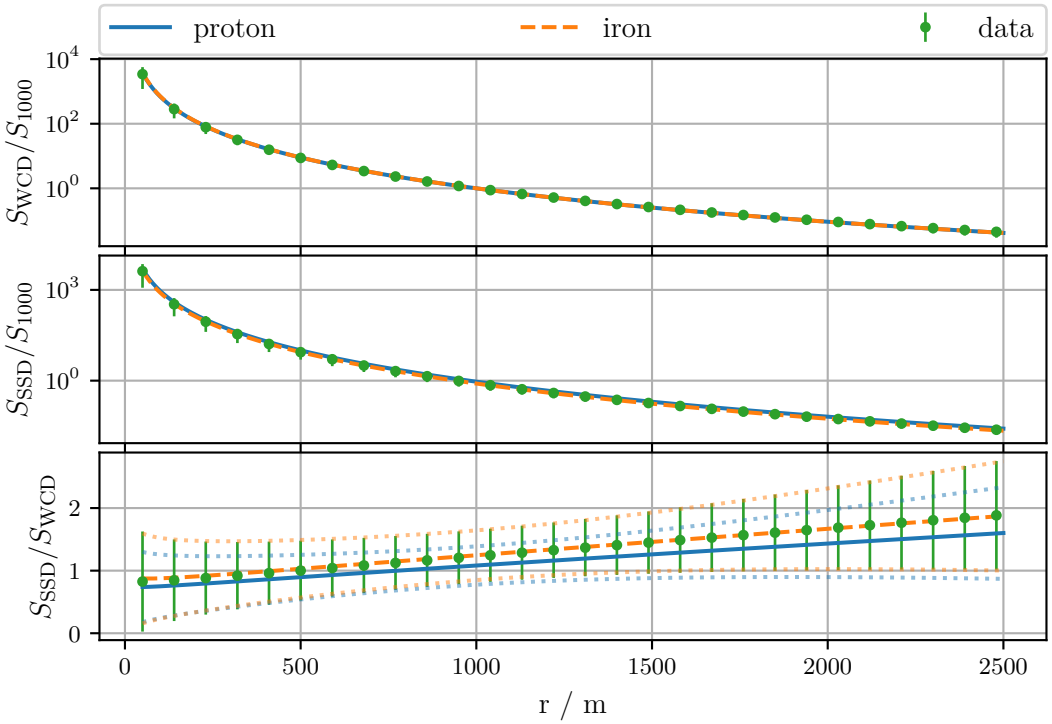

Figure 8.24: The average of the LDFs reconstructed with the WCD and SSD divided by S_{1000}^{WCD}. A comparison of data with simulations using proton and iron as primary particles is given. *Top, center:* For simulations with proton and iron only the average is shown for clarity. For data, arbitrary equally distant points along the LDF are given with the width of the distributions. *Bottom:* Solid and dashed lines represent the mean ratio of the LDFs of the WCD and the SSD. The dotted lines indicate the width of the distributions. Data points are also shown together with the width of the distribution.

promises significantly better separation. The analysis shown here is only a first step towards a measurement of the composition.

For the following analysis, the data at a distance from the shower core of 1000 m will be used. Other works have studied the systematic uncertainty due to the parametrization of the LDF on the determined signals [105]. The uncertainty was found to be the lowest at a distance of 1000 m and it is, therefore, a reasonable choice here. The merit factors at this distance are also very close to the maximum for all energies.

8.6.4 The composition

In figure 8.26, the distributions of the ratio of the signals in the WCD and SSD, determined by evaluating the LDFs at 1000 m from the shower core, are given. A shift between the simulated distributions for proton and iron is apparent. It allows for a study of the average composition of all measured events. Due to the significant overlap of the distributions for proton and iron primaries, a determination of the primary particle type on an event-by-event basis seems unrealistic with this analysis. As it does not contain all information of the measurement such as the exact shape of the LDF, better results can be expected from more

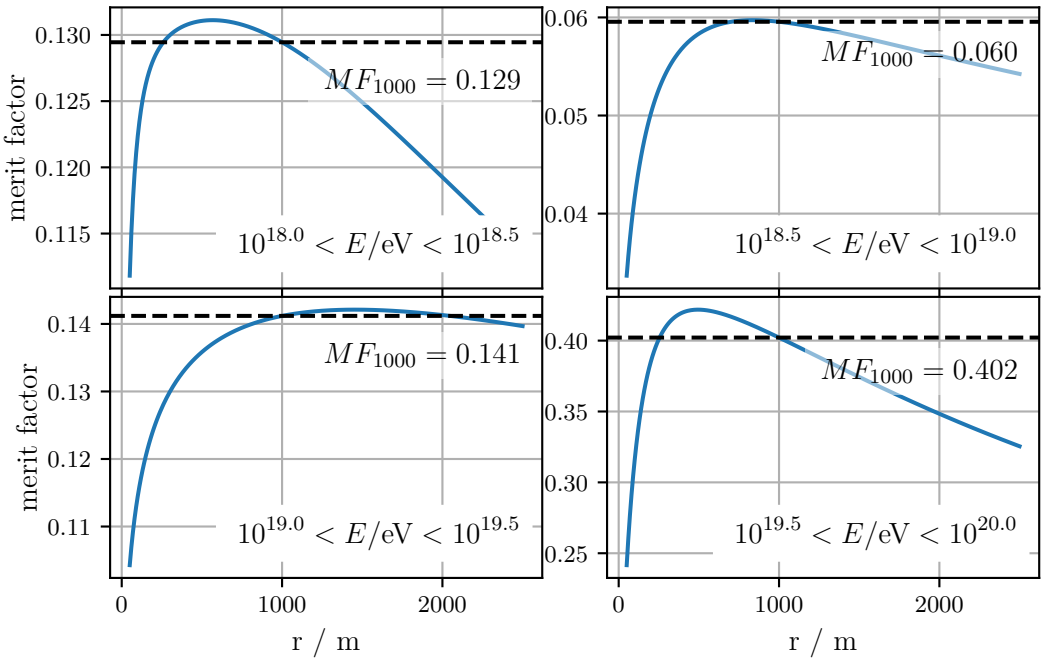

Figure 8.25: The merit factors as defined in equation (8.10) for discrimination between proton and iron induced air showers determined from simulations. Energies are reconstructed by the SD and not taken from the simulation. The black dashed lines indicate the merit factor at 1000 m from the shower core.

complex analyses. This is also indicated by the larger merit factor found in [36] compared to the analysis presented here.

The data is in very good agreement with the iron distribution for all energies. Due to the steep spectrum only 11 events are contained in the highest energy bin leading to large uncertainties. The resulting energy dependent composition from calculating the mean and its uncertainty for all distributions is given in figure 8.27. As seen before, the data is well described by simulations with iron primary particles. A contribution from other primary particles is not necessary. The composition is independent of the energy.

An additional observable feature is the decrease of the average ratio $\langle S_{1000}^{\mathrm{WCD}}/S_{1000}^{\mathrm{SSD}}\rangle$. This is a result of the relative reduction of the muon content in an air shower with increasing energy as was shown in section 2.4.2.

Systematic uncertainties

Different sources of systematic uncertainties have an impact on the final result. The main origin of these is the tuning of the analysis on simulations and the application on data. The deviations between simulations and data can significantly affect the final result.

A source of systematic uncertainty is the muon excess that was observed in data compared to simulations (cf. sec. 2.4.3). As muons produce a relatively higher signal in the WCD than in the SSD, increasing the number of muons would also result in a higher ratio $S_{1000}^{\mathrm{WCD}}/S_{1000}^{\mathrm{SSD}}$. According to the measurements, the number of muons in an air shower has to be increased by a factor of 1.3 to 1.8 to match the data [48]. As the hadronic interaction model EPOS-LHC used here produces a rather high number of muons, a value at the lower end of 30 % is

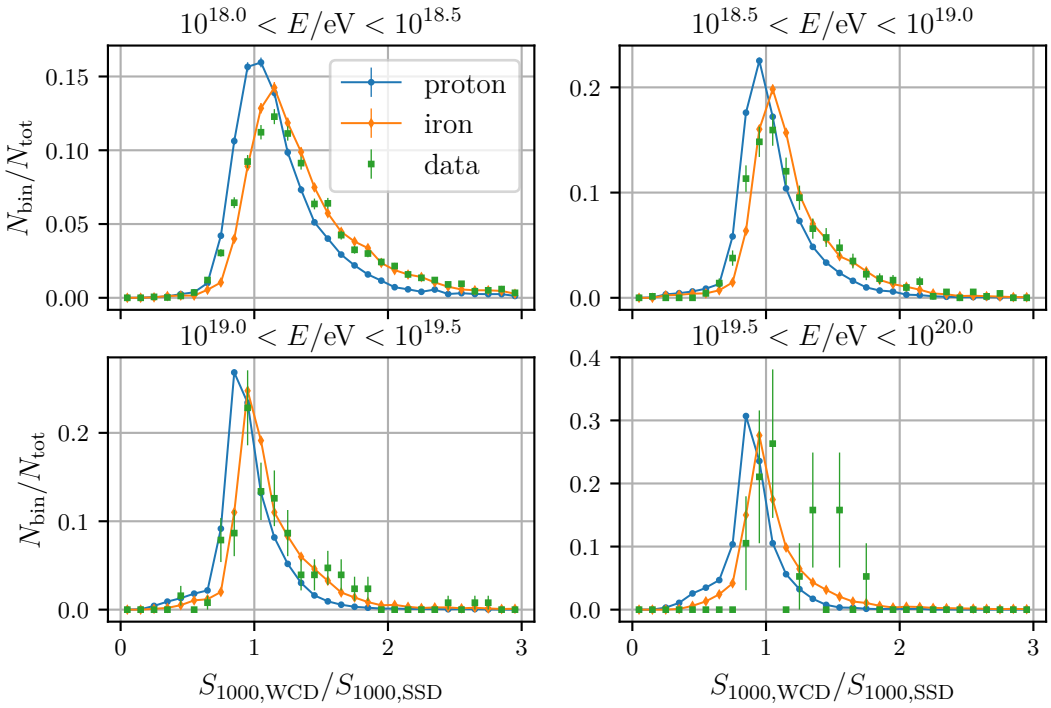

Figure 8.26: Distribution of the ratio of the LDF of the WCD and SSD at 1000 m from the shower core. The histograms are normalized to the total number of events per dataset. The distributions for proton and iron primary particles are obtained from simulations. Energies are reconstructed by the SD and not taken from the simulation.

assumed. In order to estimate the impact of a higher muon number, their influence on the total estimated signals must be derived. In the simulations, for each individual station the total signal S, the number of muons N_μ, the number of electrons N_e, the number of photons N_γ and the total number of particles N_{tot} is given for the WCD and SSD separately. N_{tot} also contains other particles that were not mentioned before, such as hadrons. They are connected by

$$S = \sum_{i=\mu,e,\gamma,\mathrm{other}} S_i N_i \tag{8.11}$$

with S_i representing the average signal produced by one particle of type i and $N_{\mathrm{other}} = N_{\mathrm{tot}} - N_\mu - N_e - N_\gamma$. In order to understand the impact of additional muons, S_μ needs to be known for the WCD and SSD, respectively. It can be obtained by fitting equation (8.11) to the simulations where S and the N_i are known. The values for S_i are dependent on the energy and zenith angle of the particles. Here, they are determined for each energy bin separately. In addition, the data is split in five equal bins in $\cos(\theta)$. In the composition analysis, the LDF is evaluated at 1000 m from the shower core. Hence, for estimating the systematic uncertainty only data of stations being in a range of 900 m to 1100 m from the shower core is taken into account. The stations must also be hit by at least five muons to have a significant contribution. Equation (8.11) is fit to the data for each bin in energy and zenith separately to obtain individual S_i. These allow to determine the average fraction f_μ of the signal produced by muons through averaging over the signal produced by muons

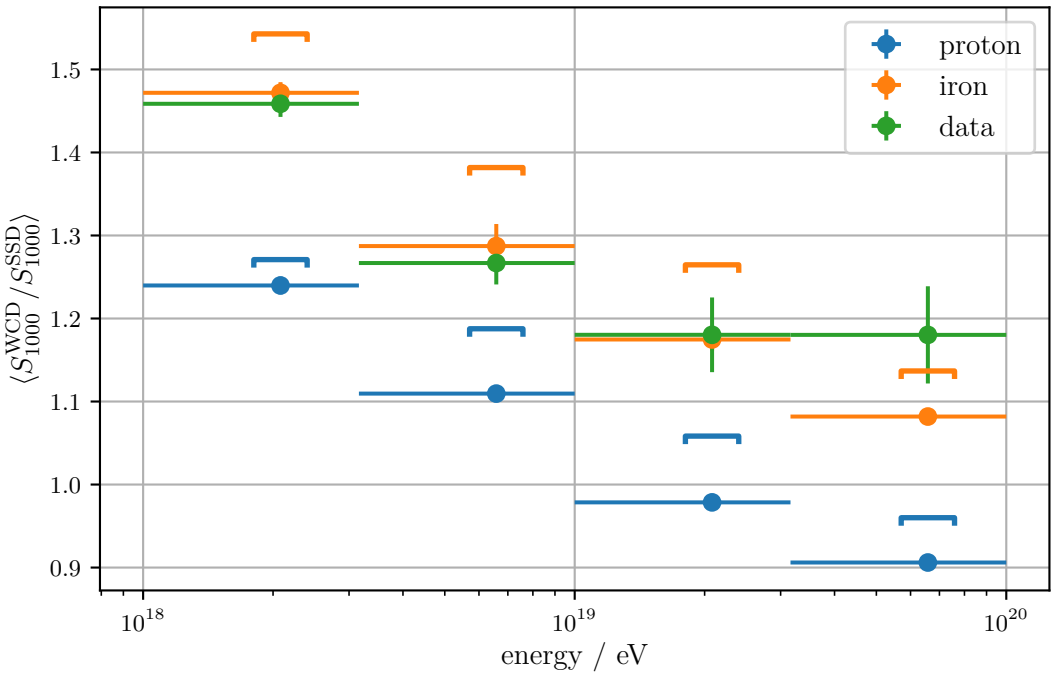

Figure 8.27: The composition as determined from the ratio of the signals in the WCD and SSD at 1000 m from the shower core. An estimate of the systematic uncertainty due to the lack of muons seen in simulations is given by the caps. For details see text.

divided by the total signal at a station:

$$f_\mu = \langle \frac{S_\mu N_\mu}{S} \rangle \qquad . \tag{8.12}$$

The values for f_μ are shown in figure 8.28 for all energy and zenith bins separated for proton and iron primaries and for the WCD and SSD. At the lowest energy bin, the number of contained events is low due to the small shower size such that this bin should again be taken with some doubt. The fraction of signal produced by muons in the SSD is lower than in the WCD as expected. Parabolas are fit to achieve a reasonable parametrization of the zenith dependency.

Using these parabolic parametrizations, the composition analysis is repeated. For each signal S_{1000}^{WCD} or S_{1000}^{SSD}, a corresponding fraction f_μ is scaled up by the muon excess of 30 % before taking the average as shown in figure 8.27. The result is given by the caps in that figure. Compared to the original analysis, the conclusion would be a lighter but mixed composition. Only at the highest bin, the best agreement is still with a pure iron composition.

It should be noted that this ansatz is influenced by several effects. As the total energy of the shower is unchanged, adding muons would result in removing other particles or at least removing energy from them. This is not taken into account here and is probably impossible as long as no proper hadronic interaction model is able to reproduce the correct number of muons as seen in data. The spatial distribution of the additional muons is unknown. For this analysis it is assumed that it follows the same distribution as is simulated. This

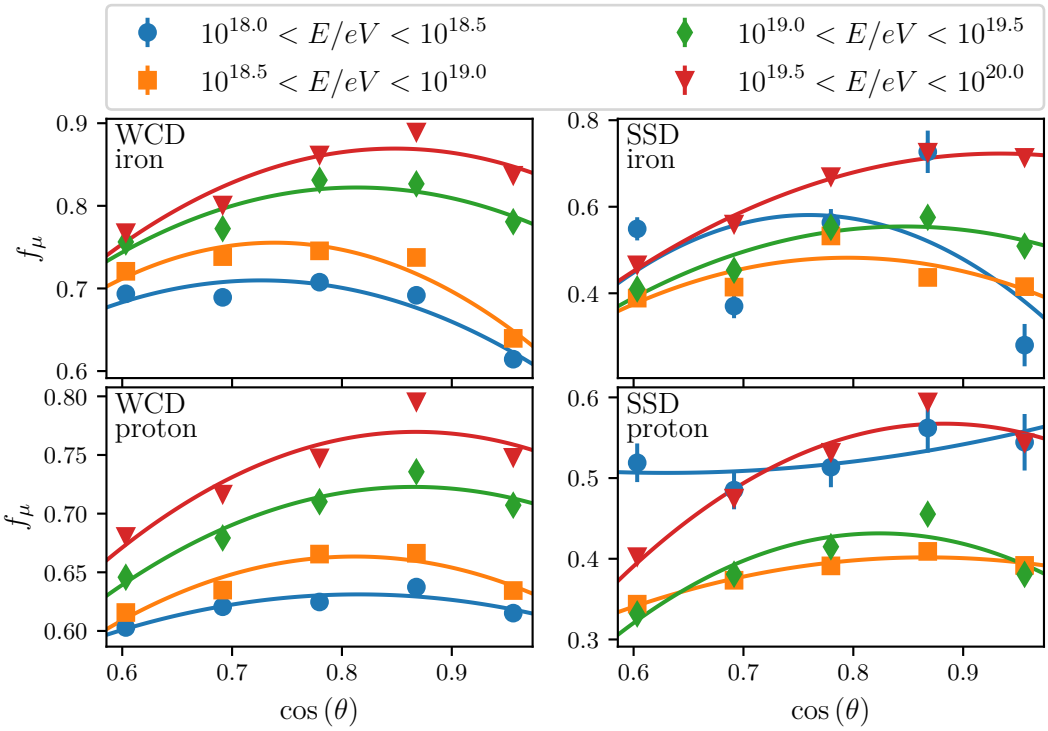

Figure 8.28: The signal fraction f_μ produced by muons in different energy and zenith bins, for simulated air showers from iron and proton primary particles. Parabolic fits are denoted by the solid lines. The parabola for the lowest energy for the SSD with proton as primary particle is the only convex one. Within the uncertainties (not shown here) it is compatible with a concave parabola.

must not be true. Due to the lack of knowledge also this effect cannot be quantized and must be left for future studies. A last point that is not taken into account here is a possible energy dependency of the magnitude of the muon excess. Due to the tuning of the hadronic interaction models to accelerator data and extrapolation towards higher energies it is likely that also the discrepancy between simulation and data increases with the energy.

The second source of systematic uncertainty is the used hadronic interaction model for performing the simulations. There are three widely used hadronic interaction models: EPOS-LHC [211], which is also used in this analysis, QGSJETII-04 [213] and Sybill [214]. They differ for instance in the number of produced muons (cf. fig. 2.8) resulting in deviations of the signals in the SSD and WCD. The uncertainty can be studied by repeating the same analysis with the other hadronic interaction models. As these simulations were not available, this was not done here. As can be seen from figure 2.8, the muon number deviates by a few percent between the different models. This is also the maximum effect to be expected on the ratio $S_{1000}^{\mathrm{WCD}}/S_{1000}^{\mathrm{SSD}}$.

8.6.5 Conclusions

The data are in very good agreement with the simulations of air showers initiated by iron as primary particle both in the mean but also in the overall shape of the distributions. This is a very surprising observation. Data from the FD of the Pierre Auger Observatory suggests

a change in the composition from rather proton like data towards iron in the region studied here (cf. sec. 2.4.3). As has been shown, this discrepancy might arise from the muon excess in data. Taking that effect into account, the composition presented here also changes from a light mixed one towards iron.

The systematic uncertainties make an interpretation difficult due to the significant impact of the muon number on the ratio of the signals in the SSD and WCD. Further studies will need to be carried out to properly understand these effects in the future.

Analyses which focus on the shape of the LDFs instead of the ratio might also be less affected by the muon excess. Especially multivariate analyses taking into account multiple characteristics of the air shower might reduce the dependency on the muon number in the simulations.

This analysis, despite being short and simple, could already show the possibilities that arise from the installation of the SSD. It will allow for composition studies based only on the SD compared to previous analyses where the FD data had to be used. The higher duty cycle will result in large statistics and extend the measurement of the composition to higher energies.

Chapter 9

Conclusion

The Pierre Auger Observatory, being the largest detector of cosmic ray induced air showers, is currently undergoing a major upgrade called AugerPrime. While several parts of the observatory are improved, the main component is the installation of the Scintillator Surface Detector (SSD) on top of the existing WCD stations. They will enhance the sensitivity on the primary mass composition of cosmic rays and improve the studies on the origin of Ultra High Energy Cosmic Rays (UHECRs).

A first analysis using 77 SSDs indicates the possibility for composition studies using only the Surface Detector (SD) of the Pierre Auger Observatory. The results are compatible with pure iron over the studied energy range from 10^{18} eV to 10^{20} eV. The study is subject to significant systematic uncertainties due to the lack of knowledge of the hadronic interactions at the highest energies. Future analyses with more data and more involved techniques might reduce these uncertainties.

A total of 135 SSDs was built by the mechanical workshop of the Phyiscs Institute III A at the RWTH Aachen University. A test stand was commissioned by the author of this thesis in order to verify the correct functionality of these detectors. The data was analyzed with respect to the light yield and the light tightness of the SSDs. All detectors were found to have a sufficient light yield with on average 26.6 p.e.. A light leak was detected for one SSD that could be repaired by the mechanical workshop.

Within the scope of this thesis, the optical components of a Silicon Photomultiplier (SiPM) based optical module have been developed. The designed light guides were optimized for the application in the SSD and their performance was studied and proven in several laboratory measurements. The optical module was installed in prototypes of the SSD deployed at the Pierre Auger Observatory in the Argentinean Pampas. From the collected data, a detailed study of their performance could be performed. Air showers were successfully measured and reconstructed using the information from the optical module. A comparison with data from conventional Photomultiplier Tubes (PMTs) revealed at least similar performance for the SiPMs. Especially the single p.e. resolution allows for a better understanding of the behavior of the detector and hence the data.

The performance of SiPMs was studied in detail also in laboratory measurements with special focus on their dynamic range. Several experiments were conducted to measure the intrinsic parameters of SiPMs and a simulation that allows for a precise understanding of

the behavior of SiPMs over a wide range of applications was developed. It was verified by exposing an SiPM to a bright light pulse far in the regime of non-linear response. The application of an algorithm developed by the author of this thesis allowed for the reconstruction of the incident number of photons even for light fluxes of > 10 photons per cell within 100 ns.

These experiments have proven the maturity of SiPMs also for the applications in large scale observatories such as cosmic ray detectors.

Appendices

A Background found in software triggered traces of SSD tests

Different types of signals produce significant background when searching for single p.e. pulses in the software triggered traces of the SSD tests. In figure A.1, a histogram of the wavelet value is given with respect to the determined charge for the found pulses. The same was already shown as well in figure 5.9. Examples of found pulses that contribute to the three different regions marked in the figure are given in figure A.2. There are as well three different type of background noise that contribute to these regions. The ones in region 3 and 2(1) as marked in figure A.2, originate from the DRS4 evaluation board. The high positive peaks are a known artifact of the digitization. The source of the signals shown in region 1 and 2(2) is unknown. They only appear occasionally and do not affect all test runs. All these background contributions can well be distinguished from the single p.e. signals with wavelet values above 5 and a charge between 1×10^6 and 2×10^6 electrons.

B Testing of two SSDs at KIT

Two SSDs produced in Aachen with IDs 23 and 52 were transported and tested in the test stand of the KIT. It consists of a muon tomograph that was formerly used as a central tracker in the KASCADE experiment [206]. The main characteristic is its position resolved determination of the light yield of the detector allowing for a study of the detector homogeneity. In addition, the measurement allows for a cross calibration of the systematic differences of the test stands in Aachen and at KIT.

The measurements were performed by the local staff of KIT together with the author of this thesis. The data analysis for determination of the homogeneity and the light yield was also conducted by the local staff to avoid differences compared to their standard procedure. The conversion of the data taken in Aachen to data comparable with that measured at KIT was done by the author of this thesis.

In figure B.1, the homogeneity of the two SSDs is shown. The result is very good with no significant variations in the light yield of the detector. Some slight variation between different bars is visible but this effect is negligible. The average light yield measured at KIT and in Aachen is given in table B.1. For the measurement in Aachen, the weighted average of the light yield of the left and right side is determined. At KIT, the light yield is corrected for the zenith angle of the incident muon to determine the Vertical MIP (VMIP).

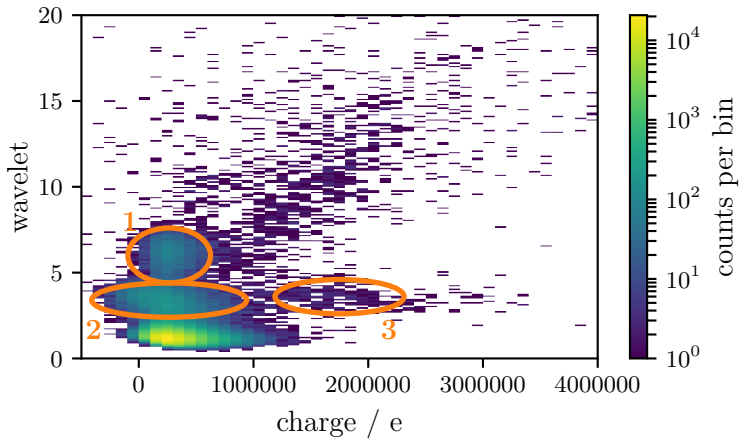

Figure A.1: A histogram of the wavelet with respect to the determined charge for single p.e. pulse candidates. Three regions with different found background are marked. Their origin is described in the text.

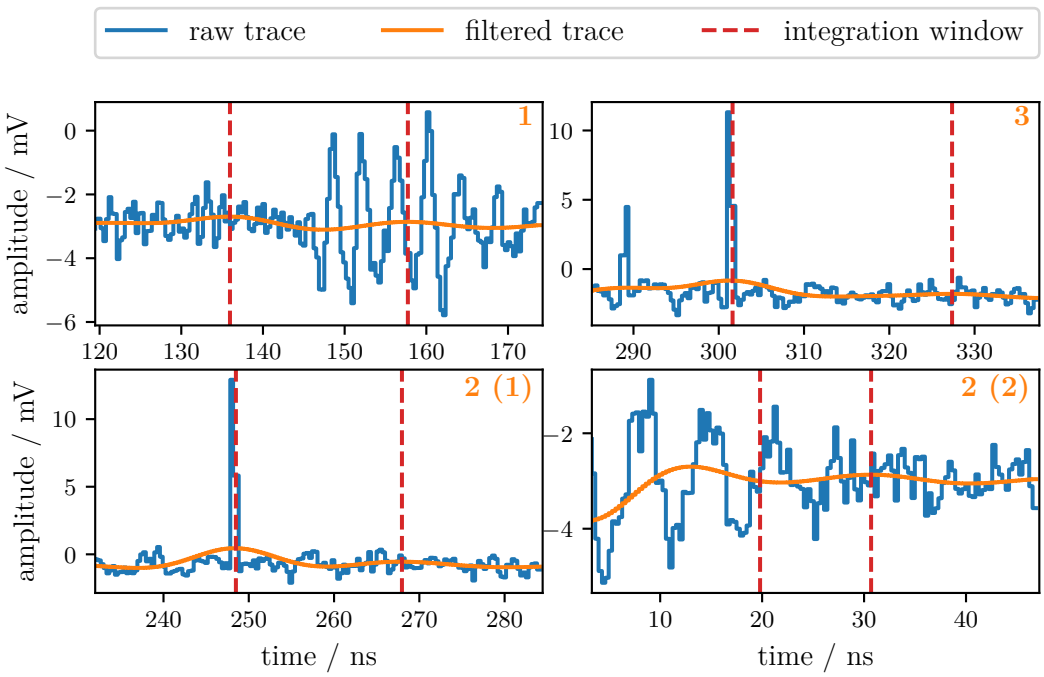

Figure A.2: Examples of signals that contribute to the background marked in figure A.1. The number in the top right of the plots corresponds to the regions marked with circles in the other figure. For region 2, two different types of signals were found.

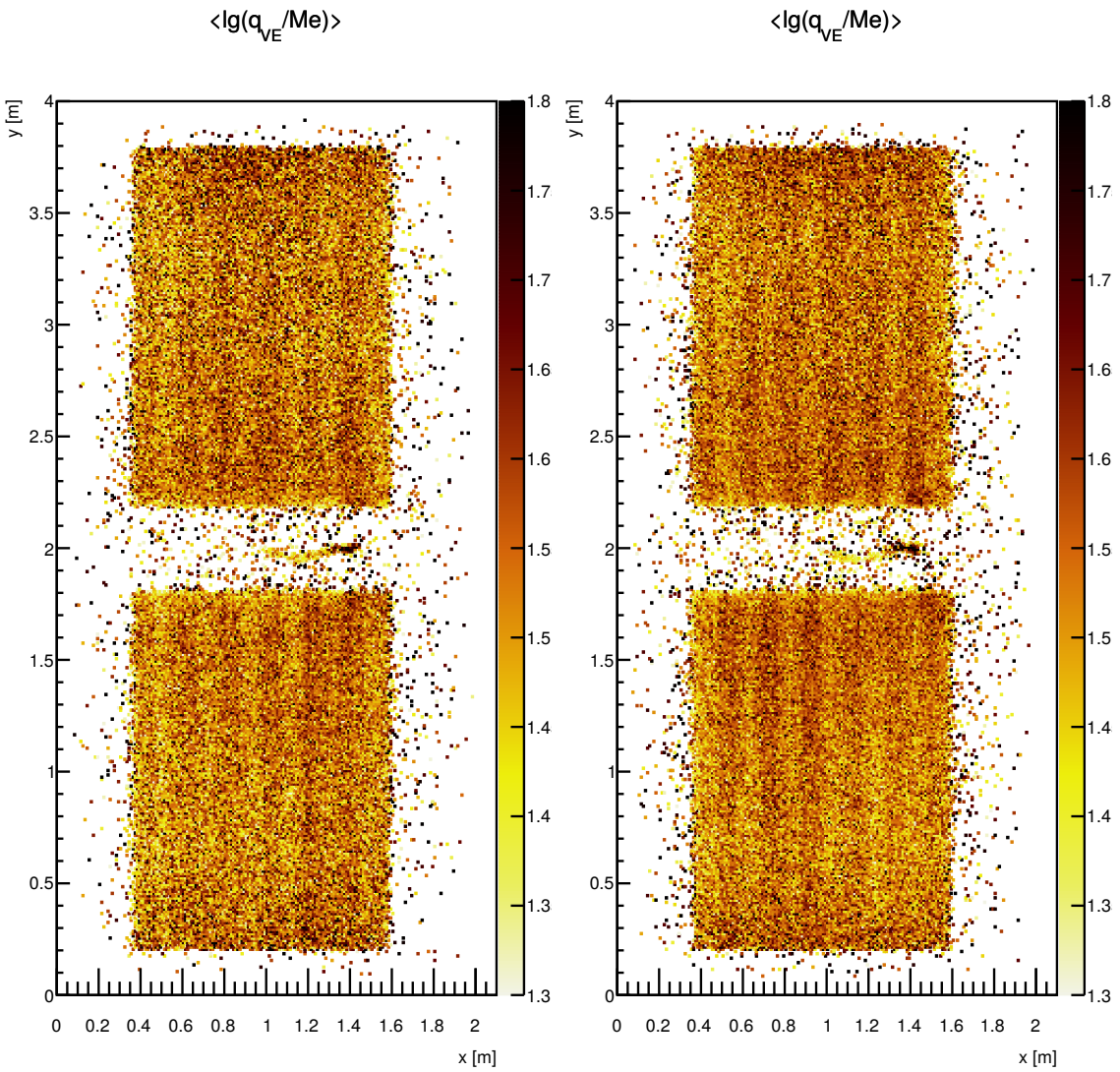

(a) ID 23 (b) ID 52

Figure B.1: Homogeneity for the two SSDs measured in the muon tomograph at KIT. Color coded is the average logarithmic signal measured at the specific position. For both detectors, homogeneity is very good.

	Aachen			KIT		
SSD	left	right	μ	MIP	VMIP	VMIP/μ
23	27.5 ± 2.0	27.3 ± 2.8	27.4 ± 1.4	26.4	23.0	0.839 ± 0.043
52	32.0 ± 5.4	27.0 ± 1.7	27.4 ± 3.8	26.8	22.5	0.82 ± 0.11

Table B.1: Results for the light yield as measured for the two SSDs in Aachen and at KIT. The mean μ is weighted by the uncertainties for the measurement of the left and right side. VMIP corresponds to the signal a *vertical* MIP would produce.

It is independent of the angular distribution of the incident muons and therefore a good calibration quantity.

The factors for converting the MIP measured in the Aachen test stand to VMIP measured at KIT are in good agreement. An average conversion factor of $VMIP/\mu = 0.837 \pm 0.038$ is determined.

C Parameters of Hamamatsu S13360-60XXPE SiPMs

Model	N_{cells}	R_{q} / kΩ	C_{d} / fF	C_{q} / fF	C_{g} / pF
S13360-6025PE	57600	750	20.6	1.6	41.1
S13360-6050PE	14400	340	87.6	3.5	69.3

Table C.1: Values given on the capacitances and resistors according to the schematics given in figure 6.9. The variations between different sensors of the same type is 10 % for the capacitances and 20 % for the quenching resistor [181]. These uncertainties correspond to the maximum possible and not to Gaussian standard deviations.

D Optical characteristics of the integrating sphere

An integrating sphere has a highly diffusely reflecting inner surface. Small openings on the surface allow to place light sources or sensors. A positioning directly opposite of each other should be avoided in order to prevent direct light to reach the sensor.

To understand the impact of the integrating sphere on a short light pulse, a Monte Carlo simulation has been implemented. The light source simply corresponds to photons that are emitted perpendicular to the surface of the sphere. Whenever a photon interacts with a surface it is randomly reflected with a probability R or absorbed with probability $1 - R$. The direction of the reflected photon is randomly chosen from an isotropic distribution. When the photon hits an area on the surface of the sphere with radius r, it is considered detected. The propagation time from the source to the detector is stored.

In figure D.1 the time distribution for a Thorlabs IS200-4 [184] with $R = 0.99$, $r = 0.25$" and radius of the integrating sphere $R_{\text{sphere}} = 1$" is given. All photons are emitted at the same time at the source. This is a valid approximation as the true width is only ~ 100 ps. A total of 500 000 initial photons has been simulated. An exponential decay time $\tau = (3.44 \pm 0.01)$ ns is determined through a fit.

E The Nelder-Mead minimization algorithm

The Nelder-Mead algorithm for minimization of scalar functions was proposed in [188]. Here, a short (and incomplete) introduction into the working principle is given.

For a real function of N parameters, a simplex is defined as a set of $N + 1$ different points in the N dimensional parameter space. For instance, for a space of two parameters, the simplex corresponds to a triangle.

The algorithm starts from an initial simplex which can, in principle, be arbitrarily chosen. In many applications and also in the optimization applied in section 6.6.8 an initial vector

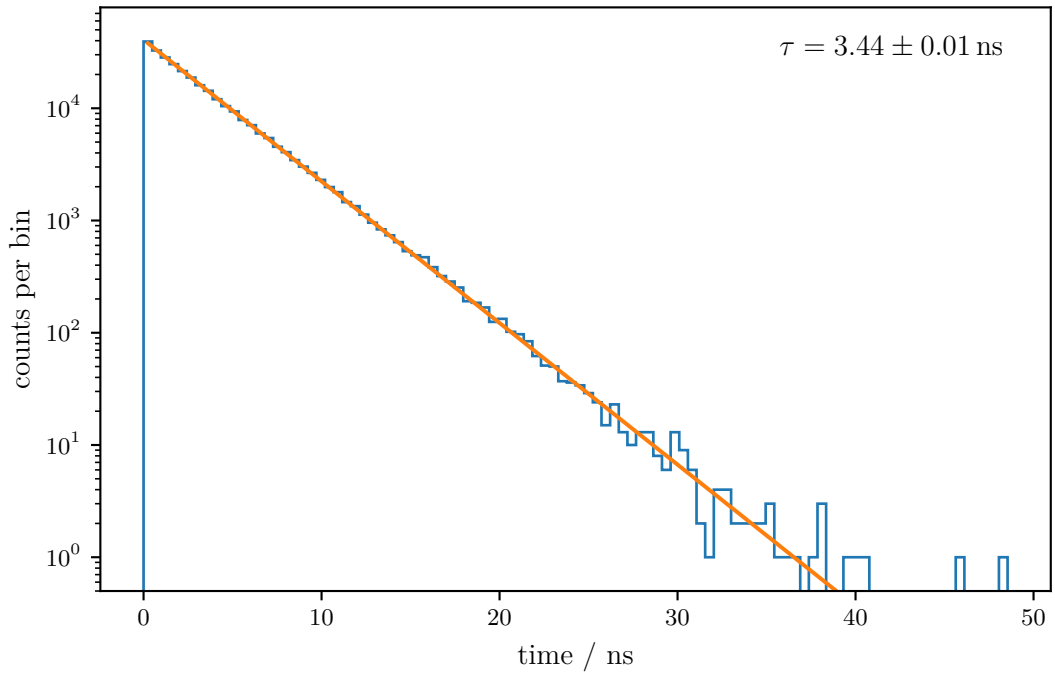

Figure D.1: Resulting simulated travel time for a photon from the emission from the light source until reaching the light sensor. An exponential fit is performed which yields the decay time τ.

of parameters $\mathbf{p}_0$ is constructed and the additional N points are derived from it by changing one parameter:

$$\mathbf{p}_i = \mathbf{p}_0 + c_i \mathbf{e}_i \tag{E.1}$$

with $\mathbf{e}_i$ being the unit vector along one dimension and c_i an arbitrary constant.

The function to be minimized (typically a Log-Likelihood- or χ^2-function) is evaluated at each point $\mathbf{p}_i$. The worst function value f_w, best function value f_b and second best function value f_s are selected. The point $\mathbf{p}_w$ with the largest function value f_w is tried to be optimized. First, it is mirrored along the centroid of the other points to create a new point $\mathbf{p}_m$ and the function is evaluated again.

Depending on the function value f_m at $\mathbf{p}_m$ different operations are performed:

1. If $f_b \leq f_m < f_s$ the new point is kept and the algorithm starts with the new simplex again.

2. If $f_m < f_b$, the point $\mathbf{p}_m$ is expanded in the direction of the previous mirroring to create a new point $\mathbf{p}_e$ with function value f_e. The point $\mathbf{p}_m$ or $\mathbf{p}_e$ which has the lower function value is kept and a new simplex is created.

3. If $f_m > f_s$, the simplex is contracted. For $f_w < f_m$ the point halfway between $\mathbf{p}_w$ and the centroid is calculated. In the opposite case, the point halfway between $\mathbf{p}_m$ and the centeroid is determined. If this new point yields a better function value than f_w, it is kept to create a new simplex. Otherwise, the whole simplex is shrunk in the direction of the best point $\mathbf{p}_b$.

fit	$\mathbf{p}_i$	R_q / kΩ	C_d / fF	C_g / pF	g / 10^5	p_x / %	ΔV_ov / V
1	0	750	20.6	41.1	7	7	0.3
	i	600	18.54	36.99	6.3	3	0
	opt	844	20.6	38.6	6.93	5.9	0.29
2	0	750	20.6	41.1	7	7	0.3
	i	900	22.66	45.21	7.7	10	0.5
	opt	785	20.8	42.1	7.18	6.9	0.31
3	0	730	20.5	40	7.1	5	0
	i	850	19	44	6.5	3	0.4
	opt	789	20.8	40.2	7.28	4.7	0.24
4	0	650	20.7	42	7	5	0
	i	850	19	38	6.5	1	0.4
	opt	796	20.8	40.9	7.37	4.0	0.18
5	0	730	20.5	40	7.1	5	0
	i	850	19	44	6.5	3	0.4
	opt	758	21.2	43.7	6.90	3.9	0.16
$\langle x \rangle$		794 ± 31	20.84 ± 0.22	41.1 ± 1.9	7.13 ± 0.21	5.1 ± 1.3	0.236 ± 0.066
reference		790.4 ± 6.4	20.6 ± 2.1	41.1 ± 4.1	7	7 ± 0.2	0.305 ± 0.048

Table E.1: The parameters for the initial simplices used for the fit presented in section 6.6.8. The first row for each fit corresponds to the parameter $\mathbf{p}_0$. The values in the second row are used for the variation of $\mathbf{p}_0$ to create the other points $\mathbf{p}_i$ and in the third row the parameters after the optimization are given. In row $\langle x \rangle$, the mean and RMS of the results of the five fits are given. The reference values are taken from the following sources: R_q and ΔV_ov have been determined in sections 6.6.1 and 6.2.1, respectively, of this thesis. C_d, C_g and g are given by the manufacturer [181] with an uncertainty of 10 %. p_x was measured in [155].

For the application presented in section 6.6.8, several different initial simplices were chosen. The values for $\mathbf{p}_0$ and for its variation are given in table E.1 together with the resulting parameters after optimization.

F Smoothing of reconstructed photon distributions

The time distributions of the photon arrival times reconstructed with the algorithm presented in section 6.8.2 can contain a negative number of photons in some of the time bins due to fluctuations. A negative number of photons is unphysical and these negative fluctuations are removed by accounting for it in the neighboring positive bins. The algorithm that was implemented for this task is presented in the following. It was optimized for this kind of analysis where noise can lead to an oscillatory pattern rather than random white noise.

First, the distribution is split into sections of consecutive negative or positive samples, respectively. For each of the negative and positive sections i, the integrated signal $S_i^{\mathrm{neg/pos}}$ is calculated. In the following, all signals are made positive, so that for the negative sections S_i^{neg} corresponds to the negative integral. The amplitudes of the distribution in the negative

sections are set to zero. These will be accounted for in the positive sections. Two cases have to be distinguished depending if the first sections is positive or negative.

If the first section is a positive one, its signal S_1^{pos} is compared to that of the following negative section S_1^{neg}. If $S_1^{\text{neg}} \geq S_1^{\text{pos}}$, all amplitudes in the first positive section are set to zero and the signal $\Delta S_1 = S_1^{\text{neg}} - S_1^{\text{pos}}$ is added to S_2^{neg}. If $S_1^{\text{neg}} < S_1^{\text{pos}}$, the amplitudes A_j of the samples in the positive section are reduced by $A_j \cdot S_1^{\text{neg}}/S_1^{\text{pos}}$. This accounts for the originally following negative samples and reduces the amplitude in the positive section. For all following positive sections this procedure is repeated.

In case of a first negative section, the algorithm is the same as before. The only difference is the comparison of a negative section with the *following* positive section while previously it was vice versa.

The algorithm effectively reduces especially contributions from oscillations that occasionally arise in the unfolding procedure and makes sure no negative number of photons is apparent in the distribution.

G Linear dynamic range of a 40 ns incident pulse

In section 6.8.5, the reconstruction of the incident number of photons is performed for an incident pulse with a length of 100 ns. The same procedure is repeated for a shorter pulse of only 40 ns with the resulting dynamic range and uncertainties given in figures G.1 and G.2, respectively. The results are very similar to those observed for a 100 ns pulse length. Due to the shorter pulses, the maximum achievable number of incident photons is lower and a study can only be performed up to 10^6 incident photons compared to 4×10^6 for the long pulse. Over all the range, the reconstructed number of photons exceeds the incident number of photons by up to 9 % with a maximum around 2×10^5. The systematic uncertainty is again dominated by the overvoltage and the quenching resistor. It reaches 20 % at 10^6 incident photons. This is larger compared to the uncertainty of 12 % in the case of the long pulse but expected due to the higher number photons per time in the case of the shorter pulse.

H Construction of a Winston cone

The Winston cone is a non-imaging, rotationally symmetric light collector. It was introduced in [200] and a good description can be found in [215].

A sketch of the geometry is shown in figure H.1. The surface is described by a tilted parabola. The construction follows the idea of a creating a cut-off angle θ_{max} for the incident light above that all light rays are reflected out of the cone. Below θ_{max}, all light rays are transmitted to the exit window. The parabola is tilted such that its focal point F is at the opposite edge of the exit window.

In the reference frame given by (r', z'), the functional form is given as:

$$r'^2 = 4f\,(z' + f) \tag{H.1}$$

with f being the focal length of the parabola.

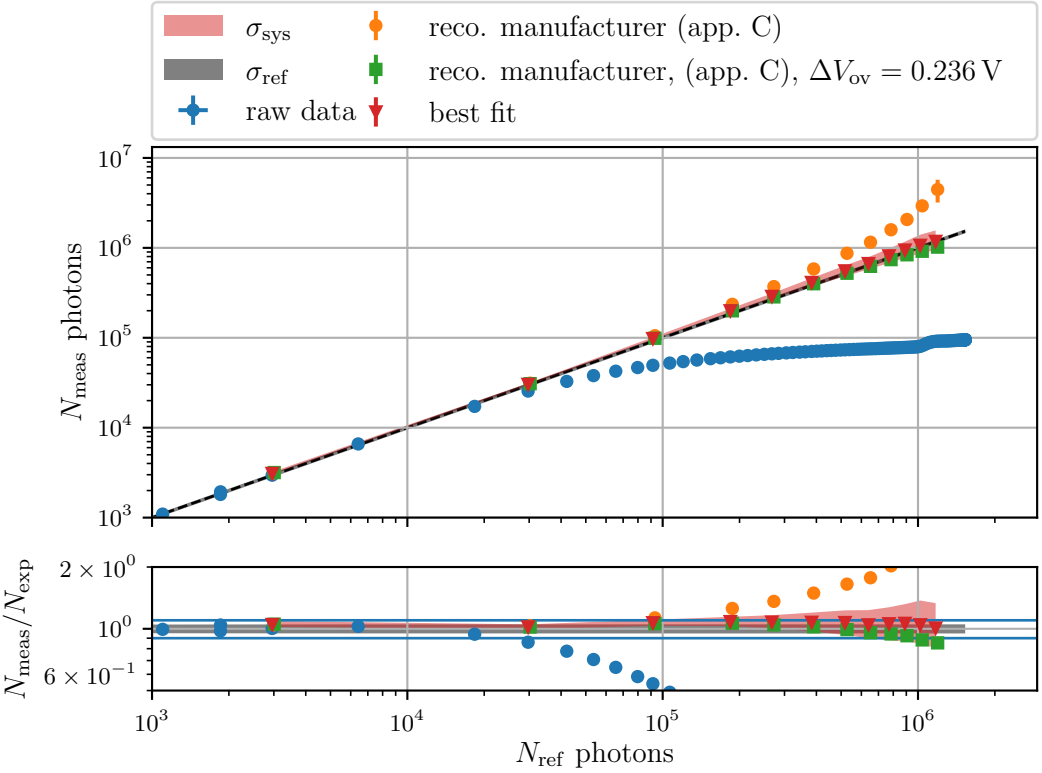

Figure G.1: The reconstructed dynamic range for the measurement with 40 ns pulse width. Reconstructions were performed with the *best fit* values of section 6.6.8, those given by the *manufacturer* with and without a shift in the overvoltage corresponding to the best fit. The black shaded area corresponds to the uncertainty originating from the determination of the reference number of photons. The red shaded area indicates the systematic uncertainty from the *best fit* results. The blue horizontal lines correspond to 10 % deviation from linearity.

This shape can be transformed into the more intuitive coordinate system of (r, z) by a rotation around θ_{max} and translation along a'. The resulting parabola is given as

$$\begin{aligned}(r\cos\theta_{\text{max}} + z\sin\theta_{\text{max}})^2 + a'r\,(1+\sin\theta_{\text{max}})^2 - 2a'z\cos\theta_{\text{max}}\,(1+\sin\theta_{\text{max}}) \\ - a'^2\,(3+\sin\theta_{\text{max}})\,(1+\sin\theta_{\text{max}}) = 0 \qquad .\end{aligned} \tag{H.2}$$

The shape is described by only two parameters, the exit window radius a' and the cut-off angle θ_{max}. The other parameters such as the length of the cone L and the radius of the entrance window a can be derived from these:

$$\begin{aligned} L \cdot \tan\theta_{\text{max}} &= a + a' \\ a \cdot \sin\theta_{\text{max}} &= a' \qquad . \end{aligned}$$

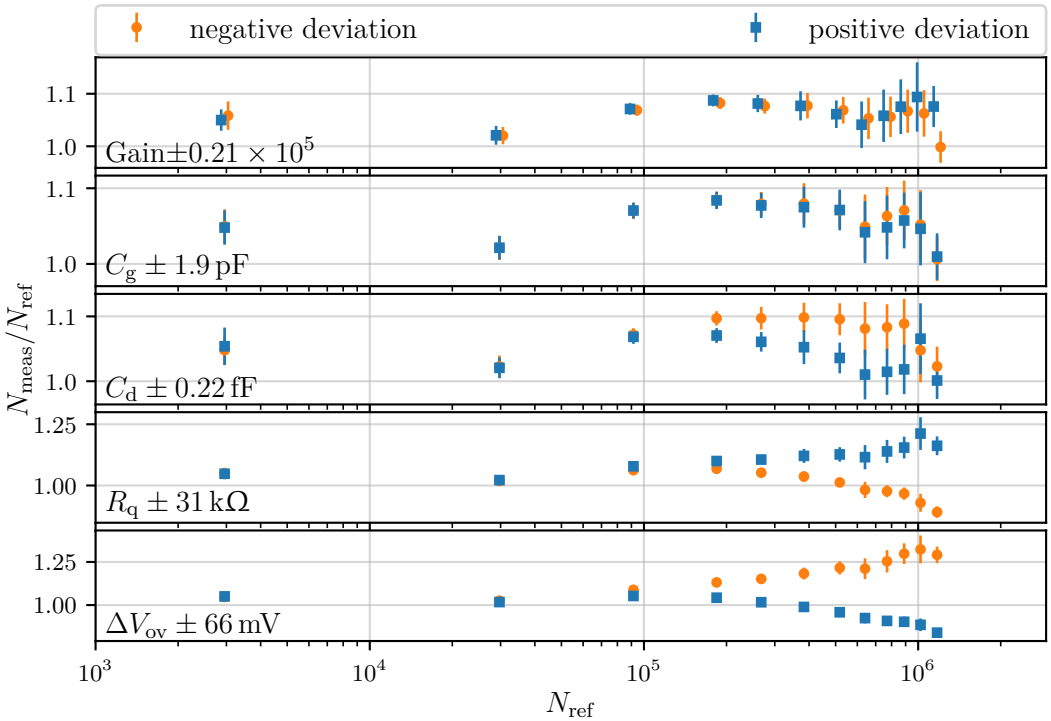

Figure G.2: The impact of the uncertainties of the intrinsic SiPM parameters on the reconstructed number of incident photons. Note the different y-scales.

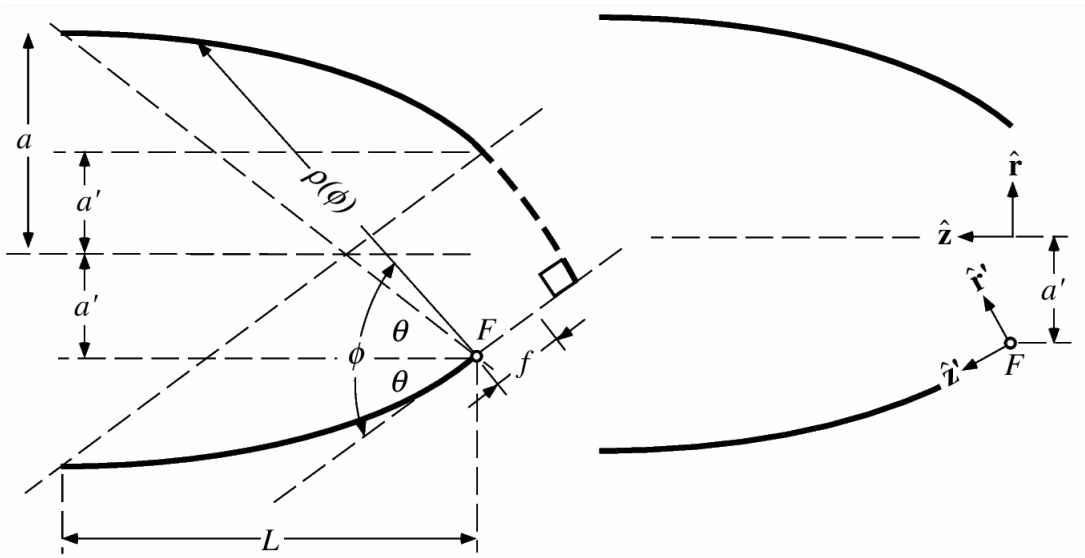

Figure H.1: A sketch of the geometry of a Winston cone. Taken from [215].

I Determination of baseline and total signal from traces measured at the Pierre Auger Observatory

The Offline framework of the Pierre Auger Observatory [209] implements a dedicated algorithm to determine the baseline of measured signal traces and to extract the total signal. It is optimized for the application with PMT signals. For the optical module presented in this thesis some modifications had to be implemented due to the different pulse shape to properly determine the signals and baselines. Here, the default algorithm will be presented and modifications for the SiPM based optical module will be mentioned where applicable.

I.1 The baseline

The baseline is determined in two steps. First, *flat pieces* are determined where the baseline is stable and second, the baseline in those flat pieces is calculated and inter- or extrapolated for the missing parts.

A piece of the trace is considered flat if its length exceeds a minimum length l_{min} and the absolute difference in amplitude for all samples of the piece with the first sample does not exceed a maximum deviation σ_{max}. If the first sample of the first found flat piece is only found after a maximum sample $N_{\mathrm{s,max}}$, the whole collection of flat pieces is considered bad. This makes sure that a flat piece will be found in the region before the trigger where no signal is expected. The algorithm is repeated with σ_{max} increased by 1 adc count until the first flat piece starts in the required region.

For all flat pieces, the mean amplitude is determined. This is the baseline in those regions. For the holes between the flat pieces, the baseline is interpolated linearly if no sample in that region exceeds the baseline before the hole. If at least one sample in the hole exceeds the baseline before the hole, the change of the baseline in each sample is weighted by the signal in that sample. This results in a non-linear interpolation for the transition between the two flat pieces. It allows for a proper change from the region before the trigger to the undershoot if the parameters are adjusted to detect the undershoot region as a flat piece.

The default parameters and those chosen for the two SSDs equipped with the SiPM based optical module are given in table I.1. The comparably high noise in the CG channel makes necessary a higher starting value for the σ_{max}. The large number of single p.e. pulses requires only a shorter l_{min} than in the default as the baseline should only be found between two single p.e. pulses but not contain them.

The other channels have similar properties as the PMT. The higher noise in the HG channel of station 41 make necessary a small increase in the starting value for σ_{max}. The undershoot has also been found to be more pronounced than for the PMT. To allow for proper finding of the baseline also in the undershoot region, l_{min} has also been reduced slightly for the HG and LG channels.

I.2 The signal

The signal is searched for in the region after $N_{\mathrm{s,max}}$ that was introduced in the previous section. A signal is considered to be found when the amplitude of at least N_{sig} consecutive samples exceeds the baseline by a threshold A_{min}. For the LG channels, the regions found in the HG channels are used. For the PMTs this algorithm works well because of the short pulses with high amplitude. For the SiPMs it is problematic because of the lower but longer pulses. The minimum amplitude A_{min} therefore excludes a significant portion of

	default		SSD station 41			SSD station 59		
	UB	UUB	CG	HG	LG	CG	HG	LG
l_{min}	40	120	30	50	100	30	60	100
$\sigma_{\mathrm{max,start}}$	2	2	30	6	2	30	2	2
$N_{\mathrm{s,max}}$	200	600	600	600	600	600	600	600
N_{sig}	2	8	8	8	8	8	8	8
A_{min}	3	12	0	0	0	0	0	0
$A_{\mathrm{sig,min}}$	-	-	300	4	4	300	4	4

Table I.1: Parameters used in the algorithm for the determination of the baseline and calculation of the total signal.

the pulses. For the signals from the SiPMs, A_{min} is therefore reduced but an additional threshold $A_{\mathrm{sig,min}}$ for the highest sample within one signal region is introduced. Only if this threshold is exceeded the whole region is considered being a signal. The chosen parameters are given in table I.1.

Bibliography

[1] V. F. Hess, "Über Beobachtungen der durchdringenden Strahlung bei sieben Freiballonfahrten", *Phys. Z.* **13** (1912) 1084.

[2] P. Auger et al., "Extensive Cosmic-Ray Showers", *Rev. Mod. Phys.* **11** (1939) 288, DOI:10.1103/RevModPhys.11.288.

[3] A. Watson, "The highest-energy cosmic-rays - the past, the present and the future", *EPJ Web Conf.* **210** (2019) 00001, DOI:10.1051/epjconf/201921000001, arXiv:1901.06676.

[4] K.-H. Kampert and A. A. Watson, "Extensive air showers and ultra high-energy cosmic rays: a historical review", *The European Physical Journal H* **37** (2012) 359, DOI:10.1140/epjh/e2012-30013-x, arXiv:1207.4827.

[5] R. Battiston, "The antimatter spectrometer (AMS-02): A particle physics detector in space", *NIM A* **588** (2008) 227 , DOI:10.1016/j.nima.2008.01.044.

[6] P. Picozza et al., "PAMELA – A payload for antimatter matter exploration and light-nuclei astrophysics", *Astroparticle Physics* **27** (2007) 296 , DOI:10.1016/j.astropartphys.2006.12.002.

[7] A. Aab et al., The Pierre Auger collaboration, "The Pierre Auger Cosmic Ray Observatory", *NIM A* **798** (2015) 172 , DOI:10.1016/j.nima.2015.06.058, arXiv:1502.01323.

[8] T. Abu-Zayyad et al., "The surface detector array of the Telescope Array experiment", *NIM A* **689** (2012) 87 , DOI:10.1016/j.nima.2012.05.079.

[9] T. Antoni et al., The KASCADE collaboration, "The cosmic-ray experiment KASCADE", *NIM A* **513** (2003) 490 , DOI:10.1016/S0168-9002(03)02076-X.

[10] R. Alves Batista et al., "Open Questions in Cosmic-Ray Research at Ultrahigh Energies", *Frontiers in Astronomy and Space Sciences* **6** (2019) 23, DOI:10.3389/fspas.2019.00023, arXiv:1903.06714.

[11] A. Letessier-Selvon and T. Stanev, "Ultrahigh energy cosmic rays", *Rev. Mod. Phys.* **83** (2011) 907, DOI:10.1103/RevModPhys.83.907, arXiv:1103.0031.

[12] M. Spurio, *Particles and Astrophysics: A Multi-Messenger Approach*. Springer International Publishing, Cham, 2015, DOI:10.1007/978-3-319-08051-2.

[13] M. Tanabashi et al., The Particle Data Group collaboration, "Review of Particle Physics", *Phys. Rev.* **D98** (2018) 030001, DOI:10.1103/PhysRevD.98.030001.

[14] J. R. Hörandel, "Models of the knee in the energy spectrum of cosmic rays", *Astroparticle Physics* **21** (2004) 241 , DOI:10.1016/j.astropartphys.2004.01.004, arXiv:astro-ph/0402356.

[15] W. D. Apel et al., The KASCADE Grande collaboration, "Kneelike structure in the spectrum of the heavy component of cosmic rays observed with KASCADE-Grande", *Phys. Rev. Lett.* **107** (2011) 171104, DOI:10.1103/PhysRevLett.107.171104, arXiv:1107.5885.

[16] Thoudam, S. et al., "Cosmic-ray energy spectrum and composition up to the ankle: the case for a second galactic component", *A&A* **595** (2016) A33, DOI:10.1051/0004-6361/201628894, arXiv:1605.03111.

[17] F. Fenu, The Pierre Auger collaboration, "The cosmic ray energy spectrum measured using the Pierre Auger Observatory", in *Proceedings, 35th International Cosmic Ray Conference (ICRC 2017)*, vol. ICRC2017, p. 486, 2017.

[18] R. Jansson and G. R. Farrar, "A new model of the galactic magnetic field", *The Astrophysical Journal* **757** (2012) 14, DOI:10.1088/0004-637x/757/1/14.

[19] R. Aloisio, V. Berezinsky and M. Kachelriess, "Ultrahigh energy cosmic rays spectra in top-down models", *Nucl. Phys. Proc. Suppl.* **136** (2004) 319, DOI:10.1016/j.nuclphysbps.2004.10.023, arXiv:astro-ph/0409222.

[20] V. Berezinsky, "Ultrahigh-energy cosmic rays from cosmological relics", *Nuclear Physics B - Proceedings Supplements* (1998) , DOI:10.1016/S0920-5632(99)00222-4, arXiv:astro-ph/9811268.

[21] V. A. Kuzmin and I. I. Tkachev, "Ultrahigh-energy cosmic rays and inflation relics", *Phys. Rept.* **320** (1999) 199, DOI:10.1016/S0370-1573(99)00064-2, arXiv:hep-ph/9903542.

[22] A. Aab et al., The Pierre Auger collaboration, "Search for photons with energies above 10^{18} eV using the hybrid detector of the Pierre Auger Observatory", *JCAP* **1704** (2017) 009, DOI:10.1088/1475-7516/2017/04/009, arXiv:1612.01517.

[23] E. Fermi, "On the Origin of the Cosmic Radiation", *Phys. Rev.* **75** (1949) 1169, DOI:10.1103/PhysRev.75.1169.

[24] E. Fermi, "Galactic Magnetic Fields and the Origin of Cosmic Radiation.", *Astrophys. J.* **119** (1954) 1, DOI:10.1086/145789.

[25] A. De Angelis and M. J. M. Pimenta, *Introduction to Particle and Astroparticle Physics: Questions to the Universe*. Springer Milan, Milano, 2015, DOI:10.1007/978-88-470-2688-9.

[26] R. Alves Batista et al., "CRPropa 3 - a Public Astrophysical Simulation Framework for Propagating Extraterrestrial Ultra-High Energy Particles", *JCAP* **1605** (2016) 038, DOI:10.1088/1475-7516/2016/05/038, arXiv:1603.07142.

[27] "GALPROP", 2019. https://galprop.stanford.edu/.

[28] A. Obermeier et al., "The Boron-to-carbon Abundance Ratio and Galactic Propagation of Cosmic Radiation", *The Astrophysical Journal* **752** (2012) 69, DOI:10.1088/0004-637X/752/1/69, arXiv:1204.6188.

[29] G. Giacinti, M. Kachelrieß and D. V. Semikoz, "Explaining the Spectra of Cosmic Ray Groups above the Knee by Escape from the Galaxy", *Phys. Rev.* **D90** (2014) 041302, DOI:10.1103/PhysRevD.90.041302, arXiv:1403.3380.

[30] M. S. Pshirkov et al., "Deriving the global structure of the galactic magnetic field from faraday rotation measures of extragalactic sources", *The Astrophysical Journal* **738** (2011) 192, DOI:10.1088/0004-637x/738/2/192.

[31] T. Antoni et al., The KASCADE collaboration, "KASCADE measurements of energy spectra for elemental groups of cosmic rays: Results and open problems", *Astropart. Phys.* **24** (2005) 1, DOI:10.1016/j.astropartphys.2005.04.001, arXiv:astro-ph/0505413.

[32] M. Amenomori et al., The TIBET III collaboration, "The All-particle spectrum of primary cosmic rays in the wide energy range from 10^{14} eV to 10^{17} eV observed with the Tibet-III air-shower array", *Astrophys. J.* **678** (2008) 1165, DOI:10.1086/529514, arXiv:0801.1803.

[33] A. M. Hillas, "The Origin of Ultra-High-Energy Cosmic Rays", *Annual Review of Astronomy and Astrophysics* **22** (1984) 425, DOI:10.1146/annurev.aa.22.090184.002233.

[34] K. Greisen, "End to the cosmic ray spectrum?", *Phys. Rev. Lett.* **16** (1966) 748, DOI:10.1103/PhysRevLett.16.748.

[35] G. T. Zatsepin and V. A. Kuzmin, "Upper limit of the spectrum of cosmic rays", *JETP Lett.* **4** (1966) 78.

[36] A. Aab et al., The Pierre Auger collaboration, "The Pierre Auger Observatory Upgrade - Preliminary Design Report", arXiv:1604.03637.

[37] A. Aab et al., The Pierre Auger collaboration, "Observation of a large-scale anisotropy in the arrival directions of cosmic rays above 8×10^{18} eV", *Science* **357** (2017) 1266, DOI:10.1126/science.aan4338, [https://science.sciencemag.org/content/357/6357/1266.full.pdf].

[38] A. Yushkov, The Pierre Auger collaboration, "Mass composition of cosmic rays with energies above $10^{17.2}$ eV from the hybrid data of the Pierre Auger Observatory", in *Proceedings, 36th International Cosmic Ray Conference (ICRC 2019)*, vol. ICRC2019, p. 482, 2019, https://pos.sissa.it/358/482/pdf.

[39] R. Engel, D. Heck and T. Pierog, "Extensive Air Showers and Hadronic Interactions at High Energy", *Annual Review of Nuclear and Particle Science* **61** (2011) 467, DOI:10.1146/annurev.nucl.012809.104544.

[40] A. Aab et al., The Pierre Auger collaboration, "Data-driven estimation of the invisible energy of cosmic ray showers with the Pierre Auger Observatory", *Phys. Rev.* **D100** (2019) 082003, DOI:10.1103/PhysRevD.100.082003, arXiv:1901.08040.

[41] S. Cecchini and M. Spurio, "Atmospheric muons: experimental aspects", *Geoscientific Instrumentation, Methods and Data Systems Discussions* **2** (2012) 603, DOI:10.5194/gid-2-603-2012, arXiv:1208.1171.

[42] Y.-S. Tsai, "Pair production and bremsstrahlung of charged leptons", *Rev. Mod. Phys.* **46** (1974) 815, DOI:10.1103/RevModPhys.46.815.

[43] W. Heitler, *The Quantum Theory of Radiation*, Dover Books on Physics. Dover Publications, 1984.

[44] J. Matthews, "A Heitler model of extensive air showers", *Astropart. Phys.* **22** (2005) 387, DOI:10.1016/j.astropartphys.2004.09.003.

[45] J. R. Hörandel, "Cosmic rays from the knee to the second knee: 10^{14} to 10^{18} eV", *Mod. Phys. Lett.* **A22** (2007) 1533, DOI:10.1142/S0217732307024139, arXiv:astro-ph/0611387.

[46] D. Heck et al., "CORSIKA: A Monte Carlo code to simulate extensive air showers", *FZKA-6019* (1998) .

[47] K.-H. Kampert and M. Unger, "Measurements of the cosmic ray composition with air shower experiments", *Astroparticle Physics* **35** (2012) 660, DOI:10.1016/j.astropartphys.2012.02.004, arXiv:1201.0018.

[48] A. Aab et al., The Pierre Auger collaboration, "Muons in Air Showers at the Pierre Auger Observatory: Mean Number in Highly Inclined Events", *Phys. Rev.* **D91** (2015) 032003, DOI:10.1103/PhysRevD.91.032003, arXiv:1408.1421.

[49] O. Deligny, The Pierre Auger collaboration, "The energy spectrum of ultra-high energy cosmic rays measured at the Pierre Auger Observatory and at the Telescope Array", in *Proceedings, 36th International Cosmic Ray Conference (ICRC 2019)*, vol. ICRC2019, p. 234, 2019, https://pos.sissa.it/358/234/pdf.

[50] A. Aab et al., The Pierre Auger collaboration, "An Indication of Anisotropy in Arrival Directions of Ultra-high-energy Cosmic Rays through Comparison to the Flux Pattern of Extragalactic Gamma-Ray Sources", *The Astrophysical Journal Letters* **853** (2018) L29, DOI:10.3847/2041-8213/aaa66d, arXiv:1801.06160.

[51] M. Ackermann et al., "2FHL: The Second Catalog of Hard Fermi-LAT Sources", *The Astrophysical Journal Supplement Series* **222** (2016) 5, DOI:10.3847/0067-0049/222/1/5, arXiv:1508.04449.

[52] M. Ackermann et al., "GeV Observations of Star-forming Galaxies with the Fermi Large Area Telescope", *The Astrophysical Journal* **755** (2012) 164, DOI:10.1088/0004-637X/755/2/164, arXiv:1206.1346.

[53] P. Erdogdu et al., "The Dipole anisotropy of the 2 Micron All-Sky Redshift Survey", *Mon. Not. Roy. Astron. Soc.* **368** (2006) 1515, DOI:10.1111/j.1365-2966.2006.10243.x, arXiv:`astro-ph/0507166`.

[54] M. Kachelriess, "Lecture notes on high energy cosmic rays", arXiv:`0801.4376`.

[55] I. Frank and I. Tamm, *Coherent Visible Radiation of Fast Electrons Passing Through Matter*, pp. 29–35. In Bolotovskii et al. [56], 1991. DOI:10.1007/978-3-642-74626-0_2.

[56] B. M. Bolotovskii, V. Y. Frenkel and R. Peierls, eds., *Selected Papers*. Springer Berlin Heidelberg, Berlin, Heidelberg, 1991.

[57] R. Engel, *Indirect Detection of Cosmic Rays*, pp. 593–632. In Grupen and Buvat [58], 2012. DOI:10.1007/978-3-642-13271-1_24.

[58] C. Grupen and I. Buvat, eds., *Handbook of Particle Detection and Imaging*. Springer Berlin Heidelberg, Berlin, Heidelberg, 2012.

[59] J. Linsley, "Evidence for a Primary Cosmic-Ray Particle with Energy 10^{20} eV", *Phys. Rev. Lett.* **10** (1963) 146, DOI:10.1103/PhysRevLett.10.146.

[60] N. Chiba et al., "Akeno Giant Air Shower Array (AGASA) covering 100 km2 area", *NIM A* **311** (1992) 338 , DOI:10.1016/0168-9002(92)90882-5.

[61] D. B. Tridon et al., "The MAGIC-II gamma-ray stereoscopic telescope system", *NIM A* **623** (2010) 437 , DOI:10.1016/j.nima.2010.03.028.

[62] K. Bernlöhr et al., The H.E.S.S. collaboration, "The optical system of the H.E.S.S. imaging atmospheric Cherenkov telescopes. Part I: layout and components of the system", *Astroparticle Physics* **20** (2003) 111 , DOI:10.1016/S0927-6505(03)00171-3.

[63] R. Cornils et al., The H.E.S.S. collaboration, "The optical system of the H.E.S.S. imaging atmospheric Cherenkov telescopes. Part II: mirror alignment and point spread function", *Astroparticle Physics* **20** (2003) 129 , DOI:10.1016/S0927-6505(03)00172-5.

[64] H. Anderhub et al., "Design and Operation of FACT – The First G-APD Cherenkov Telescope", *JINST* **8** (2013) P06008, DOI:10.1088/1748-0221/8/06/P06008, arXiv:`1304.1710`.

[65] D. J. Bird et al., "Detection of a Cosmic Ray with Measured Energy Well beyond the Expected Spectral Cutoff due to Cosmic Microwave Radiation", *The Astrophysical Journal* **441** (1995) 144, DOI:10.1086/175344, arXiv:`astro-ph/9410067`.

[66] A. Aab et al., The Pierre Auger collaboration, "Measurement of the radiation energy in the radio signal of extensive air showers as a universal estimator of cosmic-ray energy", *Phys. Rev. Lett.* **116** (2016) 241101, DOI:10.1103/PhysRevLett.116.241101.

[67] W. R. Leo, *Techniques for Nuclear and Particle Physics Experiments: A How-to Approach*, vol. 2. Springer Berlin Heidelberg, Berlin, Heidelberg, 1994, DOI:10.1007/978-3-642-57920-2_2.

[68] H. Kolanoski and N. Wermes, *Teilchendetektoren: Grundlagen und Anwendungen.* Springer Berlin Heidelberg, Berlin, Heidelberg, 2016, DOI:10.1007/978-3-662-45350-6_3.

[69] S. I. Eidelman and B. A. Shwartz, *Interactions of Particles and Radiation with Matter*, pp. 3–23. In Grupen and Buvat [58], 2012. DOI:10.1007/978-3-642-13271-1_1.

[70] L. Landau, "On the energy loss of fast particles by ionization", *J. Phys.(USSR)* **8** (1944) 201.

[71] T. Antoni, "Myon Density Measurements with the KASCADE Central Detector", arXiv:`astro-ph/0103363`.

[72] A. Letessier-Selvon et al., "Layered water Cherenkov detector for the study of ultra high energy cosmic rays", *NIM A* **767** (2014) 41, DOI:10.1016/j.nima.2014.08.029, arXiv:`1405.5699`.

[73] C. Peters, *Development of scintillator detectors for measuring muons and air showers*, Ph.D. thesis, RWTH Aachen University, 2019. DOI:10.18154/RWTH-2019-05267.

[74] L. Middendorf, *Data acquisition for an SiPM based muon detector*, Ph.D. thesis, RWTH Aachen University, 2019. DOI:10.18154/RWTH-2018-225274.

[75] C. Peters et al., "The muon detector prototype AMD for the determination of the muon content in UHECRs", in *Proceedings, 34th International Cosmic Ray Conference (ICRC 2015)*, vol. ICRC2015, p. 596, 2015, `https://pos.sissa.it/236/596/pdf`.

[76] A. Letessier-Selvon and P. Billoir, "Separating the muonic and electromagnetic components of a shower through the matrix formalism for a two-fold detector." Internal note of the Pierre Auger Collaboration GAP2015-045, 2015.

[77] V. Verzi, The Pierre Auger collaboration, "Measurement of the energy spectrum of ultra-high energy cosmic rays using the Pierre Auger Observatory", in *Proceedings, 36th International Cosmic Ray Conference (ICRC 2019)*, vol. ICRC2019, p. 450, 2019, `https://pos.sissa.it/358/450/pdf`.

[78] I. Allekotte et al., The Pierre Auger collaboration, "The surface detector system of the Pierre Auger Observatory", *NIM A* **586** (2008) 409 , DOI:10.1016/j.nima.2007.12.016, arXiv:`0712.2832`.

[79] J. Abraham et al., The Pierre Auger collaboration, "The fluorescence detector of the Pierre Auger Observatory", *NIM A* **620** (2010) 227 , DOI:10.1016/j.nima.2010.04.023, arXiv:`0907.4282`.

[80] The Pierre Auger collaboration, "Techniques for measuring aerosol attenuation using the Central Laser Facility at the Pierre Auger Observatory", *Journal of Instrumentation* **8** (2013) P04009, DOI:10.1088/1748-0221/8/04/p04009.

[81] F. Arqueros et al., The Pierre Auger collaboration, "The Central Laser Facility at the Pierre Auger Observatory", in *Proceedings, 29th International Cosmic Ray*

Conference (ICRC 2005), vol. 8, pp. 335–338, 2005, http://www.icrr.u-tokyo.ac.jp/can/icrc2005/Proceedings/Vol-18/18335-usa-malek-M-abs1-he15-poster.pdf.

[82] T. Huege, The Pierre Auger collaboration, "Radio detection of cosmic rays with the Auger Engineering Radio Array", *EPJ Web Conf.* **210** (2019) 05011, DOI:10.1051/epjconf/201921005011.

[83] C. B. Bonifazi, The Pierre Auger collaboration, "Angular Resolution of the Pierre Auger Observatory", in *Proceedings, 29th International Cosmic Ray Conference (ICRC 2005)*, vol. 7, pp. 17–20, 2005, http://www.icrr.u-tokyo.ac.jp/can/icrc2005/Proceedings/Vol-17/17017-bra-bonifazi-C-abs1-he14-oral.pdf.

[84] M. Ave, The Pierre Auger collaboration, "Reconstruction accuracy of the surface detector array of the Pierre Auger Observatory", in *Proceedings, 30th International Cosmic Ray Conference (ICRC 2007): Merida, Yucatan, Mexico, July 3-11, 2007*, vol. 4, pp. 307–310, 2007, arXiv:0709.2125, http://lss.fnal.gov/cgi-bin/find_paper.pl?conf-07-482.

[85] B. R. Dawson, The Pierre Auger collaboration, "Hybrid Performance of the Pierre Auger Observatory", in *Proceedings, 30th International Cosmic Ray Conference (ICRC 2007): Merida, Yucatan, Mexico, July 3-11, 2007*, vol. 4, pp. 425–428, 2007, arXiv:0706.1105, http://lss.fnal.gov/cgi-bin/find_paper.pl?conf-07-371.

[86] V. Verzi, The Pierre Auger collaboration, "The Energy Scale of the Pierre Auger Observatory", in *Proceedings, 33rd International Cosmic Ray Conference (ICRC2013)*, p. 0928, 2013, http://www.cbpf.br/%7Eicrc2013/papers/icrc2013-0928.pdf.

[87] J. Schulz, "Status and Prospects of the Auger Engineering Radio Array", in *Proceedings, 34th International Cosmic Ray Conference (ICRC 2015)*, vol. ICRC2015, p. 615, 2015, https://pos.sissa.it/236/615/pdf.

[88] B. Schmidt, "Ein lichtstarkes komafreies Spiegelsystem", *Mitteilungen der Hamburger Sternwarte in Bergedorf* **7** (1938) 15.

[89] PHOTONIS, *photomultiplier tubes, XP3062, product specification*, http://www.hzcphotonics.com/products/XP3062.pdf, Sept., 2019.

[90] F. Nerling et al., "Universality of electron distributions in high-energy air showers—description of cherenkov light production", *Astroparticle Physics* **24** (2006) 421 , DOI:10.1016/j.astropartphys.2005.09.002.

[91] M. Giller et al., "Energy spectra of electrons in the extensive air showers of ultra-high energy", *Journal of Physics G: Nuclear and Particle Physics* **30** (2004) 97, DOI:10.1088/0954-3899/30/2/009.

[92] J. Pękala et al., "Atmospheric multiple scattering of fluorescence and cherenkov light emitted by extensive air showers", *NIM A* **605** (2009) 388 , DOI:10.1016/j.nima.2009.03.244.

[93] T. K. Gaisser and A. M. Hillas, "Reliability of the method of constant intensity cuts for reconstructing the average development of vertical showers", in *Proceedings, 15th International Cosmic Ray Conference (ICRC 1977)*, vol. 8, pp. 353–357, 1977.

[94] M. J. Tueros, The Pierre Auger collaboration, "Estimate of the non-calorimetric energy of showers observed with the fluorescence and surface detectors of the Pierre Auger Observatory", in *Proceedings, 33rd International Cosmic Ray Conference (ICRC2013)*, p. 0705, 2013, http://www.cbpf.br/%7Eicrc2013/papers/icrc2013-0705.pdf.

[95] Pierre Auger Observatory. Flickr. https://www.flickr.com/people/134252569@N07/.

[96] PHOTONIS, *Photomultiplier XP1805*, http://www.hzcphotonics.com/products/XP1805.pdf, Sept., 2019.

[97] X. Bertou, The Pierre Auger collaboration, "Performance of the Pierre Auger Observatory Surface Array", in *Proceedings, 29th International Cosmic Ray Conference (ICRC 2005)*, vol. 7, pp. 1–4, 2005, http://www.icrr.u-tokyo.ac.jp/can/icrc2005/Proceedings/Vol-17/17001-arg-bertou-X-abs1-he14-oral.pdf.

[98] X. Bertou, The Pierre Auger collaboration, "Calibration and Monitoring of the Pierre Auger Surface Detectors", in *Proceedings, 28th International Cosmic Ray Conference (ICRC 2003)*, vol. 1.5, pp. 813–816, 2003, http://www-rccn.icrr.u-tokyo.ac.jp/icrc2003/PROCEEDINGS/PDF/203.pdf.

[99] J. Abraham et al., The Pierre Auger collaboration, "Trigger and aperture of the surface detector array of the pierre auger observatory", *NIM A* **613** (2010) 29 , DOI:10.1016/j.nima.2009.11.018, arXiv:1111.6764.

[100] F. Aglietta et al., The Pierre Auger collaboration, "Response of the Pierre Auger Observatory Water Cherenkov Detectors to Muons", in *Proceedings, 29th International Cosmic Ray Conference (ICRC 2005)*, vol. 7, pp. 83–86, 2005, http://www.icrr.u-tokyo.ac.jp/can/icrc2005/Proceedings/Vol-17/17083-fra-suomijarvi-T-abs1-he14-poster.pdf.

[101] A. Aab et al., The Pierre Auger collaboration, "Reconstruction of inclined air showers detected with the Pierre Auger Observatory", *Journal of Cosmology and Astroparticle Physics* **2014** (2014) 019, DOI:10.1088/1475-7516/2014/08/019, arXiv:1407.3214.

[102] K. Kamata and J. Nishimura, "The Lateral and the Angular Structure Functions of Electron Show-
ers", *Progress of Theoretical Physics Supplement* **6** (1958) 93, DOI:10.1143/PTPS.6.93, [http://oup.prod.sis.lan/ptps/article-pdf/doi/10.1143/PTPS.6.93/5270594/6-93.pdf].

[103] K. Greisen, "Cosmic Ray Showers", *Annual Review of Nuclear Science* **10** (1960) 63, DOI:10.1146/annurev.ns.10.120160.000431.

[104] D. Barnhill et al., The Pierre Auger collaboration, "Measurement of the Lateral Distribution Function of UHECR Air Showers with the Pierre Auger Observatory",

in *Proceedings, 29th International Cosmic Ray Conference (ICRC 2005)*, vol. 7, pp. 291–294, 2005, `http://www.icrr.u-tokyo.ac.jp/can/icrc2005/Proceedings/Vol-17/17291-usa-bauleo-PM-abs2-he14-poster.pdf`.

[105] D. Newton, J. Knapp and A. Watson, "The optimum distance at which to determine the size of a giant air shower", *Astroparticle Physics* **26** (2007) 414 , DOI:10.1016/j.astropartphys.2006.08.003.

[106] J. Hersil et al., "Observations of Extensive Air Showers near the Maximum of Their Longitudinal Development", *Phys. Rev. Lett.* **6** (1961) 22, DOI:10.1103/PhysRevLett.6.22.

[107] A. Schulz, The Pierre Auger collaboration, "The measurement of the energy spectrum of cosmic rays above 3×10^{17} eV with the Pierre Auger Observatory", in *Proceedings, 33rd International Cosmic Ray Conference (ICRC2013)*, p. 0769, 2013, `http://www.cbpf.br/%7Eicrc2013/papers/icrc2013-0769.pdf`.

[108] A. Aab et al., The Pierre Auger collaboration, "An Indication of Anisotropy in Arrival Directions of Ultra-high-energy Cosmic Rays through Comparison to the Flux Pattern of Extragalactic Gamma-Ray Sources", *The Astrophysical Journal* **853** (2018) L29, DOI:10.3847/2041-8213/aaa66d.

[109] F. R. Klinkhamer, "Potential sensitivities to Lorentz violation from nonbirefringent modified Maxwell theory of Auger, HESS, and CTA", *Phys. Rev. D* **82** (2010) 105024, DOI:10.1103/PhysRevD.82.105024.

[110] F. R. Klinkhamer and M. Risse, "Ultrahigh-energy cosmic-ray bounds on nonbirefringent modified Maxwell theory", *Phys. Rev. D* **77** (2008) 016002, DOI:10.1103/PhysRevD.77.016002.

[111] K.-H. Kampert and M. Unger, "Measurements of the cosmic ray composition with air shower experiments", *Astroparticle Physics* **35** (2012) 660 , DOI:10.1016/j.astropartphys.2012.02.004.

[112] B. Pont, The Pierre Auger collaboration, "A Large Radio Detector at the Pierre AugerObservatory – Measuring the Properties of CosmicRays up to the Highest Energies", in *Proceedings, 36th International Cosmic Ray Conference (ICRC 2019)*, vol. ICRC2019, p. 395, 2019, `https://pos.sissa.it/358/395/pdf`.

[113] M. Platino, The Pierre Auger collaboration, "AMIGA - Auger Muons and Infill for the Ground Array of thePierre Auger Observatory", in *Proceedings, 31st Interational Cosmic Ray Conference (ICRC 2009)*, 2009, `https://galprop.stanford.edu/elibrary/icrc/2009/preliminary/pdf/icrc0184.pdf`.

[114] F. Suarez, The Pierre Auger collaboration, "The AMIGA muon detectors of the Pierre Auger Observatory: overview and status", in *Proceedings, 33rd International Cosmic Ray Conference (ICRC2013)*, p. 0712, 2013, `http://www.cbpf.br/%7Eicrc2013/papers/icrc2013-0712.pdf`.

[115] Hamamatsu Photonics, *Photomultiplier Tube R8619 datasheet*, `https://www.hamamatsu.com/resources/pdf/etd/R8619_TPMH1331E.pdf`, Dec, 2014.

[116] A. Castellina, The Pierre Auger collaboration, "The dynamic range of the AugerPrime Surface Detector: technical solution and physics reach", in *Proceedings, 35th International Cosmic Ray Conference (ICRC 2017)*, vol. ICRC2017, p. 397, 2017.

[117] T. Suomijärvi, The Pierre Auger collaboration, "New electronics for the surface detectors of the Pierre Auger Observatory", in *Proceedings, 35th International Cosmic Ray Conference (ICRC 2017)*, vol. ICRC2017, p. 450, 2017.

[118] J. Zorn et al., "The first measurement with the FD operated at a reduced PMT gain." Pierre Auger internal note, GAP2015-021, Mar., 2015.

[119] T. Huege, "Radio detection of cosmic ray air showers in the digital era", *Phys. Rept.* **620** (2016) 1, DOI:10.1016/j.physrep.2016.02.001, arXiv:`1601.07426`.

[120] A. Aab et al., The Pierre Auger collaboration, "Observation of inclined EeV air showers with the radio detector of the Pierre Auger Observatory", *JCAP* **1810** (2018) 026, DOI:10.1088/1475-7516/2018/10/026, arXiv:`1806.05386`.

[121] R. Šmida, The Pierre Auger collaboration, "Scintillator detectors of AugerPrime", in *Proceedings, 35th International Cosmic Ray Conference (ICRC 2017)*, vol. ICRC2017, p. 390, 2017.

[122] J. Pękala, The Pierre Auger collaboration, "Production and Quality Control of the Scintillator Surface Detector for the AugerPrime Upgrade of thePierre Auger Observatory", in *Proceedings, 36th International Cosmic Ray Conference (ICRC 2019)*, vol. ICRC2019, p. 380, 2019, `https://pos.sissa.it/358/380/pdf`.

[123] A. Pla-Dalmau, A. D. Bross and V. V. Rykalin, "Extruding plastic scintillator at Fermilab", .

[124] KURARAY CO., LTD., *Wavelength Shifting Fibers*, `http://kuraraypsf.jp/psf/ws.html`.

[125] ELJEN TECHNOLOGY, *Optical Cement EJ-500*, `https://eljentechnology.com/images/products/data_sheets/EJ-500.pdf`, Jan., 2016.

[126] Hamamatsu Photonics, *Photomultiplier Tube R9420 datasheet*, `https://www.hamamatsu.com/resources/pdf/etd/R9420_TPMH1296E.pdf`, Dec, 2014.

[127] T. Bretz et al., "The Aachen Muon Detector for testing the local production of Scintillating Surface Detectors for AugerPrime", in *Proceedings, 36th International Cosmic Ray Conference (ICRC 2019)*, vol. ICRC2019, p. 203, 2019, `https://pos.sissa.it/358/203/pdf`.

[128] Paul Scherrer Institute, *DRS4 Evaluation Board*, `https://www.psi.ch/en/drs/evaluation-board`, Oct., 2019.

[129] R. Meissner, "Development and Characterisation of a Scintillator Based Muon Detector with SiPM Readout for Air Shower Experiments", Master's thesis, RWTH Aachen University, 2015.

[130] Hamamatsu Photonics, *Multi-Pixel Photon Counter S13360 series*, https://www.hamamatsu.com/resources/pdf/ssd/s13360_series_kapd1052e.pdf, Aug, 2016.

[131] OMEGA - Organisation de Micro-Electronique Générale Avancée, Centre National de la recherche scientifique, *EASIROC*, https://portail.polytechnique.edu/omega/en/products/products-presentation/easiroc.

[132] LEMO, *S Connector*, https://www.lemo.com/en/products/low-voltage-connector/s-connector?country=Global, Oct., 2019.

[133] R. Brun and F. Rademakers, "ROOT: An object oriented data analysis framework", *Nucl. Instrum. Meth.* **A389** (1997) 81, DOI:10.1016/S0168-9002(97)00048-X.

[134] S. Butterworth, "On the Theory of Filter Amplifiers", *Experimental Wireless and the Wireless Engineer* **7** (1930) 536.

[135] N. Ricker, "Wavelet functions and their polynomials", *Geophysics* **9** (1944) 314, DOI:10.1190/1.1445082, [https://pubs.geoscienceworld.org/geophysics/article-pdf/9/3/314/3241315/314.pdf].

[136] R. J. McIntyre, "Theory of Microplasma Instability in Silicon", *Journal of Applied Physics* **32** (1961) 983, DOI:10.1063/1.1736199.

[137] R. H. Haitz, "Model for the Electrical Behavior of a Microplasma", *Journal of Applied Physics* **35** (1964) 1370, DOI:10.1063/1.1713636.

[138] V. Golovin, "Avalanche Photodetector", Patent No. RU2142175, Russian Agency for Patents and Trademark, 1998.

[139] Z. Sadygov, "Avalanche Detector", Patent No. RU2102820, Russian Agency for Patents and Trademark, 1998.

[140] D. Renker and E. Lorenz, "Advances in solid state photon detectors", *Journal of Instrumentation* **4** (2009) P04004, DOI:10.1088/1748-0221/4/04/p04004.

[141] N. Otte, "The Silicon Photomultiplier: A New Device for High Energy Physics, Astroparticle Physics, Industrial and Medical Applications", *eConf* **C0604032** (2006) 0018.

[142] ON Semiconductor, *RB-Series SiPM Sensors*, https://www.onsemi.com/pub/Collateral/MICRORB-SERIES-D.PDF, May, 2019.

[143] Hamamatsu Photonics, *Multi-Pixel Photon Counter S14160 series*, https://www.hamamatsu.com/resources/pdf/ssd/s14160-1310ps_etc_kapd1070e.pdf, Nov, 2019.

[144] K. K. Ng, *Complete Guide to Semiconductor Devices, Second Edition.* John Wiley & Sons, Ltd, 2009, DOI:10.1002/9781118014769, [https://www.onlinelibrary.wiley.com/doi/book/10.1002/9781118014769].

[145] S. M. Sze and K. K. Ng, *Physics of Semiconductor Devices.* John Wiley & Sons, Ltd, 2006, DOI:10.1002/0470068329, [https://www.onlinelibrary.wiley.com/doi/book/10.1002/0470068329].

[146] F. Acerbi and S. Gundacker, "Understanding and simulating SiPMs", *NIM A* **926** (2019) 16 , DOI:10.1016/j.nima.2018.11.118.

[147] Hamamatsu Photonics, *Physics and operation of the MPPC silicon photomultiplier*, `https://hub.hamamatsu.com/jp/en/technical-note/sipm-physics-operation/index.html`, Feb, 2014.

[148] ON Semiconductor, *C-Series SiPM Sensors*, `https://www.onsemi.com/pub/Collateral/MICROC-SERIES-D.PDF`, Nov, 2018.

[149] SensL, *Introduction to SiPM - Technical Note*, `https://www.sensl.com/downloads/ds/TN%20-%20Intro%20to%20SPM%20Tech.pdf`, 2011.

[150] Hamamatsu Photonics, *Power supply for MPPC C11204-02*, `https://www.hamamatsu.com/resources/pdf/ssd/c11204-02_kacc1242e.pdf`, Nov, 2019.

[151] Tektronix, *Keithley Series 6400 Picoammeter*, `https://www.tek.com/keithley-low-level-sensitive-and-specialty-instruments/keithley-series-6400-picoammeters`, 2019.

[152] C. Günther, "Temperature dependence of the SiPMs and the front-end electronics for AugerPrime", Bachelor's thesis, RWTH Aachen University, 2016.

[153] T. Bretz et al., "A compact and light-weight refractive telescope for the observation of extensive air showers", *Journal of Instrumentation* **13** (2018) P07024, DOI:10.1088/1748-0221/13/07/P07024, arXiv:`1804.01781`.

[154] J. Schumacher, "Front-end Electronics for Silicon Photomultipliers", Master's thesis, RWTH Aachen University, 2014.

[155] J. Schumacher, *Exploring silicon photomultipliers for the upgrade of the Pierre Auger observatory*, Ph.D. thesis, RWTH Aachen University, 2019. DOI:10.18154/RWTH-2019-01541.

[156] G. Vuye et al., "Temperature dependence of the dielectric function of silicon using in situ spectroscopic ellipsometry", *Thin Solid Films* **233** (1993) 166 , DOI:10.1016/0040-6090(93)90082-Z.

[157] M. V. Nemallapudi et al., "SiPM angular response and enhanced light extraction", in *2013 IEEE Nuclear Science Symposium and Medical Imaging Conference (2013 NSS/MIC)*, pp. 1–5, Oct, 2013, DOI:10.1109/NSSMIC.2013.6829586.

[158] D. Wilson, "Angular Dependence of the Relative Photon Detection Efficiency of Silicon Photomultipliers", Bachelor's thesis, RWTH Aachen University, 2012.

[159] W. G. Oldham, R. R. Samuelson and P. Antognetti, "Triggering phenomena in avalanche diodes", *IEEE Transactions on Electron Devices* **19** (1972) 1056, DOI:10.1109/T-ED.1972.17544.

[160] G. Zappalà et al., "Study of the photo-detection efficiency of FBK high-density silicon photomultipliers", *Journal of Instrumentation* **11** (2016) P11010, DOI:10.1088/1748-0221/11/11/p11010.

[161] P. Eckert et al., "Characterisation studies of silicon photomultipliers", *NIM A* **620** (2010) 217 , DOI:10.1016/j.nima.2010.03.169.

[162] A. Otte et al., "A measurement of the photon detection efficiency of silicon photomultipliers", *NIM A* **567** (2006) 360 , DOI:10.1016/j.nima.2006.05.145.

[163] J. Bourbeau and Z. Hampel-Arias, "Pyunfold: A python package for iterative unfolding", *The Journal of Open Source Software* **3** (2018) 741, DOI:10.21105/joss.00741.

[164] G. D'Agostini, "A Multidimensional unfolding method based on Bayes' theorem", *Nucl. Instrum. Meth. A* **362** (1995) 487, DOI:10.1016/0168-9002(95)00274-X.

[165] Hamamatsu Photonics, *Multi-Pixel Photon Counter S10362 series*, `https://www.hamamatsu.com/`.

[166] A. N. Otte, "On the efficiency of photon emission during electrical breakdown in silicon", *NIM A* **610** (2009) 105 , DOI:10.1016/j.nima.2009.05.085.

[167] F. Rehbein et al., "Performance of SensL MicroFJ-60035-TSV SiPMs with and without optically coupled light guides", *JINST* (2020) tbp.

[168] W. Sul, C. Lee and G. Cho, "Influence of Guard-Ring Structure on the Dark Count Rates of Silicon Photomultipliers", *IEEE Electron Device Letters* **34** (2013) 336, DOI:10.1109/LED.2012.2236296.

[169] M. L. Knoetig, The FACT collaboration, "FACT - Long-term stability and observations during strong Moon light", in *Proceedings, 33rd International Cosmic Ray Conference (ICRC2013)*, p. 0695, 2013, arXiv:`1307.6116`, `http://www.cbpf.br/%7Eicrc2013/papers/icrc2013-0695.pdf`.

[170] A. Haungs, The JEM-EUSO collaboration, "Towards a SiPM based fluorescence camera for JEM-EUSO", in *Proceedings, 34th International Cosmic Ray Conference (ICRC 2015)*, vol. ICRC2015, p. 643, 2015, `https://pos.sissa.it/236/643/pdf`.

[171] S. I. Cooper, The CMS collaboration, "Phase I Upgrade of the CMS Hadron Calorimeter", *Nuclear and Particle Physics Proceedings* **273-275** (2016) 1002 , DOI:10.1016/j.nuclphysbps.2015.09.157.

[172] N. Otte et al., "The sipm — a new photon detector for pet", *Nuclear Physics B - Proceedings Supplements* **150** (2006) 417 , DOI:10.1016/j.nuclphysbps.2004.08.048.

[173] S. Fukuda et al., "The Super-Kamiokande detector", *NIM A* **501** (2003) 418 , DOI:10.1016/S0168-9002(03)00425-X.

[174] S. Cova et al., "Avalanche photodiodes and quenching circuits for single-photon detection", *Appl. Opt.* **35** (1996) 1956, DOI:10.1364/AO.35.001956.

[175] F. Corsi et al., "Electrical characterization of silicon photo-multiplier detectors for optimal front-end design", in *2006 IEEE Nuclear Science Symposium Conference Record*, vol. 2, pp. 1276–1280, Oct, 2006, DOI:10.1109/NSSMIC.2006.356076.

[176] F. Corsi et al., "Modelling a silicon photomultiplier (SiPM) as a signal source for optimum front-end design", *NIM A* **572** (2007) 416 , DOI:10.1016/j.nima.2006.10.219.

[177] J. Bird, *Electrical Circuit Theory and Technology*. Routledge, 6 ed., 2017.

[178] Wolfram Research, Inc., "Mathematica, Version 12.0." `https://www.wolfram.com/mathematica`.

[179] R. Joppe, "Preparation and first applications of a digital SiPM", Bachelor's thesis, RWTH Aachen University, 2017.

[180] Rohde & Schwarz, *HMP4000 Netzgeräteserie*, `https://www.rohde-schwarz.com/de/produkt/hmp4000-produkt-startseite_63493-47360.html`, 2019.

[181] Hamamatsu Photonics, *private communication*, 2020.

[182] M. Rongen and M. Schaufel, "Design and evaluation of a versatile picosecond light pulser", *JINST* **13** (2018) P06002, DOI:10.1088/1748-0221/13/06/P06002, arXiv:`1805.00822`.

[183] Stanford Research Systems, *Digital Delay/Pulse Generator*, `https://thinksrs.com/downloads/pdfs/catalog/DG535c.pdf`.

[184] Thorlabs Inc., *IS200-4 - ⌀2" Integrating Sphere*, `https://www.thorlabs.com/thorproduct.cfm?partnumber=IS200-4`, May, 2020.

[185] C. Heidemann, *Optical Set-Up for Automatised SiPM Characterisation*, Ph.D. thesis, RWTH Aachen University, 2016.

[186] Agilent Technologies, *Agilent InfiniiVision 3000 X-Series Oscilloscopes*, `http://web.mit.edu/6.115/www/document/agilent_mso-x_manual.pdf`, 2013.

[187] F. James, *Minuit - Function Minimization and Error Analysis*, `https://root.cern.ch/sites/d35c7d8c.web.cern.ch/files/minuit.pdf`, 1994.

[188] J. A. Nelder and R. Mead, "A Simplex Method for Function Minimization", *The Computer Journal* **7** (1965) 308, DOI:10.1093/comjnl/7.4.308.

[189] Hamamatsu Photonics, *Si photodiodes with BNC connector*, `https://www.hamamatsu.com/resources/pdf/ssd/s2281_series_kspd1044e.pdf`, May, 2020.

[190] T. Bretz et al., "SiPMs – A revolution for high dynamic range applications", in *Proceedings, 35th International Cosmic Ray Conference (ICRC 2017)*, vol. ICRC2017, p. 472, 2017.

[191] I. Valiño, "The flux of ultra-high energy cosmic rays after ten years of operation of the Pierre Auger Observatory", in *Proceedings, 34th International Cosmic Ray Conference (ICRC 2015)*, vol. ICRC2015, p. 271, 2015, `https://pos.sissa.it/236/271/pdf`.

[192] L. Su and F. Li, "Deconvolution of Defocused Image with Multivariate Local Polynomial Regression and Iterative Wiener Filtering in DWT Domain", *Mathematical Problems in Engineering* (2010) 605241, DOI:10.1155/2010/605241.

[193] N. Wiener, *Extrapolation, interpolation, and smoothing of stationary time series: with engineering applications*. Technology Press of the Massachusetts Institute of Technology, 1964.

[194] Hamamatsu Photonics, *Si APD, MPPC*, `https://www.hamamatsu.com/resources/pdf/ssd/e03_handbook_si_apd_mppc.pdf`, May, 2020.

[195] A. Biland et al., "FACT - Status and Experience from Three Years Operation of the First SiPM Camera", in *Proceedings, 34th International Cosmic Ray Conference (ICRC 2015)*, vol. ICRC2015, p. 1032, 2015, `https://pos.sissa.it/236/1032/pdf`.

[196] T. Bretz et al., "An integrated general purpose SiPM based optical module with a high dynamic range", *JINST* **13** (2018) P06001, DOI:10.1088/1748-0221/13/06/P06001, arXiv:`1803.04841`.

[197] C. Peters et al., *Prospects of Silicon Photomultipliers for Ground-Based Cosmic Ray Experiments*. `https://journals.jps.jp/doi/pdf/10.7566/JPSCP.19.011030`. DOI:10.7566/JPSCP.19.011030.

[198] J. Kemp et al., "Air Shower Measurement with a SiPM Based Scintillator Detector", in *Proceedings, 36th International Cosmic Ray Conference (ICRC 2019)*, vol. ICRC2019, p. 311, 2019, `https://pos.sissa.it/358/311/pdf`.

[199] Saint-Gobain, *BC-600 Optical Cement datasheet*, 2016.

[200] R. Winston, "Light collection within the framework of geometrical optics∗", *J. Opt. Soc. Am.* **60** (1970) 245, DOI:10.1364/JOSA.60.000245.

[201] DentalChip Service Center, 21684 Stade, Germany, `http://www.dentalchip.de`.

[202] Zemax LLC, *OpticStudio*, `https://www.zemax.com/products/opticstudio`, 2019.

[203] S. Nieswand, "Measurement of the exit characteristics of light from optical multimode plastic fibres", Master's thesis, RWTH Aachen University, 2014.

[204] Epoxy Technology, *EPO-TEK 310M-2 Product Information Sheet*, `http://www.epotek.com/site/administrator/components/com_products/assets/files/Style_Uploads/310M-2.pdf`, 2017.

[205] A. Biland et al., "Calibration and performance of the photon sensor response of FACT – The First G-APD Cherenkov telescope", *JINST* **9** (2014) P10012, DOI:10.1088/1748-0221/9/10/P10012, arXiv:`1403.5747`.

[206] P. Doll et al., "Muon tracking detector for the air shower experiment KASCADE", *Nucl. Instrum. Meth.* **A488** (2002) 517, DOI:10.1016/S0168-9002(02)00560-0.

[207] D. Schmidt, *Sensitivity of AugerPrime to the masses of ultra-high-energy cosmic rays*, Ph.D. thesis, Karlsruher Institut für Technologie (KIT), 2019. DOI:10.5445/IR/1000093730.

[208] A. Taboada Núñez, *Analysis of the First Data of the AugerPrime Detector Upgrade*, Ph.D. thesis, Karlsruher Institut für Technologie (KIT), 2020. DOI:10.5445/IR/1000104548.

[209] S. Argiro et al., "The Offline Software Framework of the Pierre Auger Observatory", *Nucl. Instrum. Meth. A* **580** (2007) 1485, DOI:10.1016/j.nima.2007.07.010, arXiv:`0707.1652`.

[210] "Napoli+Praha library of CORSIKA and Offline (hybrid) showers." `https://www.auger.unam.mx/AugerWiki/NapoliLibrary`, internal note.

[211] T. Pierog et al., "EPOS LHC: Test of collective hadronization with data measured at the CERN Large Hadron Collider", *Phys. Rev. C* **92** (2015) 034906, DOI:10.1103/PhysRevC.92.034906, arXiv:`1306.0121`.

[212] P. Ferreira, *t.b.a*, Ph.D. thesis, RWTH Aachen University, 2021.

[213] S. Ostapchenko, "Monte carlo treatment of hadronic interactions in enhanced pomeron scheme: Qgsjet-ii model", *Phys. Rev. D* **83** (2011) 014018, DOI:10.1103/PhysRevD.83.014018.

[214] E.-J. Ahn et al., "Cosmic ray interaction event generator SIBYLL 2.1", *Phys. Rev. D* **80** (2009) 094003, DOI:10.1103/PhysRevD.80.094003.

[215] E. W. Weisstein, *Millimeter/Submillimeter Fourier Transform Spectroscopy of Jovian Planet Atmospheres*, Ph.D. thesis, California Institute of Technology, 1996.

Declaration of pre-released partial results

Partial results of this work have already been pre-released in the following publications. The author of this thesis is author or coauthor of the publications. All publications are cited in this work where applicable:

[196] T. Bretz et al., "An integrated general purpose SiPM based optical module with a high dynamic range", *JINST* **13** (2018) P06001, DOI:10.1088/1748-0221/13/06/P06001, arXiv:1803.04841

[198] J. Kemp et al., "Air Shower Measurement with a SiPM Based Scintillator Detector", in *Proceedings, 36th International Cosmic Ray Conference (ICRC 2019)*, vol. ICRC2019, p. 311, 2019, https://pos.sissa.it/358/311/pdf

[127] T. Bretz et al., "The Aachen Muon Detector for testing the local production of Scintillating Surface Detectors for AugerPrime", in *Proceedings, 36th International Cosmic Ray Conference (ICRC 2019)*, vol. ICRC2019, p. 203, 2019, https://pos.sissa.it/358/203/pdf

[190] T. Bretz et al., "SiPMs – A revolution for high dynamic range applications", in *Proceedings, 35th International Cosmic Ray Conference (ICRC 2017)*, vol. ICRC2017, p. 472, 2017

The development of the electronics of the SiPM based optical module has been performed by Johannes Schumacher. The MiniAMD used in the test stand for the SSDs has been developed by Lukas Middendorf and Christine Peters. Their work is cited where applicable:

[155] J. Schumacher, *Exploring silicon photomultipliers for the upgrade of the Pierre Auger observatory*, Ph.D. thesis, RWTH Aachen University, 2019. DOI:10.18154/RWTH-2019-01541

[73] C. Peters, *Development of scintillator detectors for measuring muons and air showers*, Ph.D. thesis, RWTH Aachen University, 2019. DOI:10.18154/RWTH-2019-05267

[74] L. Middendorf, *Data acquisition for an SiPM based muon detector*, Ph.D. thesis, RWTH Aachen University, 2019. DOI:10.18154/RWTH-2018-225274

Acronyms

ADC Analog-to-Digital-Converter. 45, 59, 158, 159, 172, 174, 176

AERA Auger Engineering Radio Array. 38, 49

AGN Active Galactic Nucleus. 23

AMD Aachen Muon Detector. 149

AMIGA Auger Muons and Infill for the Ground Array. 48

APD Avalanche Photodiode. 75

CDAS Central Data Acquisition System. 44

CG Calibration Gain. 133, 160, 171, 172, 174, 204

CLF Central Laser Facility. 38

CMB Cosmic Microwave Background. 13

DAQ Data Acquistion. 54, 55

DCR Dark Count Rate. 86, 87, 130, 163, 166–170

DRS4 Domino Ring Sampler of version 4. 57, 59, 61, 64, 195

DSA Diffusive Shock Acceleration. 9

EASIROC Extended Analogue SI-pm ReadOut Chip. 56

FADC flash Analog-to-Digital-Converter. 43, 48

FD Fluorescence Detector. 37–42, 45–47, 49, 187, 188

FoV Field of View. 39

FPGA Field Programmable Gate Array. 48

FWHM Full Width at Half Maximum. 69, 70

G-APD Geiger-mode Avalanche Photodiode. 75, 79, 80, 89, 97

GMF Galactic Magnetic Field. 6, 10

HEAT High Elevation Auger Telescopes. 37–39

HG High Gain. 48, 160, 170–172, 174, 204

HV High Voltage. 49, 53, 57–60, 69

IACT Imaging Air-Cherenkov Telescope. 28, 88, 122

KIT Karlsruhe Institute of Technology. 54, 70, 152, 153, 195, 197, 198

LDF Lateral Distribution Function. 28, 45, 46, 48, 174, 177, 178, 180–183, 185, 188

LED Light-Emitting Diode. 82, 85, 99, 101, 112, 113, 115, 138, 149

LG Low Gain. 48, 158, 204

MiniAMD Mini Aachen Muon Detector. 54–57, 59, 61, 62, 66, 149, 225

MIP Minimum Ionizing Particle. 30, 31, 53, 54, 56, 59, 60, 65, 67–70, 133, 149–151, 160, 162, 163, 167, 170–172, 174, 177, 179, 198

MPV Most Probable Value. 30–32, 69, 160, 163, 170

NIM Nuclear Instrumentation Module. 57

NSB Night Sky Background. 47, 49

p.d.f. Probability Density Function. 163–166

p.e. Photon Equivalent. 54, 59–62, 64–67, 69, 70, 82, 87, 107, 108, 111–113, 116, 119, 123–125, 129, 130, 132, 133, 149–151, 160, 163–167, 170, 180, 195, 196, 204

PCB Printed Circuit Board. 99, 130, 132, 133, 135

PDE Photon Detection Efficiency. 79, 82, 84–86, 94–96, 98, 99, 103, 106, 107, 111, 113, 114, 116, 139, 142

PMMA Polymethyl Methacrylate. 53, 130, 134–136, 139, 140, 146–149

PMT Photomultiplier Tube. 39, 40, 43, 44, 47–49, 52–55, 57–61, 66, 67, 87–89, 129, 130, 132, 134, 142, 147, 152–154, 157–160, 162, 168–172, 174, 176, 179, 180, 204

PPA Preproduction Array. 180

PVC Polyvinyl Chloride. 53, 57, 58, 132

RMS Root Mean Square. 110, 115, 155, 159, 200

SBG Starburst Galaxy. 23, 24

SD Surface Detector. 37–39, 41–49, 51, 157, 158, 184, 185, 188

SDP Shower Detector Plane. 41, 42

SHV Safe High Voltage. 57

SiPM Silicon Photomultiplier. 2, 56, 60, 75, 76, 79–103, 106–108, 110–126, 129–136, 139–142, 144–154, 157–160, 162, 163, 166–174, 176, 178–180, 191, 192, 203–205, 225

SMA Sub-Miniature-A. 57, 59

SNR Signal-to-Noise Ratio. 106, 124, 133

sPMT Small PMT. 47, 48

SSD Scintillator Surface Detector. 48, 49, 51–55, 57, 58, 60, 61, 64–67, 69, 70, 72, 73, 122, 129, 130, 132–135, 139, 144, 147, 149, 152–155, 157–160, 163, 167–174, 176–188, 191, 195, 197, 204, 205, 225

SSH Secure Shell. 56

TA Telescope Array. 22, 23, 29

UART Universal Asynchronous Receiver/Transmitter. 133

UB Unified Board. 43, 47, 48, 159, 180

UHECR Ultra High Energy Cosmic Ray. 5, 7, 12, 13, 21–24, 28, 29, 33, 37, 47, 129

UMD Underground Muon Detector. 47–49, 51

USB Universal Serial Bus. 130, 132, 133

UUB Upgraded Unified Board. 47, 48, 61, 130, 132, 133, 159–161, 167, 168, 171, 174, 180

UV ultraviolett. 138

VCSEL Vertical Cavity Surface Emitting Laser. 99, 100, 102

VEM Vertical Equivalent Muon. 44, 45, 177

WCD Water-Cherenkov Detector. 33, 34, 37, 47, 48, 51, 159, 160, 162, 163, 168, 169, 172, 177–188, 191

WLS Wavelength Shifting. 51, 53, 56, 129, 130, 133–135, 138–140, 149, 150, 170, 180

XLF eXtreme Laser Facility. 38

Acknowledgements - Danksagungen

Das Erstellen dieser Dissertation wäre nicht möglich gewesen ohne die tatkräftige Unterstützung unzähliger Menschen.

Zunächst gilt mein Dank Herrn Prof. Hebbeker dafür, dass er mir die Möglichkeit gegeben hat, diese Arbeit in einer tollen Arbeitsgruppe zu erstellen und die Mitarbeit in einer großen Kollaboration unterstützte.

Bedanken möchte ich mich bei Junior-Professor Thomas Bretz für die Begutachtung dieser Arbeit sowie die gute Betreuung in wöchentlichen Meetings oder durch die schnelle Beantwortung von E-Mails. Weiterhin freue ich mich sehr über die Unterstützung bei allen Belangen, die im Austausch mit der Kollaboration von Nöten waren.

Dann gilt mein Dank den Kollegen am Institut und besonders in der Auger-Arbeitsgruppe. Die wöchentlichen Arxiv-Meetings und regelmäßigen FD-Schichten waren zwar anstregend aber haben immer Freude bereitet genauso wie die jährlichen Asados. Hervorheben möchte ich Paulo Ferreira, Adrianna García, Lukas Middendorf, Christine Peters und Johannes Schumacher, mit denen ich immer gerne zusammen gearbeitet habe. Besonders bedanken möchte ich mich bei Adrianna García und Christine Peters für das Korrekturlesen meiner Arbeit ebenso wie bei Paulo Ferreira, der gerade in der Endphase meiner Arbeit ohne Zögern meine Anfragen zum Korrekturlesen und zu neuen Simulationen beantwortet hat. Außerdem gilt mein Dank Tobias Pan für die Hilfe bei den SSD Tests.

Weiterhin möchte ich mich bei den Kollegen außerhalb der Aachener Arbeitsgruppe bedanken, die meine Arbeit unterstützt haben. Das sind ganz besonders Radomir Šmída und Darko Veberič vom KIT. Außerdem die Mitarbeiter des Observatoriums in Malargüe und dort im Besonderen Ricardo Sato.

Martin Rongen danke ich für die Bereitstellung des Picosekunden-Pulsers, ohne den die SiPM-Messungen nicht möglich gewesen wären.

Diese Arbeit wäre auch nicht möglich gewesen ohne die Unterstützung durch die Elektronik- und Mechanik-Werkstätten des III. Physikalischen Instituts A. Mein herzlicher Dank gilt allen Mitarbeitern für die angenehme Zusammenarbeit, auch wenn mal wieder spontane Wünsche geäußert wurden.

Zuletzt und doch am wichtigsten gilt mein Dank meiner Familie und meiner Freundin Esther Dombrowski für die tolle Unterstützung und gerade gegen Ende der Arbeit auch dafür, es mit mir ausgehalten zu haben.

Die in der Arbeit präsentierten Simulationen und Datenanalysen wurden teilweise mit Rechenressourcen durchgeführt, die von der RWTH Aachen University unter dem Projekt rwth0364 zur Verfügung gestellt wurden.

Eidesstattliche Erklärung

Ich, Julian Kemp

erkläre hiermit, dass diese Dissertation und die darin dargelegten Inhalte die eigenen sind und selbstständig, als Ergebnis der eigenen originären Forschung, generiert wurden.

Hiermit erkläre ich an Eides statt

1. Diese Arbeit wurde vollständig oder größtenteils in der Phase als Doktorand dieser Fakultät und Universität angefertigt;

2. Sofern irgendein Bestandteil dieser Dissertation zuvor für einen akademischen Abschluss oder eine andere Qualifikation an dieser oder einer anderen Institution verwendet wurde, wurde dies klar angezeigt;

3. Wenn immer andere eigene- oder Veröffentlichungen Dritter herangezogen wurden, wurden diese klar benannt;

4. Wenn aus anderen eigenen- oder Veröffentlichungen Dritter zitiert wurde, wurde stets die Quelle hierfür angegeben. Diese Dissertation ist vollständig meine eigene Arbeit, mit der Ausnahme solcher Zitate;

5. Alle wesentlichen Quellen von Unterstützung wurden benannt;

6. Wenn immer ein Teil dieser Dissertation auf der Zusammenarbeit mit anderen basiert, wurde von mir klar gekennzeichnet, was von anderen und was von mir selbst erarbeitet wurde;

7. Ein Teil oder Teile dieser Arbeit wurden zuvor veröffentlicht und zwar in:

   [196] T. Bretz et al., "An integrated general purpose SiPM based optical module with a high dynamic range", *JINST* **13** (2018) P06001, DOI:10.1088/1748-0221/13/06/P06001, arXiv:`1803.04841`

   [198] J. Kemp et al., "Air Shower Measurement with a SiPM Based Scintillator Detector", in *Proceedings, 36th International Cosmic Ray Conference (ICRC 2019)*, vol. ICRC2019, p. 311, 2019, `https://pos.sissa.it/358/311/pdf`

[127] T. Bretz et al., "The Aachen Muon Detector for testing the local production of Scintillating Surface Detectors for AugerPrime", in *Proceedings, 36th International Cosmic Ray Conference (ICRC 2019)*, vol. ICRC2019, p. 203, 2019, `https://pos.sissa.it/358/203/pdf`

[190] T. Bretz et al., "SiPMs – A revolution for high dynamic range applications", in *Proceedings, 35th International Cosmic Ray Conference (ICRC 2017)*, vol. ICRC2017, p. 472, 2017

Aachen, den

Julian Kemp